



The University of
Nottingham

UNITED KINGDOM • CHINA • MALAYSIA

University of Nottingham

Department of Chemical and Environmental

Engineering

Testing and Application of Wire Mesh Sensors in

Vertical Gas Liquid Two-Phase Flow

Safa Sharaf, M.Sc.

Thesis submitted to the University of Nottingham

for the degree of Doctor of Philosophy

August 2011

BEST COPY

AVAILABLE

Variable print quality

**THESIS CONTAINS
CD/DVD**

ABSTRACT

The behaviour of gas-liquid two-phase flow has been studied extensively in the past at near atmospheric pressure in small diameter pipes. However, the industrial reality is the utilisation of large diameter pipes at elevated pressures and there is significantly less information available in this area due principally to the cost of investigating large diameter pipes. This research relied on using large-scale laboratory facilities at the University of Nottingham, and on using newly developed state of the art multiphase instrumentation. This study tested and applied the wire mesh sensor (WMS). The work included in this thesis utilised the two variants of the WMS; the already established Conductivity WMS and the recently developed Capacitance WMS and the two sensors were compared against each other. The Capacitance WMS was recently supplied by HZDR (Research Institution, Germany) to the University of Nottingham. Extensive experimental campaigns were carried out with this novel sensor. The WMS was initially tested and validated against several other instruments such as high speed camera and gamma densitometry. It was subsequently applied to a large diameter bubble column and large diameter pipe with two phase flow. The aims of this project was to gain a better understanding of the flow patterns and their transitions in large diameter pipes and to provide real experimental data to assist researchers and engineers in producing relevant and physically sound models for use in larger diameter pipes. As a result of this study, novel and interesting structures which have been labelled as wisps were discovered in large diameter pipes. In addition the WMS was used extensively for the first time on bubble columns in order to assess its suitability for such an application.

ACKNOWLEDGEMENTS

It has been a pleasure and a privilege to work with Prof. Barry Azzopardi, and to study at the University of Nottingham. It has been a great learning and enjoyable experience. I am extremely grateful to Prof. Azzopardi for his informality, for his support, for his open door policy, and for providing me “space” to develop. I thank him for the many opportunities and to teach his students WELLFLO for several years. Here I wish to thank Dr. Kevin Wade from SPT Group (formerly Neotec) for giving me great support on industrial code WELLFLO and for providing me with a licence to use for my studies and to teach the students.

I wish to express my gratitude for the support of the UK Engineering and Physical Sciences Research Council (EPSRC) and the following organisations as part of the TMF consortium: ASCOMP, GL Noble Denton; BP Exploration; CD-adapco; Chevron; ConocoPhillips; ENI; ExxonMobil; FEESA; IFP Energies nouvelles; Institutt for Energiteknikk; PDVSA (INTEVEP); Petrobras; PETRONAS; SPT Group; Shell; SINTEF; Statoil and TOTAL.

TMF short for Transient Multiphase Flow is collaboration between research and industry to investigate areas of interest for both in multiphase flow and I am particularly grateful to Prof. Geoff Hewitt and Mr Colin Weil for involving me in TMF. Thanks to the University of Nottingham and the Royal Academy of Engineering for providing financial support to allow me to attend WCIPT6 in Beijing, China. I wish to thank my second supervisor Dr. Paul Langston for his great input and help with modelling and using Matlab. Many thanks to Dr. John Andresen and Prof. Nidal Hilal for the various discussions we’ve had throughout the past three years.

Sincere thanks to Dr. Uwe Hampel for giving me the opportunity, to go to HZDR (previously FZD) as a Guest Scientist, and spend three crucial months there and do several useful exercises including training on the wire mesh sensor. I thank him for his enthusiasm and good sense of humour. I acknowledge the Saxony state for providing financial assistance for my placement at HZDR. Here I also wish to thank everyone at HZDR for welcoming me in Dresden. In particular, I wish to thank Dr. Sebastian Thiele, and Mr. Mathias Beyer and Dr. Cornilius Zippe. I hope to visit HZDR again in the future. Special thanks to Dr. Marco Da Silva, one of the main inventors of the wire mesh sensor. I highly appreciated his input and feedback over the past couple of years. I wish to thank Dr. Maria Fujosova-Zednikova for coming to the UK and for our collaboration on bubble columns.

I wish to thank ALL the wonderful technicians we have in our department. They are the unsung heroes. I thank Vikki, Marion and Fred for lab support. On the manufacturing side, I wish to thank everyone including Phil, Mick, Jim, Reg, Terry and Mel. Thanks to Paul for his excellent support on the various rigs. I wish to thank all my colleagues who are part of the multiphase team: Ryuhei, Mohammed, Lokman, Mukhtar, Abdul, Maggie, Aime, Nazrul, Bayo, Valente, Donglin, Vicky and Timothy. Special thanks to Peter van der Meulen. We achieved a great deal when we put our heads together! I wish to thank the library staff for all their help in obtaining my ILL papers and journals. In particular I wish to thank Jennifer Coombes, and Sue Bingham.

Finally, I wish to thank all my family for their support, encouragement and patience. I wish to dedicate this thesis to them and especially to my late father. I hope they are all proud of this effort.

TABLE OF CONTENTS

ABSTRACT	II
ACKNOWLEDGEMENTS	III
TABLE OF CONTENTS	V
LIST OF FIGURES	VIII
LIST OF TABLES	XVI
CHAPTER 1: INTRODUCTION	1
1.1. Multiphase flows	1
1.2. A brief historical note	3
1.3. Applications and problems	4
1.4. Aims and objectives.....	10
1.5. Outline of Thesis.....	11
CHAPTER 2: LITERATURE REVIEW	13
2.1. Introduction to Gas-Liquid flow	13
2.2. Flow Patterns	14
2.3. Gas Fraction.....	19
2.4. Slip Ratio U_R	22
2.5. Pressure Drop.....	23
2.6. Homogeneous Flow	23
2.7. Separated Flow	24
2.8. Frictional Pressure Drop	25
2.9. Signatures of the flow (PDF & PSD)	29
2.10. Structures in the flow.....	31
2.11. Flow Pattern Maps.....	32
2.12. What is churn flow?.....	38
2.12.1. Structures in churn flow.....	44
2.13. Flow pattern models	46
2.14. Flow pattern Transitions	47
2.15. Large Diameter Pipe Investigations.....	51
2.16. Mechanistic vs. Empirical Modelling.....	56
2.17. Computational Modelling in two-phase flow	57
CHAPTER 3: INSTRUMENTATION AND FACILITIES	60
3.1. Two-phase instruments (Intrusive vs. non-intrusive)	60
3.2. ECT.....	62
3.3. Conductance Probes.....	64
3.4. Specialist Instrument Wire Mesh Sensor (WMS)	66
3.4.1. Historical Background	66
3.4.2. Conductivity WMS and Capacitance WMS	68
3.4.3. What is the WMS measuring?	70
3.4.4. Operation of the WMS.....	71
3.5. Visualisation of the flow (Qualitative Data).....	79
3.6. Quantitative Data	81
3.7. Bubble Size Distribution.....	85
3.8. Test Facilities.....	86
3.8.1. Bubble Columns	86
3.8.2. 5 inch/127mm closed loop facility	89

CHAPTER 4: TESTING OF THE WMS.....	95
4.1. Introduction.....	95
4.2. Comparison between WMS and Gamma Ray	97
4.3. Experimental Methodology	98
4.4. Data Processing and Calibration.....	101
4.5. Results	104
4.6. Discussion.....	110
4.7. Comparison between CondWMS and CapWMS	114
4.7.1. 2D Visualisation	114
4.7.2. Three Dimensional Plots.....	115
4.7.3. Time Series	116
4.7.4. PDF	118
4.7.5. Statistical Analysis.....	118
4.7.6. Time Averaged Local Void Fraction.....	119
4.7.7. Radial Profiles	121
4.7.8. Bubble Size Distribution.....	122
4.7.9. Further comparisons	123
4.8. Comparison between WMS and ECT.....	125
4.9. Comparison between 50mm and 67mm pipe data.....	127
4.10. High speed camera testing of the WMS	128
4.11. Summary.....	131
CHAPTER 5: BUBBLE COLUMNS.....	132
5.1. Introduction.....	132
5.1.1. Bubble Column Design	133
5.1.2. Injection Methods	134
5.1.3. Flow maps and patterns in bubble columns.....	135
5.1.4. Void Fraction.....	136
5.1.5. Homogeneous/Heterogeneous Transition.....	139
5.1.6. Bubble Size Distribution.....	140
5.1.7. Bubble rise and slip velocity.....	142
5.1.8. Published experimental work	144
5.2. Experimental Techniques applied to bubble columns	146
5.3. Experimental details for this work.....	147
5.4. Results	150
5.4.1. Level Swell	150
5.4.2. Time Series and PDF	151
5.4.3. Frequencies (PSD).....	153
5.4.4. Cross-sectional averaged void	153
5.4.5. Radial profiles of void fraction.....	156
5.4.6. Bubble size distribution	157
5.4.7. Visualisation: Local voids	159
5.4.8. Visualisation: Cross-sectional voids.....	161
5.5. Comparison between 67mm and 127mm columns.....	167
5.6. WMS experiments with aqueous saline solutions	170
5.7. Comparison of data with published correlations	171
5.7.1. Level Swell	171
5.7.2. WMS cross-sectionally averaged void fraction.....	173
5.7.3. WMS radial profiles	174

5.7.4. Bubble size measured by WMS.....	175
5.8. Bubble Column Modelling	177
5.8.1. First modelling methodology.....	179
5.8.2. Second modelling methodology	180
5.8.3. Third modelling methodology	181
5.8.4. Fourth modelling methodology	183
5.8.5. Bubble Shape.....	185
5.8.6. Modelling conclusions and further modelling work.....	187
5.9. Summary.....	188
CHAPTER 6: LARGE DIAMETER PIPES	189
6.1. Introduction.....	189
6.2. Experimental Matrix.....	190
6.3. Results	190
6.3.1. Time series.....	191
6.3.2. Time and space averaged void fraction	191
6.3.3. Radial void profiles.....	196
6.3.4. Bubble size distribution/bubble size resolved voids.....	197
6.3.5. Visualisation (cross-sectional voids).....	199
6.4. Correlation of overall frequencies	203
6.5. Test of engineering methods with WMS data	204
6.5.1. Test for pressure drop	205
6.5.2. Test for void Fraction	207
6.5.3. Test for flow pattern	210
6.6. Comparison between 67 and 127mm diameter pipes	211
6.7. Wisp frequencies in churn flow.....	222
6.8. Flow pattern map(s) for the 127mm riser	226
6.9. CFD Simulation.....	227
6.10. Summary.....	230
CHAPTER 7: CONCLUSIONS/FURTHER WORK	231
7.1. Conclusions	231
7.2. Future Work.....	233
PUBLICATIONS	238
BIBLIOGRAPHY	240
NOMENCLATURE.....	254
APPENDIX A	256
APPENDIX B	261
APPENDIX C	277
APPENDIX D	281

LIST OF FIGURES

CHAPTER 1

Figure 1.1- Multiphase flow Schematic-Source Thermopedia.com	2
Figure 1.2- Early examples of two-phase flows: (Left) Hero's Turbine, (Right) 17th Century Compressor.....	3
Figure 1.3- Schematic of an offshore oil facility (Azzopardi, 2006).....	4
Figure 1.4- Pressure drop, from the well to the pipeline to the riser.	6
Figure 1.5- Offshore oil/gas extraction.....	7
Figure 1.6- Differences between large diameter (>100mm) and small diameter pipes (<100mm). Taylor bubbles not vident in tube on left. Also shown are wave profiles.	8
Figure 1.7- Comparison of bubble size distributions for 50mm and 200mm diameter pipes, superficial gas/liquid velocities of 0.53 m/s and 1 m/s respectively.	9
Figure 1.8- Deepwater Milestones (Source: www.Shell.com)	10

CHAPTER 2

Figure 2.1- Two-phase flow patterns; gas flow rate increasing from left to right.....	15
Figure 2.2- Slug/Churn/Annular in a cross-section of pipe	17
Figure 2.3- The different definitions of void fraction.....	20
Figure 2.4- Lockhart-Martinelli Graph.....	26
Figure 2.5- Pressure gradient of air-water mixture in a vertical tube.	28
Figure 2.6- Time series and PDF profiles (Costigan & Whalley, 1997)	29
Figure 2.7- Flow identification by PSD for Wispy Annular Flow.	30
Figure 2.8- Structures as identified by Sekoguchi et al. (1997)	31
Figure 2.9- Hewitt and Roberts flow pattern map (1969).....	32
Figure 2.10- Empirical flow-pattern map (Owen, 1986)	33
Figure 2.11- Flow map by Taitel et al. (1980).....	33
Figure 2.12- Combined Flow Map	34
Figure 2.13- Vertical flow pattern map according to Duns-Ros (1963).	35
Figure 2.14- Momentum flux flow map (Air-water)	36
Figure 2.15- Weber No flow map (Air-water).....	37
Figure 2.16- Momentum Flux flow map (Steam-Water 35 & 70 bar).	37
Figure 2.17- Weber No flow map. (Steam-Water 35 & 70 bar).....	37
Figure 2.18- Flooding and Flow Reversal (Hewitt, Themopedia.com).....	39
Figure 2.19- The effect of gas superficial velocity on liquid entrainment	43
Figure 2.20- Entrainment rate for churn and annular flow at 2 bar	44
Figure 2.21- Sausage like objects in the gas core: (a) Hernandez et al. (2010). (b) Hewitt et al. (1969), (c) Prasser et al. (2002).	45
Figure 2.22- (Left) Frequencies of slug/huge waves/disturbance.....	45
Figure 2.23- Sample data from Schlegel et al (2009).	55
Figure 2.24- Flow maps (Left) 20 bar, (right) 90 bar. Red lines are experimental transition points, and black lines are theoretical. ..	56
Figure 2.25- CFD modelling in two-phase gas-liquid flow.....	58

CHAPTER 3

Figure 3.1- Latest developments in multi-phase measurements: x-ray CT.....	61
Figure 3.2- ECT system.....	63
Figure 3.3- Photo of conductance probes	65
Figure 3.4- The evolution of the wire mesh sensor.....	66
Figure 3.5- Electrical Schematic of WMS.....	68
Figure 3.6- Velocity measuring WMS.....	69
Figure 3.7- Electronic boxes.....	69
Figure 3.8- HS video compared to WMS data.....	70
Figure 3.9- Typical matrix for the sensor, shown is the 32x32 Matrix.....	71
Figure 3.10- Incorrect connection of modules (left) vs. correct connection (right).....	72
Figure 3.11- Conductivity WMS Software screenshot.....	73
Figure 3.12- First version of CapWMS (Nov 2008-Dec 2010).....	74
Figure 3.13- Second version of CapWMS (Jan 2011-Present).....	74
Figure 3.14- Old Calibration menu for CapWMS (Nov 2008-Dec 2010).....	76
Figure 3.15- New calibration menu for CapWMS (Jan 2011-Present).....	77
Figure 3.16- Processing raw files	79
Figure 3.17- Visualisation Software to display binary v. files	79
Figure 3.18- 2D Images; longitudinal, and cross-sectional	80
Figure 3.19- 3D images showing detailed structures.....	80
Figure 3.20- Time Series of void fraction.....	81
Figure 3.21- Local voids (Time resolved)	82
Figure 3.22- Procedure to check orientation of matrix of voids.....	82
Figure 3.23- Radial void fraction with integration area examples	83
Figure 3.24- Space resolved void fraction.....	83
Figure 3.25- Matrix generated by a 32x32 sensor for one frame. Local voids expressed as % between 0-100%.....	84
Figure 3.26- A 3D image constructed from the 32x32 matrix shown above...	84
Figure 3.27- Decomposition of voids into bubble size distribution	85
Figure 3.28- 2 inch bubble column, position of 16x16 WMS is shown.....	86
Figure 3.29- 5 inch bubble column, position of 32x32 WMS is shown.....	86
Figure 3.30- 5 inch bubble column injectors	87
Figure 3.31- 5 inch pipe flow facility and design of the WMS used.....	89
Figure 3.32- Design of 127mm Flanges, using 3D CAD (Inventor)	92
Figure 3.33- (Left) Old design of WMS and (right) new design of WMS	92

CHAPTER 4

Figure 4.1- Fixed Densitometer set-up. Graph on the right shows WMS (y-axis) vs. GD (x-axis).....	97
Figure 4.2- 3D schematic of the hydraulic test facility.....	100
Figure 4.3- Side view of gamma densitometer on a moving platform.....	100
Figure 4.4- Top view of the densitometer.....	100
Figure 4.5- Matrix showing the gas and liquid superficial velocities.....	101
Figure 4.6- Calibration graphs for 14 minutes for one half of the pipe.....	103
Figure 4.7- Calibration graphs for 2 minutes for one half of pipe.....	103
Figure 4.8- Time averaged local void fraction Position 5 left (capacitance), and Position 12 right (conductance).....	104
Figure 4.9- Visual plots of flow patterns.....	105

Figure 4.10- Gamma Densitometer count rates for all gas superficial velocities for all 16 positions.	106
Figure 4.11- Gamma Densitometer count rates for all gas superficial velocities for all 16 positions.	107
Figure 4.12- % Difference in void values between GD and WMS for positions 1/16 and 5/12.	107
Figure 4.13- Mean void fraction vs. gas sup. velocity (GD and WMS).	108
Figure 4.14- Chord Averaged void fraction (GD) vs. line averaged void fraction (WMS) for positions 5 and 12	109
Figure 4.15- Chord Averaged void fraction (GD) vs. line averaged void fraction (WMS) for positions 7 and 10	109
Figure 4.16- Chord Averaged void fraction (GD) vs. line averaged void fraction (WMS) for positions 6 and 11	109
Figure 4.17- Chord Averaged void fraction (GD) vs. line averaged void fraction (WMS) for positions 4 and 13	110
Figure 4.18- Visual plots of flow regimes.	114
Figure 4.19- Capacitance 3D visuals for $U_{gs}=0.05-1.4\text{m/s}$, at $U_{ls}=0.2\text{m/s}$ and 0.7m/s	115
Figure 4.20- Conductance 3D visuals for $U_{gs}=0.05-1.4\text{m/s}$, at $U_{ls}=0.2\text{m/s}$ and 0.7m/s	115
Figure 4.21- Time Series, capacitance WMS $U_{gs}=0.051, 0.153\text{m/s}$, $U_{ls}=0.2, 0.7\text{m/s}$	116
Figure 4.22- Time Series, conductance WMS $U_{gs}=0.051, 0.153\text{m/s}$, $U_{ls}=0.2, 0.7\text{m/s}$	116
Figure 4.23- Time Series, capacitance WMS $U_{gs}=0.28, 0.467\text{m/s}$, $U_{ls}=0.2, 0.7\text{m/s}$	116
Figure 4.24- Time Series, conductance WMS $U_{gs}=0.28, 0.467\text{m/s}$, $U_{ls}=0.2, 0.7\text{m/s}$	116
Figure 4.25- Time Series, capacitance WMS $U_{gs}=0.942, 1.4\text{m/s}$, $U_{ls}=0.2, 0.7\text{m/s}$	117
Figure 4.26- Time Series, conductance WMS $U_{gs}=0.942, 1.4\text{m/s}$, $U_{ls}=0.2, 0.7\text{m/s}$	117
Figure 4.27- Capacitance WMS PDF plots $U_{gs}=0.05-1.4\text{m/s}$, at $U_{ls}=0.2\text{m/s}$ and 0.7m/s	117
Figure 4.28- Conductance WMS PDF plots $U_{gs}=0.05-1.4\text{m/s}$, at $U_{ls}=0.2\text{m/s}$ and 0.7m/s	118
Figure 4.29- CapWMS plots for $U_{gs}=0.05-1.4\text{m/s}$, at $U_{ls}=0.2\text{m/s}$ (left) and 0.7m/s (right)	118
Figure 4.30- CondWMS plots for $U_{gs}=0.05-1.4\text{m/s}$, at $U_{ls}=0.2\text{m/s}$ (left) and 0.7m/s (right)	119
Figure 4.31- Local voids: (Left) $U_{gs} 0.051\text{m/s}$ $U_{ls} 0.2\text{m/s}$ (Right) $U_{gs} 0.153\text{m/s}$ $U_{ls} 0.2\text{m/s}$	119
Figure 4.32- Local voids: (Left) $U_{gs} 0.280\text{m/s}$ $U_{ls} 0.2\text{m/s}$ (Right) $U_{gs} 0.467\text{m/s}$ $U_{ls} 0.2\text{m/s}$	119
Figure 4.33- Local voids: (Left) $U_{gs} 0.942\text{m/s}$ $U_{ls} 0.2\text{m/s}$ (Right) $U_{gs} 1.401\text{m/s}$ $U_{ls} 0.2\text{m/s}$	120
Figure 4.34- Local voids: (Left) $U_{gs} 0.051\text{m/s}$ $U_{ls} 0.7\text{m/s}$ (Right) $U_{gs} 0.153\text{m/s}$ $U_{ls} 0.7\text{m/s}$	120
Figure 4.35- Local voids: (Left) $U_{gs} 0.280\text{m/s}$ $U_{ls} 0.7\text{m/s}$ (Right) $U_{gs} 0.467\text{m/s}$ $U_{ls} 0.7\text{m/s}$	120

Figure 4.36- Local voids: (Left) U_{gs} 0.942m/s U_{ls} 0.7m/s	
(Right) U_{gs} 1.401m/s U_{ls} 0.7m/s	120
Figure 4.37- Radial voids for CapWMS.	
(Left) U_{ls} =0.2m/s, (right) U_{ls} =0.7m/s	121
Figure 4.38- Radial voids for CondWMS.	
(Left) U_{ls} =0.2m/s, (right) U_{ls} =0.7m/s	121
Figure 4.39- Bubble Size Distribution for CapWMS.	
(Left) U_{ls} =0.2m/s, (right) U_{ls} =0.7m/s	122
Figure 4.40- Bubble Size Distribution for CondWMS.	
(Left) U_{ls} =0.2m/s, (right) U_{ls} =0.7m/s	122
Figure 4.41- Comparison between CondWMS and CapWMS.....	123
Figure 4.42- Electrical output from the CapWMS	
for conductivities of 1-10000 μ S/cm	124
Figure 4.43- Difference in void fraction between	
CapWMS and CondWMS. Conductivity varied between 1-1000 μ S/cm	124
Figure 4.44- ECT vs. WMS. (Left) 0 Deg inclination and	
(right) 90 Deg inclination	125
Figure 4.45- ECT vs. WMS. (Left) 10 Deg inclination and	
(right) 60 Deg inclination	126
Figure 4.46- ECT vs. WMS. (Left) 80 Deg Inclination and	
(right) a data set at low gas superficial velocities with 90 Deg inclination....	126
Figure 4.47- CondWMS (67mm) vs. Cap/CondWMS (50mm)	
vs. GD (50mm); U_{ls} =0.2m/s	127
Figure 4.48- CondWMS (67mm) vs. Cap/CondWMS (50mm)	
vs. GD (50mm); U_{ls} =0.7m/s	128
Figure 4.49- Six images showing the Taylor bubble progressively passing	
through a 24x24 sensor (dotted line) in silicone oil-air in 67mm pipe.....	129
Figure 4.50- Six images showing the Taylor bubble progressively passing	
through a 32x32 sensor (dotted line) in air-distilled water in 127mm pipe....	129
Figure 4.51- HS and WMS images of an artificially created plug.	
To save space, the last image is rotated 90 degrees.....	130

CHAPTER 5

Figure 5.1- Bubble Column configurations - 5 different types.....	133
Figure 5.2- Static gas injectors; four different types.	135
Figure 5.3- Flow map for the bubble column	136
Figure 5.4- Radial void pattern map for air-water flow	
in vertical pipes, obtained by Serizawa and Kataoka (1988).....	138
Figure 5.5- Representation of the void fraction profile	
and homogeneous/heterogeneous transition region (Zahradnik et al, 1997)..	139
Figure 5.6- Experimental data of void fraction vs.	
U_{gs} for different types of water.	144
Figure 5.7- Left: Void for various injectors.	
Right: Radial void (Harteveld 2005)	145
Figure 5.8- Table summarising the experiments	148
Figure 5.9- Level swell measurements. (Left): Distilled/tap water	
with Spider injector. (Right): Various liquids with homogeneous injector....	150
Figure 5.10- Low/Medium/High void fraction;	
air-distilled water with spider (127mm)	151

Figure 5.11- Low/Medium/High void fraction; air-tap water with hom. injector (127mm).....	151
Figure 5.12- Low/Medium/High void fraction; air-silicone oil, hom. injector (127mm).....	151
Figure 5.13- Low/Medium/High void fraction; air-silicone oil, 3mm holes (67mm)	152
Figure 5.14- Maximum/Mean/Minimum void fraction for (left) Air-Silicone Oil and (right) Air-Tap water	152
Figure 5.15- Frequencies for air-silicone oil (extracted from time series)	153
Figure 5.16- (Left) Air-Distilled Water swell vs. CapWMS void fraction with the spider injector. (Right) +/-10% added to level swell values.....	154
Figure 5.17- Homogeneous Injector: (Left) Air-silicone oil vs. CapWMS void fraction. (Right) Air-silicone oil corrected level swell vs. CapWMS void fraction.	154
Figure 5.18- Homogeneous Injector: (Left) Air-tap water vs. CapWMS vs. CondWMS void fraction. (Right) Air-tap water level swell vs. CondWMS (1000/2500Hz).....	155
Figure 5.19- Radial Profiles for air-distilled water, with spider/CapWMS...	156
Figure 5.20- Radial Profiles air-silicone oil, for a homogeneous injector and the CapWMS.....	156
Figure 5.21- Radial Profiles for air-tap water, with a homogeneous injector and the CondWMS.	157
Figure 5.22- BSD for air-distilled water, with a spider injector and the CapWMS.....	158
Figure 5.23- BSD for air-silicone oil, with a homogeneous injector and the CapWMS	158
Figure 5.24- BSD for air-tap water, with a homogeneous injector and the CondWMS.	159
Figure 5.25- 2D contour plots for air-distilled water with a spider	160
Figure 5.26- 2D contour plots for air-tap water with a hom. injector.....	160
Figure 5.27- 2D contour plots for air-Silicone oil with a hom. injector.....	160
Figure 5.28- 2D contour plots for air-Silicone oil with 3mm holes	160
Figure 5.29- 2D Air-distilled water visualisation for the 127mm diameter column and spider injector	162
Figure 5.30- 2D Air-tap water visualisation for the 127mm diameter column and homogeneous injector	163
Figure 5.31- 2D Air-silicone oil visualisation for the 127mm diameter column and homogeneous injector	164
Figure 5.32- 2D Air-silicone oil visualisation for the 67mm diameter column and 3mm injector	165
Figure 5.33- Images extracted from high speed videos for air-water, in the 127 mm bubble column with a homogeneous injector.....	166
Figure 5.34- Mean Void Fraction. (Left) 67mm column, (right) 67mm vs. 127mm.....	167
Figure 5.35- Bubble size distribution in the 67mm column at $U_{ls}=0$ m/s.....	167
Figure 5.36- Max bubble size against superficial gas velocity; 67mm vs. 127mm	168
Figure 5.37- Radial profiles for the 67mm column; superficial gas velocities of 0.047 to 0.203 m/s	168

Figure 5.38- Radial profiles for the 67mm vs. 127mm columns for the corresponding gas velocities.....	169
Figure 5.39- Dominant Frequencies for 67mm and 127mm columns with Air-Silicone Oil.....	169
Figure 5.40- Mean void fraction vs. superficial gas velocity CondWMS	170
Figure 5.41- Radial void profiles. (Left) 1 $\mu\text{S}/\text{cm}$ and (right) 30 $\mu\text{S}/\text{cm}$	170
Figure 5.42- Radial void profiles. (Left) 400 $\mu\text{S}/\text{Cm}$ and (right) 1000 $\mu\text{S}/\text{cm}$	171
Figure 5.43- Level Swell data for the 127mm bubble column compared against published correlations.....	172
Figure 5.44- Void fraction correlations vs. WMS data for air-water	173
Figure 5.45- Void fraction correlations vs. WMS data for air-silicone oil....	173
Figure 5.46- Radial profiles vs. Wu et al. modified/original.....	174
Figure 5.47- Radial profiles vs. Wu et al modified/original.....	174
Figure 5.48- Radial profiles vs. Wu et al modified/original.....	175
Figure 5.49- Bubble size vs. gas velocity.(Left) Air-water (right) Air-oil	175
Figure 5.50- Data from Hartevelde (left); comparison of bubble size by Hartevelde with Gaddis and Vogelpohl (right)	176
Figure 5.51- Voidage history for one bubble.....	178
Figure 5.52- Model 1: Bubbles aligned	179
Figure 5.53- Screenshot of the physical properties defined in the code for the model. Q_g is varied appropriately.	179
Figure 5.54- Model 1 vs. WMS data. Air-water (left), air-silicone oil (right)	180
Figure 5.55- Model 2: Staggered bubbles.....	180
Figure 5.56- An example of void fraction variation with time for model 2 ..	181
Figure 5.57- Model 2 vs. WMS data with air-water,.....	181
Figure 5.58- Model 3: Random bubbles with velocities (v) and diameters (d)	182
Figure 5.59- Typical void fraction profile for model 3.....	182
Figure 5.60- Model 3 vs. WMS data for air-water	183
Figure 5.61- Model 4: Void fraction vs. WMS data using area-based and volume-based experimentally obtained bubble size distributions	184
Figure 5.62- Distribution curves for the WMS vs. model 4 for one run with air-water. (Left): Area based BSD, (right): volume based BSD.	184
Figure 5.63- Bubble shapes: (a) spherical and (b) elliptical	185
Figure 5.64- d_e/d_m for air-water (left) and d_e/d_m for air-silicone oil (right)	186

CHAPTER 6

Figure 6.1- A selection of WMS time series data for the 127mm pipe.	191
Figure 6.2- Effect of gas and liquid superficial velocities on the mean void fraction.	192
Figure 6.3- Effect of gas and liquid superficial velocities on the mean film thickness.	192
Figure 6.4- Effect of gas and liquid superficial velocities on the ratio of void fractions measured by the WMS to the void fractions measured by the conductance probes	193
Figure 6.5- PDF profiles for the time series in Fig 6.1.....	194
Figure 6.6- Radial Profiles for the 127mm pipe.	

Superficial liquid velocity 0.013 m/s.....	196
Figure 6.7- Radial Profiles for the 127mm pipe.	
Superficial liquid velocity 0.073 m/s.....	196
Figure 6.8- Radial Profiles for the 127mm pipe.	
Superficial liquid velocity 0.27 m/s.....	197
Figure 6.9- Radial Profiles for the 127mm pipe.	
Superficial liquid velocity 0.66 m/s.....	197
Figure 6.10- BSD for 127mm pipe. Liquid superficial velocity 0.073 m/s...	198
Figure 6.11- BSD for 127mm pipe. Liquid superficial velocity 0.27 m/s.....	198
Figure 6.12- BSD for 127mm pipe. Liquid superficial velocity 0.66 m/s.....	198
Figure 6.13- Flow Visualisation with the WMS in centre of pipe;	
$U_{ls} = 0.013\text{m/s}$; 24 runs.....	199
Figure 6.14- Flow Visualisation with the WMS in centre of pipe;	
$U_{ls} = 0.073\text{m/s}$; 24 runs.....	200
Figure 6.15- Flow Visualisation with the WMS in centre of pipe;	
$U_{ls} = 0.27\text{ m/s}$; 23 runs.....	200
Figure 6.16- Flow Visualisation with the WMS in centre of pipe;	
$U_{ls} = 0.66\text{ m/s}$; 21 runs.....	201
Figure 6.17- Run 689. (Left): vertical and (right):	
horizontal sectional view in the centre of the pipe	202
Figure 6.18- Effect of the Lockhart-Martinelli parameter	
on the gas and liquid based St Numbers.....	203
Figure 6.19- Effect of the Lockhart-Martinelli parameter	
on the gas and liquid based St Numbers (2 nd level of data filtration).....	203
Figure 6.20- Comparison of pressure gradient	205
Figure 6.21- Comparison of pressure gradient	206
Figure 6.22- (Left): Gravitational pressure drop	206
Figure 6.23- WMS void fraction compared against void predicted by CISE	207
Figure 6.24- WMS void fraction compared against void predicted by CISE	207
Figure 6.25- (Left): Void fraction predicted by CISE compared	
against WMS void fraction,	
(right): void fraction predicted by Chisholm compared against WMS void ..	208
Figure 6.26- Comparison between computational (WELLFLO)	
generated void fraction and experimental (WMS) void fraction.....	209
Figure 6.27- Wisps in churn flow.	211
Figure 6.28- Flow maps.	
(Left): superficial velocity map and (right): momentum flux map.....	212
Figure 6.29- Two orthogonal diametric slices in the centre of the pipe.	
(Left): 67mm and (right): 127mm	213
Figure 6.30- Time series, film thickness and film to diameter ratio.....	214
Figure 6.31- (Left): PDF and (right): PSD.	215
Figure 6.32- (Left): Radial profile (right): BSD for 67mm and 127mm	215
Figure 6.33- averaged void fractions resolved by bubble size classes	215
Figure 6.34- (Left): 127mm, point 16x16 and (right): 67mm, point 12x12 ..	216
Figure 6.35- 2D axial slices of void for run 143 on the 67mm pipe.....	217
Figure 6.36- 2D axial slices of void for run 489 on the 127mm pipe.....	217
Figure 6.37- 3D void maps for run 489 on the 127mm pipe.	218
Figure 6.38- Wisps in 3D for (left): 67 mm pipe and (right): 127mm pipe...	219
Figure 6.39- Air-water (left) air-silicone oil (right) for the 67mm pipe.	220
Figure 6.40- Mechanisms of atomisation and drop break up	221

Figure 6.41- Effect of gas and liquid flow rates on overall frequency	223
Figure 6.42- The effect of gas and liquid velocities on wisp and overall frequency for the 127mm diameter pipe.	224
Figure 6.43- (Left): Effect of gas and liquid flow rate on wisp frequency....	224
Figure 6.44- Wisp frequency plotted against a modified Weber number (left) and as a dimensionless group map (right). .	225
Figure 6.45- Entrainment fraction against gas sup. velocity 10-50m/s	226
Figure 6.46- Flow map for the 127mm diameter pipe.....	227
Figure 6.47- Mesh profile used for the CFD simulation.....	228
Figure 6.48- CFD generated void fraction.....	229
Figure 6.49- CFD generated velocity vectors.....	229

APPENDICES

Figure B1- One crossing point processing of wire mesh sensor.....	261
Figure B2- Capacitive models used for the CapWMS	264
Figure B3- coefficient a_{ij} for averaging the void fraction, and $a_{i,j,m}$ for radial gas fraction profiles.	266
Figure B4- Example of data handling to generate time/space resolved void fraction	267
Figure B5- Matrix of local voids generated by WMS, example of 32x32	268
Figure C1- Measured vs calculated gamma void fraction with dynamic bias error.	280
Figure D1- Time series: air-distilled water; Spider Injector; 127mm bubble column; CapWMS	283
Figure D2- Time series: air-tap water; Hom. Injector; 127mm column; CondWMS	283
Figure D3- Time series: air-silicone oil; Hom. Injector; 127mm column; CapWMS	284
Figure D4- Time series: air-silicone oil; Hom. Injector; 67mm column; CapWMS (I)	284
Figure D5- Time series: air-silicone oil; Hom. Injector; 67mm column; CapWMS (II)	285
Figure D6- PDF: air-distilled water; Spider Injector; 127mm bubble column; CapWMS	286
Figure D7- PDF: air-tap water; Hom. Injector; 127mm column; CondWMS.....	286
Figure D8- PDF: air-silicone oil; Hom. Injector; 127mm column; CapWMS	286
Figure D9- PDF: air-silicone oil, hom. injector, 67mm column, CapWMS	287
Figure D10- Local voids: air-distilled water; Spider Inj; 127mm column; CapWMS.....	287
Figure D11- Local voids: air-tap water; Hom. Injector; 127mm column; CondWMS	288
Figure D12- Local voids: air-silicone oil; Hom. Injector; 127mm column; CapWMS	288
Figure D13- Local voids: air-silicone oil; Hom. Injector; 67mm column; CapWMS	289

LIST OF TABLES

CHAPTER 1

Table 1.1- Single phase vs. multiphase, single component vs. multi component.	2
--	---

CHAPTER 2

Table 2.1- C Values	26
Table 2.2- Comparison of D/σ for three data sets.....	36
Table 2.3- Comparison of correlations with flow specific models	46
Table 2.4- Comparison of experimental vs. theoretical transition models	51
Table 2.5- Experimental work on large diameter pipes.....	53
Table 2.6- Summary of popular Mechanistic/Empirical correlations.....	57

CHAPTER 3

Table 3.1- Review of the main experimental techniques in gas-liquid flow ...	60
Table 3.2- Properties of Liquids	94

CHAPTER 6

Table 6.1- Experimental Matrix with run numbers.	190
Table 6.2- HS Camera compared with WMS results.....	210
Table 6.3- Mean void fraction and mean film thickness for two diameters ..	214

APPENDICES

Table D1- CapWMS matrix for air-distilled water; Spider Injector; 127mm bubble column	281
Table D2- CondWMS matrix for air-tap water; Hom Injector; 127mm bubble column.....	281
Table D3- CondWMS matrix for air-silicone oil; Hom Injector; 127mm bubble column.....	282
Table D4- CapWMS matrix for air-silicone oil, 67mm vertical column, 3mm hole injector.....	282

1. CHAPTER 1: INTRODUCTION

1.1. Multiphase flows

Multiphase flows are ubiquitous, which makes them arguably more important than single phase systems. However, they must be treated as an entirely separate subject as they are significantly more complex than single phase systems. Examples of multiphase systems can be found in many fields and applications, some of which are obvious, and others less so. Volcanoes, weather systems and fizzy drinks are all examples of multiphase systems. Study of multiphase flow has been described as a black art, where challenges include the mechanisms of multiphase flow propagation along a pipe, how to pump a mixture comprising gas and liquid and how to measure the mixture's flowrate (King, 1990).

It is possible to have two, three or even four phase systems and this is not to be confused with the traditional physics based definition of phases of matter. In this case, a phase is a macroscopic state of matter which is homogeneous in chemical composition and physical structure (Corradini, 1998). The three main phases are solid, liquid and gas (ignoring plasma as a phase). For example a four phase gas-liquid-liquid-solid system, consisting of gas-water-oil-sand, is common in the oil and gas industry. This project is focused on investigating two-phase gas-liquid flow, which again has many important industrial applications, such as in the chemical, nuclear and petroleum industries. Within two phase flows it is possible to have several combinations, which are gas-solid, gas-liquid, liquid-liquid and liquid-solid. It is also possible to have multi-component flow, for example in blood flow the plasma/platelet corpuscles can be described as two phase/multi-component flow (Corradini, 1998). Table 1.1 shows a summary adapted from Crowe (1998):

Component	Phase	
	Single Phase Flow	Multiphase Flow
Single	Single-phase, Single component Flow of water, oil and O ₂ .	Two-phase, Single component Flow of water and steam.
Multiple	Single-phase, multi component Flow of air and liquid polymer mixture.	Multi-phase, multi component Flow of air, water and particles.

Table 1.1- Single phase vs. multiphase, single vs. multi component, Crowe (1998).

A map describing how multiphase flow breaks down into separate constituents is shown in Figure 1.1. Several terms shown in this map under the two-phase subheading will be defined and used throughout this research study.

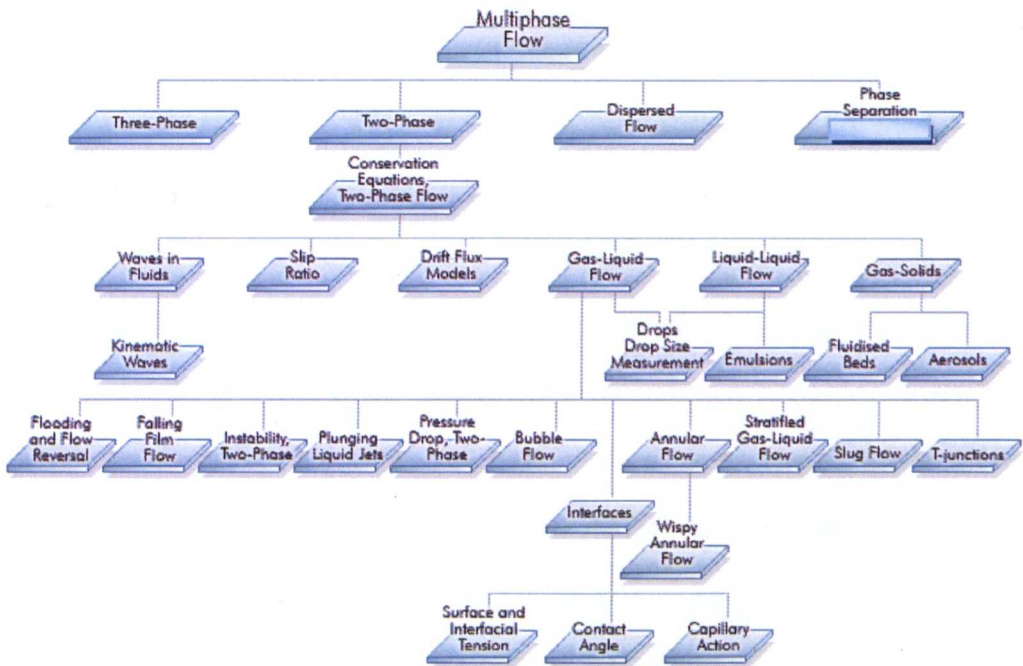


Figure 1.1- Multiphase flow Schematic (Source: www.thermpedia.com, 2011)

1.2. A brief historical note

Examples of two-phase flows can be found throughout the history of science and technology. Hero's Turbine, or 'Aeolipile', as shown in Figure 1.2 was invented around two thousand years ago by the Greek scientist Hero of Alexandria.

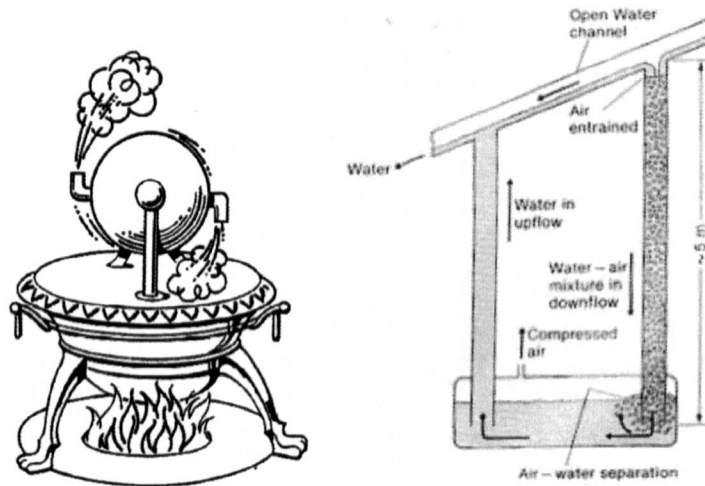


Figure 1.2-Early examples of two-phase flows: (Left) Hero's Turbine, (Right) 17th Century Compressor.

Hero's turbine was primarily a toy, where a ball was suspended on a pivot and a flame heated a small reservoir of water underneath the ball until it turned to steam. The steam was then directed to exit from nozzles located on the ball, which caused the ball to rotate due to Newton's laws. This principle was initially used to open temple doors and was also the precursor to the jet and steam engines. It is interesting to note that Akagawa et al. (1984) studied this device two thousand years later. Chisholm (1983) discussed a more recent example of a two-phase system, which was an air compressor used in the 17th century AD for application in metal smelting (Figure 1.2). The earliest publication regarding two-phase flow according to Chisholm (1983) was by Theremin (1830), and two-phase flow was first mentioned by Kosterin in 1943. This was followed by Martinelli et al. (1944), and Gouse (1966) published a bibliography of

two-phase flow research comprising 8000 references. Useful textbooks in this field include Wallis (1969), Hewitt (1978), Whalley (1987), Collier (1994), Levy (1999), Kleinstreuer (2003), Crowe (2006) and Azzopardi (2006).

Gas-liquid flow is still a relatively new subject area, with around half a century of research behind it. It is also a fairly specialised field of engineering, with many avenues that have not yet been explored. However, this is changing with the rapid advancement of technology, computational power and modern instrumentation.

1.3. Applications and problems

This project was motivated by the requirements of the oil and gas industry and it addresses the vital issue of the prediction of the behaviour of multiphase flows in large diameter vertical pipes in onshore and offshore production facilities. Multiphase flow can occur in various locations in an offshore facility, such as in the bottom of the well, in the pipelines along the sea bed and up the riser to the separator (Figure 1.3). It can be seen from this figure that the pipes can be horizontal, inclined or vertical, and flow assurance engineers are tasked with ensuring continuous and maximum oil production in the most cost effective way.

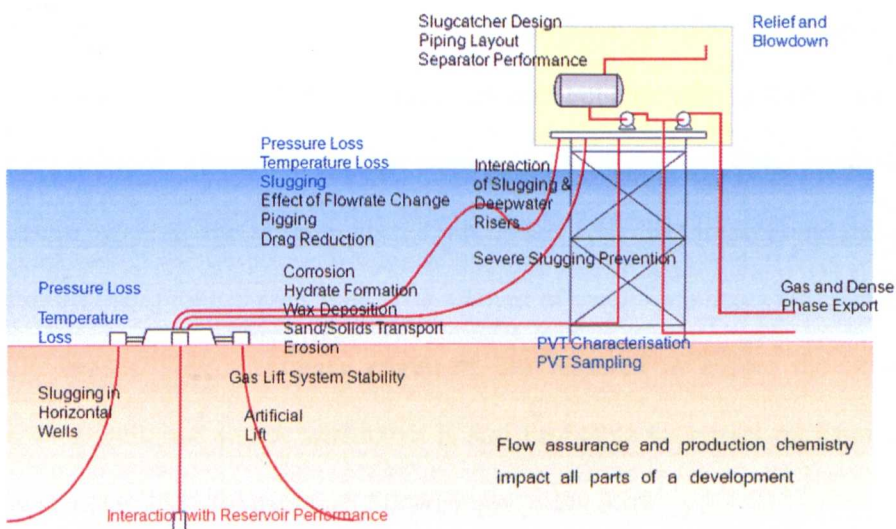


Figure 1.3- Schematic of an offshore oil facility (Azzopardi, 2006).

Selecting a riser or a well tube below the sea bed with an incorrect diameter could have a significant impact on the rate of oil/gas extraction and hence production and profitability, due to it being too small or too large. The pipes must also be designed correctly for example with the right amount of insulation to ensure temperatures don't allow the formation of hydrates and wax, which can block the pipe and stop production. The costs from rectifying these problems and replacing pipelines after the rig is built can run into many millions of dollars, meaning it is vital that the engineers get it right at the design stage. The recent oil spillage in the Gulf of Mexico demonstrated the need for accurate predictions in this field and the prevention of equipment failures; otherwise the financial and environmental costs of clean up operations are huge and potentially catastrophic.

Multiphase flow in pipelines is very complex and difficult to predict as it exhibits many phenomena that aren't encountered in single phase flow, such as backflow, phase change, phase mixing and different flow patterns. Some flow patterns can result in serious problems such as slugging (severe or hydrodynamic). With some pipe lengths running up to several kilometres, more than one flow pattern may be present in the same pipe. For example, an oil pipe may just have oil flowing at the bottom, whereas higher up the pipe, the pressure drops and bubbles start to form, creating a multiphase mixture. Therefore, another important consideration is the prediction of this pressure drop. As the oil is extracted, reservoirs will drop in pressure and in the amount of oil they produce over time. The amount of water -watercut- will increase as the oil decreases. Flow assurance engineers are required to ensure the economic viability of a well, and to ask whether it is still profitable to extract oil from a well with a watercut of 99% for example. Surprisingly, often it is.

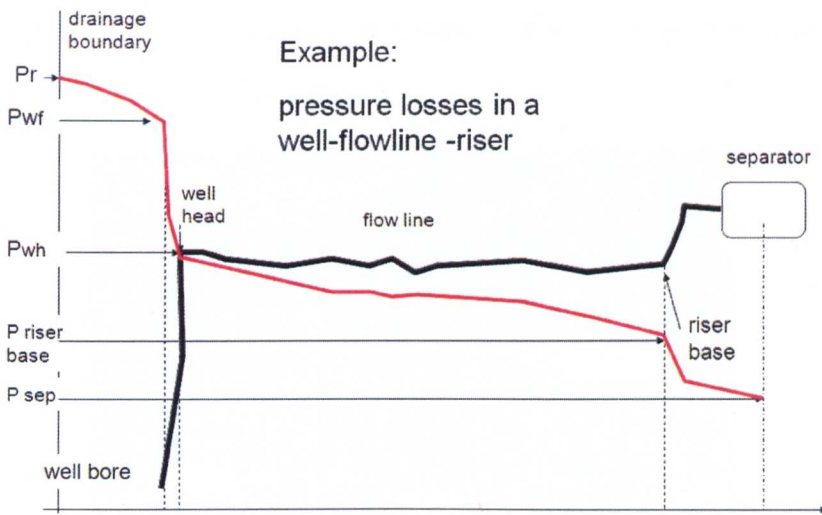


Figure 1.4-Pressure drop, from the well to the pipeline to the riser (Source: Olga Training documentation).

Figure 1.4 shows an example of the variation in pressure drop in a full offshore system, starting from the well, through to the pipeline, and finally going up the riser. The pressure is constantly dropping, and applying single phase pressure drop predictions will result in errors. It is clear from the gradients of the lines that the vertical pipes have bigger pressure drops than the horizontal pipes. This is due mainly to gravity, which would have less of an impact on horizontal pipes. Large diameter pipes are being used in offshore oil and gas rigs to minimise these pressure drops in particular due to frictional losses and turbulence in order to maximise flowrates and hence oil production. Multiphase flow in pipes can be transient, i.e. time varying as well as steady state, meaning that different modelling techniques are required. Examples of transient flow conditions include shut down/re-start of wells, slugging, variable flow rates, pigging, blow-down, tube ruptures, valve failures and tripping of pumps/compressors. In this research study it is assumed that conditions are constant or steady-state. The riser is essentially a vertical or near-vertical pipe, connecting the seabed collection pipe network (the flowlines) to a sea-surface installation, which is typically a floating receiving and processing vessel, sometimes known as an FPSO

(Figure 1.5). These are often used for extracting oil and gas from wells if the depth is too great to build a platform cost effectively.

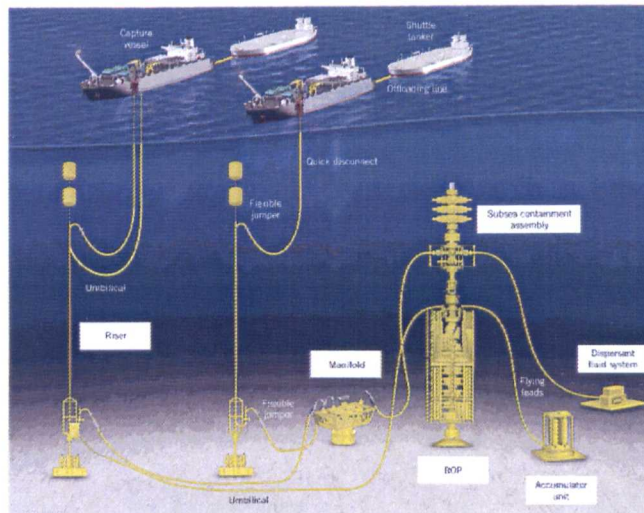


Figure 1.5-Offshore oil/gas extraction (Source: www.marineblog.com, 2010)

The oil and gas industry is currently operating in extremely challenging economic conditions, with the oil price having experienced significant fluctuations over the past few years. A recent article (The Engineer, 2009) stated that each person in the UK uses around 125kWhr of energy every day. This is equivalent to 125 40 Watt light bulbs on around the clock. If half of the available UK land space was covered with wind farms, this would generate around 800W per person, or 20kWhr per day, which is still significantly less than recent demand. The trend in this demand is upwards.

This is the scale of the energy crisis globally, and it is believed that in the short to medium term, the reliance on oil and gas for energy will continue until viable alternative energy sources are commercially tapped. These energy alternatives are essential, as oil and gas are finite resources. Investments in oil and gas offshore systems have been, and will continue to be, huge (around \$35 billion up to 2005), with the riser systems accounting for around 20% of the costs (Azzopardi, private communication).

Current multiphase research methods have been based on measurements from smaller diameter tubes (typically 25-75 mm) and on the interpretation of these measurements in terms of the flow patterns occurring in such tubes. However, the limited amount of data available shows that the flow patterns in larger tubes may be quite different, and that the detailed phenomena may also vary within a given flow pattern. For example, there is some evidence to suggest that slug flow of the normal type, with liquid slugs separated by Taylor bubbles of classical shape, may not exist in large pipes. This can be seen in Figure 1.6 (Prasser et al, 2007a), which also shows the difference in wave structures (Azzopardi et al, 1983).



Figure 1.6-Differences between large diameter (>100mm) and small diameter pipes (<100mm). Taylor bubbles not evident in tube on left. Also shown are wave profiles.

Bubble size distributions measured by Prasser et al. (2004) also displayed significant differences for small diameter and large diameter pipes (Figure 1.7). The second peak for 200mm diameter pipes is broader and less prominent than for 50mm pipes as shown in Figure 1.7 below. Offshore risers were relatively short and had modest diameters. However, as the oil and gas fields are being depleted, and as demand for oil and gas continues to grow globally, the oil and gas companies are being forced to look further afield for replacement reserves with the potential for economic development.

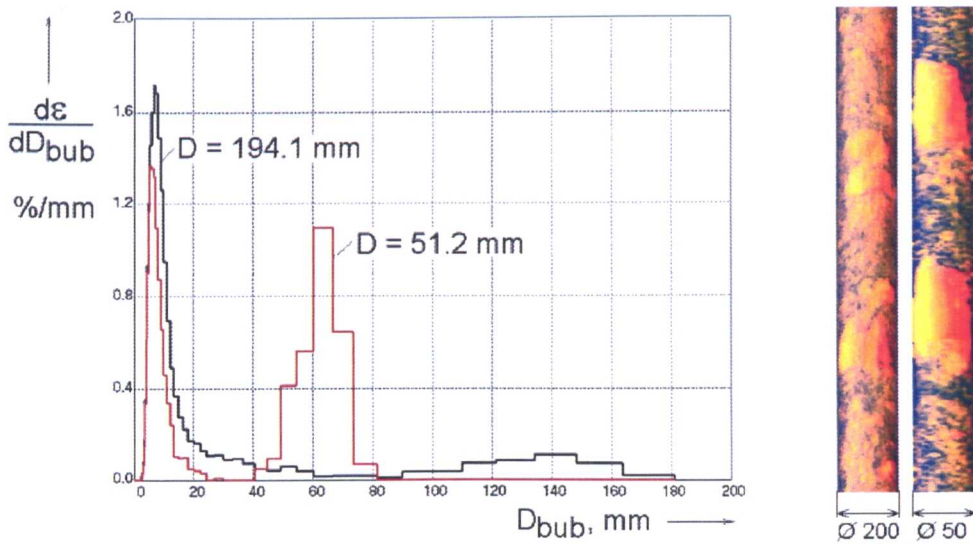


Figure 1.7- Comparison of bubble size distributions for 50mm and 200mm diameter pipes, superficial gas/liquid velocities of 0.53 m/s and 1 m/s respectively.

This has led to an increased interest in deeper waters, harsher environments and more remote locations, most notably in the Gulf of Mexico, the Brazilian Campos basin, west of the Shetland Isles and the Angolan Aptian basin.

Many of the major deepwater developments are located in water depths exceeding 1km, for example Elf's Girassol exploration field at 1300m and Petrobras' Roncador project at 1500-2000m. To transport the fluid produced from systems such as these with the available pressure driving forces has led naturally to the specification of risers of much greater diameter (typically 300 mm) than those used previously (typically 75 mm). Shell recently broke the record for the deepest drilling and production facility in the world with the Perdido project, located in the Gulf of Mexico. This facility will be operating in waters over 2200m deep, and drilling a further 2400m below the sea bed, as shown in Figure 1.8. Therefore, the trend for the oil and gas industry is clear, with a shift towards longer and larger diameter pipes in deeper waters.

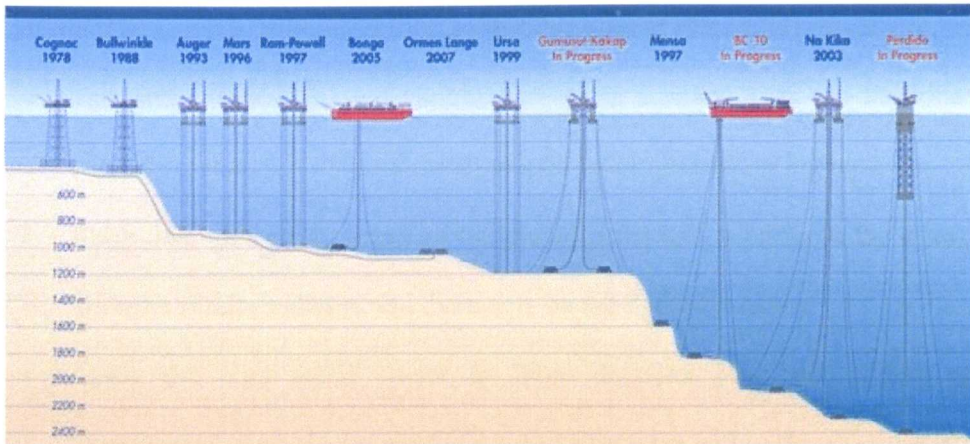


Figure 1.8-Deepwater Milestones (Source: www.Shell.com, 2011)

1.4. Aims and objectives

This project continues the research conducted at the University of Nottingham in the area of gas-liquid flow. It will build on the recent studies by Ombere-Iyari (2006), Hernandez-Perez (2007) and Kaji (2008). This research will address both scientific and industrial needs as outlined above in helping researchers and engineers understand gas-liquid flow in large diameter risers in offshore production facilities. This will be achieved by undertaking direct experimental investigations on a moderately large diameter pipe built at the University of Nottingham, which avoids the necessity for conducting experiments on smaller diameter pipes and then applying inaccurate upscaling calculations. Experiments will be performed in which the phase distribution about the pipe cross section will be measured using novel instrumentation in the form of a wire mesh sensor. The University of Nottingham is the first institute in the world to acquire a capacitance wire mesh sensor from the inventors HZDR (formerly FZD), based in Dresden, Germany. This follows ongoing collaboration between the University of Nottingham and HZDR over several years, during which a number of joint papers have been published. Churn flow is a flow regime that has been the subject of little research to date and is not well understood and will therefore be further investigated in this project.

Therefore the main scientific objectives set for this project are:

- Test and validate the two variant wire mesh sensors. This can be done by comparing this type of sensor with several other multiphase instruments.
- Apply the wire mesh sensor to bubble columns and investigate the effect of different fluids, injectors and diameters on the hydrodynamics.
- Apply the wire mesh sensor to large diameter pipe and collect data, investigating in particular churn flow and structures within this flow pattern.

1.5. Outline of Thesis

As the title of the thesis suggests, this study is split into two parts. The project is primarily experimental in nature and a large amount of novel data will be presented and analysed. The first part of the thesis describes the testing of the specialist instrument (wire mesh sensor, which will often be abbreviated as WMS), and the second part discusses the implementation of the sensor. The two applications that will be covered in this study are two phase gas-liquid mixtures in bubble columns and the flow of two-phase gas liquid mixtures in large diameter pipes. The following gives a succinct breakdown of the order and content of chapters in this thesis.

Chapter 1: A brief background and the rationale for carrying out this work.

Chapter 2: This Chapter contains the literature survey and a critical review of the relevant published work on gas-liquid flows. This does not include a discussion of bubble columns, material for which is presented in Chapter 5.

Chapter 3: This Chapter contains detailed information about the various rigs that are used in this project, in addition to a comprehensive background and explanation of the WMS. There are two variants of this sensor that have both been used in this project.

Chapter 4: This Chapter describes the tests carried out to determine the accuracy and limitations of the WMS, which makes use of the work that was carried out by the author during a placement at HZDR in the summer of 2009. Both variants of the wire mesh sensor were tested and compared with gamma densitometry. The capacitance WMS is a fairly new instrument that has not yet been used extensively. Therefore this is a necessary activity, which forms the testing phase of the sensor and improves the confidence in the results gathered during this project.

Chapter 5: This chapter presents and analyses the data collected from both variants of the WMS on a number of bubble columns of various diameters and with various liquids. This is the first of two chapters on the application of the WMS to two-phase flow systems. Some modelling work is conducted and included in this section.

Chapter 6: This chapter contains the extensive data set obtained on the 127 mm diameter rig with the WMS. The processed data is presented, analysed and compared with that gathered with other instruments. New insights are formed into the behaviour of two-phase flows in large diameter pipes. This chapter also contains a CFD simulation that is compared with the experimental results.

Chapter 7: This chapter contains a summary of the main findings from this research project, and makes several suggestions and recommendations for future work.

It is not possible to include all the data collected during this research project in the thesis. Therefore a DVD is attached with the thesis, which contains significant amount of the novel data that has been collected, in particular for Chapter 6 for the large diameter pipe. It is highlighted in each Chapter, where extra material is available for review on the DVD. The way the DVD is organised is self-explanatory and requires no special software in order to operate it.

2. CHAPTER 2: LITERATURE REVIEW

2.1. Introduction to Gas-Liquid flow

Gas-liquid flow is arguably the most complicated system to analyse out of the four possible combinations of two-phase flow, due to the infinitely deformable interface between the gas and liquid phases. There is the added complication that the gas phase is also compressible. Gas-liquid flows can occur in horizontal, vertical and inclined pipes, where each of these orientations will have its own characteristics, pressure drops and flow patterns. This research primarily investigates vertical gas-liquid flow, with both the gas and liquid “mixture” travelling upwards against gravity, which is known as co-current flow. It is important to note that this is on the “macro” scale, and that in the “micro” scale in vertical gas-liquid flow, the term “micro-gravity” is often used to indicate that in very small diameter pipes the gravity is negligible.

Gas-liquid two-phase flow is encountered in many important industrial applications in the oil, gas, chemical and nuclear industries. Applications include (Chisholm, 1983):

- Water tube boilers and reboilers.
- Water reactors in the nuclear industry (*).
- Gas lift pumps and oil wells; geothermal wells and volcanoes.
- Oil and gas transportation pipes and processing equipment.
- Refrigerators and process condensers.

(*) Boiling water reactor “BWR” exhibits two phase steam-water flow in normal operating conditions, whereas with pressurised water reactor “PWR” steam-water flow occurs in accident situations.

2.2. Flow Patterns

When two fluids with different physical properties flow simultaneously in a pipe, there is a wide range of possible resulting flow patterns. The surface tension and gravity are the crucial physical parameters in determining the flow pattern in the pipe. The surface tension keeps the pipe walls wet, and it also encourages small liquid drops and small gas bubbles to be spherical in nature. The result of the gravitational force is that the liquid tends to be pulled to the bottom of the pipe (Ghajar, 2005).

The multiphase flow may be classified as diabatic or adiabatic, which means it occurs with or without heat addition or removal at the channel wall. An example of adiabatic flow without heat transfer would be gas-oil or air-water flow in pipelines, which is the type of flow that will be investigated and analysed in this project. In this type of flow, the flow patterns change as the inlet mass flow rates of the gas or liquid are altered or as the velocity and void distributions develop along the channel. This is in contrast with diabatic flow, where boiling, dryout and phase change can occur (Corradini, 1998). Many different names have been given to these various patterns, with as many as 84 having been reported in the literature (Rouhani et al, 1983). The variations in nomenclature are partly due to the subjective nature of flow pattern definitions, and partly due to the variety of names given to what are essentially the same geometric flow patterns. However, these classifications can be reduced to five main flow patterns as shown in Figure 2.1, which is in contrast to one-phase flow, where their characterisation as laminar, transitional or turbulent is much simpler. For two-phase flow, bubbly and annular flows are often labelled as “continuous flow” whereas slug and churn flow are termed as “intermittent flow”. These flow patterns are dependent on various parameters, which are volumetric flow rate of each phase, pressure,

density, viscosity and surface tension of the phases, pipe inclination and pipe diameter (Delhaye et al, 1979).

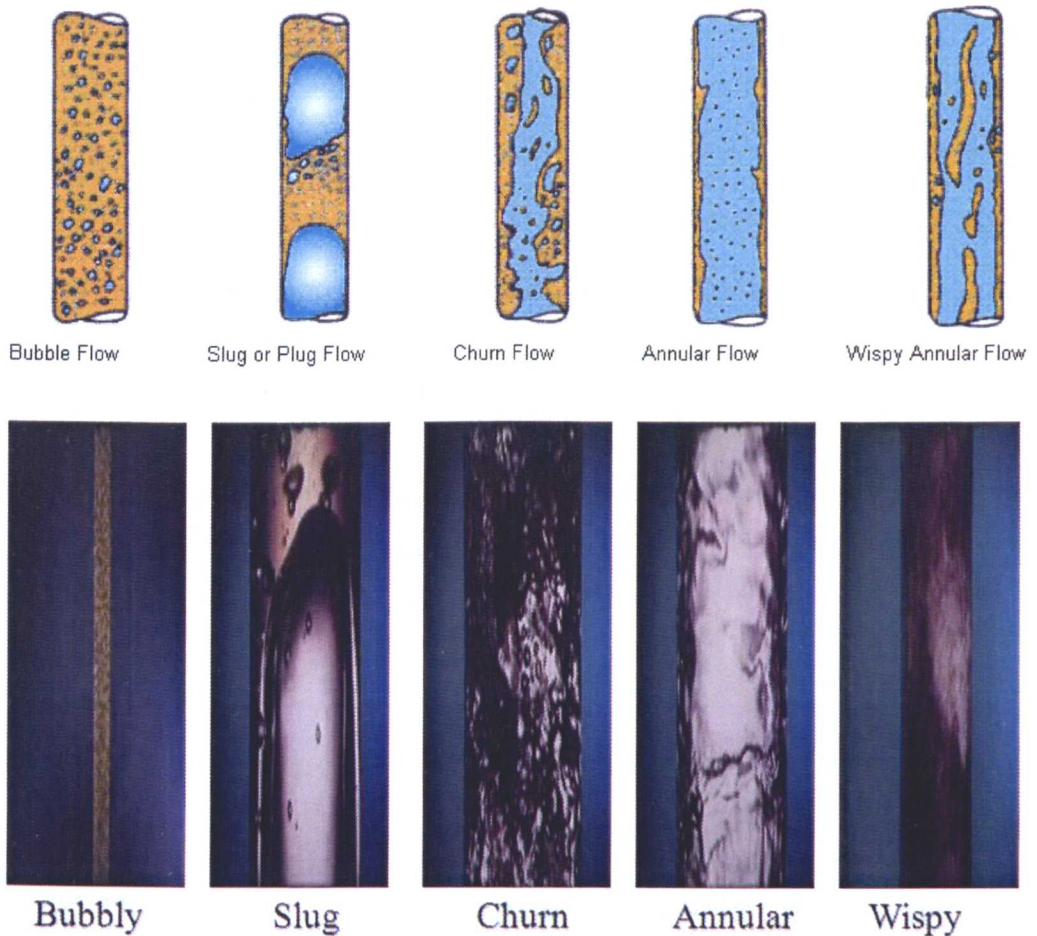


Figure 2.1-Two-phase flow patterns; gas flow rate increasing from left to right (Sources: www.thermapedia.com, 2011 & Rhodes (1980))

Bubble Flow

Many bubbles can be observed as the gas is dispersed in the form of discrete bubbles in the *continuous* liquid phase. These bubbles vary in size and shape and generally are non-uniform in size and concentration. However, they are much smaller than the diameter of the tube itself and they rise inside the liquid due to buoyancy, which promotes collisions. In some circumstances, they congregate at the pipe centre, and in others, they are distributed near the pipe walls. The sizes of the bubbles and the

distribution of their sizes are important parameters that need to be considered. The importance of bubble size has only been recognised comparatively recently (Song et al, 1995). In any bubble flow, two opposing processes are at work, which are bubble coalescence as a result of bubble collisions, and bubble break up as a result of turbulence in the liquid phase. At low liquid velocities when turbulence is small, bubble coalescence dominates and the equilibrium bubble size is large. These larger bubbles have distorted, constantly varying shapes, and they rise with a spiral or zigzag trajectory, which promotes collisions. At higher velocities turbulence is increased, and the equilibrium bubble size is smaller. These smaller bubbles are essentially spherical, and they rise rectilinearly, reducing the number of collisions. This leads to the two sub-regimes described above being termed as “discrete bubble” (low turbulence) and “dispersed or poly-dispersed bubble” (high turbulence).

Slug or Plug Flow

With an increasing gas void fraction, the proximity of the bubbles becomes closer such that bubbles collide and coalesce to form larger bubbles, with the bubble size tending towards that of the channel (cross-section of the pipe). These bubbles have a characteristic shape similar to a bullet, with a hemispherical nose and a blunt tail end. They are commonly referred to as “Taylor bubbles” or sometimes “Dumitrescu bubbles”, and are considered as the “plugs”. The Taylor bubbles are separated from one another by “slugs” of liquid and small bubbles may be present. Small bubbles may also be present in the wake behind the slug regions. The behaviour of the entrained gas travelling in between the Taylor bubbles is not well understood. Taylor bubbles are surrounded by a thin liquid film, situated between them and the tube wall, which may flow downward due to the force of gravity even though the net flow of fluid is upward. Therefore, slug flow displays *intermittency* in the flow direction,

which results in a significant change in the shear stress/frictional pressure gradient, resulting in negative values that are not consistent with some correlations.

Churn flow

Increasing the superficial gas velocity results in the structure of the flow becoming unstable after the break down of the Taylor bubbles. The gas-liquid mixture travels up and down in an oscillatory or churning motion, but with a net upward flow. The instability is the result of the relative parity of the gravity and shear forces acting in opposing directions on the thin film of liquid surrounding the Taylor bubbles. This flow pattern is in fact an intermediate pattern between the slug flow and annular flow regimes (Figure 2.2).

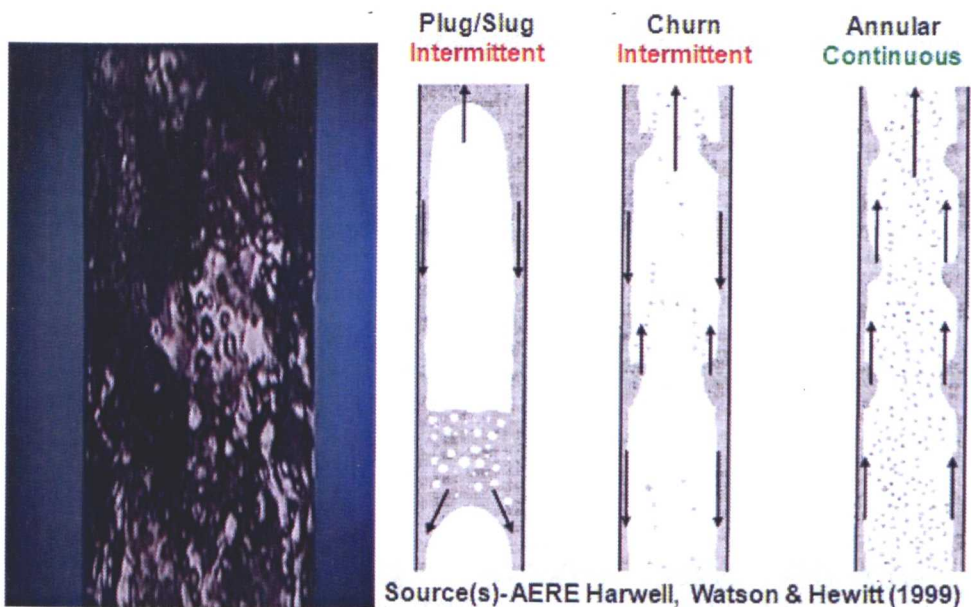


Figure 2.2-Slug/Churn/Annular in a cross-section of pipe

Churn flow is an important pattern, which often covers a fairly wide range of gas flow rates. At the lower end of the range, churn flow may be regarded as a broken-up form of slug flow, with occasional bridging across the tube by the liquid phase. At the higher end of the range of gas flow rates, churn flow may be considered as a degenerate form of annular flow, with variation in the direction of the film flow and

very large waves being formed on the interface as shown in Figure 2.2. In this higher range, the term 'semi-annular flow' has sometimes been applied. A mechanistic description of the gas-liquid interaction in the churn flow regime is very difficult. Churn flow is the flow pattern that is the focus of research in this project, and it will be investigated in more detail.

Annular Flow

Once the interfacial shear of the high velocity gas on the liquid film becomes dominant over the gravitational force, the liquid is expelled from the centre of the tube and flows as a thin film on the wall, which forms an annular ring of liquid, "wetting" the wall. The gas flows together with the liquid as a continuous phase up the centre of the tube, as shown in Figure 2.2. The interface between them is disturbed by high frequency waves and ripples. Waves are formed on the surface of the liquid film and the amplitude of the waves increases as the gas velocity increases. In addition, liquid may be entrained in the gas core as small droplets, and the fraction of liquid that is entrained may be balanced by the re-deposition of droplets from the gas core onto the liquid film. The liquid phase is always moving upwards, whether as droplets or a film, which is what distinguishes annular flow from churn flow, although in both flow patterns there is a continuous gas core. Pure annular flow, without any entrained droplets present at all, is probably not realisable in practice for most gas-liquid applications.

Wispy-Annular Flow

This unusual flow pattern was first identified by Bennett et al. in 1965. If the liquid flow rate is increased further, large liquid objects may be observed within the gas core. These have been termed 'wisps'. Their appearance has been compared to ectoplasm.

This has been classified as a separate flow pattern by Hewitt-Roberts (1969) although several other flow maps don't refer to it. Hawkes et al. (2000, 2001) have suggested that the wisps arise from agglomeration of the drops that must be present in large concentrations within the gas core. Under some circumstances, bubbles of gas may be entrained in the liquid film. This flow pattern is important in a wide range of industrial applications, such as in nuclear reactors and power station boilers.

2.3. Gas Fraction

The void or gas fraction ε_g is a dimensionless quantity that varies between 0 to 1, or is sometimes expressed as a percentage between 0-100%, which indicates the fraction of a geometry or temporal domain occupied by the gas phase. It is probably the most significant quantity that could be measured in two-phase flow (Bertola, 2003). It is sometimes referred to as "liquid hold-up", which is equal to $1 - \varepsilon_g$. Void fraction is a function of many parameters, such as the fluid physical properties, pipe dimensions, angle of inclination, phase flow rates and system pressure. It is an important quantity in two-phase pressure drop prediction, flow pattern transitions, heat transfer and sizing of process and control equipment, such as slug catchers, separators, two-phase pumps and control valves. The gas fraction will change progressively along the pipe length, due to the change in fluid pressure and temperature (Saleh 2002). The void fraction will determine the two-phase density, two-phase viscosity and the relative average velocity between the two phases. Understanding where the liquid or gas is located inside the pipe and how it is distributed (the phase distribution) is of great importance to many industries.

A local time-averaged void fraction may be determined by measuring the cumulative residence time of the gas phase over a total time interval t . Such a measurement may

be made using electrical or optical probes (Hewitt 1978). Alternatively, at any instant of time, a line passing through the channel normal to the channel axis will lie partly in the liquid phase and partly in the gas phase. An instantaneous line-averaged or **chordal** void fraction may be defined as the length of the line submerged in the gas phase over the total length of the line within the channel. Such a measurement may be made using the attenuation of an x-ray or γ -ray beam (Hewitt 1978). Similarly, an instantaneous **area** (or volume) averaged void fraction may be defined as the area (or volume) of the channel occupied by the gas phase divided by the cross sectional area (or total volume) of the channel. The **volume** averaged gas fraction may be measured using quick-closing valves at the entrance and exit of the channel (Hewitt 1978). The space and time averaged gas fractions will be equal only in the circumstance when the flow is steady and one-dimensional. These definitions are summarised in Figure 2.3 (Thome, 2004).

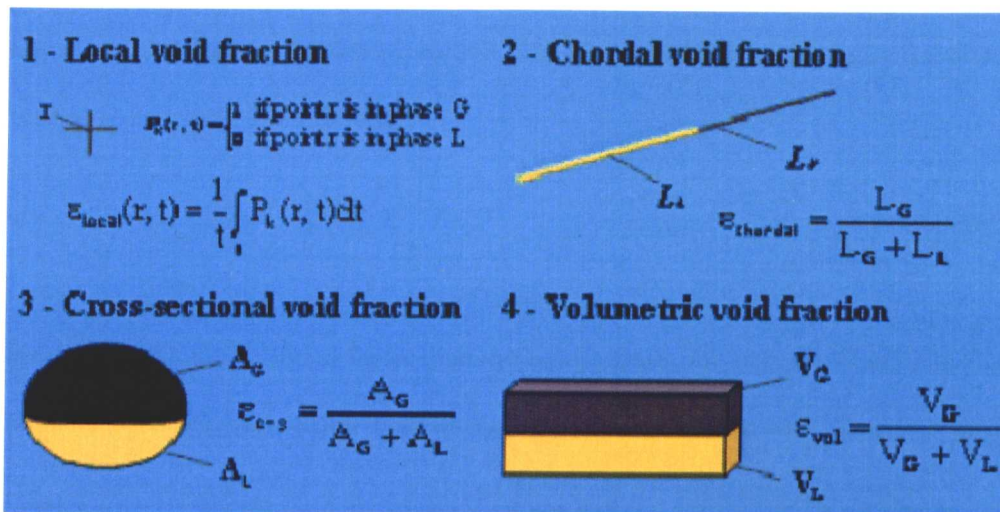


Figure 2.3-The different definitions of void fraction, Thome (2004)

It is important to differentiate between the different types of void fraction, as it is occasionally the case that they are treated as being the same in some literature, which is clearly not correct. In this report, all four types of void fraction will be encountered

as they have been defined above. A general expression for the void fraction can be derived as follows (Azzopardi, 2003, 2006), where the flow rate and cross-sectional area can be eliminated:

$$\varepsilon_g = \frac{1}{1 + U_R \frac{\rho_g(1-x_g)}{\rho_l x_g}} \quad (2.1)$$

$$U_R = \frac{u_g}{u_l} = \frac{U_{gs}(1-\varepsilon_g)}{U_{ls}\varepsilon_g} \quad (2.2)$$

$$\frac{u_g}{u_l} = \frac{Q_g / A_g}{Q_l / A_l} \quad (2.3)$$

From equation (2.1), the higher the quality x_g the bigger the void fraction will be. U_R is known as the slip ratio or velocity ratio, which is a dimensionless quantity. In this report, ε_g is generally the cross-sectional void fraction. Note that u_g and u_l are the true phase velocities in equation (2.2). When $u_g = u_l$ then $U_R = 1$ in equation (2.1) and this is known as the homogeneous flow model. The homogeneous void or gas fraction is given as (Azzopardi, 2003, 2006):

$$\varepsilon_{gH} = \frac{1}{1 + \frac{U_{ls}}{U_{gs}}} = \frac{1}{1 + \frac{(1-x_g)\rho_g}{x_g\rho_l}} \quad (2.4)$$

The gas phase tends to travel faster than the liquid phase, for example in annular flow the gas core would flow faster than the liquid film on the pipe wall. This is because $\rho_l > \rho_g$, which implies $U_R > 1$ and this will be known as the separated flow model.

At this stage ε_g is unknown, therefore U_{ls} and U_{gs} can be calculated, and these are known as the phase superficial velocities. These are the theoretical velocities each phase would possess if it flowed on its own within the entire pipe cross-section, and they can be calculated as long as the flow rate of each phase is known. The mixture

velocity is defined as the sum of these two superficial velocities, which are given for the gas and liquid as:

$$U_{gs} = \frac{Q_g}{A_g + A_l} = \frac{\dot{m} x_g}{\rho_g}; \quad U_{ls} = \frac{Q_l}{A_g + A_l} = \frac{\dot{m}(1 - x_g)}{\rho_l} \quad (2.5)$$

The quality can also be expressed in terms of the superficial velocities as follows:

$$x_g = \frac{U_{gs} \rho_g}{U_{gs} \rho_g + U_{ls} \rho_l} \quad (2.6)$$

In order to calculate ϵ_g , it is first necessary to determine U_R when $U_R > 1$.

2.4. Slip Ratio U_R .

Several correlations have been reported for U_R . Some of these are empirical, and some analytical. Examples of these can be found in works by, Zivi (1964), Zuber (1967), CISE (1970), Smith (1971), Chisholm (1972) and HTFS. Details of two of these correlations by Chisholm and CISE are given below.

Chisholm Correlation

Chisholm's correlation provides a very simple, reasonably accurate result, and is useful for determining a quick estimate of U_R :

$$U_R = \left[1 - x_g \left(1 - \frac{\rho_l}{\rho_g} \right) \right]^{0.5} \quad (2.7)$$

CISE Correlation

Premoli et al. (1970), also known as the CISE correlation, yielded a more complicated expression for U_R . CISE correlation is generally the most accurate applicable correlation (Whalley 1987, Hills et al 1997), and it is summarised in Appendix A.

HTFS at Harwell have generated another correlation for U_R in terms of three empirically chosen parameters, and based on a large experimental database (Azzopardi, 2003):

$$U_R = f \left(\left(\dot{m}_g + \dot{m}_l \right), \frac{\varepsilon_{gH}}{1 - \varepsilon_{gH}}, \frac{\rho_g}{\rho_l} \left(\frac{\eta_l}{\eta_g} \right)^{0.2} \right) \quad (2.8)$$

Computer programs for designing heat exchangers, such as MTasc, use equations such as equation 2.8 in a commercial context. HTFS correlation has been shown to be very accurate; however, details are proprietary and only available to subscribers. Correlations have in general been derived from data obtained from small diameter pipes. The important question is can they be applied to larger diameter pipes with minimal errors? This thesis will test some of these engineering methods and compare them with experimental values.

2.5. Pressure Drop

Apart from the void fraction, the next important quantity that requires definition for two-phase flow is the pressure drop. There are several methodologies for calculating the pressure drop, and these will be explained in this section. Calculating the pressure drop is a major requirement for two phase flow, which is involved in the calculation of flow rates under a given head loss, and of pumping requirements for a given flow rate. More information about the pressure drop can be found in Appendix A.

2.6. Homogeneous Flow

The simplest approach to analysing two-phase flow is homogeneous flow, where the liquid and gas are replaced by a theoretical single phase fluid travelling with one velocity (equivalent to the liquid and gas phases travelling with equal velocities). The phase temperatures and pressures are also assumed to be equal. The corresponding pressure drop for homogeneous flow is (Whalley, 1987 and Hewitt, 1998):

Change in momentum= Wall Shear Stress+Gravitational Force+Pressure Force

$$-\frac{dp}{dz} = -\left(\frac{dp}{dz}\right)_{friction} - \left(\frac{dp}{dz}\right)_{gravitation} - \left(\frac{dp}{dz}\right)_{acceleration} \quad (2.9)$$

$$-\frac{dp}{dz} = \frac{\tau}{S} + \rho_H g \sin \beta + \dot{m}^2 \frac{d}{dz} \left(\frac{1}{\rho_H} \right) \quad (2.10)$$

2.7. Separated Flow

For separated flow, the two phases are no longer assumed to flow with same velocities. Essentially, this is a 1D approach i.e. all changes occur along the pipe. A “generalised” equation is given by (Hewitt 1998, Azzopardi 2006):

$$-\frac{dp}{dz} = \frac{\tau}{S} + \rho_{MP} g \sin \beta + \dot{m}^2 \frac{d}{dz} \left[\sum_{s=1}^n \frac{x_s^2}{\rho_s \varepsilon_s} \right] \quad (2.11)$$

The pressure drop equation can also be written as (see Appendix A for more details):

$$-\Delta p = \int_{z_1}^{z_2} \frac{4 f_{lo}}{d} \frac{\dot{m}^2}{2 \rho_l} \phi_{lo}^2 dz + \int_{z_1}^{z_2} [\varepsilon_g \rho_g + (1 - \varepsilon_g) \rho_l] g \sin \beta dz + \left[\dot{m}^2 \left(\frac{x_g^2}{\varepsilon_g \rho_g} + \frac{(1 - x_g)^2}{(1 - \varepsilon_g) \rho_l} \right) \right]_{z_1}^{z_2} \quad (2.12)$$

In vertical flow the majority of pressure loss will be due to the gravity or head of liquid at low quality values. It should be noted that for higher velocities and quality, frictional and accelerational losses contribute a greater part to the total pressure drop, and therefore cannot be neglected at the higher flow rates (Saleh, 2002, Takacs, 2005).

The accelerational term tends to be important when there is a phase change in the form of evaporation or condensation. In this research, the accelerational term will be assumed to be small and can be neglected; hence equation (2.12) can be simplified to:

$$-\Delta p = \int_{z_1}^{z_2} \frac{4 f_{lo}}{d} \frac{\dot{m}^2}{2 \rho_l} \phi_{lo}^2 dz + \int_{z_1}^{z_2} [\varepsilon_g \rho_g + (1 - \varepsilon_g) \rho_l] g dz \quad (2.13)$$

From equation (2.13), the gravitational pressure drop can be seen to be dependent on ε_g and therefore as ε_g is increased, the gravitational pressure drop decreases. This is behind the use of artificial gas lift in vertical facilities in the oil industry. As the gas is injected into the system, the void fraction is increased, therefore the gravitational pressure drop decreases, and this subsequently reduces the pumping power requirements.

2.8. Frictional Pressure Drop

The two phase frictional pressure drop can be considered as the product of a single phase frictional pressure gradient multiplied by a two phase multiplier ϕ_{lo}^2 :

$$-\Delta P_{frictional} = \int_{z_1}^{z_2} \frac{4 f_{lo}}{d} \frac{\dot{m}^2}{2 \rho_l} \phi_{lo}^2 dz = \frac{4 f_{lo}}{d} \frac{\dot{m}^2}{2 \rho_l} \int_{z_1}^{z_2} \phi_{lo}^2 dz \quad (2.14)$$

It is not possible to measure the frictional pressure drop directly, so this term is obtained by subtracting the measured acceleration (unless this is neglected) and gravity components from the measured total pressure drop. There are many frictional pressure drop correlations presented in the literature, for example Martinelli-Nelson (1948), Lockhart-Martinelli (1949), Bankoff (1960), Duckler (1964), Thom (1964), Baroczy (1966), Chawla (1968), Gronnerud (1972), Beggs and Brill (1973), Chisholm (1973), Friedel (1979), Muller-Steinhagen and Heck (1986).

Hewitt (1998) reported that Whalley (1980) made an extensive comparison and evaluation between various published correlations and the HTFS proprietary database (which consisted of over 25,000 data points). The following recommendations were made:

- $\frac{\eta_l}{\eta_g} < 1000$ and $\dot{m} < 2000 \text{ kg/m}^2\text{s}$, then Friedel (1979) correlation should be used.

- $\frac{\eta_l}{\eta_g} > 1000$ and $\dot{m} > 100 \text{ kg/m}^2\text{s}$, then Chisholm (1973) correlation should be used.
- $\frac{\eta_l}{\eta_g} > 1000$ and $\dot{m} < 100 \text{ kg/m}^2\text{s}$, then Lockhart-Martinelli (1949) should be used.

Friedel, Chisholm and Lockhart-Martinelli correlations will be introduced below.

Lockhart-Martinelli/ Chisholm Correlations

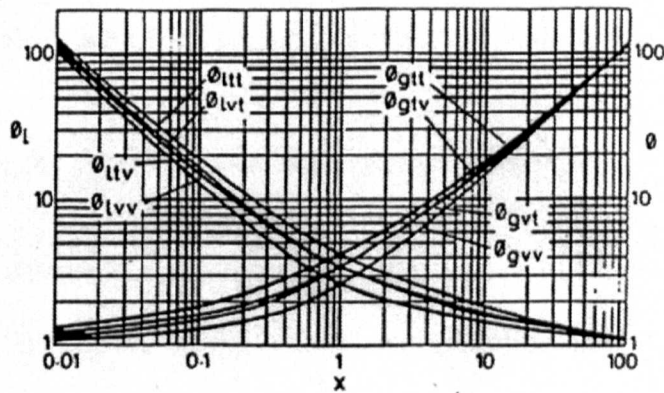


Figure 2.4-Lockhart-Martinelli Graph, Azzopardi (2010).

Lockhart-Martinelli (1949) produced a value for the multiplier in graphical form as shown in Figure 2.4. Two sets of four lines are plotted based on each phase being either laminar (viscous) or turbulent at local conditions, which can be calculated using Re number. For turbulent flow, $Re > 2000$. Chisholm (1973) determined equations to fit this graph in order to generate equation 2.15. The C values for equation 2.15 are

$$\text{given in Table 2.1 as } \phi_l^2 = 1 + \frac{C}{X} + \frac{1}{X^2} \quad (2.15)$$

C	20	12	10	5
Gas	t	t	v	v
Liquid	t	v	t	v

Table 2.1-C Values, Azzopardi (2010).

Friedel Correlation

For most fluids, $\frac{\eta_l}{\eta_g} < 1000$. For example, for the two-phase air-water mixture then:

$$\frac{\eta_l}{\eta_g} = 53.867 \text{ (at normal pressure).}$$

The Friedel (1979) correlation is therefore recommended, which is a fairly complicated expression that is given in Appendix A. HTFS at Harwell (Azzopardi, 2003) have also published correlations for ϕ_{lo}^2 , which are of the form

$$\phi_{lo}^2 = f(\dot{m}_{TP}, \Lambda, X), \text{ where } \Lambda \text{ is the Baroczy property index: } \Lambda = \frac{\rho_g}{\rho_l} \left(\frac{\eta_l}{\eta_g} \right)^{0.2} \text{ and } X$$

is the Lockhart-Martinelli parameter. The equation is proprietary and only available to subscribers to HTFS. Levy (1999) reported that the EPRI correlation is also being used, which was developed by Chexal et al. (1986).

Pressure Gradient

The pressure will vary from one flow pattern to another. The onset of slug flow is accompanied by a sharp decrease in the pressure gradient down to a minimum value (Owen 1986). As the gas velocity is further increased, the pressure gradient initially increases significantly with the onset of churn flow. It reaches a maximum and then drops, subsequently passing through a minimum value. Eventually the pressure gradient increases again with the onset of annular flow as the gas flow rate increases, as shown in Figure 2.5. The figure also shows how the various correlations described earlier compare with experimental data from Owen (1986). Most perform well except for the homogeneous approximation.

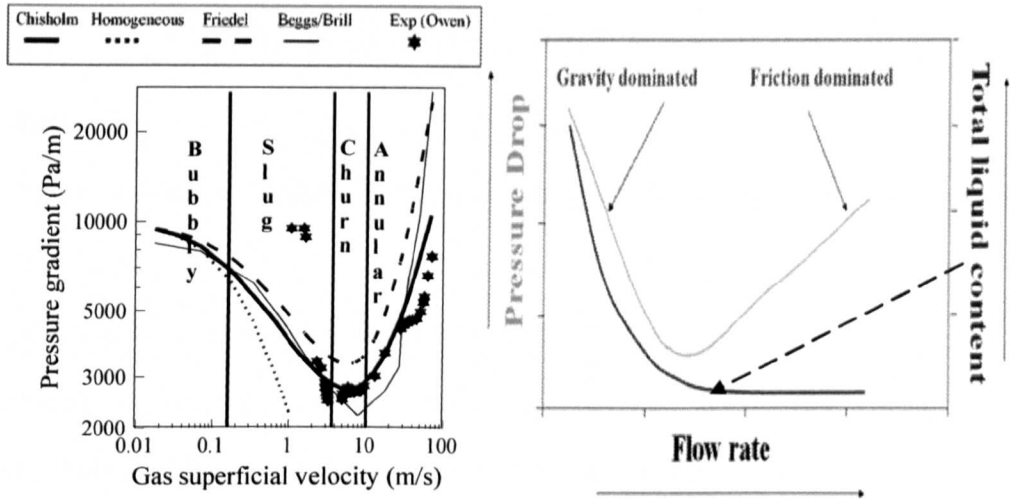


Figure 2.5-Pressure gradient of air-water mixture in a vertical tube. Azzopardi (2010)

A similar graph to Figure 2.5 was recently presented by Duang Prasert et al. (2008). The downward part of the curve will be dominated by gravity as the flow rate is low, and hence flow-dependent frictional losses will also be low. This continues up to a minimum value, and then the frictional pressure drop will exceed the gravitational forces at the higher flow rates. From an industrial perspective, some flow patterns are considered to be more beneficial than others depending on the situation and application. For example, bubbly flow is desirable in chemical reactors and in the oil and gas industry. The reason for this slug and churn flows can cause pressure fluctuations, hence significant vibration and potential damage to equipment and pipework, meaning in some cases expensive solutions such as slug catchers may be required. However, slug and churn flows may be favoured over bubbly/mist flows which are difficult to deal with by separators due to the presence of very small bubbles and drops. Slug flow can also assist in cleaning up pipes by acting as a virtual “pig”, and can also aid solid transportation. Annular flow is a particularly stable type of flow and can be found in many industries. For example it may be applied to cool down pipes through the formation of the liquid film on the pipe wall. It also occurs in more applications than any other type of flow (Rhodes, 1980).

2.9. Signatures of the flow (PDF & PSD)

PDF

Direct observation through a transparent pipe section, particularly through a high speed camera, can allow visual and qualitative interpretation of the flow inside the pipe. However, this is very subjective, and in early projects such as Bennett et al. (1965), researchers formed a consensus through anonymous voting. Visual observations are also problematic, because the flow at the pipe wall is often obscured by bubbles, particularly at higher velocities, meaning that it is difficult to know what is happening deep inside the pipe through this approach alone. A more objective approach is to gather signals from instruments and then interpret those signals quantitatively. What becomes obvious is that certain signatures are observed for particular types of flow, for example through the time series of void fraction and through the probability density function or PDF. The PDF is a histogram or amplitude variation of the frequencies of the void fractions. Researchers who applied this approach include Jones et al. (1975) and Costigan et al. (1997).

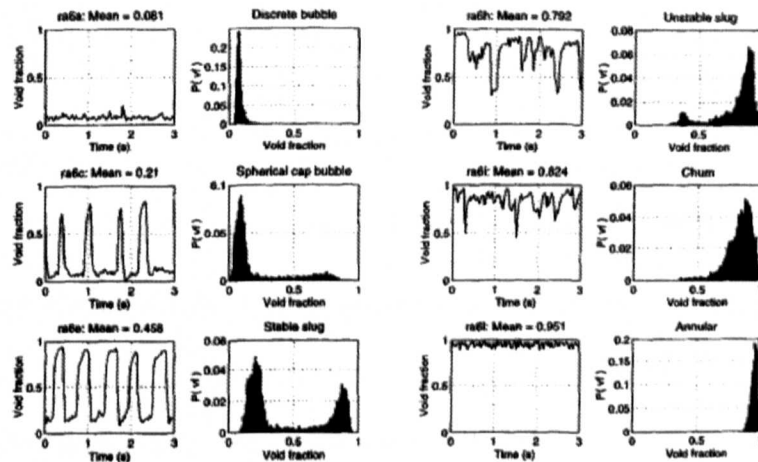


Figure 2.6-Time series and PDF profiles (Costigan & Whalley, 1997)

Figure 2.6 shows typical PDF profiles for the flow patterns described earlier in this section. It is interesting to note that for bubbly flow there is a single peak at low voids

of 0.2-0.3, Slug flow contains two peaks (1st peak-liquid, 2nd peak-gas), churn occurs at voids above 0.5-0.6, which has a single peak with a tail, and finally annular flow has a single peak at high voids of 0.8-0.9.

PSD

Dominant frequencies can be obtained by using the Power Spectrum Density (PSD). Hubbard and Dukler (1966) used the PSD of pressure fluctuations to identify three different types of flow in horizontal pipes, which are separated flow, dispersed flow and intermittent flow. Hawkes and Hewitt (1995) measured the power spectral density of pressure gradient fluctuations in wispy annular flow, and their results are shown in Figure 2.7. Two peaks appear in the spectrum, one at ~5 Hz and a second at ~16 Hz.

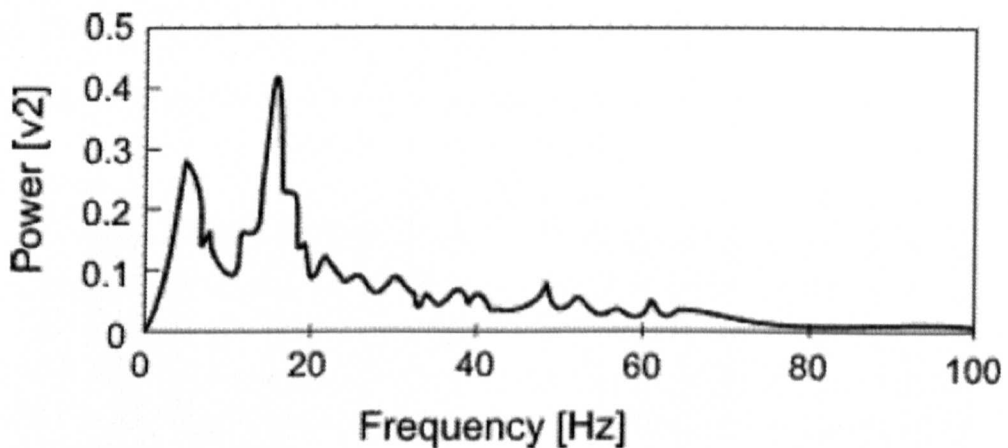


Figure 2.7-Flow identification by PSD for Wispy Annular Flow.

Geraci (2005), Ombere-Iyari (2006), Hernandez-Perez (2007) and Kaji (2008) have all used the PDF together with the PSD approach in their work, and this will also be used in this project. Kaji (2008) uses a fairly novel PSD method, with a cosine windowing function to filter the signal, particularly at higher frequencies. It can be concluded from the PDF and PSD that most flow patterns are characterised by periodic structures. In addition, it can be seen there is a variation in void fraction as well as pressure gradient from one flow pattern to another.

2.10. Structures in the flow

Sun et al. (1999) reported that Zuber (1965) and Wallis (1969) put forward the concept of kinematic or void waves in two-phase flow, which considered that the void fraction waves played an important role in gas-liquid two-phase flow. Sekoguchi and Mori (1997) used multiple point probes to extract further information about the flow, and they identified that Taylor bubbles and liquid slugs occurred in slug flow “S”, huge waves “H” in churn flow and disturbance waves “D” in annular flow. Their work was pioneering in identifying that several different structures can occur simultaneously. For example, slugs “S” and huge waves “H”, or huge wave “H” and disturbance waves “D” occurring together for the same flow condition can be seen in Figure 2.8. Since the plot expresses distance (y-axis) against time (x-axis), the gradients of the lines represent the velocities. Huge waves have steeper gradients than disturbance waves, and hence higher velocities.

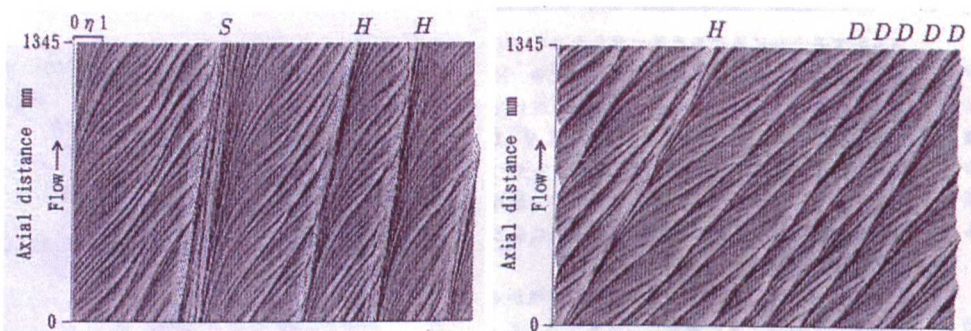


Figure 2.8-Structures as identified by Sekoguchi et al. (1997)

Similar structures were reported by Damsohn et al. (2009). The disturbance waves for small (0.032m) and large (0.125m) diameter pipes were captured by Azzopardi and Gibbons (1983) (Figure 1.6 in Chapter 1). It is interesting to note that the waves in small diameter pipes are coherent around the tube circumference, whereas for large diameters, there is no circumferential identity and the waves are localised to fairly small areas. They are not perpendicular to the main flow, but curve as bow waves.

2.11. Flow Pattern Maps

Flow pattern data are often represented on an x-y map, where common variables for x and y are liquid and gas superficial velocities. There are numerous maps of this kind published in the literature; however, these are specific to a particular combination of fluids and geometry. The most common method for constructing a flow map is to identify the flow pattern at a set of conditions covering the field and then to sketch in the boundary lines separating the different patterns (Azzopardi 2003).

One of the most popular flow pattern maps for vertical flow is that of Roberts-Hewitt (1969), as shown in Figure 2.9. This map was constructed using data from a 0.032m diameter pipe for air-water at 0.4-4.5 bar(g), and from steam-water data by Bennett et al. (1965) for a 0.0127m diameter pipe at elevated pressures of 35 and 70 bar(g). The map uses the momentum flux for gas ($\rho_g U_{gs}^2$) against liquid ($\rho_l U_{ls}^2$) instead of the superficial velocities of liquid against gas to cover a wider variety of fluids and geometries, in order to take into account the densities of the phases.

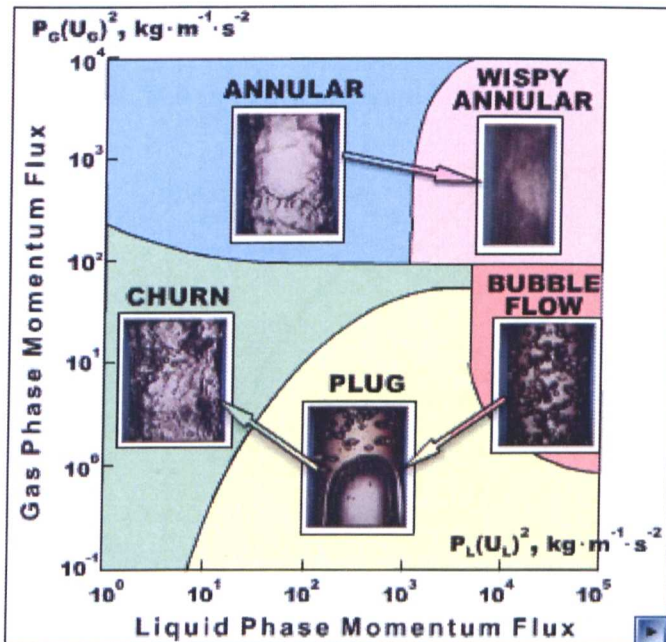


Figure 2.9-Hewitt and Roberts flow pattern map (1969).

Most of the flow maps in the literature have been constructed for small to medium diameter pipes, and no reliable universal flow map has yet been produced (Azzopardi 2003). This is illustrated by the map in Figure 2.12, extracted by Azzopardi et al. (2004), where there is an apparent lack of agreement among the different flow maps.

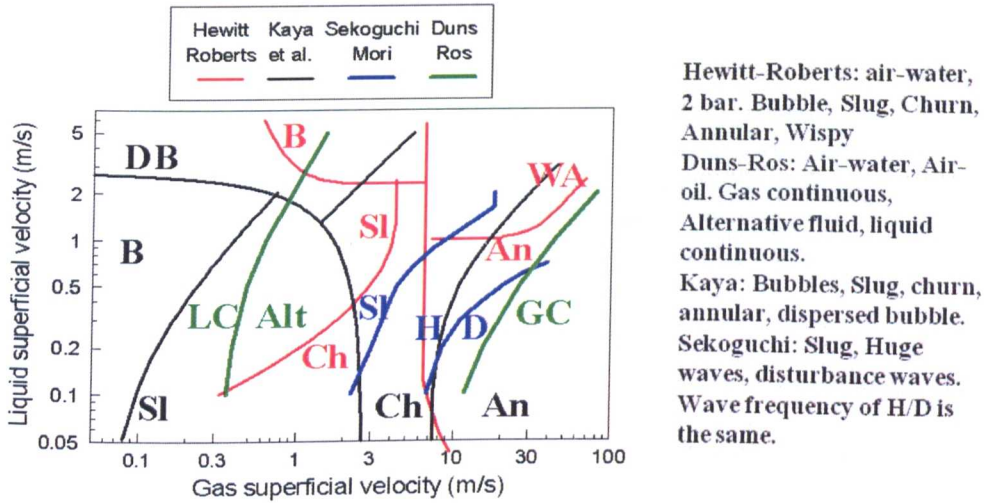


Figure 2.12-Combined Flow Map (Hewitt-Roberts, Duns-Ros, Kaya and Sekoguchi)

There does not appear to be a consensus among researchers on the best co-ordinate system for these maps, and many dimensional and dimensionless numbers have been proposed for the x-y axis. Duns-Ros (1963) used the following two dimensionless groups to describe the flow patterns:

$$\text{Liquid velocity Number } N = u_{ls} \sqrt[4]{\frac{\rho_l}{g\sigma_l}} = 1.938 u_{ls} \sqrt[4]{\frac{\rho_l}{\sigma_l}} \quad (2.16)$$

$$\text{Gas Velocity Number } RN = u_{gs} \sqrt[4]{\frac{\rho_l}{g\sigma_l}} = 1.938 u_{gs} \sqrt[4]{\frac{\rho_l}{\sigma_l}} \quad (2.17)$$

The corresponding flow pattern map is shown in Figure 2.13. This map is fairly popular in the oil and gas industry.

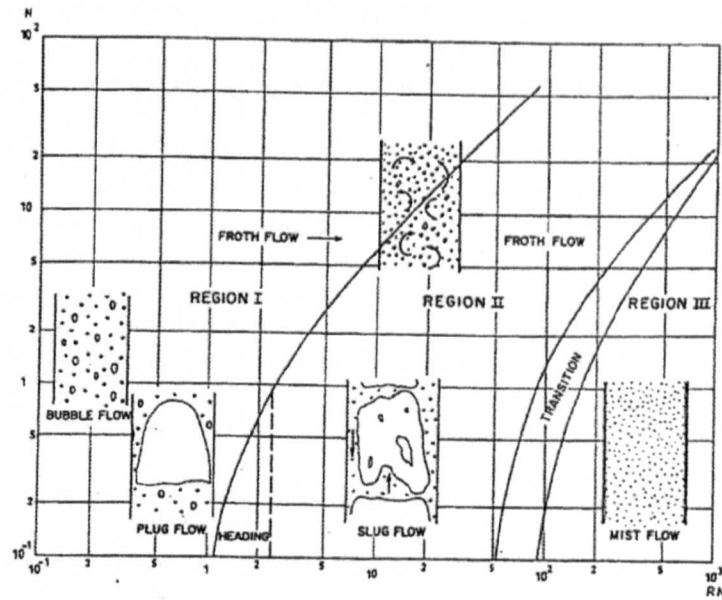


Figure 2.13 -Vertical flow pattern map according to Duns-Ros (1963).

Taitel and Duckler (1976) have also produced a flow pattern map for horizontal flow using several dimensionless numbers that include the density and viscosity of the phases, as well as the pipe diameter and angle of elevation. Using dimensionless groups is popular in single phase flow, and it is certainly a powerful approach, because a flow map with dimensionless parameters can allow it to be used for pipes of different diameters and fluid properties. Therefore the important question is could a new dimensionless map be proposed using popular dimensionless numbers? For example, Reynolds (Re), Froude (Fr) and Weber (We) numbers could be considered. Expressing these groups mathematically:

$$Re = \frac{\rho u D}{\eta} \quad (2.18)$$

$$Fr = \sqrt{\frac{\rho u^2}{\Delta \rho g D}} \quad (2.19)$$

$$We = \frac{\rho u^2 D}{\sigma} \quad (2.20)$$

The Froude number expresses the ratio of the inertial force to the gravitational force.

The effect of using ρu^2 was shown by Hewitt-Roberts (1969). The Weber number multiplies ρu^2 by D/σ , and the Weber number basically expresses the ratio of the inertial force to the surface tension force. An exercise was carried out to investigate the use of the We number for both the x and y co-ordinates. Figure 2.14 shows the familiar momentum flux flow map for air-water by Hewitt-Roberts, together with the conversion of this map to the Weber number shown in Figure 2.15. Figure 2.16 and Figure 2.17 represent a similar exercise for steam-water using Bennett et al's data. It can be inferred from comparing these flow pattern maps qualitatively that the We number flow pattern maps generate similar boundaries to the momentum flux maps. Table 2.2 explains why this is the case, and it can be seen that the ratio of the diameter to the surface tension is the same for air-water and steam-water at 35 bar, and only 55% larger for steam-water at 70 bar.

	Air-H ₂ O (4.5bar)	Steam-H ₂ O (35 bar)	Steam-H ₂ O (70 bar)
D	0.032	0.0127	0.0127
σ	0.072	0.0279	0.0179
D/ σ	0.44	0.45	0.7

Table 2.2-Comparison of D/ σ for three data sets

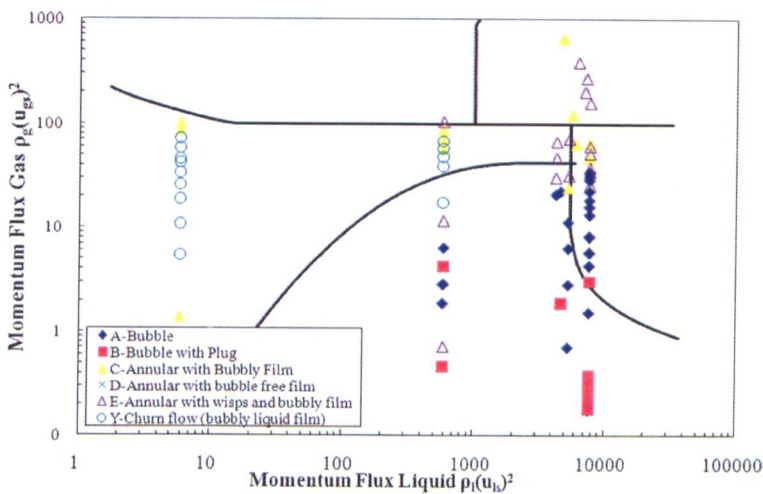


Figure 2.14 - Momentum flux flow map (Air-water)

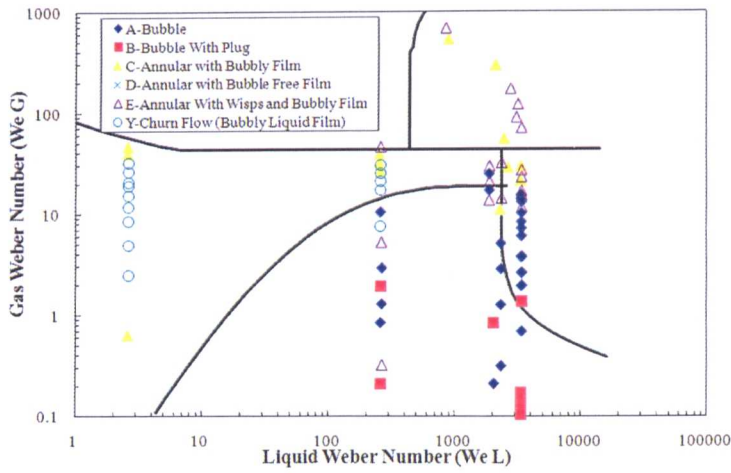


Figure 2.15 – Weber No flow map (Air-water)

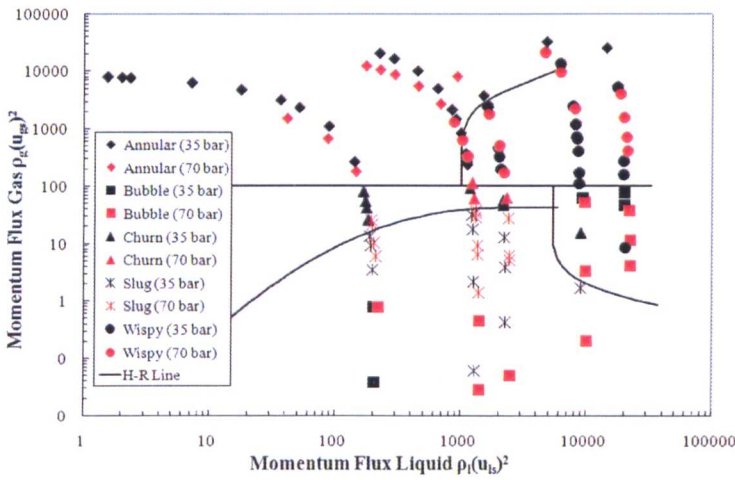


Figure 2.16 -Momentum Flux flow map (Steam-Water 35 & 70 bar).

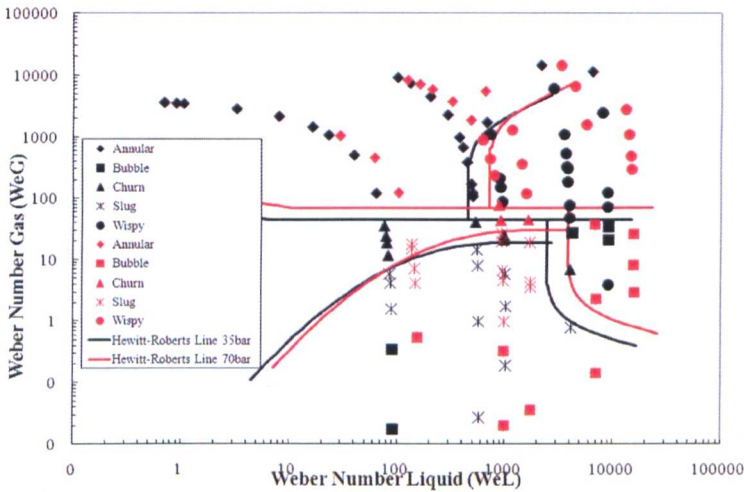


Figure 2.17- Weber No flow map. (Steam-Water 35 & 70 bar)

2.12. What is churn flow?

Due to the complexity and instability (intermittency) of churn flow, with Azzopardi (2009) postulating that this flow is “chaotic” in nature, it is probably the least well understood flow pattern. Barbosa et al (2001a) made an attempt at modelling churn flow in a small diameter pipe however there is currently no thorough and complete model for churn flow (Azzopardi, 2006). Intriguingly Azzopardi (2008) also found similarities between gas-solid flow patterns and churn flow in gas-liquid flow. A number of leading researchers in this field have often stated that churn flow is a very important flow pattern, perhaps even more so than the other intermittent flow patterns, such as slug flow, which receive much more attention. This is because churn covers a large area in the flow map between slug and annular flows. A simplistic explanation of churn flow was given earlier in this report. This flow pattern is surrounded with controversy, and some researchers argue that it does not even exist. For example, Mao and Dukler (1993) published the paper “The myth of churn flow?”, which Hewitt and Jayanti (1993) responded to with “To churn or not to churn”. Barbosa et al. (2001a) presented “Churn flow: myth, mystery and magic”. It is clear there is lack of agreement on how to define churn flow.

Three ideas have been put forward for defining developed churn flow:

- (a) Churn-turbulent flow (also in bubble columns) as proposed by Zuber et al (1965).
- (b) Developing slug flow as proposed by Taitel et al. (1980).
- (c) Individual flow region between slug and annular flow as proposed by Hewitt and Hall Taylor (1970). The focus of this thesis will be on this final definition.

Jayanti and Hewitt (1992) reported that there are four major schools of thought for the transition from slug to churn flow:

(a) Entrance effect mechanism: Taitel et al. (1980) and Dukler and Taitel (1986) considered churn flow as a developing slug flow, due to an entrance effect.

(b) Bubble coalescence mechanism: Brauner et al (1986) attributed the transition to the entrainment of bubbles in the liquid slug and their subsequent coalescence.

(c) Wake effect mechanism: Mishima and Ishii (1984) attributed the transition to the reduction of the liquid slug length, which would lead to a strong wake effect of the Taylor bubble and the destabilisation and destruction of the slug itself.

(d) Flooding mechanism: Nicklin and Davidson (1962), Wallis (1962), McQuillan and Whalley (1985a) and Govan et al. (1991) attributed the transition to the effect of reduced local flooding of the liquid film due to gravity around the Taylor bubble and flowing in counter-current to the gas. One of the crucial experiments on deciding the mechanism for the onset of churn flow was the investigation of the effect of pressure on the transition by Watson and Hewitt (1999). The flooding mechanism was the only one to give a correct indication of the effect of pressure. Flooding is of considerable industrial importance (Hewitt, 1996). It is the limiting condition for the operation of reflux condensers, it limits the ingress of water in postulated loss-of coolant accidents in nuclear reactors and, as described above, it governs the transition from slug to churn flow. Consider the flooding mechanism shown in Figure 2.18, for counter-current flow i.e. gas and liquid flowing in opposite directions.

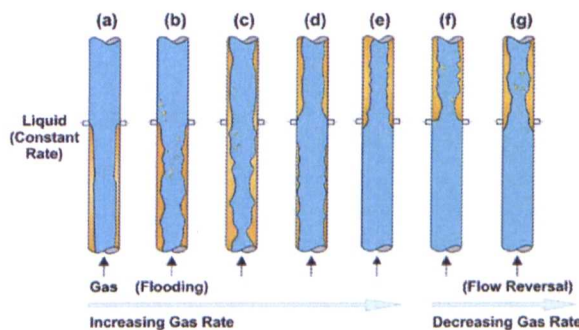


Figure 2.18-Flooding and Flow Reversal (Hewitt, Themopedia.com)

Liquid is introduced in the middle of the pipe, which is allowed to fall under gravity as a film. This is (a) in Figure 2.18. As the gas rate is increased, then flooding occurs in (b) and the liquid starts to travel upwards. It then travels upwards and downwards in (c) and (d), until case (e), when all the flow is flowing upwards. At this stage, if the gas flow rate is reduced, liquid first hangs at the liquid inlet point. Then if the gas flow is further decreased, liquid begins to fall below the injector (g), which is known as flow reversal.

Detailed experimental work on flooding was carried out by Govan et al. (1991). Flooding waves were found to be created in the Taylor bubbles as the transition to churn flow is approached (Jayanti et al, 1993). Flooding waves do not exist in slug or annular flow (Hewitt et al, 1985). Kaji et al. (2009) used several pairs of ring probes and cross-correlated the data from several pairs. They focussed on the Taylor bubble region and found that there were both positive and negative velocities around the slug/churn transition. This shows that there clearly was flooding occurring at the film around the Taylor bubble.

For small diameter pipes, McQuillan and Whalley (1985b) developed a theory that embodied the Wallis (1969) correlation for flooding. Jayanti and Hewitt (1992) extended the theory by introducing a new flooding correlation, which took into account the length of the falling film.

$$\text{Dimensionless superficial gas velocity } u_g^* = \frac{U_{gs} \sqrt{\rho_g}}{(g D_i (\rho_l - \rho_g))^{1/2}} \quad (2.21)$$

$$\text{Dimensionless superficial liquid velocity } u_l^* = \frac{U_{ls} \sqrt{\rho_l}}{(g D_i (\rho_l - \rho_g))^{1/2}} \quad (2.22)$$

For flooding $u_g^* = 1$. These numbers are essentially a balance between the inertial forces and the gravitational forces, normally known as the Fr number. u_g^* and u_i^* are inter-related by the following equation:

$$\sqrt{u_g^*} + c_1 \sqrt{u_i^*} = c_2 \quad (2.23)$$

$$c_1 = 0.1928 + 0.01089 \left(\frac{L}{D} \right) - 3.754 \times 10^{-5} \left(\frac{L}{D} \right)^2 \quad \text{for } L/d \leq 120 \quad (2.24)$$

$$c_1 \approx 1 \quad \text{for } L/d > 120 \quad (2.25)$$

In the limiting case for zero downflow of liquid i.e. when flooding or flow reversal occurs, then $u_g^* = 1$ and:

$$u_g^* = \frac{U_{gs} \sqrt{\rho_g}}{(g D_i (\rho_l - \rho_g))^{1/2}} = 1 \quad (2.26)$$

$$U_{gs} \sqrt{\rho_g} = (g D_i (\rho_l - \rho_g))^{1/2} \Rightarrow U_{gs} = \frac{(g D_i (\rho_l - \rho_g))^{1/2}}{\sqrt{\rho_g}} \quad (2.27)$$

Equation (2.27) predicts an increase in flooding velocity with increasing tube diameter. There is a large scatter observed when $\sqrt{u_g^*}$ is plotted against $\sqrt{u_i^*}$ (Govan et al, 1991).

In large pipes, a different mechanism to flooding was proposed, since the wave is not continuous about the pipe as was seen earlier. Drops are formed off the more local waves, as gas either drags the drop upwards or gravity drags it downwards. The balance of drag up and gravity down depends on the size of a droplet, which cannot be more than a critical diameter. As explained previously, the balance between the inertial and surface tension forces is known as the Weber number or We. According to Hinze (1955), if $We > 13$, the droplet will break up in motion due to the inertial forces. However, if $We < 13$ the drop will survive due to surface tension. Azzopardi (1983)

considered two key mechanisms for droplet break-up, namely “bag” and “ligament” break-up, which are related to the We number.

Another dimensionless constant can be extracted:

$$WeFr_g = \frac{\rho_g u_g^2 D_l}{\sigma} \frac{\rho_g u_g^2}{g(\rho_l - \rho_g) D_l} = \frac{\rho_g^2 u_g^4}{g\sigma(\rho_l - \rho_g)} \quad (2.28)$$

This is commonly referred to via $(We Fr_g)^{0.25}$, which is called the Kutatdeladze number or Ku_g . Pushkina et al. (1969) proposed that $Ku_g=3.2$ for large diameter pipes, although $We=13$ will give a Ku_g value of 2.5 (Whalley, 1987).

$$(We.Fr_g)^{0.25} = Ku_g = \left(\frac{\rho_g^2 U_{gs}^4}{g\sigma(\rho_l - \rho_g)} \right)^{0.25} \quad (2.29)$$

$$Ku_g = \frac{U_{gs} \sqrt{\rho_g}}{(g\sigma(\rho_l - \rho_g))^{1/4}} = 3.2 \quad (2.30)$$

$$\frac{U_{gs} \sqrt{\rho_g}}{(g\sigma(\rho_l - \rho_g))^{1/4}} = 3.2 \Rightarrow U_{gs} \sqrt{\rho_g} = 3.2(g\sigma(\rho_l - \rho_g))^{1/4} \quad (2.31)$$

$$U_{gs} = \frac{3.2(g\sigma(\rho_l - \rho_g))^{1/4}}{\sqrt{\rho_g}} \quad (2.32)$$

It is interesting to note that here U_{gs} is independent of the diameter, or rather that diameter has no effect. A similar equation to (2.23) can be written as:

$$\sqrt{Ku_g} + c_3 \sqrt{Ku_l} = c_4 \quad (2.33)$$

McQuillan et al. (1985) obtained a value for u_g^* of approximately 0.9, which covered many experimental results. McQuillan and Whalley (1985b) carried out a systematic comparison of flooding equations against a bank of 2762 experimental data points available at the time. They concluded that a modified version of the equation of

Alekseev et al. (1972) was the most accurate, due to the scatter with Wallis' correlation.

$$Ku = 0.286 Bo^{0.26} Fr^{-0.22} \left(1 + \frac{\eta_l}{\eta_w}\right)^{-0.18} \quad (2.34)$$

Some researchers claim the amount of liquid travelling as drops or entrained liquid varies with U_{gs} , in a decreasing then increasing manner. For example, Wallis (1962) proposed this theory as displayed in Figure 2.19 (left). Barbosa et al. (2002) proposed the following correlation for entrainment (Figure 2.19; right):

$$E_{fr} = 3.4255 D_t^2 \sqrt{\frac{\rho_l \dot{m}_l}{\rho_g \dot{m}_g}} + 0.0095 \quad (2.35)$$

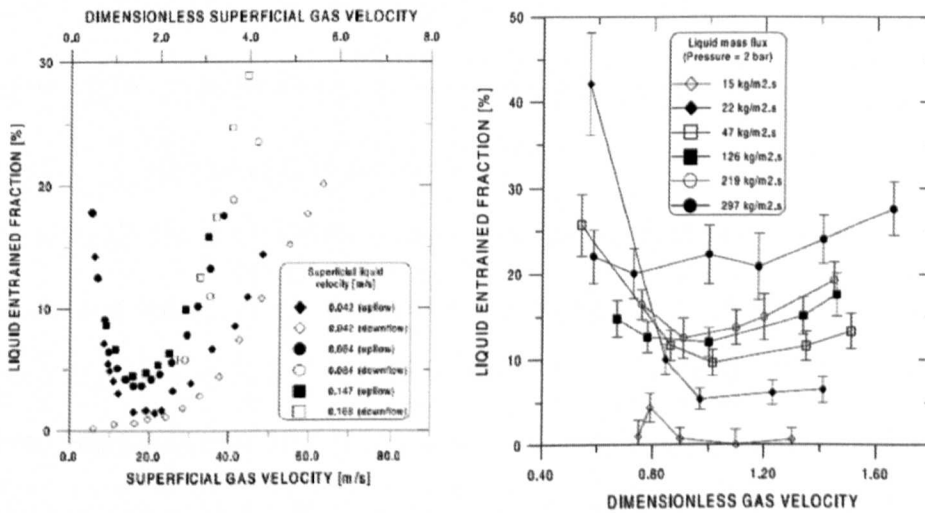


Figure 2.19-The effect of gas superficial velocity on liquid entrainment

Azzopardi and Wren (2004) however casted doubts on this idea. They considered data collected from a T-junction, and concluded that the entrained fraction has a very weak dependence on the gas flow rate. Azzopardi and Wren subsequently proposed a simplified correlation, which is independent of diameter, where:

$$E_f = 0.47 U_{gs}^{0.16} U_{ls}^{0.35} \quad \text{for } U_{gs} < 5 \text{ m/s} \quad (2.36a)$$

$$E_f = 0.6 U_{ls}^{0.35} \quad \text{for } U_{gs} > 5 \text{ m/s} \quad (2.36b)$$

Recently, Ahmad et al. (2010) published a new correlation for the entrainment rate, shown in equation 2.37. Figure 2.20 shows the variation in entrainment at 2 bar.

$$\frac{E_{Churn}}{E_{Annular,local}} = -8.73u_g^* + 9.73 \quad (2.37)$$

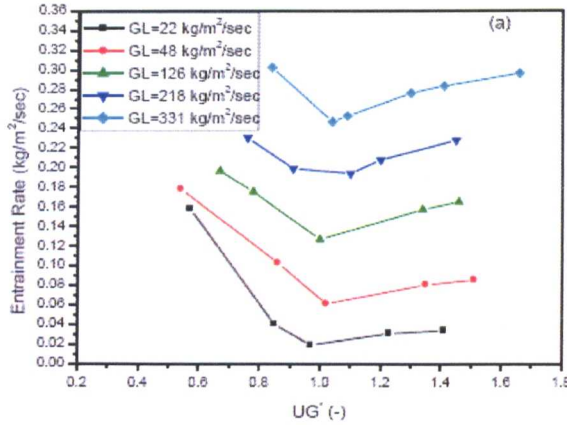


Figure 2.20-Entrainment rate for churn and annular flow at 2 bar (Ahmad et al, 2010)

2.12.1. Structures in churn flow

Hernandez-Perez et al. (2010) recently reported the existence of unusual structures present in a vertical air-water mixture at gas velocities of $U_{ls}=0.25\text{m/s}$ and $U_{gs}=5.7\text{m/s}$ in a 67mm diameter pipe. These were measured using the WMS. The structures occur in the churn region and they have been labelled as “wisps”. These are similar to the wisps in wispy-annular flow reported by Hewitt-Roberts in a 32mm pipe (1969) obtained with x-rays, and Prasser et al. (2002a), in a 51 mm pipe (Figure 2.21) measured using the WMS. However, the gas velocity was lower than that observed by Hewitt/Prasser. For example, Prasser et al. (2002) reported these structures occurring at $U_{ls}=1\text{m/s}$ and $U_{gs}=10\text{m/s}$ in the annular region, and not for churn flow. The work of Hernandez-Perez et al. (2010) indicates that the wisps might be a product of a process of atomisation from the liquid film, which does not proceed to completion. This phenomenon could be considered as a function of the fluid’s inertia compared to its surface tension, or rather the We number.

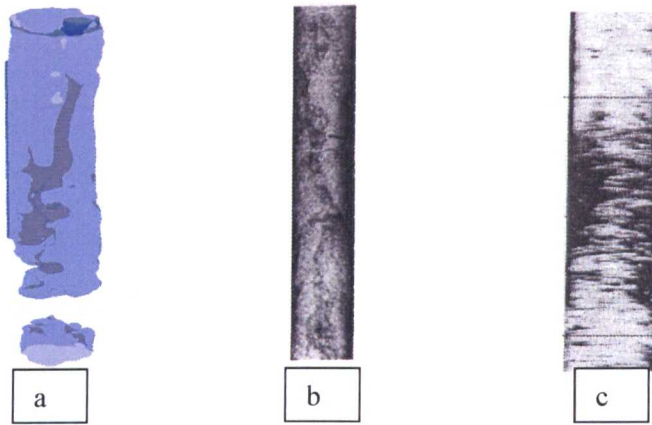


Figure 2.21-Sausage like objects in the gas core: (a) Hernandez et al. (2010), (b) Hewitt et al. (1969), (c) Prasser et al. (2002)

For the 67mm pipe (Hernandez et al), We_g was calculated as 36. For the 32mm pipe (Hewitt-Roberts), We_g was 26, and for the 51 mm pipe (Prasser et al), We_g was 84. Figure 2.22 shows the frequencies of the periodic structures reported by Sekoguchi and Mori (1997). The frequencies fall and rise systematically with increasing gas superficial velocity. The frequencies of huge and disturbance waves show similarities to those of wisps and disturbance waves reported by Hawkes et al. (2000).

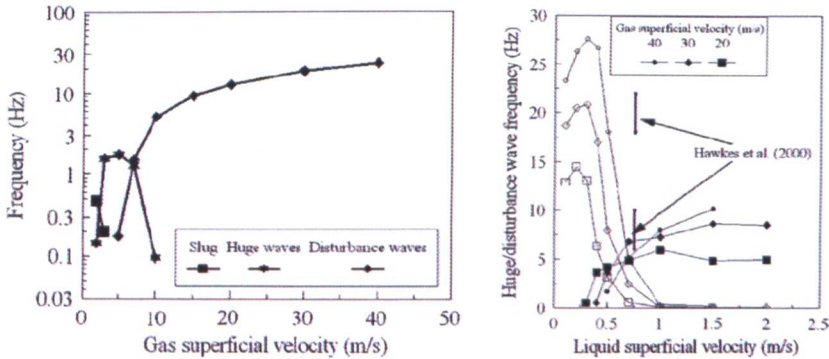


Figure 2.22-(Left) Frequencies of slug/huge waves/disturbance waves reported by Sekoguchi et al (1997). Pipe= 26 mm, pressure = 2 bar, liq superficial velocity = 0.1 m/s. These frequencies are compared with those obtained by Hawkes et al (right)

The important questions to be answered in this thesis are do these structures also occur in large diameter pipes in the churn region, and do they occur with other two phase mixtures such as air-oil? How do wisps form and why? Why haven't they been reported in the past? Are these structures caused by the WMS?

2.13. Flow pattern models

For the main flow patterns, the available models in the literature were compared with experimental data by Holt et al. (1999) and Azzopardi and Hills (2003). This exercise was carried out for small diameter pipes, and involved using drift flux correlations for bubble flow. Slug flow was dealt with by a mechanistic description involving separate sections around and between the Taylor bubbles, and finally the de Cachard and Delhaye model and an annular flow model were used for both churn and annular patterns. The results are shown in Table 2.3.

Flow pattern	Model/ Correlation	Data points	Correction factor	Range factor
Bubbly	Bubbly flow model	181	1.003	1.162
	Friedel/CISE	181	1.008	1.165
Slug	Slug flow model	1495	0.854	1.720
	Friedel/CISE	1495	1.031	1.828
Churn	Churn flow model	524	1.155	3.370
	Annular flow model	524	0.975	1.693
	Friedel/CISE	514	0.809	1.861
Annular	Annular flow model	3556	0.540	5.010
	Friedel/CISE	3545	1.0171	1.788

Table 2.3-Comparison of correlations with flow specific models, Azzopardi & Hills (2003)

Holt et al. (1999) concluded that the drift flux model performs very well. The comparison of the model predictions with the churn flow data is somewhat disappointing and it is interesting to note that the annular flow model performed better than the churn model in predicting the churn flow pressure drops. This observation, regarding the performance of annular models in predicting data from churn flow systems, is consistent also with that of Whalley (1987).

2.14. Flow pattern Transitions

The transitions between different flow patterns do not always occur as predicted by the flow maps above. Often the transitions are gradual, and sometimes a few experimental points lie on the wrong side of the transition lines. The lines should therefore be considered as bands or zones of indeterminate width (Azzopardi 2003). Typically for small diameter pipes, the void fraction of gas is between 25 and 30% when the transition from bubble to slug flow occurs. The bubbles coalesce to form the large Taylor bubble, and as the gas flow rate is increased, the pattern changes from bubble, to plug, to churn, to annular and finally to wispy annular flow. The transitions below are summarised by Azzopardi (2003, 2006). These results are mainly for small diameter pipes.

Bubble to Slug Transition

As described earlier, potentially there could be two different transitions. The first is discrete bubble to slug, and the second is dispersed bubble to slug.

Discrete bubble to slug

Taitel et al. (1980) used the concept of a critical void fraction to define the transition in terms of superficial velocities.

$$u_l = \frac{U_{ls}}{(1 - \epsilon_g)} \quad \text{and} \quad u_g = \frac{U_{gs}}{\epsilon_g} \quad (2.38)$$

$$\text{Harmatty (1960) proposed } V_T = u_g - u_l = 1.53 \left(\frac{g\sigma\Delta\rho}{\rho_l^2} \right)^{1/4} \quad (2.39)$$

Setting ϵ equal to the critical value of 0.25 gives $U_{ls} = 3U_{gs} - 1.15 \left(\frac{g\sigma\Delta\rho}{\rho_l^2} \right)^{1/4}$

$$\text{Slug occurs if } U_{ls} < 3U_{gs} - 1.15 \left(\frac{g\sigma(\rho_l - \rho_g)}{\rho_l^2} \right)^{1/4} \quad (2.40)$$

Dispersed bubble to slug

Brauner and Barnea (1986) considered the balance between dispersive forces and surface tension forces, which results in the equation:

$$2 \left[\frac{0.4 \sigma}{\Delta \rho g} \right]^{1/2} \left(\frac{\rho_l}{\sigma} \right)^{3/5} \left[\frac{2}{D_t} 0.046 \left(\frac{D_t}{\nu_l} \right)^{-0.2} \right] (U_{gs} + U_{ls})^{1.12} = 0.725 + 4.15 \left(\frac{U_{gs}}{U_{gs} + U_{ls}} \right)^{1/2} \quad (2.41)$$

This can be solved for the slug-dispersed bubble boundary when:

$$\epsilon_g = \frac{U_{gs}}{U_{gs} + U_{ls}} = 0.52 \quad (2.42)$$

There is an upper limit on the possible void fraction in bubbly flow due to the close packing of bubbles. Taitel et al. (1980) take this value to be 0.52. There is insufficient published data that clearly identifies the dispersed bubble pattern for a thorough test of these models (Azzopardi, 2006).

Hewitt (2005) believes this traditional view of the transition is possibly incorrect, and more likely is due to the formation of void waves, which lead to bubbles packing more closely and therefore the probability of them coalescing increases leading to plug (slug) flow. Evidence for this can be found in Beisheuvel and Gorissen (1990).

Slug to Churn

Liquid slug results in churn flow rather than dispersed bubble flow if $U_{ls} < 0.92 U_{gs}$.

Watson and Hewitt (1999) have compared the predictions of several correlations with some extensive air/water data at 1.2, 3 and 5 bar in a 32 mm tube. The main

conclusion was that the equation by Jayanti and Hewitt (1992) presented earlier gives the correct trend. A simple semi-empirical correlation has been developed by Porteous (1969), which yields the following approximate criterion for the establishment of churn flow:

$$U_{gs} = 0.105 \left[\frac{gD(\rho_l - \rho_g)}{\rho_g} \right]^{1/2} \quad (2.43)$$

Ombere-Iyari and Azzopardi (2007) found that the PDF method failed to predict the slug to churn transition.

Churn to Annular

For the churn/annular transition, the approach employed by McQuillan and Whalley (1985b) is used, based on Taitel et al. (1980). There is a critical gas flow rate for which an increase ensures that the liquid flows upwards with the gas and for which a decrease allows the liquid to fall under gravity. This flooding or flow reversal point can be predicted using:

$$Ku = \frac{U_{gs} \rho_g^{1/2}}{[\sigma g \Delta \rho]^{1/4}} \geq 3.1 \Rightarrow U_{gs} \geq 3.1 \left[\frac{g \sigma (\rho_l - \rho_g)}{\rho_g^2} \right]^{1/4} \quad (2.44)$$

$$u_g^* = \frac{U_{gs} \rho_g^{1/2}}{[gD\Delta\rho]^{1/2}} > 1 \Rightarrow U_{gs} > \left[\frac{gD(\rho_l - \rho_g)}{\rho_g} \right]^{1/2} \quad (2.45)$$

This transition is a gradual one. The flooding waves (with intermediate zones of falling films) that are characteristic of churn flow gradually die out, the liquid films between the waves begin to move upwards and disturbance waves are formed on them that lead to further entrainment (extensive entrainment occurs also from the flooding waves) (Pickering et al, 2001).

If the flow is of the annular type (or the Taylor bubble aspect of slug flow) the film thickness δ is related to the void fraction by the following equation:

$$\delta = \frac{D}{2} (1 - \sqrt{\varepsilon_g}) \quad (2.46)$$

Van der Meulen et al. (2010) found that the two popular flooding equations given above (the Wallis parameter and the Kutateladze number) do not accurately predict the churn/annular transition for large diameter pipes. They found that the work of Sekouchi and Mori (1997) gave a better estimate of the transition.

Annular to wispy Annular Transition

According to the Hewitt-Roberts map, this transition occurs at some critical gas and liquid momentum flux. However, this is fairly subjective. Very little research has been published in the annular to wispy annular transition (Rhodes, 1980). Hawkes et al. (2000, 2001) looked at this transition in more detail, and Collier et al (1994) gave an equation proposed by Wallis (1969):

$$U_{gs} = \left(7 + 0.06 \frac{\rho_l}{\rho_g} \right) U_{ls} \quad (2.47)$$

The wispy annular region usually corresponds to the case where u_g^* is greater than unity and u_l^* is greater than 2.5 to 3 (i.e. for high mass fluxes). Here, the core structures develop not unlike void waves (except that they are now concentration waves) and these have a very strong influence on the flow behaviour (Hewitt, 1997).

McQuillan and Whalley (1985a) carried out a systematic comparison among the published transition equations, and compared them with experimental data of 1399 points. Their findings are summarised in Table 2.4.

		Experimental Flow Pattern				
Predicted Flow Pattern		Bubble	Slug	Churn	Annular	Total
	Bubble	182	36	3	4	225
	Slug	36	126	9	0	171
	Churn	25	180	317	97	619
	Annular	4	13	12	355	384

Table 2.4-Comparison of experimental vs. transition models, McQuillan & Whalley(1985a)

It is interesting to note that most of the models perform well, except for churn flow, as despite having the most data points, a significant number of those points fall into either the Slug or Annular category.

2.15. Large Diameter Pipe Investigations

There is a general consensus that “large” diameter pipes can be considered to be greater than 100mm in diameter, and a number of studies have been carried out on pipe diameters in excess of 100mm in the vertical orientation. The majority of published papers appear to be mainly for air-water and steam-water mixtures, and there is very little published work on large diameter air-oil pipes. Ali (2009) carried out a literature review ranging from 1976 to 2007. Table 2.5 gives a summary of the investigations carried out on large diameter pipes, mainly for air-water, that has been adapted from Ali (2009) and updated. Recently, Lucas et al. (2010) presented a new database on air-water flows in a large diameter pipe of 200mm.

An important consideration will be how some of the methods and models mentioned in this chapter function when applied to large diameter pipes. In small diameter tubes, churn flow may not develop at all and the flow changes from slug flow to annular.

Several studies have shown the interesting absence of slugs in large diameter pipes, where there is a direct transition from bubble to churn flow, for example Hills (1976), Cheng et al. (1998) and Ohnuki and Akimoto (2000). Ohnuki and Akimoto (2000) reported “churn-froth”, “churn-slug” and “churn bubbly” regimes in their 200 mm pipe, in conditions where traditional slug flow would be expected, and slug flow was not observed in these bigger pipes. This has implications for industries that use large diameter pipes and extrapolate data obtained from small diameter pipes to predict the behaviour of large diameter pipes; clearly this approach is full of uncertainties.

Pickering et al. (2001) stated that it is unlikely that the mechanism of flooding in counter-current flow described earlier, which is used to describe the transition from slug to churn, can apply for large diameter pipes since the slug flow bubbles do not exist in the same form as they do for smaller diameter pipes. Furthermore, direct experiments on flooding in large diameter pipes (Watson, 1999) show that the mechanism present is quite different. Thus, in small diameter pipes, flooding waves are formed that are coherent around the tube periphery and which can be swept up the tube as a result of forces on them by the gas core. Between these waves, there would be a falling liquid film. However, in flooding experiments in large diameter pipes, the waves are not coherent around the pipe, but are localised in short regions around the circumference. These local flooding waves are not swept upwards by the gas phase as the forces on them are insufficient, (Jayanti et al, 1992). Instead, the non-coherent waves are broken up into droplets, which are then levitated by the gas phase. This process continues until the annular flow region is reached.

Researcher	Year	Fluid system	Pipe Ø(mm)	L/D	Ugs (m/s)	Uls (m/s)	Pressure (MPa)	Bubble Injection Method	Flow regime observed
Hills	1976	Air - water	150	70	0.62-3.5	0.5 - 2.6	0.1	Vertical pipe at the center of test section at the base	Bubbly, Large bubbles with froth and Churn
Shiple	1984	Air - water	457	12.34	5	2	0.1	Cross shaped sparger	Bubbly
Van der Welle	1985	Air - water	100	-	Not given	0.9-2.5	0.1	Not given	Not given
Clark and Flemmer	1986	Air - water	100	10	-	-	0.1	-	Bubbly, Large cap bubbles
Hashemi et al.	1986	Air - water	305	9.41	1.16	0.06	0.1	Air injection before elbow in horizontal run	Bubbly, Large cap bubbles, Churn and Annular
Ohnuki and Akimoto	1996	Air - water	480	4.2	0.02 - 0.87	0.01 - 0.2	0.1	Sinter inlet and Nozzle at inlet	Uniform bubbly, Agitated Bubbly, some Cap bubbles and Churn
Cheng et al.	1998	Air - water	150	70	1.113	1.25	0.1	Sparger cap at the base of Riser	Bubbly, occasional Cap bubbles, and Churn
Hibiki and Ishii	2000	N2 - water	102	53.9	0.286	0.387	0.1	No horizontal section	Bubbly, occasional Cap bubbles, and Churn
Ohnuki and Akimoto	2000	Air - water	200	61.5	4.7	1.06	0.1	Porous sintered tube cap	Uniform bubbly, Agitated Bubbly, Churn-bubbly, Churn-slug and Churn-froth
Shoukri et al.	2000	Air - water	100 & 200	43	0.02 - 15.5	0 - 1.8	0.1	Circular disc of shower head geometry	Bubbly, Churn and Annular
Prasser et al.	2002	Air - water	200 mm	-	0.037 - 1.30	1	0.1	Conical perforated head	Uniformly agitated bubbly and Churn
Sun et al.	2002	Air - water	112.5	106.7	0.122	0.011 and 0.15	0.1	-	Bubbly, Distorted cap bubbly and Churn
Hibiki and Ishii	2003	N2 - water	102	53.9	0.146	0.198	0.1	With horizontal section	Bubbly, occasional Cap bubbles, and Churn
Sun et al.	2003	Air - water	101.6	40	0.502	0.058 - 1.03	0.1	Three Sintered spargers units	Bubbly, occasional Cap bubbles, and Churn
Omebere et al. (VERTICAL)	2004	N2 - Naptha	189	264.5	4	15	2.0 and 9.0	Vertical pipe in the center of the base & pipe in base with side outlet only	Bubble, Churn and Annular
Shen et al.	2006	Air - water	200	43	0.035-1.12	0.03-0.06	0.1	Porous ring sinter tube with grain size of 40µm, 2 x80 holes of Ø0.5mm	Dispersed Bubbly, Churn Bubbly
Omebere	2006	Air - water	127	65.6	1.1 - 15.3	0.032 - 0.3	0.2, 0.3 (abs)	Annular Injector	Churn, Annular
Schlegel	2009	Air - water	150	30	0.1 - 5.1	0.01 - 2.0	0.1	Air injectors consist of porous metal sparger.	Bubbly, Cap Bubbly, Churn
Ali	2009	Air - water	254	46	0.09-1.6	0.2-0.8	0.1	Tee and Annular sleeve	Bubbly, Agitated/Dispersed Bubbly, Churn Froth

Table 2.5-Experimental work on large diameter pipes, Adapted from Ali (2009).

Pickering et al. (2001) speculated on the transitions in large diameter pipes. Smaller bubbles coalesce (either independently or within void waves) to form spherical cap bubbles, which cannot in themselves grow to a large enough size to occupy the full pipe cross section, as in the case for small diameter pipes. The spherical cap bubbles formed will rise in concentration and may also form void waves. This will lead to coalescence of these bubbles and the formation of large voids in the centre of the channel. If the flow velocity is high enough, then the voids formed in the channel core may become continuous to form a churn or annular type flow. In the churn flow case, flooding waves will be locally formed, which would break up into droplets, the flow falling partially downwards in the associated falling films. At high enough velocities, the flow would become annular with no falling film regions. Another area of importance is that of the transition from annular to wispy annular flow. The fraction of liquid that is entrained increases with increasing diameter, in order to maintain the balance between entrainment and deposition. In agreement with this, during the experimental work conducted at the University of Nottingham it has been found that for large diameter pipes, the entrained fraction is higher than for smaller pipes.

This research study will focus on some of the most recently published works on large diameter pipes, for example Ombere-Iyari (2006). The experimental set-up used in this work was similar to the one used by Ombere-Iyari with some modifications and new instrumentation. Details of the rig and measuring instruments are given in the next chapter. Schlegel et al. (2009) published a study on large diameter pipes with air-deionised water (Figure 2.23). The paper was followed by another by Schlegel et al. (2010) recommending a set of drift-flux models that were tested on various diameter pipes.

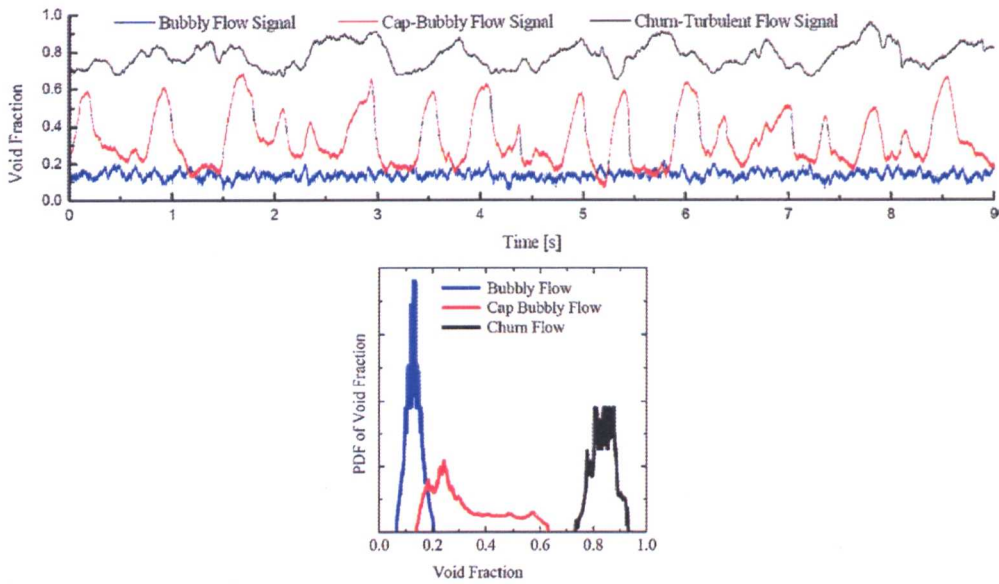


Figure 2.23-Sample data from Schlegel et al (2009). No double peak to indicate slug flow!

This project uses a pipe diameter of 127mm, which is 4 times bigger than the one used by Hewitt-Roberts. An important question is what do flow maps for a small diameter pipe look like for a large diameter pipe? Ombere-Iyari (2006, 2007) attempted to answer this question by plotting his data obtained from a 189mm diameter pipe on the Taitel and Hewitt-Roberts maps mentioned earlier (Figure 2.24). The gas-liquid mixture used was Nitrogen-Naphtha (petrol) at 20 and 90 bar. Clearly the flow maps are not performing well, even though in theory they should, as one map attempts to be more generic in physical properties (Hewitt-Roberts), and the other is semi-empirical (Taitel et al).

Ombere-Iyari (2006) also concluded that for the churn-annular transition, the work by McQuillan and Whalley (1985a) and Taitel et al. (1980) gave better predictions than those provided by Barnea (1986) and Costigan et al. (1997). He also obtained poor results when he applied the slug-to-churn transition criteria developed by Jayanti and Hewitt (1992).

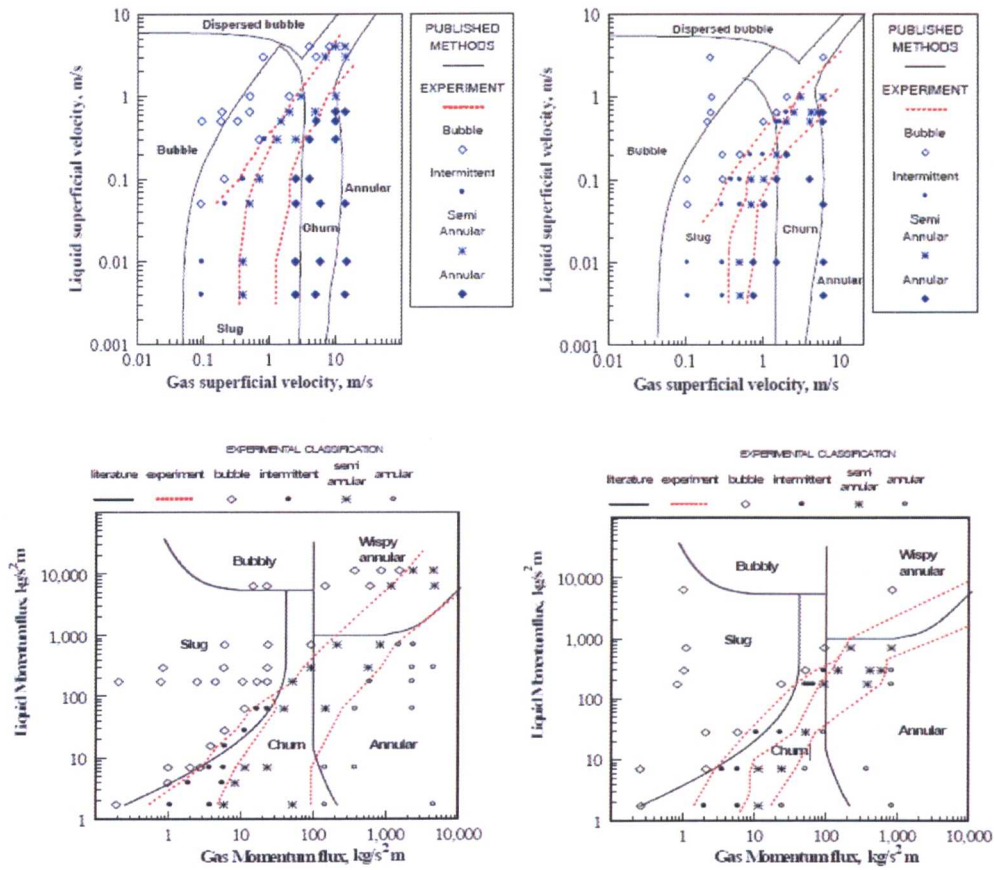


Figure 2.24-Flow maps (Left) 20 bar, (right) 90 bar. Red lines are experimental transition points, and black lines are theoretical, Ombere-Iyari, (2006).

2.16. Mechanistic vs. Empirical Modelling

Most of the above correlations and flow maps are empirical in nature. This is obtaining relationships based on specific experimental data. To be applied correctly, these correlations are normally limited to the same conditions and geometries used in the experiments in which they were deduced. This may not always be practical for industry, for example flow assurance engineers in the oil and gas sector. Mechanistic models, which incorporate more of the underlying physics, are proving to be more useful and reliable as they can be applied more generally to systems while obtaining reasonably accurate results. Many models for vertical flow, both mechanistic and empirical, have been developed and incorporated into steady-state industry code, such

as in WELLFLO (SPT Group). Some of the popular models are listed below in Table 2.6 (Pickering et al, 2001).

Model	Year	Mechanistic/Empirical	Comments
Ansari	1990	Mechanisc	Developed as part of the Tulsa University Fluid Flow Projects (TUFFP). Designed primarily for well o ws.
Aziz et al	1972	Semi-Empirical	Designed and tested for gas-condensate o ws in wells.
Duns & Ros	1963	Empirical	Developed for verc al o w of gas and liquid mixtures in wells and based on extensive experimental work using air and oil simulants
Gray	1974	Empirical	Developed by Shell for modelling verc al o ws of gas-condensate mixtures in tubes up to 3.5 inch
Hagerdorn & Brown	1965	Empirical	Developed using data gathered from a 1500 experimental well but restricted to tubing diameters of less than 1.5 inch
OLGAS	1991, 2000	Mechanisc	Developed using data collected in the 8 inch SINTEF o w loop which includes a 50m riser.
Orkiszewski	1967	Empirical	Developed for o ws in verc al and deviated wells

Table 2.6-Summary of popular Mechanistic/Empirical correlations.

Again most of these correlations were developed for small diameter pipes. Trick (2003) carried out an extensive study comparing most of the above correlations, and concluded that the OLGAS model appears to be the best method for predicting gas-water and gas-condensate pressure losses. OLGAS was also constructed from large diameter pipe data, adding to its advantage as the preferred mechanistic correlation for large diameter pipes (Dr. K. Wade, private communication). Overall, several approaches have been presented thus far in this report, such as no-slip, slip, empirical and mechanistic methodologies, which have all been employed in various industries.

2.17. Computational Modelling in two-phase flow

CFD or computational fluid dynamics is already an established field in single phase fluid mechanics, which is based on solving the Navier-Stokes equation. There are various models for turbulence, for example the $k-\varepsilon$ model, where k is the turbulent kinetic energy and ε is the rate of dissipation of turbulence. CFD has been proven to be a fairly accurate tool, and is used effectively in many industries, for example to optimise the designs of F1 cars. Running CFD simulations could be quicker than conducting lengthy experimental campaigns. CFD vendors have been recently

attempting to expand their code to simulate two-phase flow. Researchers have also published papers using CFD techniques, for example Da Riva et al. (2009) used FLUENT to investigate churn flow in a vertical pipe. It is worth noting that CFD in two-phase flow uses slightly different methodologies to the ones described earlier in this report, with the application of *phenomenological* models such as Eulerian and Lagrangian models (Lo, 2008). It is worth mentioning that some references also give details of a “Multi-fluid” model, which is a further development of the separated model described earlier. Here, separate conservation equations are written for each phase, which contain terms describing the interaction between the phases.

For dispersed flow such as bubble flow, the Lagrangian approach is used, which tracks individual particles. For stratified flows, such as annular flow, Eulerian or VOF (Volume of Fluid) is used, which tracks a volume and in particular the interface between the phases. It produces plots such as the one in Figure 2.25 (Hernandez-Perez et al, 2011). These modelling techniques vary in terms of resolution, complexity and also applicability to practical problems (Tomiyama, 1998).

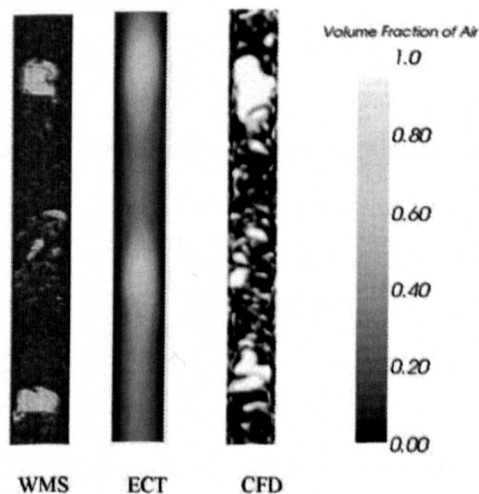


Figure 2.25-CFD modelling in two-phase gas-liquid flow.

In general, the higher the resolution, the more expensive it becomes computationally and hence the lower the applicability. In CFD, discretising a model into smaller segments results in a higher cell or mesh count rate, which in general improves the accuracy of the model. However, there is a time penalty for this. Complex flow regimes such as churn flow will require a large number of grid cells and some thought is needed in how to distribute the cells as the pipe may contain a film on the wall, as well as an active gas core with or without drops. Using a fine mesh on the film alone will be very costly computationally, as well as missing out any detail or structures that may occur in the centre of the pipe. With improving technologies and multi-processor computers, simulations are becoming faster. The attraction of CFD is clear; significant cost savings in comparison to building large experimental rigs, and it can also consider complex geometries. It is important to continue to conduct experimental work, which will help CFD modellers to fine tune their models to match the experimental data (Prasser, 2008). No doubt in the future, CFD will become a more reliable tool for two and three phase flow.

The technical background on bubble columns can be found in Chapter 5.

3. CHAPTER 3: INSTRUMENTATION AND FACILITIES

3.1. Two-phase instruments (Intrusive vs. non-intrusive)

A number of instruments have been developed over the years to investigate gas-liquid two-phase flow, and a summary of these instruments is given in Table 3.1 (Adapted from Da Silva, 2008). It can be seen from this table that there are a number of key factors to consider with multi-phase instruments, which are temporal resolution, spatial resolution, intrusiveness and cost. It is fair to say at this stage that there is still no single instrument that can favourably meet all four of these criteria.

Technique	Spatial Resolution	Temporal Resolution	Costs	Intrusive?	Comments
Needle probes (electrical, optical)	B	IV	\$	Yes	local measurement only
Optical probes (PIV, LDA, HS Camera)	A	III, IV	\$\$	No	low gas fraction only, optical access needed
Hard-field tomography (x-ray*, g-ray*, PET, MRI)	A	III	\$\$\$	No	*radiation protection
Optical tomography	B	IV	\$	No	low gas fraction only and transparent walls and fluids
Capacitance/Conductance probes	N/A	IV	\$	No	Cross-sectional averaged void fraction
Ultrasound tomography	B	III	\$\$	No	Suitable for low void fraction only
Electrical tomography (EIT, ECT, ERT)	C	III	\$	No	nonlinear, ill-posed inverse problem
Wire Mesh Sensor (WMS)	B	IV	\$	Yes	Selection of Conducting vs capacitive sensor
CFD (Simulation Tool)	B	IV	\$	N/A	Time consuming. PC based simulation

Table 3.1-Review of the main experimental techniques in gas-liquid flow

Temporal (I~minute, II~second, III~millisecond, IV~microsecond)
 Spatial (A~1mm, B~2-5mm, C>5mm).
 Cost (\$~low, \$\$~medium, \$\$\$~high)

Some of these instruments have been derived from the medical industry, for example CT (computed tomography) and MRI (magnetic resonance imaging) scanners. The latest development is the state of the art ultra-fast x-ray CT technology developed by Fisher et al (2008, 2010), which produces extraordinarily detailed images (Figure 3.1). The x-ray produces images at a high temporal and spatial resolution, and it is also non-intrusive. The disadvantages of this technique at present are cost, the bulky nature of the equipment and the safety considerations needed when working with x-ray.

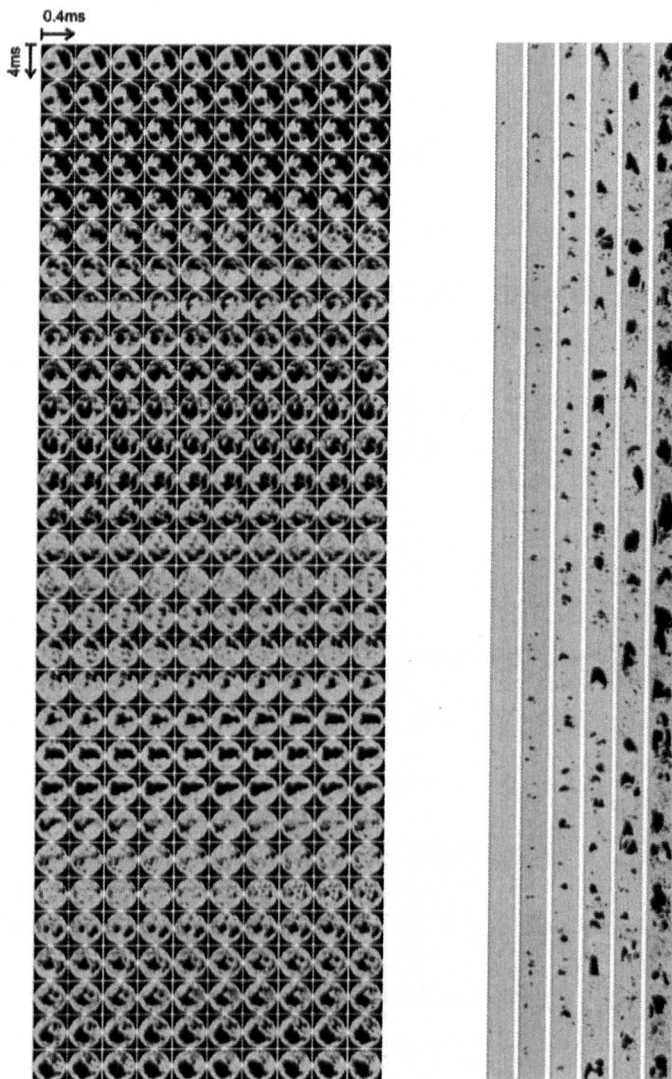


Figure 3.1-Latest developments in multi-phase measurements: x-ray CT. Data taken on a 50mm diameter pipe. (Left): Cross-section for $U_{gs}=0.534\text{ms}^{-1}$ and $U_{ls}=1.017\text{ms}^{-1}$ (Right): Views for U_{gs} in the range from $0.004\text{--}0.534\text{ms}^{-1}$ for $U_{ls}=1.017\text{ms}^{-1}$; Fisher et al (2010)

It is important to distinguish between intrusive technologies (affects the flow) and invasive (takes place inside the pipe). An instrument can therefore be invasive but not necessarily intrusive. For example, ECT systems are non-intrusive and non-invasive, ERT is invasive but non-intrusive, and WMS techniques are both invasive and intrusive. The issue of intrusiveness is an important one. If the instrument is intrusive, it limits the number of applications where it can be used in production facilities. For example, the wire mesh sensor is unlikely to be used in an offshore oil and gas riser, because it would be destroyed by the pigs that are used to clear the riser from impurities. ECT would be a more appropriate choice for such an application.

Some of these instruments can also be used to examine other types of two-phase flow. Work has been carried out in this project to compare the performance of the wire mesh sensor to ECT and conductance probes. ECT and conductance probes will therefore be described briefly in the next section.

3.2. ECT

Electrical capacitance tomography (ECT) is a non-intrusive technique that can be used for imaging and velocity measurement in flows comprising mixtures of two non-conducting materials (Azzopardi et al, 2010c). ECT can be used to investigate pneumatic conveying in a gas-solid mixture (Azzopardi et al, 2008b), which is used in the transportation of coal in power plants. ECT can also be used to measure liquid-liquid flow (Hassan and Azzopardi, 2007). Developments over the past fifteen years have resulted in fast, accurate measurement systems becoming available for laboratory research. The original ECT systems, for example Tomoflow R100, were capable of obtaining data at a rate of 200 Hz. However, recent technological advances have allowed the development of more advanced ECT systems, such as Tomoflow R5000,

which has a temporal resolution of 5000 Hz. In this system, a number of electrodes are arranged around the outside of the non-conducting pipe wall (Figure 3.2) and all of the unique capacitance pairs were measured using a Tomoflow flow imaging and analysis system (Figure 3.2). A typical ECT sensor, for example for a 67mm diameter pipe, has twin planes. Each of these planes contains eight measurement electrodes placed radially around the pipe, with guard electrodes on either side of each measuring electrode. These guard electrodes protect the field of the measuring electrodes.

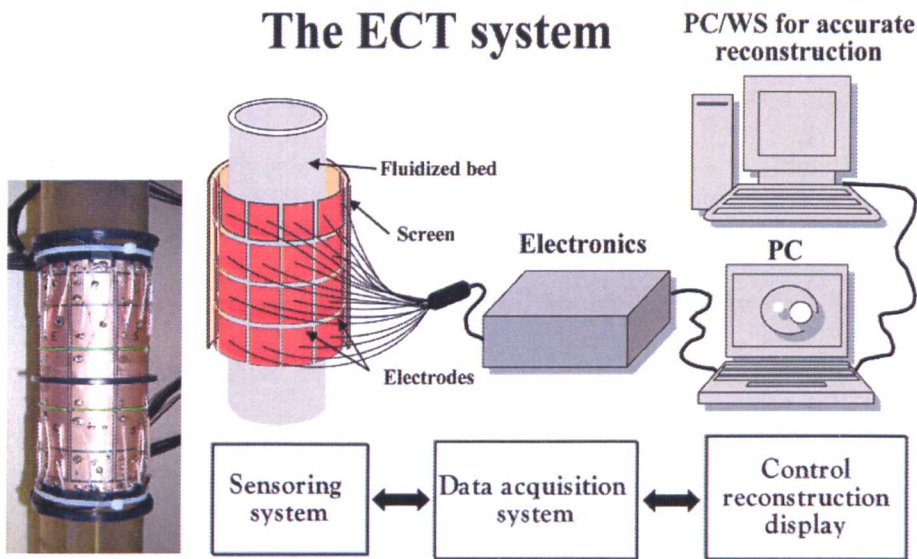


Figure 3.2-ECT system (Warsito et al, 2001), picture on the left showing the bare sensor without a cover.

The mask for the ECT is manufactured in-house at the University of Nottingham, which allows the flexibility of customising the instrument for any pipe diameter. In addition, the ECT systems' use of a twin plane non-intrusive sensor gives them the particular advantage of being able to measure structure velocities, by cross-correlating signals from one plane of sensors to the next. The system is calibrated by taking sets of readings with the pipe initially empty (gas only) and then full (liquid only). In one measurement cycle, the electrodes are excited one by one, while maintaining the others at a reference potential. The capacitance values are then collected between the resulting electrode pairs. The capacitance measurement in ECT is converted to

electrical permittivity using a look-up table linearisation, generated from calibration at various permittivities. To transform this electrical measurement into a fluid-mechanically useful measure of concentration or void fraction involves the use of a physical model that links the two.

ECT is ideal for air-oil mixtures as it is suitable for non-conducting fluids; whereas the equivalent ERT is suitable for air-water. However, with both ECT and ERT systems the spatial resolution is low in particular near the centre of pipe. The visualisation is best near the wall, where the sensors are located. The other main disadvantage with ECT/ERT is that they require the use of an image reconstruction algorithm, such as LBP, or linear back projection. This is considered to be a qualitative, non-iterative technique. There are other algorithms which are iterative and non-linear, however those techniques are slower. Finally, a well known challenge with ECT/ERT is the inverse problem, which is ill-posed or non-linear, meaning that the output is not proportional to the input. Further details and published works regarding ECT can be found in Abdulkareem et al (2009, 2010).

3.3. Conductance Probes

In gas-liquid annular-type flow, the instantaneous wall film thickness (and hence void fraction) can be determined by taking measurements of the electrical conductance between two electrodes in contact with the liquid film. Different types of electrodes, such as parallel wires, flush-wires, flush-mounted pins and flush-mounted rings have been adopted. In this study, three pairs of ring probes were flush mounted with the pipe wall. These can be seen in Figure 3.3.



Figure 3.3-Photo of conductance probes

The thickness of the rings is 3mm and the distance between the probes is 25mm, which are insulated with non-conducting acrylic resin. This gives the electrode separation distance (D_e) to pipe diameter (D_i) ratio of 0.20. The conductance probe requires calibration before it can be employed for measurements. Annular-type flow is usually simulated by placing a non-conductive rod inside the pipe, with the conductive liquid being filled in the annulus between the rod and pipe wall. This is an “ideal” situation where no bubbles exist in the liquid film, which in reality does not always occur as air bubbles will usually be present. Van der Meulen et al (2009, 2010) therefore proposed a novel way of calibrating conductance probes using beads of 3-6mm. The advantages of using conductance probes are that they provide non-intrusive measurements, they allow measurement of small impedances, they are relatively cheap, and they allow the electric field to be efficiently confined. The disadvantages are that they are measuring circumferentially averaged film thicknesses as opposed to the whole-cross sectional void, they provide no visualisation of the flow, and finally they are limited in this case to annular and transition to annular flow. It is possible however, to calibrate conductance probes for other types of flows e.g. bubbly flow (Ombere-Iyari, 2006).

3.4. Specialist Instrument Wire Mesh Sensor (WMS)

There are two variants of the wire mesh sensor (WMS), which are conductance and capacitance WMS, often abbreviated in this thesis as CondWMS/CapWMS. Both of these instruments were used in this project, therefore both variants will be described in detail in this section. The WMS can be used to investigate both gas-liquid and liquid-liquid flows, but this report will focus on the WMS applied to gas-liquid work only.

3.4.1. Historical Background

The historical background behind this novel instrument can be summarised by Figure 3.4 below:

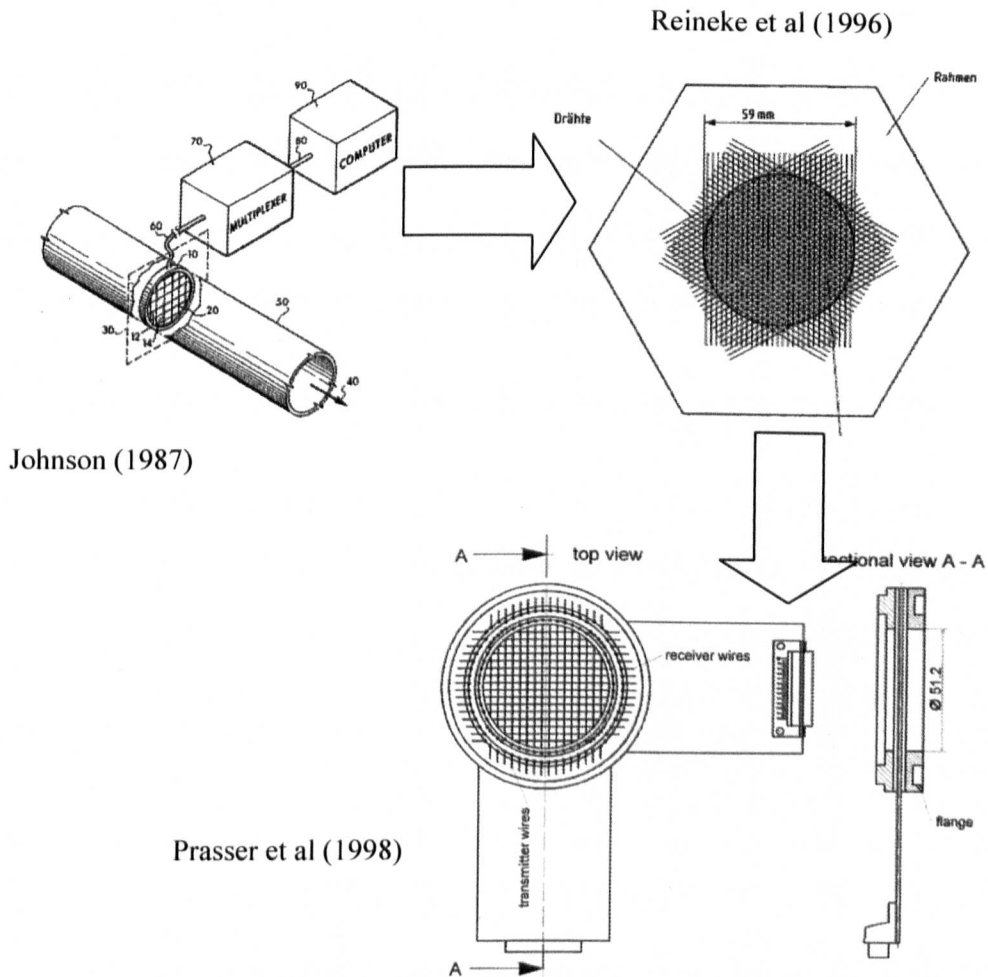


Figure 3.4- The evolution of the wire mesh sensor.

This design of the sensor first started with a patent filed by Johnson in 1987. This consisted of a crude device that had two electrode grids, but contained no imaging capability. This was followed by Reinecke et al (1996, 1998), who proposed a three plane sensor; however, this had several limitations as it required a reconstruction algorithm (Prasser et al, 1998). A two plane conductivity (conductance) wire mesh sensor with a superior temporal and spatial resolution was developed by Prasser et al (1998). The design of this sensor formed the basis for the permittivity (capacitance) wire mesh sensor recently developed by Da Silva et al (2007).

In order to operate the conductive WMS, it requires at least one continuous conductive phase, therefore it has been exclusively used for air-water, or steam-water investigations (Da Silva, 2007). However, many liquid substances are non-conducting, for example organic liquids and crude oil in the oil and gas industry, this meant the conductive WMS could not be used in such applications. Therefore, a new WMS was developed based on the measurement of the electrical permittivity (capacitance), to extend the sensor's capabilities to the detection of non-conducting fluids. A number of papers have been published since 1998 using both variants of the wire mesh sensor. For example, for the conductivity WMS, studies were completed by Prasser et al (1998-2008), Richter et al (2002), Krepper et al (2005), Manera et al (2006) and Azzopardi (2008a). For the capacitance WMS, Da Silva et al (2006, 2007a-c, 2008, 2010), Thiele et al (2008), Azzopardi et al (2010) and Szalinski et al (2010) presented various research studies. High pressure (7MPa) and high temperature (290°C) Wire Mesh Sensors have also been used, for example in Pietruske et al (2007) and Ombere-Iyari et al (2008). The CapWMS has been used in air-silicone oil investigations, and the reader is referred to Abdulkareem et al (2009, 2010) and Abdulkadir et al (2010, 2011) for more information.

3.4.2. Conductivity WMS and Capacitance WMS

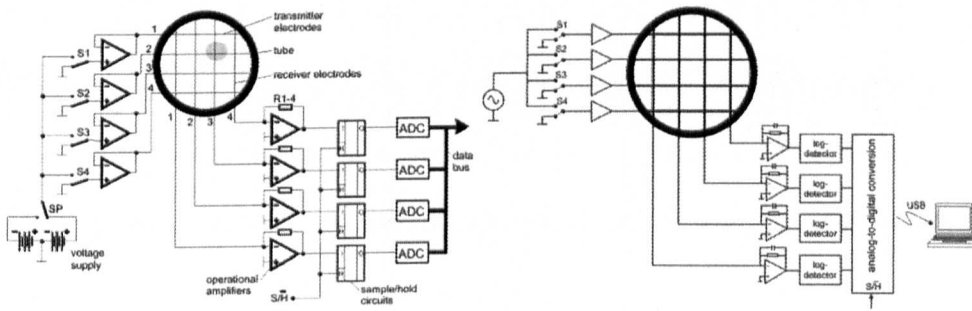


Figure 3.5-Electrical Schematic of (left) conductivity WMS and (right) capacitance WMS

The WMS consists of two parts: The acquisition sensor that sits inside the pipe which is connected with electrical leads to an electronics box that collects and stores the raw data. Figure 3.5 shows an electrical schematic of the CapWMS and CondWMS. The CapWMS has gone through a number of modifications in order to adapt to a higher capacitance range, including a faster ADC and digital processing electronics (Thiele et al, 2008). In Figure 3.5, the electronics for a 4x4 section of the sensor are shown (Da Silva et al, 2007a-c, 2008). The design of the acquisition sensor for both the conductive and capacitive WMS is the same, consisting of two arrays of wires, stretched along chords of the pipe cross-section, with one array positioned orthogonally to the other. There is a small gap between the two planes of wires.

The principle of both the conductive and capacitive sensors is the same i.e. two planes of wires, where one transmits and one receives. During the measuring cycle, the transmitter wires are activated in a successive order while all other wires are kept at the ground potential. For each time frame, a transmitter wire is activated and the receiver wires are sampled in parallel (Da Silva et al, 2007a-c). Each crossing point of the transmitter and receiver electrodes is scanned individually, generating a matrix in the x-y plane depending on the size of the sensor. The conductance wire mesh sensor has a DC input and DC output. The capacitance wire mesh sensor has an AC input and

an AC output, which is subsequently converted to DC in order to digitise the signal (ADC). This is similar to the principle of operation of Electrical Capacitance Tomography (Da Silva et al, 2007a-c); however, the WMS does not need any reconstruction algorithm to process the data. This describes the two plane sensor that is shown in Figure 3.4. However, in order to cross-correlate signals to determine for example the bubble velocities, it is possible to use a three-plane WMS as investigated by Krepper et al (2007), or alternatively to use two WMS placed at some specified distance from each other (Figure 3.6).

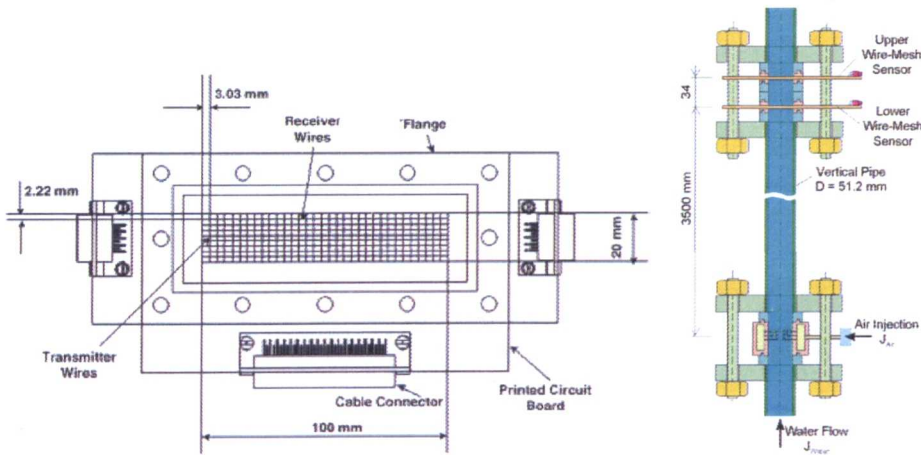


Figure 3.6-Velocity measuring WMS: (Left) 3-plane WMS, (right) two 2-plane WMS.

The CondWMS box is almost half the size of the CapWMS box (Figure 3.7). It can be seen that the boxes are fairly portable, and can be easily connected to a pipe or bubble column to conduct experimental investigations.



Figure 3.7-Electronic boxes: (Left) Conductance WMS; (Right) Capacitance WMS.

The wires for the acquisition sensor that sits inside the pipe are made from uncoated stainless steel, and they are 0.12 mm in diameter. The pressure drop across the sensor is small (approximately 3%), because the wires are distributed across the pipe coarsely and therefore will not obstruct or stop the flow. The sensor as mentioned previously is intrusive, although this is minimal as the wires of the sensor occupy only 2-3% of the cross-section of the pipe.

3.4.3. What is the WMS measuring?

This is a question that is often asked; whether the sensor is measuring undisturbed flow or the disturbance caused by the WMS itself. Prasser et al (2001) have investigated this by comparing WMS data with that from a high speed camera, and despite the fragmentation and the deceleration of the bubbles caused by the WMS, the structures generated by the WMS are represented in the measuring signal in their previous shape. For example, in Figure 3.8, bubbles are displayed as they were before they came into contact with the sensor. This issue is of little importance when a single WMS is used, but it will become a factor if two WMS sensors are used together on one pipe. The second sensor to some extent will be measuring flow that has been disturbed by the first sensor.

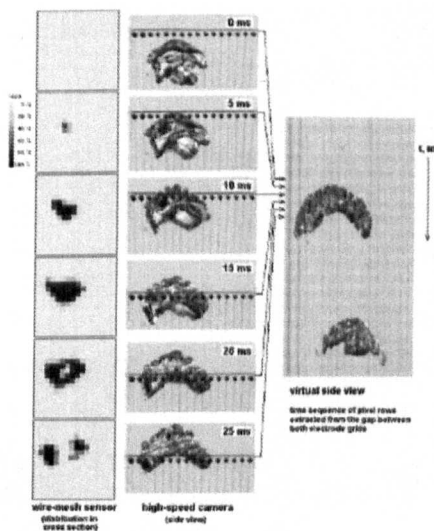


Figure 3.8-HS video compared to WMS data. The WMS signal represents the undisturbed image of the bubble.

3.4.4. Operation of the WMS

Details will now be given on how to set-up, calibrate and operate both versions of the WMS. Further information is given in the WMS documentation provided by HZDR. Once the electronics have been set-up, it is possible to acquire a large amount of data in a short space of time. The electronics box for the CapWMS is a 19" rack with active cooling. It can be used to connect up to four excitation modules (labelled 'E1'...'E4') using up to four SCSI-II cables (50 pins, 2m), and up to four receiver modules (labelled 'R1'...'R4') using up to four SCSI-III cables (68 pins, 2m). The use of these type of cables is advantageous, as it avoids the need for using significant amounts of cables that can be required for other types of sensors e.g. ECT. Each module contains sixteen single channels for excitation or sixteen channels for reception. The send and transmit modules for the CapWMS are different to those for the CondWMS and therefore are not interchangeable. However, the sensor that sits inside the pipe can be used by both the conductivity and capacitance electronics boxes.

In this project, a 16x16 two-plane wire mesh sensor was used on 50mm pipe(s), a 24x24 two-plane sensor was used on 67mm pipe(s), and a 32x32 two-plane sensor was used on 127mm pipe(s).

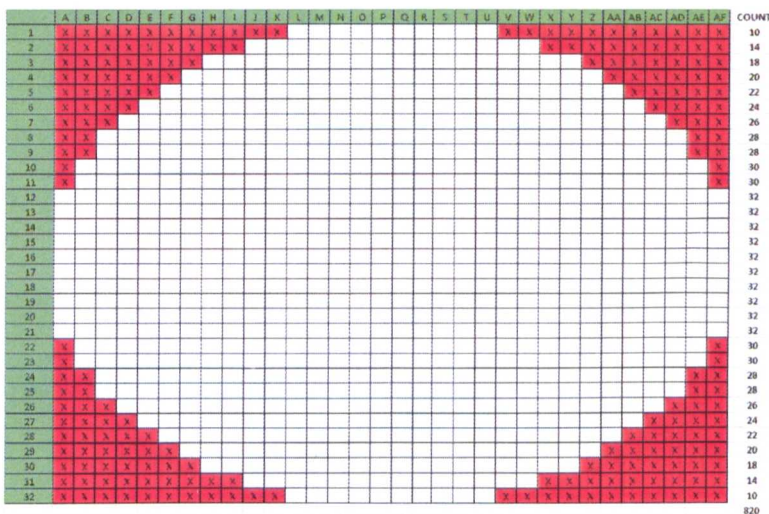


Figure 3.9-Typical matrix for the sensor, shown is the 32x32 Matrix. Red cells are excluded.

For a 32x32 sensor, the matrix of data points at the crossing points can be seen in Figure 3.9 (there exists a similar matrix for 16x16 and 24x24 sensors). The red cells are outside of the pipe and therefore are discounted. In this example, for a 32x32 sensor in a 127mm pipe, there will be a spatial resolution of approximately 4mm or 820 pixels across the full diameter. Therefore the resolution of the sensor is determined by the wire spacing, and clearly it is possible to have a higher resolution with more wires. However, this comes with the penalty of increasing the disturbance to the flow. The minimum current wire spacing is 0.5mmx0.5mm (Beyer et al, 2010).

Potentially, the box could be used for a 64x64 wire mesh sensor covering even larger pipe diameters of 200-250mm. In addition, the box could allow the installation of two 16x16 or 32x32 sensors, and therefore allow cross-correlation of signals. However, for the work conducted in this project, only one sensor was used at any one particular time. It is important to connect the correct modules on the sensor to the correct connectors on the box. Otherwise, the error shown in Figure 3.10 will occur.

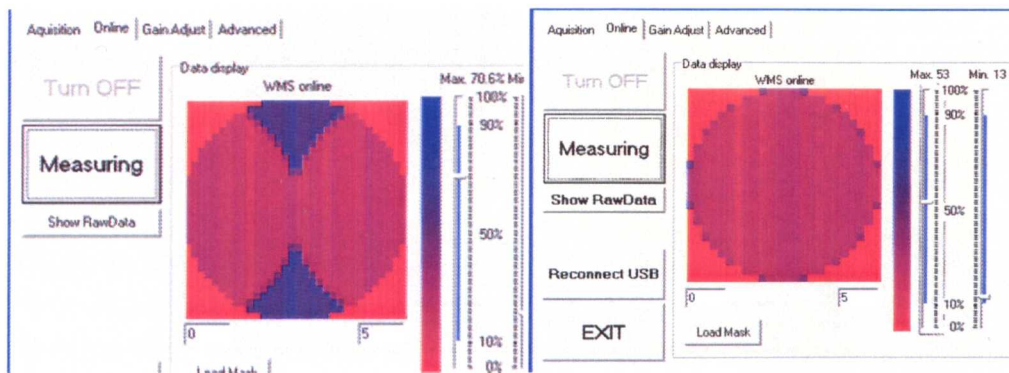


Figure 3.10-Incorrect connection of modules (left) vs. correct connection (right)

The CondWMS connects to a PC via an Ethernet cable with a dedicated IP address. The ECT box has a similar set-up. The CapWMS was configured initially with a USB connection, although as a result of the extensive testing conducted in this project, this was found not to be stable. The connection regularly disconnects along with

generation of error messages, which required resetting of the electronics. The CapWMS connection was therefore changed to an Ethernet connection, which should prove to be a more stable solution. Finally, it is worth noting that it is important to allow the equipment to warm up for 10-15 minutes before commencing the experiments.

Software Interface

The graphical user interface that controls the conductivity WMS can be seen in Figure 3.11. This is similar to the interface used to control the capacitance WMS, which has undergone slight modifications over the past 2 years. The first version can be seen in Figure 3.12, and the latest version can be seen in Figure 3.13.

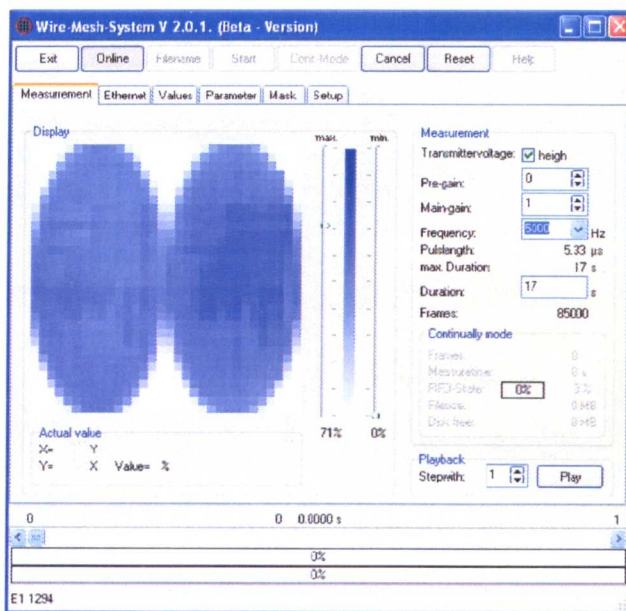


Figure 3.11-Conductivity WMS Software screenshot

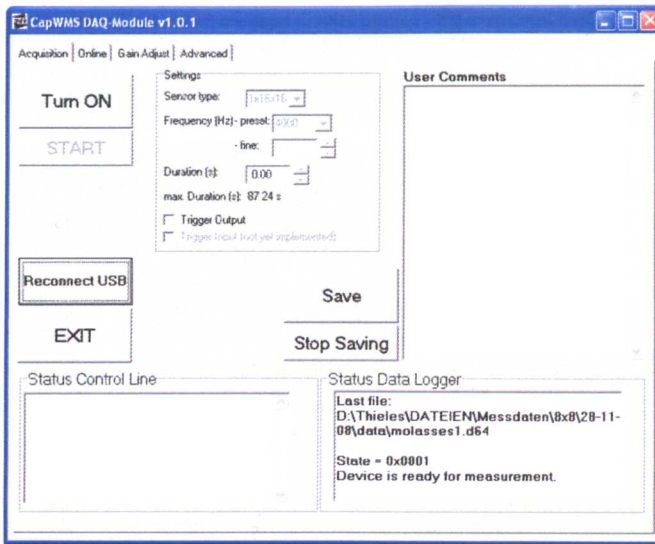


Figure 3.12-First version of CapWMS (Nov 2008-Dec 2010)

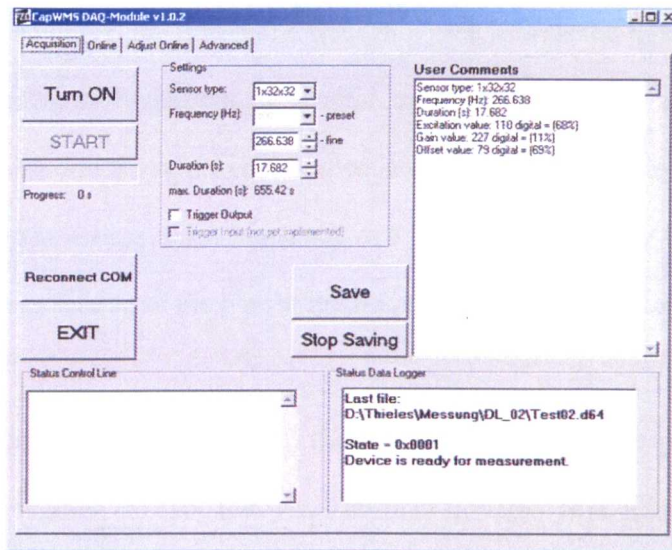


Figure 3.13-Second version of CapWMS (Jan 2011-Present)

When the CapWMS is successfully connected to the PC, it displays the message “device is ready for measurement”. The CondWMS will show a green bar at the bottom of its software interface. An important improvement to the second version of the CapWMS is the addition of a progress bar to show the progress of data acquisition when the sensor is triggered. This feature was absent from the previous version. One advantage the conductivity WMS interface still has over the capacitance WMS is that

acquiring and saving data is a one step operation. However, with the CapWMS, this takes place in two steps, which is time consuming and sometimes means a test run must be repeated, particularly if the connection fails, or 'drops'.

Calibration

For the CondWMS this is fairly straightforward, with one static calibration required with the pipe or bubble column full of liquid that must cover the full cross-section of the sensor. The transmit-voltage high, Pre-gain (pre-amplified) and main gain (main amplifier) settings can then be adjusted to give a maximum indicator below 90%. The frequency can also be adjusted. Both types of the WMS are capable of frequencies up to 10,000 Hz. However, the higher the frequency; the shorter the time the sensor will operate due to memory limitations. In general, the time was selected to be between 30-60 seconds, which was thought to be an adequate period time for data acquisition. The CapWMS operates with an input frequency of 5 MHz, which enables it to successfully scan the full cross-section of the pipe at the frequencies set by the researcher.

For the CapWMS, the calibration is a trickier process. Ideally the pipe needs to be inclined at 45 degrees, so that the wires are half covered with liquid. However, in reality this is not possible, and therefore the process requires several time consuming exercises of filling up the pipe then emptying it. This is necessary to calibrate the sensor between the two levels of permittivities it is measuring. For example, for air-water, the permittivity is 1:80, and for air-silicone oil it is 1:2.7. For calibration, the gain and offset bars must be adjusted such that when the pipe is empty, the minimum is around 10% and when it is full of liquid, the maximum is around 90%. These limits are chosen to prevent saturation in the electronics from taking place. Saturation is a difficult condition to observe directly in the output screen; however, atypical

structures or unusual oscillations can be giveaway signs. The mask also needs to be loaded to discount the crossing points outside of the pipe cross-section. It is worth noting that as the pipe is emptied and refilled during the calibration process, some small droplets remain on the wires due to surface tension. These are difficult to remove in a closed system, although pressurised air could be used in an open system to remove them, for example in a bubble column.

Once the pipe is calibrated, the same settings can be reused, although it is recommended that the researcher carries out two calibrations for every set of measurements, at the start and at the end of the process. This is because the temperature and conductivity may vary over time. The calibration menu for the CapWMS has changed slightly, and the two versions can be seen in Figure 3.14 and Figure 3.15. The latest version has been improved to include the excitation amplitude setting, which was not previously obvious and located under the “advanced” menu. The amplitude needs to be adjusted when using high conductivity liquids such as tap water. Once the calibration is complete, it is possible to either acquire data that can then be saved, or to observe the data in the “online” mode.

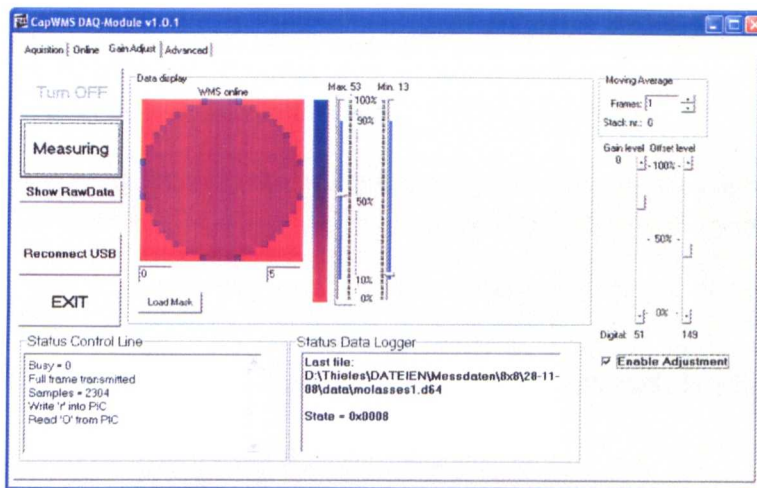


Figure 3.14-Old Calibration menu for CapWMS (Nov 2008-Dec 2010)

This is useful for demonstrations; however in online mode, the images observed are quite small, raw and unprocessed.

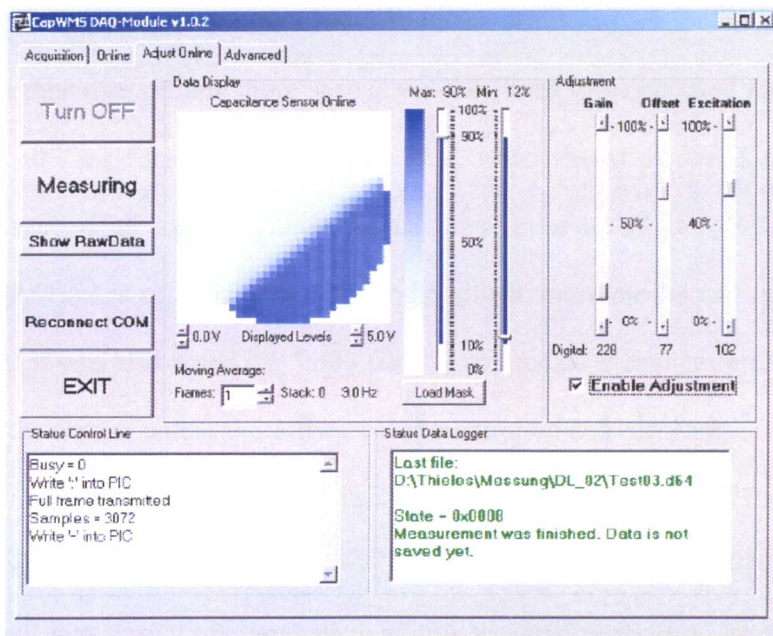


Figure 3.15-New calibration menu for CapWMS (Jan 2011-Present)

Trigger

The CondWMS can trigger other instruments, and it can be triggered externally, which makes it a flexible device. The CapWMS cannot currently be triggered by other instruments, although it can be used to trigger other instruments, such as ECT. It is a powerful methodology to have WMS and ECT sensor(s) in one pipe and triggered at the same time to collect data simultaneously. This was carried out by Azzopardi et al (2010). The triggering function can be controlled via the software interface.

Raw Data Files

The conductivity WMS generates two files for every run collected. The first file is the *.inf file, which contains the settings used by the sensor. The raw binary file has a *.mes extension. The capacitance WMS generates five files for every run collected. The first file is denoted *.d64, which contains the settings used by the sensor. The

other four files are binary files of the form *_A.bin, *_B.bin, *_C.bin and *_D.bin. Clearly the capacitance file handling needs further refinement, as technically it should be possible to generate one binary raw file in the same way as for the conductivity WMS. The four files occupy more space, and they need to be checked for every run. Generally, all four files are of the same size, which helps to see if the run was completed successfully or not. This is because sometimes not all four files are present, or one of the files is of a different size to the others, meaning the test run has to be taken again. It was also noted the *.d64 file did not update if changes are made to the settings of the sensor, unless the software is disconnected and restarted.

Data Viewer

An important step during the data acquisition is to perform regular checks while the data is being collected. One of the checks is to open the raw files in the data viewer. Sometimes the raw file cannot be opened as it is corrupted, and therefore the run must be taken again.

Data Conversion

For the conductivity WMS, the data conversion can be carried out in batch mode in DOS using the proprietary executable software supplied by HZDR. This will result in the generation of several files, including the v. file. The output file structure for the WMS is explained in Appendix B. For the capacitance WMS the v. file needs to be generated first, which is done by loading the raw files into the converter shown in Figure 3.16. The calibration files are also loaded, and the permittivity values and model must be inputted. The converter will then process one file at a time. Once all the v. files are generated, these can then be processed in batch mode to generate the other files.

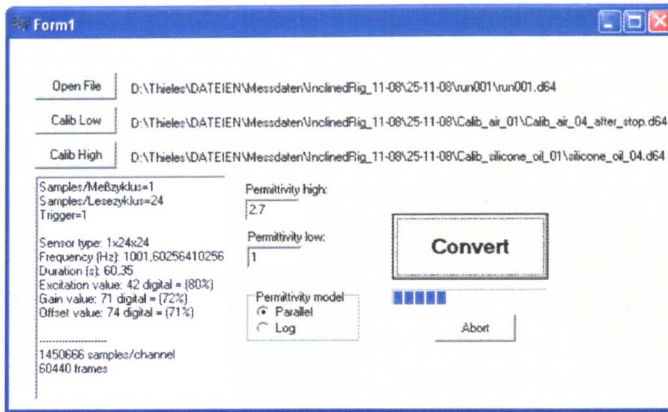


Figure 3.16-Processing raw files

3.5. Visualisation of the flow (Qualitative Data)

The disp.exe is a special viewer, which can be used to view the binary v. files as images and videos for the capacitance and conductance WMS. Horizontal and vertical sectional views can also be shown (Figure 3.17). The colour convention is generally that blue represents a liquid, and red is a gas. Each frame or image is $1/f$ Hz, for example if the frequency $f=1000\text{Hz}$, then each frame represents 0.001 seconds. In other words, for every second, there will be 1000 frames.

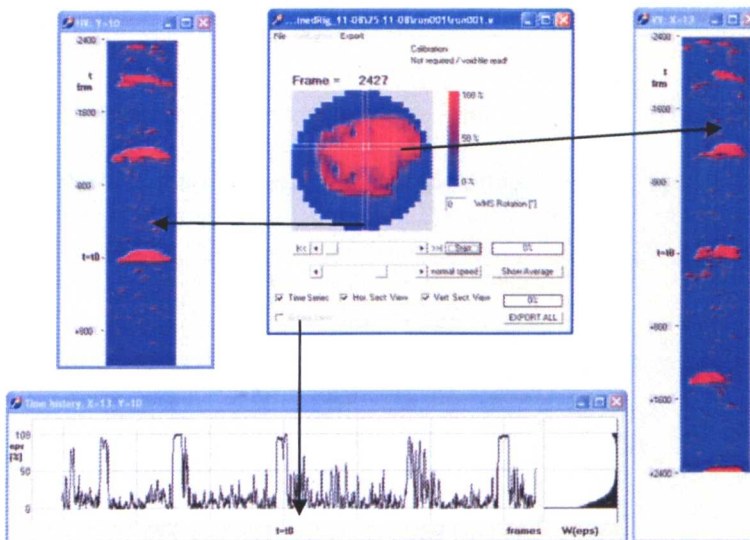


Figure 3.17-Visualisation Software to display binary v. files

It is possible to generate special images using the processing software supplied by HZDR. The visualisations can show the pipe as if the observer is looking in from the outside and it can also show flows in the middle of the pipe (Prasser et al, 2005).

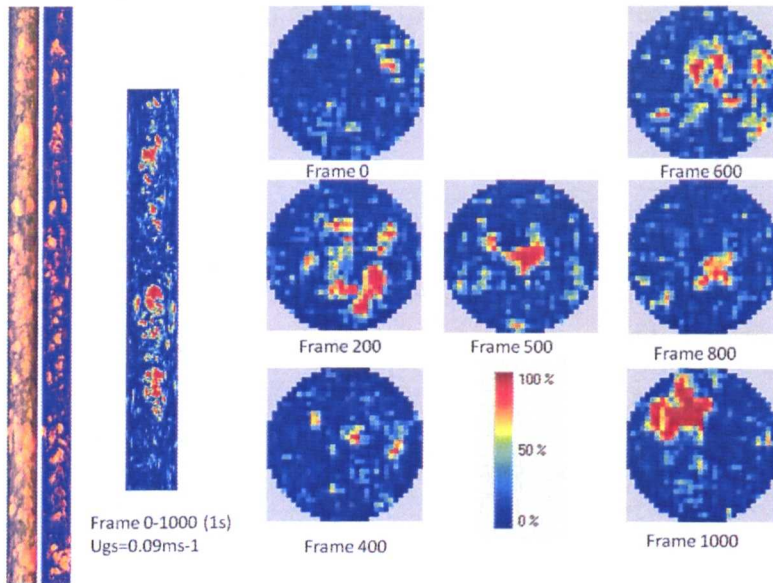


Figure 3.18-2D Images; longitudinal, and cross-sectional

It is worth noting that different sized sensors have their own individual display software, for example it is not possible to open 24x24 sensor v. files using the 16x16 disp.exe file. From the 2D cross-sections in Figure 3.18, it is possible to generate a 2D cross-sectional movie. It is also possible to generate 3D views of the data as shown in Figure 3.19 using Matlab. This is generated from the v. file. These visualisations obtainable with the WMS are one of the main advantages of this type of sensor.

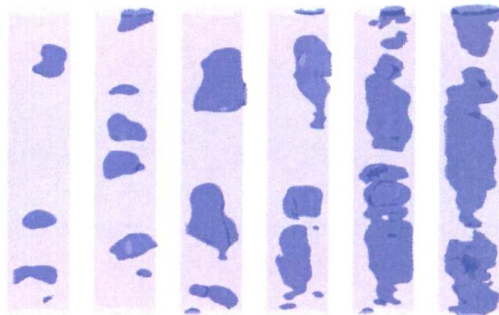


Figure 3.19-3D images showing detailed structures

3.6. Quantitative Data

The wire mesh sensor gives direct measurements of local and cross-sectional void fraction, and it does not require any special algorithm for this, which is an advantage over ECT techniques. The WMS can also be used to deduce many other parameters, which will be described below.

Time Series

The cross-sectional averaged void fraction can be extracted and plotted, as below in Figure 3.20.

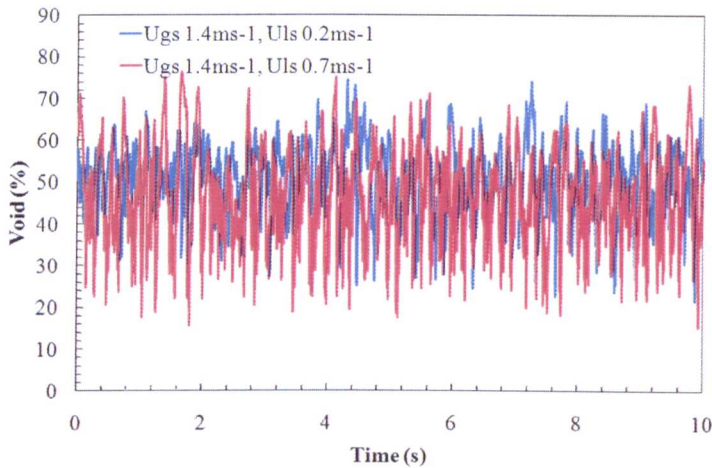


Figure 3.20-Time Series of void fraction

The PDF and other statistical data, as well as the PSD, can be derived from this data.

Local Voids

The time averaged local void matrix can be produced, an example of which is shown in Figure 3.21.

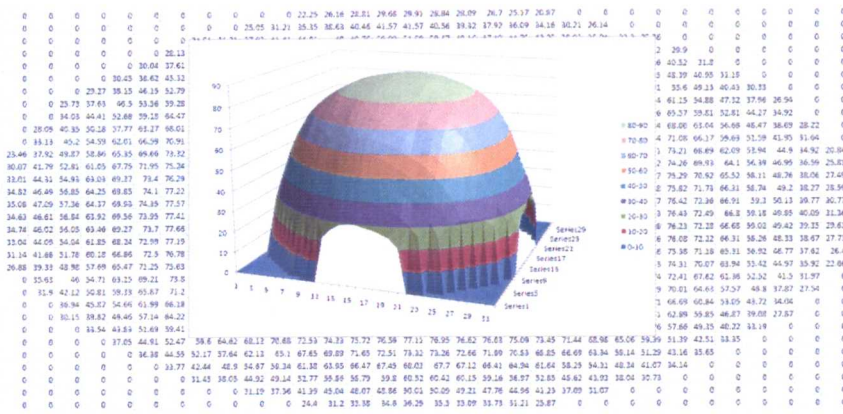


Figure 3.21-Local voids (Time averaged)

In order to check the orientation of the matrix with respect to the sensor, the procedure in Figure 3.22 must be followed.

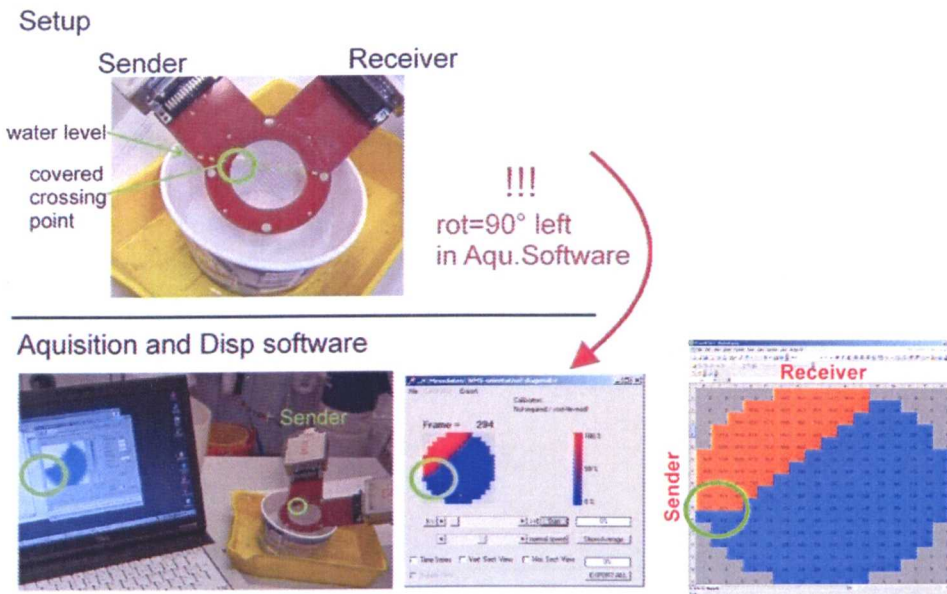


Figure 3.22-Procedure to check orientation of matrix of voids

Radial voids

Radial profiles can also be extracted from the data of the WMS (Figure 3.23). These are time and azimuth averaged gas fraction (for example inside forty ring-shaped domains for a 32x32 sensor). The x-axis displays the distance in mm of the respective

ring from the centre of the pipe. These profiles are similar to those measured by the conductivity (point) probes by Al-Oufi et al, (2010), however the point probes need to be moved manually across the diameter of the pipe which is a time consuming process. The radial profiles are however obtained relatively easily from the WMS data, as the WMS scans the full cross-section of the pipe.

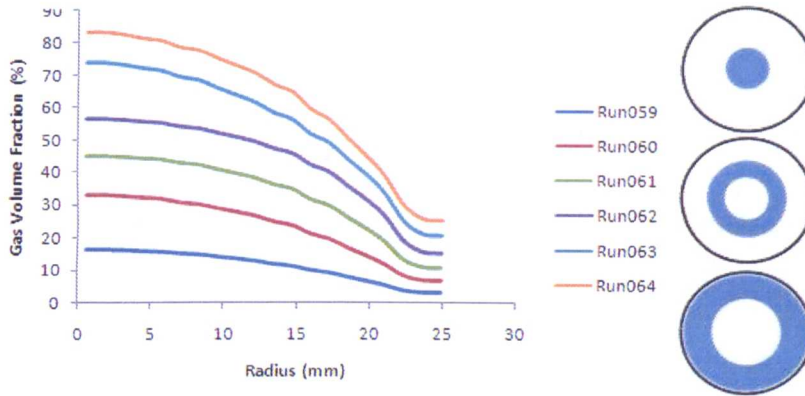


Figure 3.23-Radial void fraction with integration area examples

Space resolved void fraction

Information regarding space resolved voids can be extracted as shown in Figure 3.24 (Azzopardi et al, 2010a), which breaks down the void fraction data into the appropriate bubble sizes.

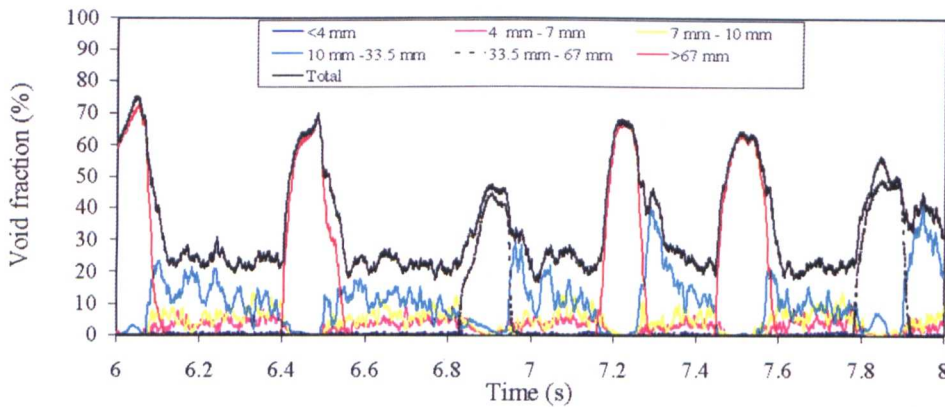


Figure 3.24-Space resolved void fraction

3.7. Bubble Size Distribution

One of the most useful parameters that can be extracted from the wire mesh sensor is the bubble size distribution (Prasser et al, 2000, 2001, 2002b). This is done by using proprietary HZDR algorithm and software, with the code constructed in Delphi. Further details are provided in Appendix B. The cross-sectional voids are broken down, as shown in Figure 3.27 below.

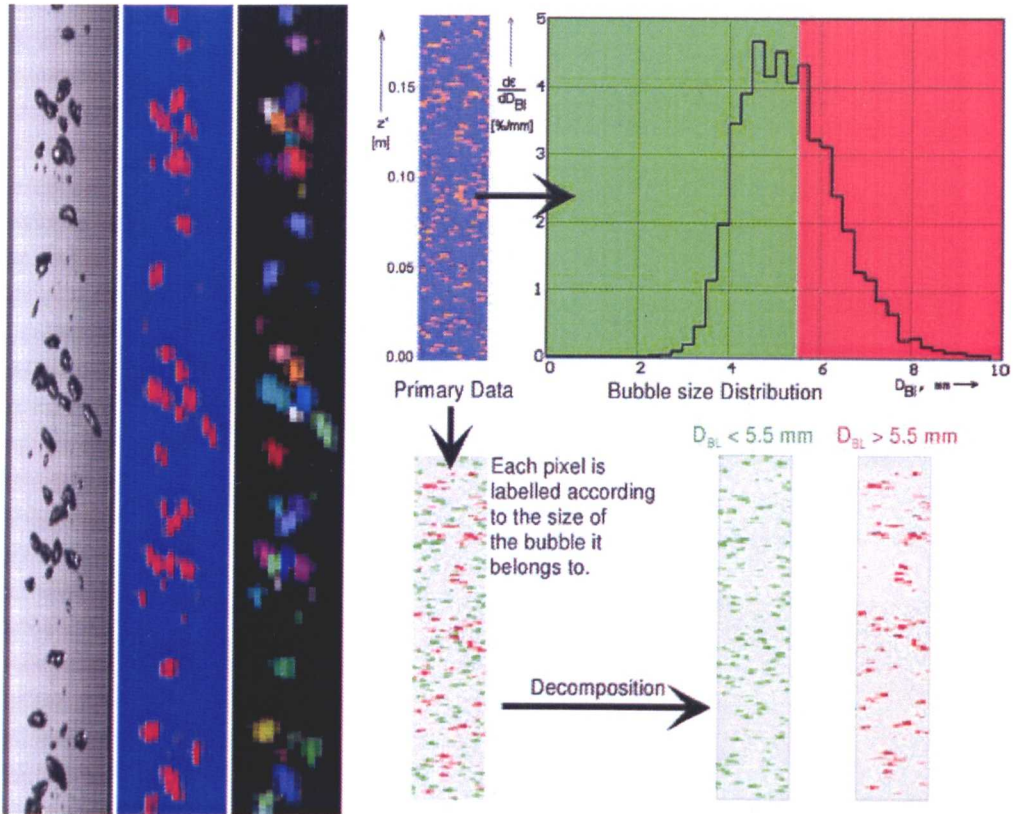


Figure 3.27-Decomposition of voids into bubble size distribution (Prasser et al, 2002b)

Comparison of the bubble diameters obtained with the WMS to those obtained with high speed video has shown there is a slight overestimation of the bubble diameters by the WMS, which will translate into the bubble size distribution (Prasser et al, 2001). One of the limitations of the wire mesh sensor is the minimum size of bubbles which the sensor can detect, which is determined by the separation distance between the transmit/receive wires. As a result, the sensor cannot detect bubbles smaller than 2mm in diameter (Prasser et al, 2002b).

3.8. Test Facilities

Details of the facilities used onsite in Germany are given in the next Chapter.

3.8.1. Bubble Columns

Two bubble columns were used, which are illustrated in Figure 3.28 and Figure 3.29.

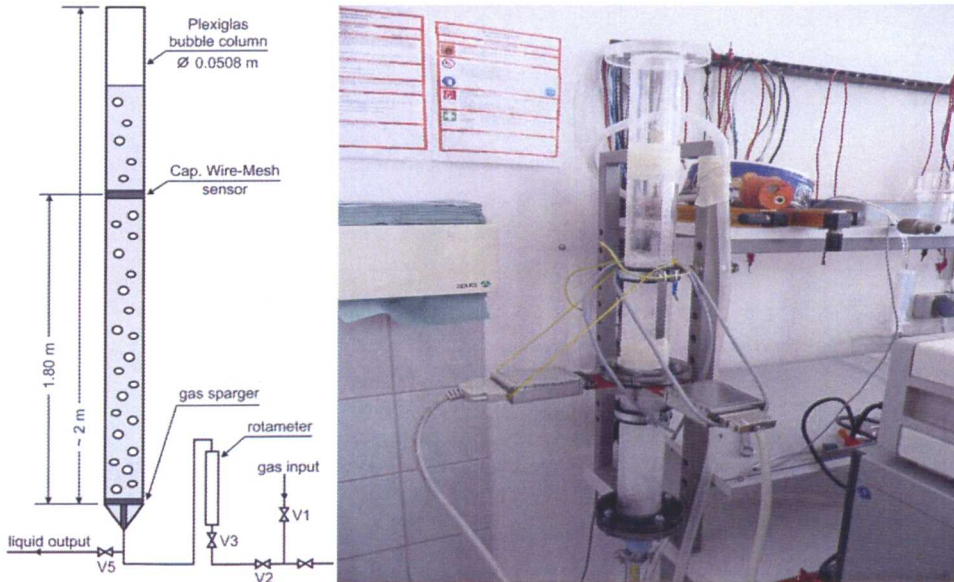


Figure 3.28-2 inch bubble column, position of 16x16 WMS is shown.

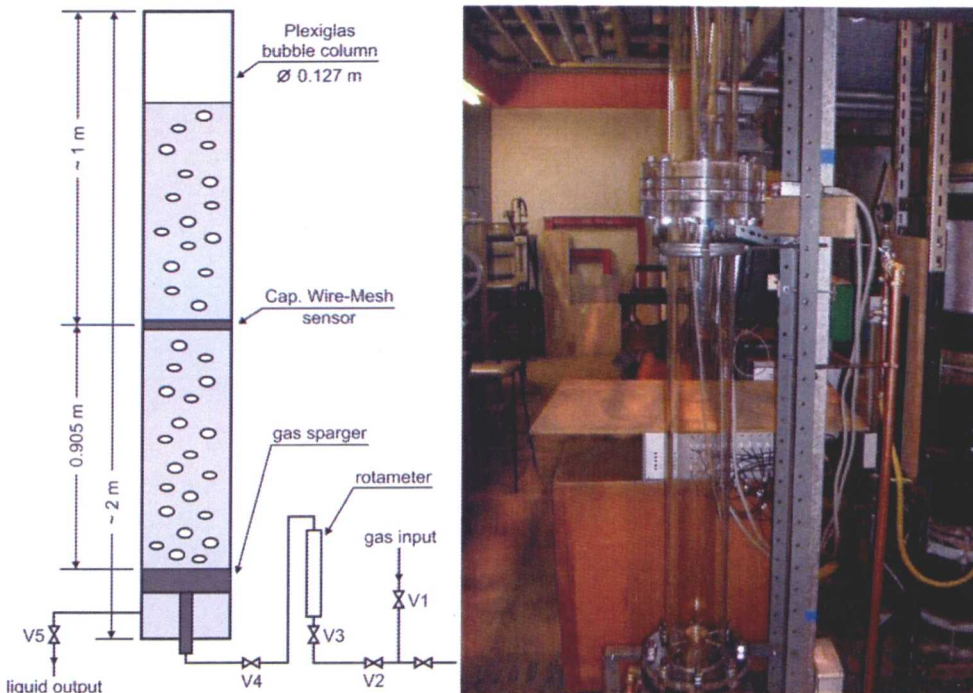


Figure 3.29-5 inch bubble column, position of 32x32 WMS is shown.

The two inch bubble column had a sintered glass injector at the bottom of the column, and the five inch bubble column had two different injectors. The first was a heterogeneous sparger with six legs, each leg having six holes of $\text{Ø}2.0\text{mm}$, spaced 5mm apart. The second was a homogeneous distributor, with a plate containing 121 $\text{Ø}0.5\text{ mm}$ holes (Figure 3.30).

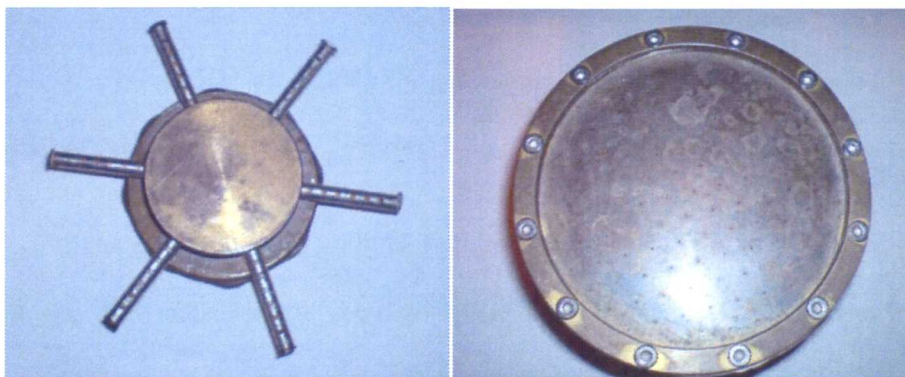


Figure 3.30-5 inch bubble column injectors

The following is the typical set-up procedure that was applied on the bubble columns. The procedure below is for the 5 inch column, and the procedure for the 2 inch is very similar, with some minor differences with the valve numbers. Particular attention is paid to the cleanliness of the bubble columns to ensure accurate measurements.

Cleaning/flushing/preparation of bubble column

1. Empty the bubble column and close all the valves. Carefully take apart Plexiglas, gas sparger and the WMS. It is recommended that protective gloves are used throughout.
2. Clean the Plexiglas and gas sparger using diluted ammonium based cleaner that does not attack the Plexiglas (inspect MSDS for safety precautions). Use a brush wetted with the cleaner for the removal of any contaminants.

3. Rinse all the parts with tap water at least three times or more. Rinse down all the parts with distilled or de-ionised water at least once. Reassemble the bubble column.

Start up procedure for the bubble column

1. Examine the apparatus. Make sure all valves are closed (especially valve V5).
2. Open valves V1, V2 and V4 for gas supply. Open valve V3 to give a low flow rate of air of 20 L/min.
3. Fill the bubble column with the required liquid, ensuring the WMS is covered. Set the gas flow rate for the required value (use V3) and wait for flow regime stabilisation. Connect the data acquisition equipment and PC, then record the data. As this is an open system, care is required so that the liquid does not overflow.

Closing procedure for bubble column when distilled or de-ionised water is used

1. Decrease the gas flow rate to the value of 20 L/min (use V3). Open the valve V5 for drainage of liquid.
2. Increase the gas flow rate to 100 L/min to dry the distributor and the walls. After drying, close the valves V3, V1 and V5.

Closing procedure for bubble column when other liquid is used

1. Decrease the gas flow rate to the value of 20 L/min (use V3). Open the valve V5 for drainage of liquid. Close the valve V5. Fill the bubble column with tap water with the volume 1L higher as the working liquid. Let the liquid flow on the walls.
2. Repeat flushing at least two times. Open the valve V5 for drainage of liquid.

3. Close the valve V5. Fill the bubble column with distilled or de-ionised water with the same volume as the tap water. Open the valve V5 for drainage of liquid.
4. Increase the gas flow rate to 100 L/min to dry the distributor and the walls. After drying, close the valves V3, V1 and V5.

3.8.2. 5 inch/127mm closed loop facility

This facility was first used by Ombere-Iyari (2006). The rig has since been modified, and a more up-to-date rig schematic is shown in Figure 3.31 (Van der Meulen, 2010).

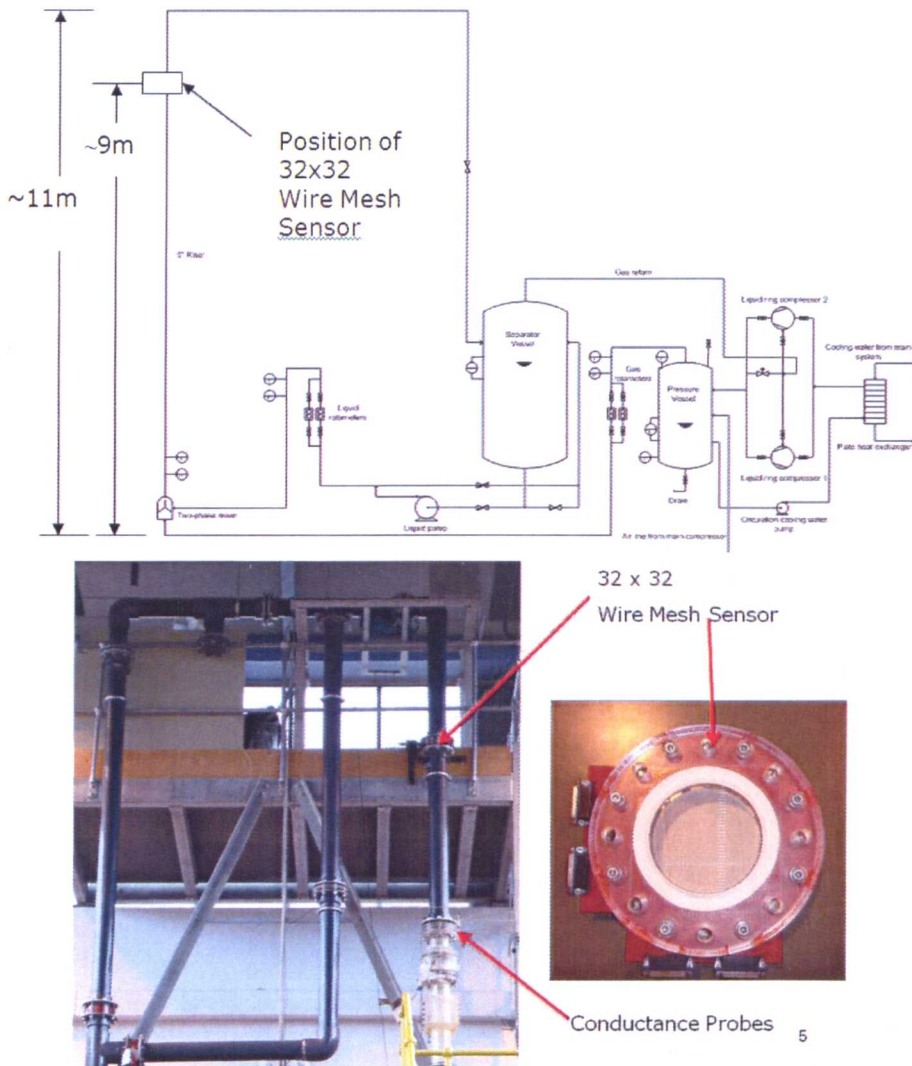


Figure 3.31- 5 inch pipe flow facility and design of the WMS used.

This is a closed loop facility, with a pipe length that is nominally 11 metres, and the pipe is kept in a vertical orientation, although it is possible to incline it. The injector used at the bottom of the riser is an annulus type injector, which allows the generation of a gas core with a liquid film to aid the establishment of churn and annular flow regimes. The internal diameter of the annulus is 3" or 76mm. Although a heat exchanger was not used, it was assumed the conditions were adiabatic, operating at room temperature of 25°C. There is a transparent section in the middle of the pipe that can be used for visual checks and high speed camera measurements. The pipe material is plastic and it has an internal diameter of 127 mm and an external diameter of approximately 140 mm.

Initially the rig is flushed a few times to remove any impurities that may be present. It is worth noting that some of the internal parts of the pump and compressor are not made from stainless-steel and therefore rust can build up over time, meaning that flushing the rig is an essential operation. In addition, a filter is necessary to ensure that large particulates will not damage the WMS, and fine meshing was used for this purpose. The two compressors have part numbers TRSC-100-700/X-C/F (T = Pompetravaini construction, R = liquid ring vacuum pump, S = single stage pump, C = design number, 100 = flange size, 700 = nominal capacity m³/h, X = reinforced shaft, C = mechanical seal, F = material of construction), and are driven by two 55KW inverters. The water centrifugal pump is made by Flowserve, part number ERPN 65-200. The liquid pump has a maximum capacity of 68m³/hr. The range for the gas superficial velocity U_{gs} was 0-17 ms⁻¹ (at 1ms⁻¹ increments), and the range for the liquid superficial velocity U_{ls} was 0-0.7ms⁻¹ (at 0.01 ms⁻¹ increments; note that the pump is capable of 2.4 ms⁻¹, but this is limited by the range of the flow meters).

Flowrate and conductance probe measurements are taken using a PC equipped with a National Instrument (NI) DAQ card.

After the rig is flushed, it is emptied using the centrifugal pump. The pump is powerful, and is capable of emptying the entire tank in a few minutes at a low setting. Subsequently, the separator that has a capacity of 1600 litres and the pressure vessel that has a pressure rating of 10 bar, are half-filled with tap water and then the rig is pressurised to 2 bar (gauge pressure). The compressors are then started up to a maximum RPM of 1500 RPM, which is then followed by the centrifugal pump. Volumetric flow rates (and hence superficial velocities) are controlled using the electronic controls and also using the graduated valves located close to the flow meters. The inflow of air and water are measured using calibrated vortex and turbine meters respectively. Ombere-Iyari (2006) calculated the maximum uncertainties in the liquid and gas flow rate measurements as 0.5% and 2.79% respectively.

The total time averaged pressure drop is measured by an electronic differential pressure detector/transmitter (Rosemount 1151 smart model), with a range of 0- 37.4 kPa and an output voltage from 1 to 5 V, (i.e. with a resolution of 9.35 kPa per volt). Two pressure tapings, separated by an axial distance of 12.9 pipe diameters, are connected to the differential pressure device across the transparent section via stainless steel tubes. The conductance probes (CP) are located at 62.7, 63.5 and 65.5 pipe diameters from the riser base, respectively. The WMS and CP are triggered at the same time, and 30 seconds of data are collected per run, at a frequency of 1000Hz. Both instruments are capable of operating at higher frequencies. In total 700 runs were completed in this experiment, with fully calibrated instruments.

In order to place the WMS onto the riser (and indeed to any pipe or bubble column) the pipe needed to be flanged, and rubber seals or O-rings were used with the WMS sensor to stop liquid leaking (Figure 3.32). Flanges were drawn using 3D CAD.

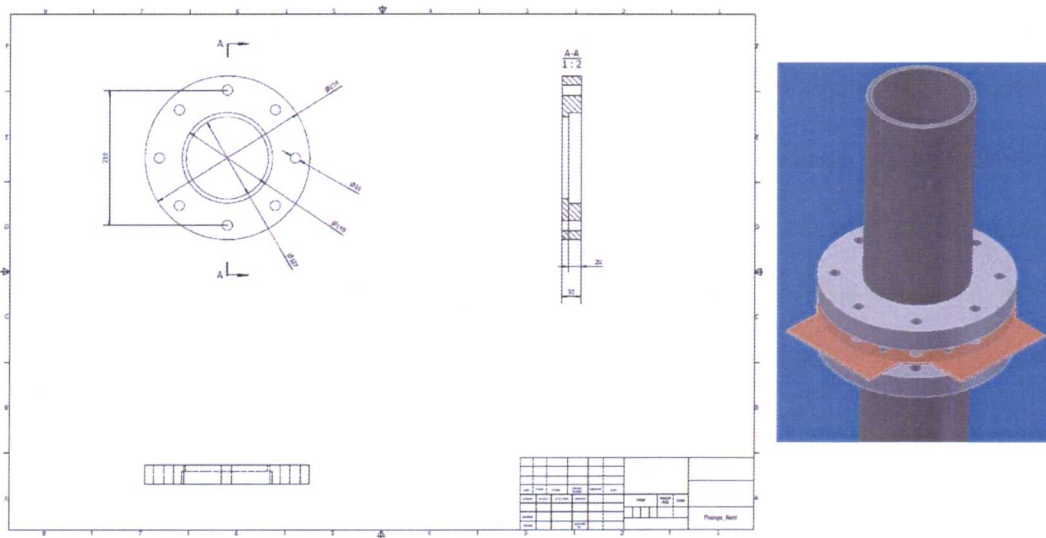


Figure 3.32-Design of 127mm Flanges, using 3D CAD (Inventor)

The flanges of the pipe need to match the flanges on the WMS. A typical design specification for a WMS can be found in Appendix B. One of the improvements to the design is the way the modules are attached to the acquisition sensor. In the current version of sensor, the modules require the use of supports, which must be manufactured separately. The newest design of the sensor has the modules orientated at 90 degrees and bracketed onto the PCB (Figure 3.33), and this is a better design.

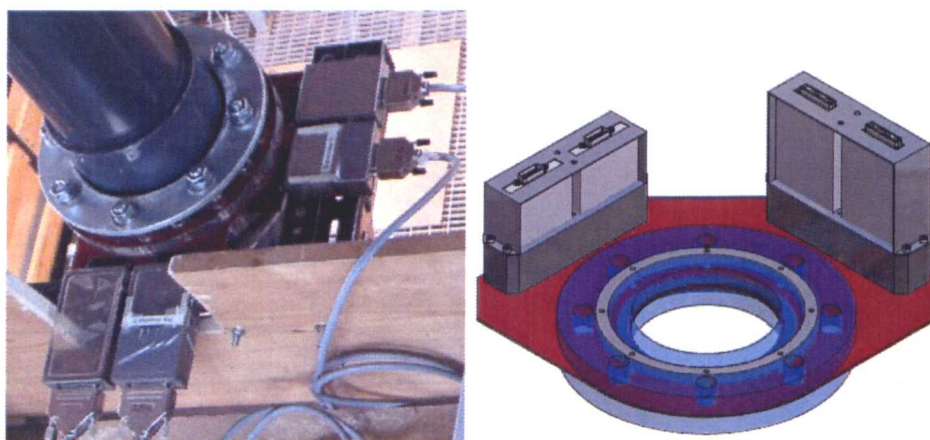


Figure 3.33-(Left) Old design of WMS and (right) new design of WMS

The wire mesh sensor was placed at a height of approximately 9.3 metres from the injector for several reasons. First, as it is an intrusive sensor, it is best to place it after any non-intrusive instruments such as the conductance probes, which were placed lower down along the riser. The second reason was to put the WMS at a safe distance from the 90 degree bend at the top. This was to stop the backflow that can sometimes occur, which would affect the measurements. The third reason was to establish fully developed flow. However, it is possible to flange the pipe at various axial positions to install the sensor, a method that would enable the tracking of the flow and allow the researcher to see how it develops along the vertical pipe.

The development lengths for establishing steady-state conditions of fully-developed two-phase flow can be significantly in excess of 100 pipe diameters (Azzopardi, 2006). Therefore, for a 127mm diameter pipe, 12.7 metres of pipe length is recommended. It is assumed in this work that steady state conditions have been attained and instabilities and transients will be ignored. Some experiments on vertical pipes indicate that as much as 200 pipe diameters or more are needed to establish fully developed flow, and such a length is rarely possible in experimental rigs due to the cost. Offshore well tubes and risers can run for several kilometres in length, and there have been proposals to build an experimental rig with a large diameter vertical pipe running for several kilometres by placing the extended pipe in a deep mine; however, the cost was found to be prohibitive. A summary of the properties of the liquids used in this research are shown in Table 3.2. These are valid for both the bubble column experiments and the two phase flow in the large diameter pipe. Therefore water was the main conductive fluid that was used, and silicone oil was the main non-conductive fluid that was used in this research study. Silicone oil is used extensively in various industries although it is not cheap. It has a much lower surface tension than water.

Parameter	Tap Water	Silicone Oil	Unit
Electrical conductivity	400-500	0	$\mu\text{S/cm}$
Relative permittivity	80	2.7	-
Density	1000	900	kg/m^3
Viscosity	1	5.25	$\text{mPa}\cdot\text{s}$
Surface tension	0.072	0.02	N/m

Table 3.2-Properties of Liquids

To conclude, the WMS has established itself as a valuable research tool that is clearly capable of producing very powerful results, empowering researchers to look deeply into the flow. It can give significant amount of data, both temporally and spatially. The resolution of the sensor is superior to many other types of sensors in this field (for example ECT); however, this comes with the associated disadvantage that the sensor is intrusive. Another advantage of the WMS is its ability to look at all types of flow regimes, whereas some of other instruments, such as conductance probes, require special calibration techniques to inspect different flow regimes. A typical sensor that has been used in this study, such as the 32x32 sensor, has 820 crossing-points acting as local probes, which sit inside the pipe. This would be difficult to reproduce with some types of intrusive sensors, for example optical probes. A 32x32 WMS has been installed on large diameter facilities, substantial amount of novel data was acquired, and results will be presented in subsequent chapters.

4. CHAPTER 4: TESTING OF WMS

4.1. Introduction

Several instruments have been developed to investigate multiphase systems. A good summary of the various techniques can be found in Hewitt (1978) and Crowe (2006). A comprehensive guide on Gamma Densitometry (GD) can be found in Johansen et al (2004), and a review of tomography was published by York (2001). The instruments can be differentiated by cost, intrusiveness and resolution, both temporal and spatial (Da Silva, 2008). The wire mesh sensor can be classed as intrusive, whereas the gamma densitometer is considered non-intrusive. Every instrument has advantages and disadvantages. While technology is constantly improving, there is no multiphase measuring instrument at present that is cheap, non-intrusive and gives the best resolution in one instrument; and compromise will always be necessary. It is also possible to combine instruments to work together and obtain more information about the flow.

High energy radiations, such as beta, gamma and x-rays, have been used extensively to investigate two-phase flows (Schrock, 1969). A number of papers have been published in this area, for example Jiang et al (1993), Kumar et al (1995), Shollenberger et al (1997), Stahl et al (2004), Manera et al (2007) and Kumara et al (2010). GD is used in industry, for example in two phase flow metering; however, it is not as widely used in research as Gamma Ray tomography or multi-beam GD, due to the ability of the latter to scan the full cross section of a pipe, as opposed to a single beam or chord. GD measures the void fraction averaged over a chord and this can place limitations on its applications. Gamma densitometry offers a more cost-effective

solution than x-ray, as it produces mono-energetic rays without the intensity fluctuations that might be present in x-rays (Stahl et al, 2004).

The quantitative measurement of cross-sectional gas void fraction or liquid holdup with wire mesh sensors is based on the averaging of the spatio-temporal gas distribution in the sensor cross-section. The accuracy of this procedure is influenced by at least two factors; a correct relation of the measured electrical values with the local void fraction (sub-pixel resolution) and an accurate processing of data at the sensor periphery. Assessing the quantitative accuracy of wire mesh sensor measurements is difficult, since there are no directly comparable instruments to test against them. However, as part of the ongoing campaign to test the WMS and check its accuracy, the WMS has been compared with various instruments, for example with Gamma Densitometry (Prasser, 2000), x-ray tomography (Prasser et al, 2005a) and Gamma-Ray tomography (Bieberle et al, 2010). It has also been compared with ECT (Azzopardi et al, 2010a) and with needle probes (Manera et al, 2009). Beyer et al (2010) summarised the main findings. The gamma radiography of an air-water flow for varying superficial velocities of both media resulting in a gas volume fraction between 0% and 100% showed that the deviations between results from the wire mesh sensor and gamma measurements are limited to $\pm 5\%$ (Prasser et al; 1998, 2000, 2005b). The radiography of a steam-water flow at atmospheric pressure confirmed this statement (Manera et al, 2007). Differences in the absolute void fraction were determined (Prasser et al, 2005a) to be $\pm 1\%$ for bubbly flow, and a systematic underestimation of approx. -4% for slug flow. Therefore, notwithstanding the facts that there are measurement uncertainties with both the WMS and the instrument it is being compared against, and also the accuracy of the gas volume fraction averaged over the flow cross-section depends on the two-phase flow pattern, these comparisons

have shown good agreement between the WMS and the various instruments mentioned.

4.2. Comparison between WMS and Gamma Ray

Integral measurements, such as with gamma densitometry, are useful in evaluating the wire mesh sensor's accuracy. Such techniques were utilised in the past at HZDR to test the accuracy of the WMS (Prasser et al 1998, 2005b). The work carried out by Prasser et al (1998, 2000) was on a fixed arrangement, with the densitometer lined up approximately across the centre of the pipe, which was compared with the conductivity WMS. The set up is shown in Figure 4.1.

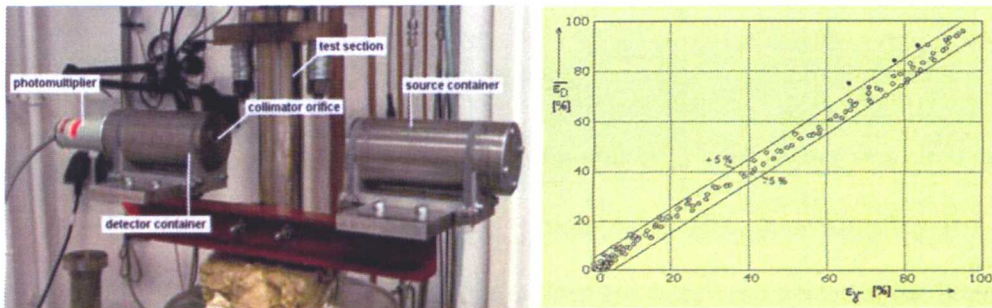


Figure 4.1-Fixed Densitometer set-up. Graph on the right shows WMS (y-axis) vs. GD (x-axis)

Gamma ray transmission measurements need integration periods longer than the temporal resolution of the WMS, which gives instantaneous local void profiles. Therefore, only time-averaged void fractions can be compared for the two instruments (Prasser et al, 2005b).

This work involved the design and manufacture of a moveable GD to enable the investigation and scanning of the whole cross-section of pipe and the comparison with WMS. Manera et al (2007) attempted a similar exercise with a steam-water mixture by utilising two densitometers with ^{51}Cr , which were placed 17 cm above and below a

conductance WMS, and scanned one half of the pipe. This work was carried out on air-water and allowed the comparison between the capacitance WMS and GD, conductance WMS and GD, and finally between the capacitance WMS and conductance WMS. While the two variants of wire mesh sensors are similar in design and they can both use the same sensor type, which sits inside the pipe, the parameters that each variant is measuring are different, the electronics are different and finally the way the data is processed is also different. Therefore it was important to see how the sensor performed by measuring parameters in the same two-phase mixture (in this case air-water), but in two different ways; one using conductance and the second using capacitance. In addition, comparing the performance of the capacitance WMS with the conductance WMS has not been attempted in the past.

4.3. Experimental Methodology

The experimental arrangement can be seen in Figures 4.2 to 4.4. Water was circulated in a closed loop (Figure 4.2) containing a vertical round pipe, approximately 1 m in length with a 50 mm internal diameter. Pressurised gas (air) was injected at the bottom of the vertical test section. The WMS and GD sensors were placed near the top of the test section (Figure 4.3) to detect the gas-liquid mixture. The GD consisted of a radiation source (^{137}Cs , half life: 30 years, activity: 430MBq) and an NaI scintillation detector facing each other across the pipe. Collimators (material: tungsten, weight: 15 kg) were placed in front of the source and detector, which provided both protective shielding and radiation collimation to a 5mm diameter pencil beam, which is close to the equivalent measurement volume used by the WMS at the crossing points, therefore a fair comparison is possible. The GD was placed approximately 1 cm below the 16x16 sensor to avoid any obstacles. The WMS sensor was located approximately 80 cm above the injector. The alignment was executed by placing the collimator in

line with a WMS flange screw, which was located approximately at the centre of pipe (Figure 4.3).

The fundamentals of the wire mesh sensor were outlined in Chapter 3. In this study, a 16x16 wire mesh sensor was employed. The separation of the sender and receiver planes of wires was 2 mm and the diameter of the wires was 0.12 mm (stainless steel). The spatial resolution of the sensor was calculated to be 3.1mm. A sampling rate or temporal resolution of 1000 pipe cross-sections per second (1000 Hz) was employed. This sensor generated a 16x16 matrix of local voids, with 208 pixels or data points inside the pipe. Data was collected with both the WMS and GD triggered simultaneously, with the GD positioned under each of the 16 wire positions. 224 runs with different flow conditions were generated.

The experiments were conducted in the following two parts:

- Run001 to Run112; GD and permittivity WMS; 8 wire positions (1st half of pipe, triggered at same time, Figure 4.4).
- Run113 to Run224; GD and conductivity WMS; 8 wire positions (2nd half of pipe, triggered at same time, Figure 4.4).

For each run the GD was activated for 120 seconds and the WMS was activated for 60 seconds. Figure 4.5 gives a summary of the gas and liquid superficial velocities that were used for each of the 16 positions. Conditions were chosen to be similar to those during a study at Nottingham in 2007 on a 67 mm diameter pipe (Szalinski et al, 2010).

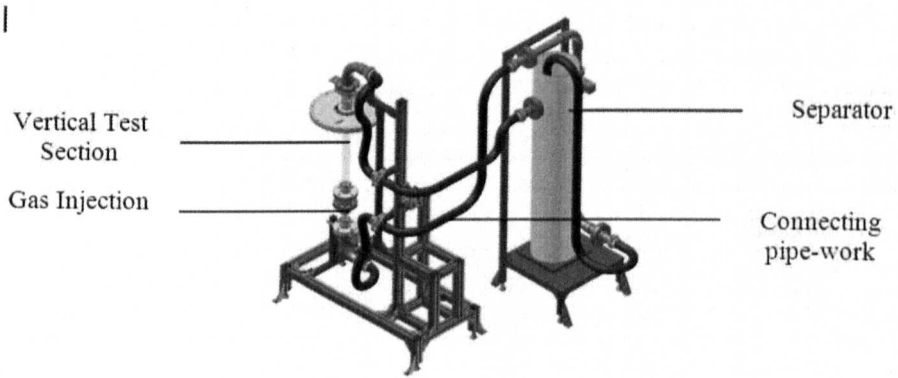


Figure 4.2- 3D schematic of the hydraulic test facility. Water is circulated in a closed loop. Gas is injected at the bottom of the vertical test section then the gas-liquid mixture passes the WMS and GD sensors placed near the top of the pipe.

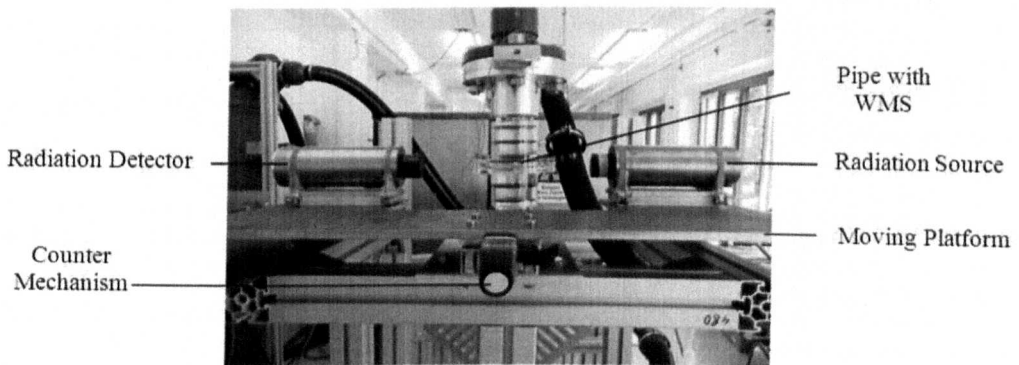


Figure 4.3-Side view of gamma densitometer on a moving platform. Placing both source and detector on the same platform ensures alignment of the beam whenever the GD is moved along the cross-section of pipe

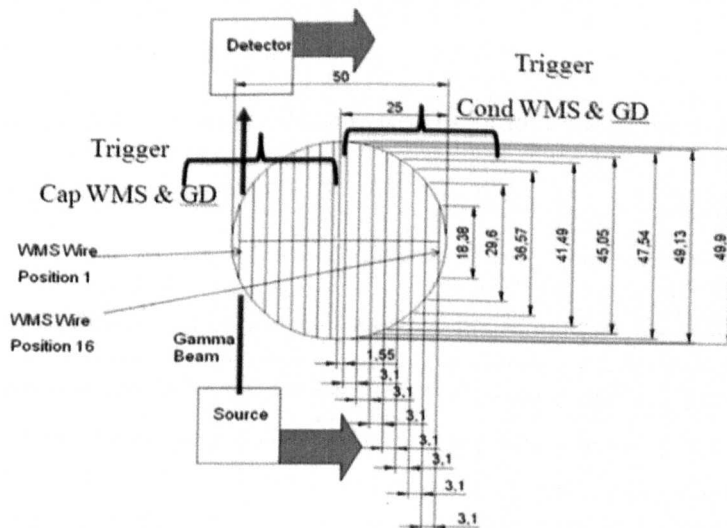


Figure 4.4-Top view of the densitometer. It was lined up below each wire of the WMS, i.e. for 16 positions in total.

Air Flow Rate	Air Velocity	Liquid Flow Rate	Liquid Velocity	Time (GD)	Time (WMS)	Frequency
(l/min)	(m/s)	(l/min)	(m/s)	(s)	(s)	(Hz)
Calibration Full				120	60	1000
Calibration Empty				120	60	1000
6.0	0.051	24.000	0.204	120	60	1000
18.0	0.153	24.000	0.204	120	60	1000
33.0	0.280	24.000	0.204	120	60	1000
55.0	0.467	24.000	0.204	120	60	1000
111.0	0.942	24.000	0.204	120	60	1000
165.0	1.401	24.000	0.204	120	60	1000
6.0	0.051	83.000	0.705	120	60	1000
18.0	0.153	83.000	0.705	120	60	1000
33.0	0.280	83.000	0.705	120	60	1000
55.0	0.467	83.000	0.705	120	60	1000
111.0	0.942	83.000	0.705	120	60	1000
165.0	1.401	83.000	0.705	120	60	1000

Figure 4.5-Matrix showing the gas and liquid superficial velocities for all 16 positions

4.4. Data Processing and Calibration

The gamma chordal void fractions were calculated using equation C3 (see calculation section in Appendix C). This equation relates the radiation intensity or count rate I of the gas-liquid mixture when flowing up the pipe to the void fraction ε . In order to use this equation, the densitometer was initially calibrated by collecting the count rate with the pipe empty I_E , and then with the pipe full of liquid I_F . All sixteen wire positions were calibrated with the densitometer in order to calculate the chordal void for all the positions. To minimise errors, each wire was initially calibrated for the GD, and then the matrix in Figure 4.5 was completed in full. Then the GD was shifted to the next wire, calibrated again, and the matrix repeated and so on, until all 16 wires were covered across the full cross section of pipe.

For the gamma count rate, trials were initially carried out at 14 minutes per run. However, for each of the 224 runs, data was collected over 2 minutes and then processed, which was also the length of time used by Prasser et al (1998, 2000) in

their fixed gamma densitometer set-up that was used for comparison with the WMS. Gamma photons interacting with the detector's scintillation crystal produce a light pulse, which is converted into a voltage pulse by a photodiode and amplifier. The pulse height is proportional to the gamma photon's energy deposition. A multi-channel analyser connected to the detector performs the pulse counting for different energy bins (channels or windows), which gives the typical distributions shown in Figures 4.6 and 4.7. Only gamma photons are considered, which deposit their full energy of 622 keV into the scintillator.

Photons with lower energy might have been scattered and therefore deviated from the straight path, which would introduce an error to the calculated attenuation value. The number of these photons is the integral under the photo-absorption peak that appears in the right hand part of the energy spectrum in Figures 4.6 and 4.7. The broader distribution of the energy values is due to the limited energy resolution of the detector. Figures 4.6 and 4.7 show the photon energy spectra for calibration measurements on an empty and full pipe, as well as for different measurement durations of 14 minutes and 2 minutes. As expected, the signal-to-noise ratio improves with the square root of the total photon number. There is initially a small peak for background radiation, which had been excluded from the calculations. Small changes in the spectra were observed, but care was taken to keep the room temperature as constant as possible. In addition, the source was protected to some extent from the elements inside the thick-walled collimator.

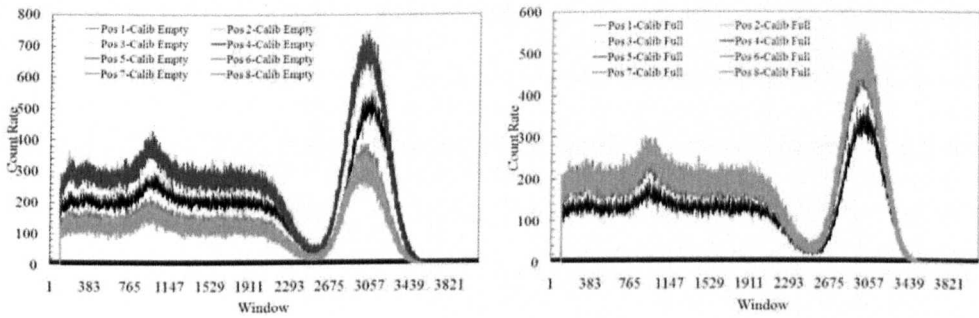


Figure 4.6-Calibration graphs for 14 minutes for one half of the pipe. (Left) Air, (right) water

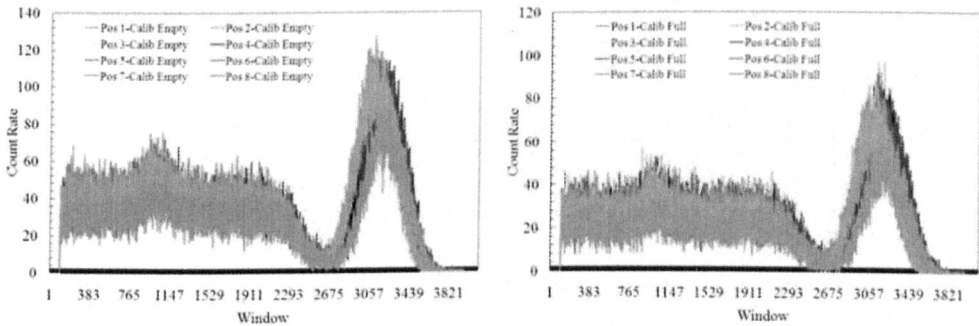


Figure 4.7-Calibration graphs for 2 minutes for one half of pipe. (Left) Air, (right) water

Calibrating the conductance WMS slightly differed from the capacitance WMS. For the conductance WMS, only one calibration is required with the pipe full of liquid, as it is detecting the conducting phase. This calibration covered all 16 positions at which the GD was set. For the capacitance WMS however, two calibrations are required as it is measuring the difference in permittivities, one with the pipe full, and the second empty. In this case, the ratio of permittivities for air and water is 1:80. In general, two calibrations were carried out, one at the beginning of the day, and one at the end. A discussion of how the conductance WMS and capacitance WMS collects and then processes the data can be found in Appendix B. Further details can be found in Prasser et al (1998) and Da Silva et al (2010).

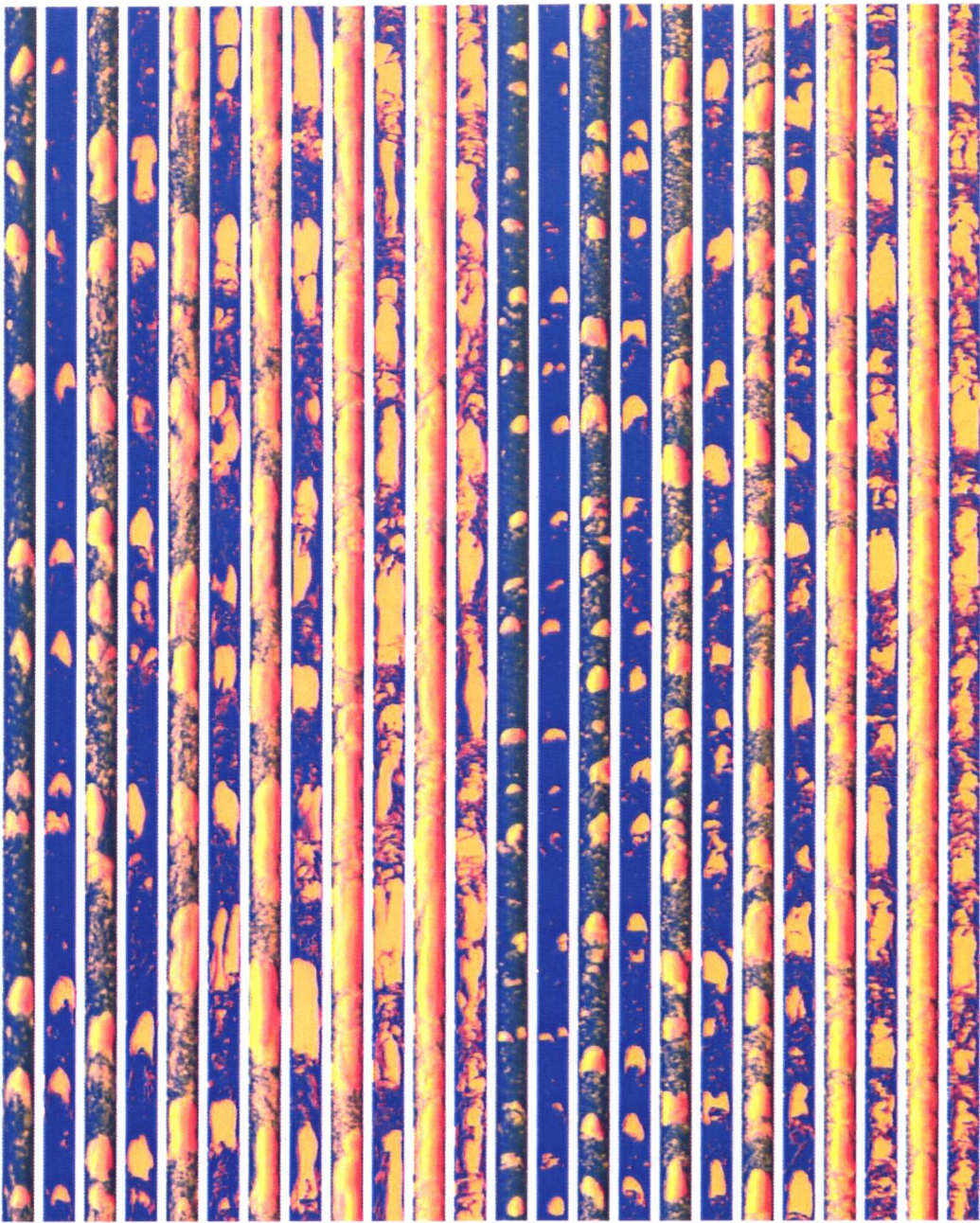
For the WMS, time averaged local void fractions over 60 seconds can be visualised as a 16x16 matrix. The local voids from the WMS for each wire position are then averaged to generate a value that is used for comparison with the chordal void fraction generated by the GD. Figure 4.8 shows a typical matrix generated by the WMS. Shown are local voids for wire positions 5 and 12. Line averaged void fraction can be deduced as shown and then compared with the chordal void fraction generated by the GD.

				Pos 5				Pos 12							
				Run064				Run162							
0	0	0	0	0	18.6	27.99	25.51	28.7	25.54	49.84	0	0	0	0	
0	0	0	22.42	32.7	39.97	42.46	44.13	48.33	45.7	40.83	32.74	18.26	0	0	
0	0	26.79	38.62	46.66	53.2	56.39	57.32	60.81	59.17	55.17	48.58	38.97	23.81	0	
0	27.02	39.31	49.2	56.55	62	64.46	66.15	69.77	68.28	64.81	59.26	50.68	38.79	19.48	
0	36.56	48.76	60.18	64.52	68.9	71.4	73.15	76.65	75	71.73	66.27	58.48	47.84	32.44	
23.62	43.03	53.83	62.41	68.73	73.46	76.23	78.01	81.36	79.77	76.34	70.91	63.52	53.65	39.76	
28.05	46.73	57.31	66.22	72.12	76.98	79.78	81.35	83.81	82.41	79.13	74.08	66.68	56.84	43.54	
30.47	48.99	60.01	68.76	74.53	79.04	81.76	83.38	85.02	83.73	80.81	75.58	67.79	58.62	45.56	
30.61	48.68	60.1	68.92	74.66	79.18	81.92	83.53	84.82	83.92	81.06	76.04	68.15	58.64	45.6	
27.62	46.35	57.93	66.61	72.47	77.09	80.07	81.77	83.31	82.42	79.59	74.64	67.09	57.26	43.56	
23.86	42.48	54.89	63.24	68.85	73.62	76.82	78.67	80.25	79.33	76.57	71.65	64.28	54.25	39.71	
0	35.22	47.62	57.11	63.35	68.58	71.74	73.64	75.79	75.11	72.19	67.17	59.88	48.83	33.34	
0	26.34	38.87	48.97	55.59	61.56	65.1	66.9	69.19	68.03	65.17	59.82	52.13	39.88	20.82	
0	0	26.35	37.25	44.46	50.73	54.93	57.08	60.49	58.3	55.13	49.44	40.12	24.21	0	
0	0	0	23.48	30.4	36.91	40.35	42.74	48.37	46.44	42.44	34.94	21.27	0	0	
0	0	0	0	0	18.04	21.1	24.16	28.84	26.23	19.52	0	0	0	0	
27.372	40.140	47.648	52.364	58.971	58.616	61.719	63.781	66.594	64.561	61.271	61.509	52.700	46.885	36.351	
0.274	0.401	0.476	0.524	0.590	0.586	0.617	0.636	0.666	0.650	0.613	0.615	0.527	0.469	0.364	

Figure 4.8-Time averaged local void fraction Position 5 left (capacitance), and Position 12 right (conductance). Line average is worked out in the highlighted rectangle. Dashed line is the edge of the pipe. Zero voids lie outside of the pipe, therefore are disregarded.

4.5. Results

Using the high resolution imaging capability of the WMS, the flow patterns investigated in these experiments were deduced. Figure 4.9 shows sections and side projections obtained from the measurements with the capacitance WMS (the conductance WMS produced similar images) using the data processing described in detail by Da Silva et al (2010). Six pairs of sections and projections per liquid superficial velocity are shown. From Figure 4.9 it is clear that the flow patterns were bubbly, slug and churn.



0.051	0.153	0.28	0.467	0.942	1.401	0.051	0.153	0.28	0.467	0.942	1.401
0.2	0.2	0.2	0.2	0.2	0.2	0.7	0.7	0.7	0.7	0.7	0.7

Figure 4.9-Visual plots of flow patterns. First row gives U_{gs} in m/s and second row is U_{ls} in m/s. For each flow condition, two side projections are shown, first as if pipe is transparent, and second in the middle of the pipe

The 16x16 WMS generated a 16x16 matrix for every 1/1000 of a second for these particular experiments. For 60 seconds, this meant that 60000 frames were generated, which is a significant amount of data. This is used to construct the images above using special processing software. It is also possible to show the local voids in the 2D cross-sectional view, and to generate 3D surface plots to quantify the void fraction and track the void fraction to see how it changes in time for all 16 crossing points. Videos animating the variation of the 2D and 3D local void fraction against time are available from the author.

Figure 4.10 shows how the count rate varied across the whole cross-section of the pipe. It summarises all 224 count rates for all gas and liquid superficial velocities for the 16 WMS wire positions. It also shows the calibration values for the pipe when it is empty and full. As expected, there is a higher count rate for the gas-filled pipe, and the difference decreases towards the sides due to the decreasing chord lengths inside the pipe. The variations mainly come from structural elements, i.e. extra absorbers in the ray paths; however, the gamma counts were almost symmetrical about the pipe centre-line. All the results are between the two calibration lines, and there is a trend for the count rate to shift upwards with increasing gas superficial velocity. The count rates drop slightly as the liquid superficial velocity is increased from 0.2 to 0.7m/s.

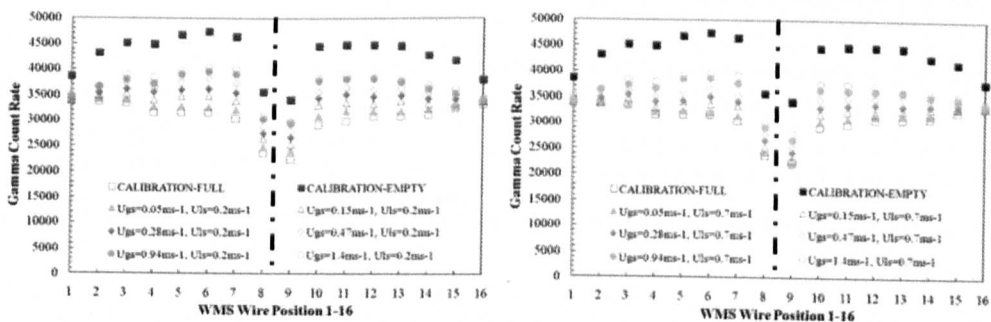


Figure 4.10-Gamma Densitometer count rates for all gas superficial velocities for all 16 positions. (Left) $U_{ls}=0.2\text{m/s}$ and (right) $U_{ls}=0.7\text{m/s}$. Dashed line indicates the pipe centre-line.

From the count rates, the gamma chordal void fraction for all 16 wire positions were extracted and these were subsequently plotted as shown in Figure 4.11, for $U_{ls}=0.2\text{m/s}$ (left) and $U_{ls}=0.7\text{m/s}$ (right).

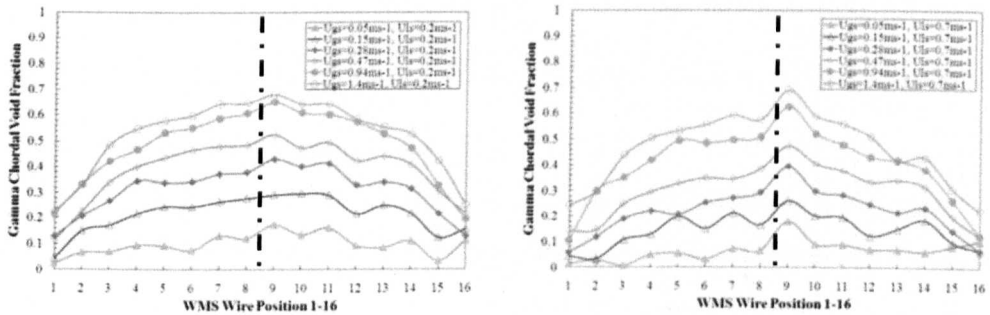


Figure 4.11-Gamma Densitometer count rates for all gas superficial velocities for all 16 positions. (Left) $U_{ls}=0.2\text{m/s}$ and (right) $U_{ls}=0.7\text{m/s}$. Dashed line indicates the pipe centre-line.

The trends in the void fractions in Figure 4.11 follow those of the count rates in Figure 4.10. Consider two scenarios; two outermost wire position(s) 1 and 16, and two close to the centre wire position(s) 5 and 12. The % difference in void values between GD and WMS for the full experimental matrix generated in those positions as shown in Figure 4.5 can be deduced, which is shown in Figure 4.12. It is clear there is a better agreement between the GD and WMS in positions 5 and 12.

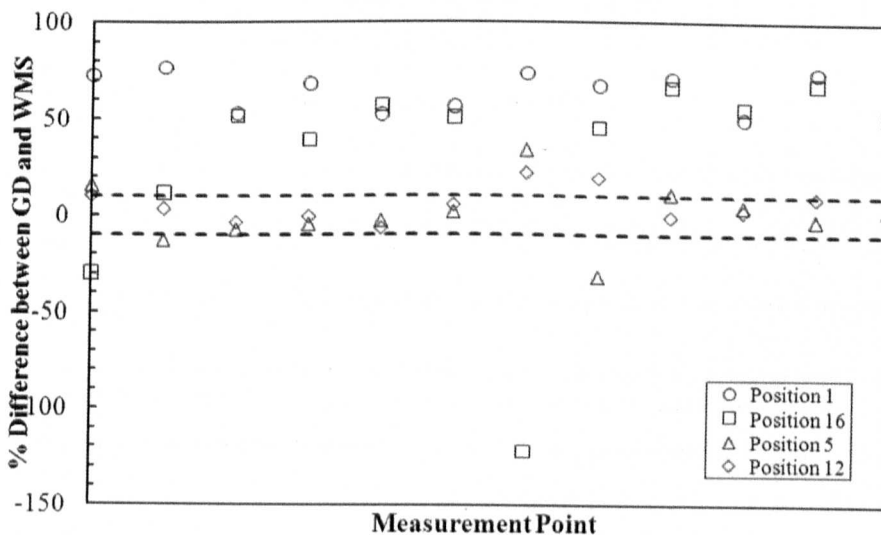


Figure 4.12-% Difference in void values between GD and WMS for positions 1/16 and 5/12. 12 data points displayed per position i.e. 2 superficial liquid velocities and 6 superficial gas velocities (x-axis).

Most of the values for positions 5 and 12 lie within a band of $\pm 10\%$, with several values falling within a band of $\pm 5\%$. Taking the chordal void fraction data for positions 5 and 12, and comparing it with the corresponding line averaged WMS void fraction data from both variants of the WMS, this data can be plotted against the gas superficial velocity. This is shown in Figure 4.13. There is a good agreement displayed between both variants of the WMS and the GD.

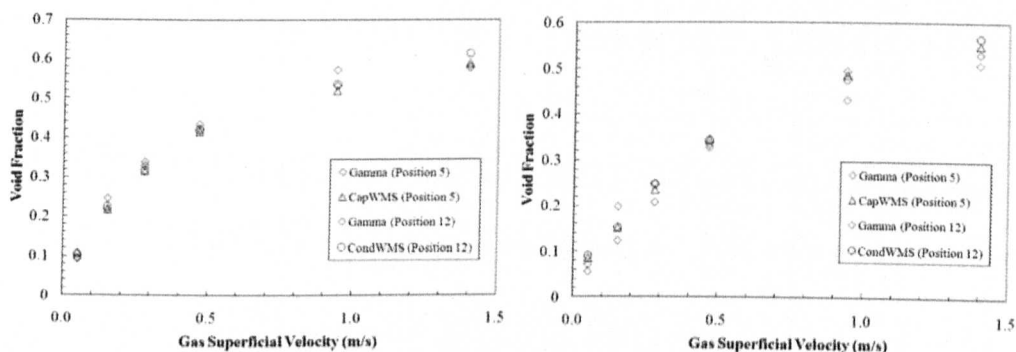


Figure 4.13-Mean void fraction vs. gas superficial velocity (gamma and WMS). (Left) liquid superficial velocity of 0.2ms^{-1} and (right) liquid superficial velocity of 0.7ms^{-1}

A better way to visualise the data in Figure 4.13 is to show the gamma chordal void vs. the WMS line averaged void for wire position(s) 5 and 12, as shown in Figure 4.14. There is again a good agreement. Figure 4.14 shows two independent sensors agreeing with the gamma densitometer in two different segments of the pipe. The agreement between the two variants of WMS is also clear. Note also that Figure 4.14 covers the full scale of gas and liquid superficial velocities as well as covering three different patterns i.e. bubble to slug to churn flows. Similar plots can be generated for other symmetrical wire positions; Figure(s) 4.15, 4.16 and 4.17 show wire positions 7/10, 6/11 and 4/13 respectively. The agreement is again clear for all of these wire positions.

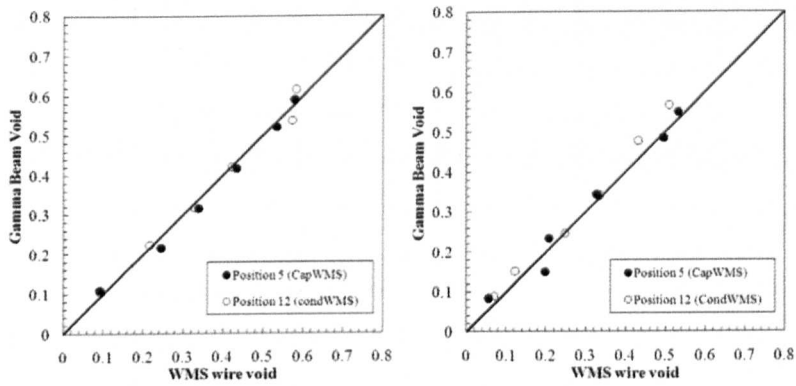


Figure 4.14-Chord Averaged void fraction (GD) vs. line averaged void fraction (WMS) for positions 5 and 12. (Left) liquid superficial velocity of 0.2ms^{-1} and (right) liquid superficial velocity of 0.7ms^{-1}

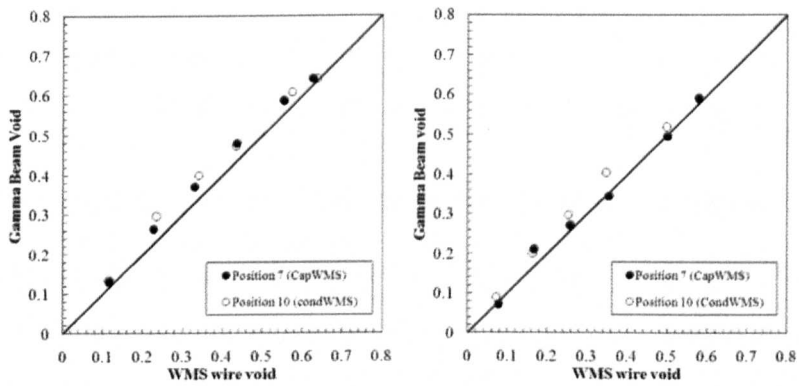


Figure 4.15-Chord Averaged void fraction (GD) vs. line averaged void fraction (WMS) for positions 7 and 10. (Left) liquid superficial velocity of 0.2ms^{-1} and (right) liquid superficial velocity of 0.7ms^{-1}

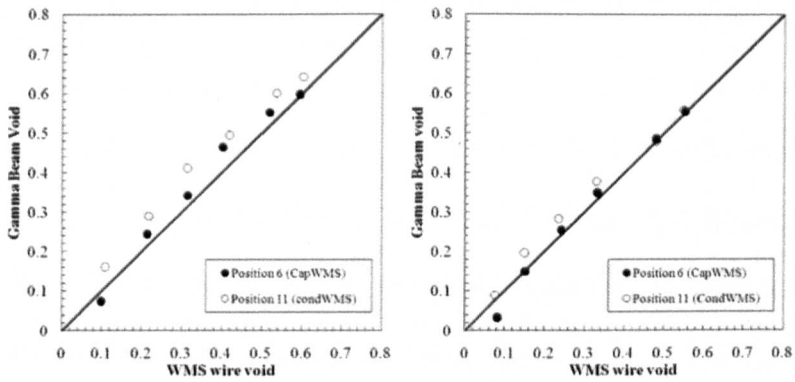


Figure 4.16-Chord Averaged void fraction (GD) vs. line averaged void fraction (WMS) for positions 6 and 11. (Left) liquid superficial velocity of 0.2ms^{-1} and (right) liquid superficial velocity of 0.7ms^{-1}

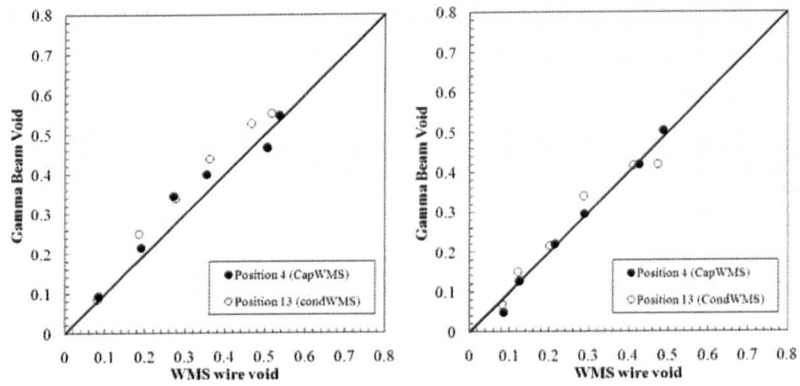


Figure 4.17-Chord Averaged void fraction (GD) vs. line averaged void fraction (WMS) for positions 4 and 13. (Left) liquid superficial velocity of 0.2ms^{-1} and (right) liquid superficial velocity of 0.7ms^{-1}

4.6. Discussion

In general, there was a very good agreement between Gamma Densitometry and the WMS in the central portion of the pipe. As the WMS was moved towards the edge of the pipe however, there were large differences. One potential explanation for the large difference in voids between GD and WMS readings, particularly near the pipe wall, is due to the fact the GD has a lower “control volume” at the edge of the pipe, therefore it sees less of the flow. The WMS has local measurements even at the periphery of the pipe, with six crossing points. Near the edges of the pipe, there are geometrical considerations that need to be taken into account, which will be obscuring and affecting the path of the radiation for the densitometer, although in theory this should be covered by the calibration process. If the pipe is divided into sections, the cross-sectional shape of the pipe at the wall is almost trapezoidal, whereas it is a more regular shape in the central part of the pipe. Kumara et al (2010) calculated the geometrical factor to be approximately 1% at the pipe wall. Results in these experiments suggest this is too low. Results by Manera et al (2007) also showed larger differences between gamma and wire mesh sensor measurements at the wall than near the centre of the pipe.

The accuracy of the WMS is around +/- 5% (Prasser et al, 2005b), but this does not cover the large differences between the WMS and GD at the pipe wall. A number of other errors could be contributing to the difference at the pipe wall. The local voids by the WMS all around the pipe wall are significantly lower than the overall cross-sectional averaged void fraction. There are possible inaccuracies in the gamma beam location relative to the wires. A manual moving platform will be less accurate than a servo-motor controlled set-up, which allows more precision in locating the GD. There is a possibility that developing, as opposed to fully developed, flow was being measured. In the set-up, there was 1 metre of pipe length for flow development, but Azzopardi (2006) suggests pipe lengths of up to 100 times the pipe diameter could be necessary to establish developed flow. Piper (1974), Hewitt (1978), Kumar et al (1995), Stahl et al (2004) and Kumara et al (2010) list several issues in using Gamma Densitometry. Some of these are discussed as follows:

(a) Radiation: Natural difficulties in handling radioactive material. A fairly strong source ^{137}Cs was used in these experiments; this required thick and heavy shielding, and the wearing of a dosimeter throughout these experiments.

(b) Accuracy: There is a fundamental inaccuracy in the measurement of void fraction due to radiation statistical fluctuations. This can be minimised using long counting times, and strong sources. A number of different gamma sources are available; these have varying photon energies, half-lives and emission ratios. With ^{137}Cs , it has both a high photon energy and emission ratio, which makes it a good all-round source to use. Statistical and dynamic bias errors are discussed in Appendix C.

(c) Influence of void orientation: There are two limiting cases and the equations used in calculating the chordal void fraction implied the gas-liquid mixture exists in layers perpendicular to the radiation source (vertical flow). A different equation is necessary when the gas-liquid mixture exists in parallel to the radiation source (horizontal flow). See Gamma Densitometry calculation (Appendix C) for further details.

(d) Effect of tube wall: In making void fraction measurements as were carried out in this experiment, the beam passes through variable wall thickness. Using a single beam to take an average over the whole tube, there is a stronger weighting for those parts of the tube where the beam path lengths through the plastic wall are lower.

(e) Time fluctuation effects: Gas-liquid flows such as those encountered in these experiments were time-varying. For example slug flow, where the void fraction fluctuates periodically between 0 and 1 (or 0% to 100%). If the absorption is exponential, then clearly the average signal does not represent the mean void-fraction that the WMS measures. One way round this issue as suggested by Hewitt (1978) is to use two gamma beams instead of one, but with different energies. The ratio of the time-averaged intensities from the two beams gives a measure of void fraction, and the use of the ratio gives a result for mean void fractions in a time-varying flow, which is closer to the true value than the equivalent mean obtained from a single beam.

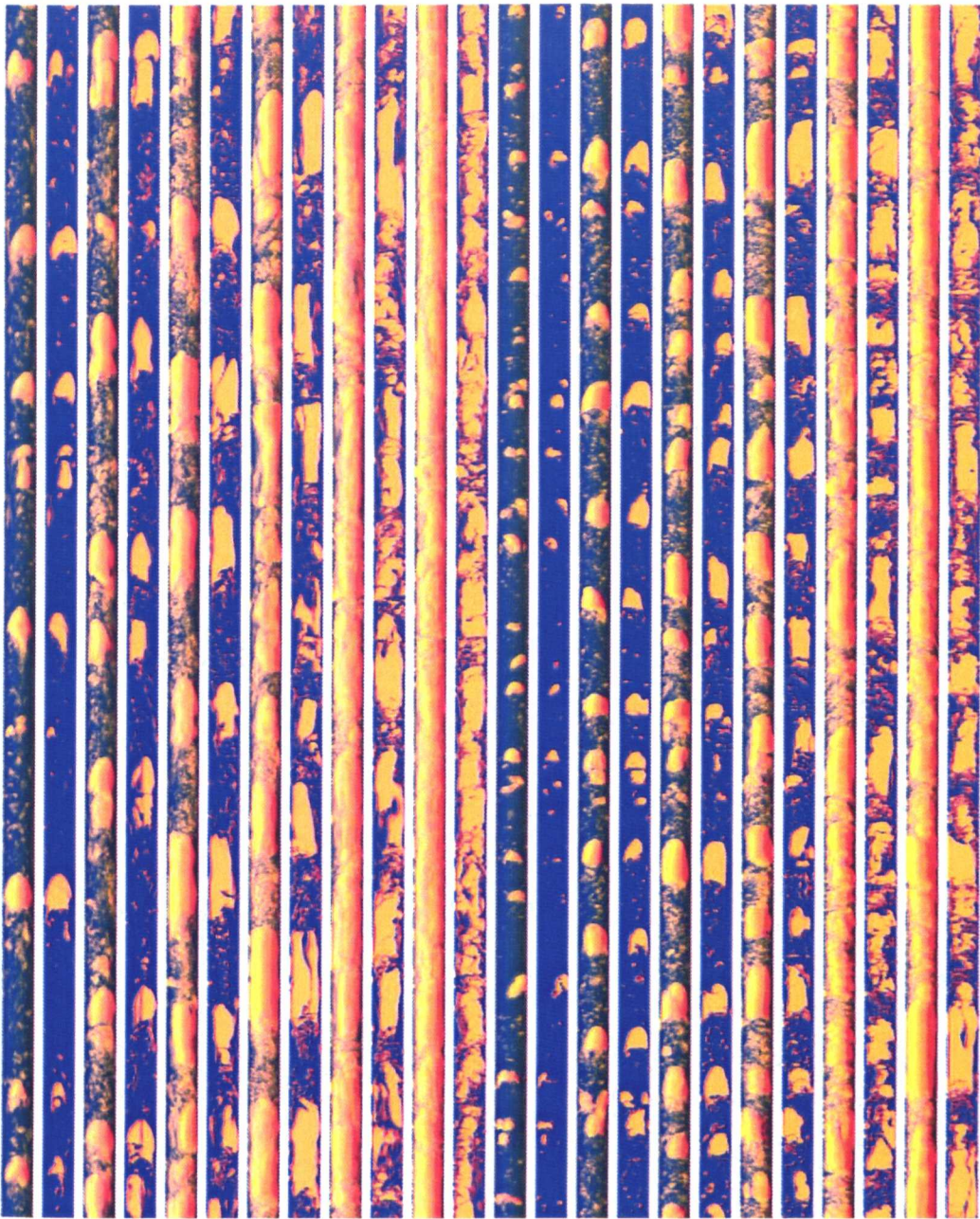
This work suggests that using other newly developed instruments by HZDR, such as the FMS (film measurement sensor) and the x-ray tomograph will be more suitable for investigating voids at the pipe wall in detail. Needle probes that compared well with WMS measurements and gave local void measurements to a high degree of accuracy (Manera et al, 2009) are probably not suitable for pipe wall investigations, since flow

disturbance of such a probe near the pipe wall can be high. Unpublished experimental data acquired at HZDR comparing the WMS against ROFEX (ultrafast x-ray CT), showed that the WMS overestimated the void fraction at the wall. Interestingly, the x-ray scanner also showed zero voids at the wall in some cases. The ROFEX has a higher resolution than the WMS, and small bubbles appear more round than in WMS images. Other experimental approaches are also possible, for example the GD could be moved so that it is aligned exactly with the WMS wires as opposed to being placed 1 cm below them. Finally, a gamma-ray tomograph could be used, which would give a scan of the full-section of pipe as opposed to just a single chord that is produced by the GD.

4.7. Comparison between CondWMS and CapWMS

4.7.1. 2D Visualisation

From the results of this work, a further exercise can be carried out comparing the CondWMS with the CapWMS. This is based on the assumption that the flow is symmetrical. This comparison can be done both qualitatively by inspecting the visualisation generated from both sensors, and quantitatively by carrying out a statistical analysis. To begin with, the flow regimes that the WMS generates can be compared. Figure 4.18 shows the visualisation generated by the CondWMS for all gas superficial velocities at the two liquid superficial velocities. This can be compared with the one given earlier in this report in Figure 4.9, which was generated by the CapWMS. Qualitatively, they look similar and predict similar flow regimes.



0.051	0.153	0.28	0.467	0.942	1.401	0.051	0.153	0.28	0.467	0.942	1.401
0.2	0.2	0.2	0.2	0.2	0.2	0.7	0.7	0.7	0.7	0.7	0.7

Figure 4.18- Visual plots of flow regimes. First row U_{gs} in m/s, second row U_{ls} in m/s. For each flow condition, two projections are shown; the first is transparent pipe, the second is middle of pipe

4.7.2. Three Dimensional Plots

This process can be taken one step further by converting the 2D images into 3D, to improve the visualisation of the structures. Figure 4.19 shows the 3D plots for the CapWMS and Figure 4.20 for the CondWMS. Qualitatively, there is a good agreement, with the size and periodicity in the structures matching in many instances.

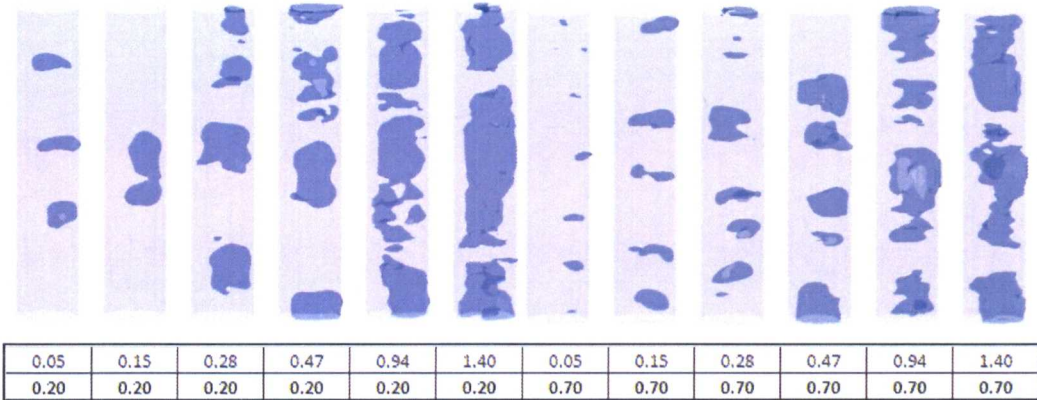


Figure 4.19-Capacitance 3D visuals for $U_{gs}=0.05-1.4\text{m/s}$, at $U_{ls}=0.2\text{m/s}$ and 0.7m/s

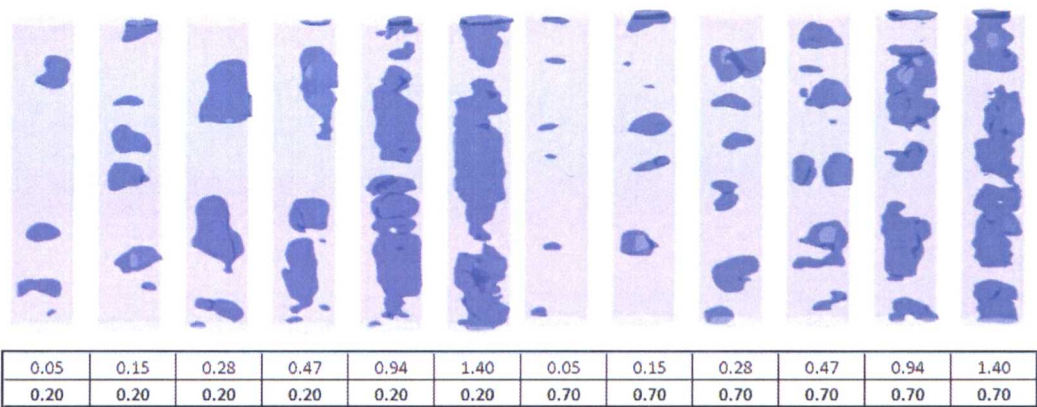


Figure 4.20-Conductance 3D visuals for $U_{gs}=0.05-1.4\text{m/s}$, at $U_{ls}=0.2\text{m/s}$ and 0.7m/s

4.7.3. Time Series

To continue with the quantitative comparison, the time series of cross-sectionally averaged void fraction was plotted (Figure 4.21) to (Figure 4.26). Although there is significant fluctuation in the void over time, the trend between the two sensors looks similar. It can also be seen how the void shifts to a higher value with an increasing gas superficial velocity. Both sensors exhibit this tendency.

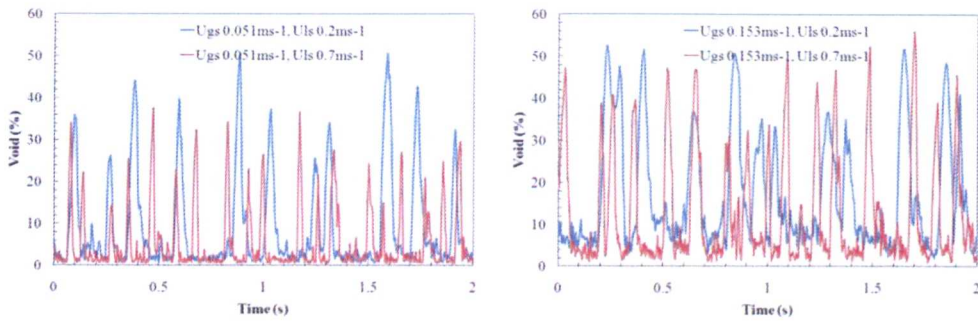


Figure 4.21-Time Series, capacitance WMS $U_{gs}=0.051, 0.153\text{m/s}$, $U_{ls}=0.2, 0.7\text{m/s}$

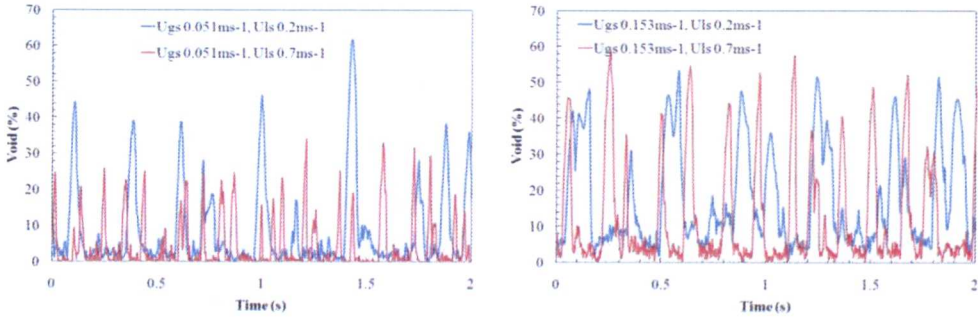


Figure 4.22- Time Series, conductance WMS $U_{gs}=0.051, 0.153\text{m/s}$, $U_{ls}=0.2, 0.7\text{m/s}$

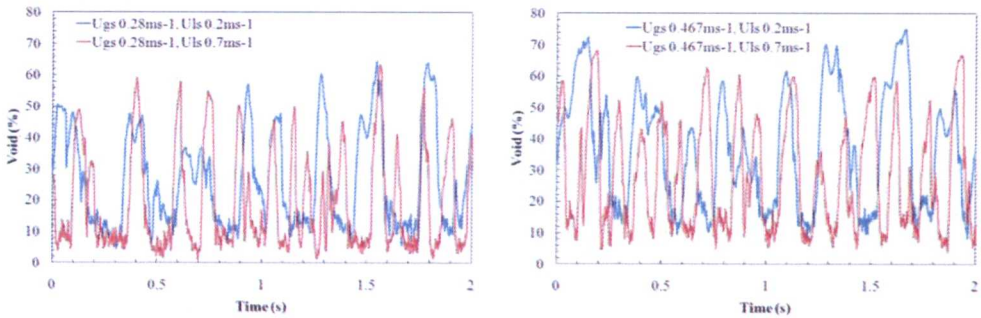


Figure 4.23- Time Series, capacitance WMS $U_{gs}=0.28, 0.467\text{m/s}$, $U_{ls}=0.2, 0.7\text{m/s}$

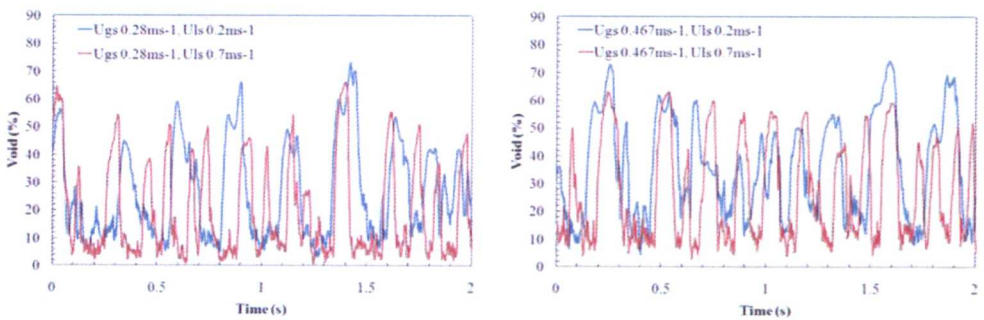


Figure 4.24- Time Series, conductance WMS $U_{gs}=0.28, 0.467\text{m/s}$, $U_{ls}=0.2, 0.7\text{m/s}$

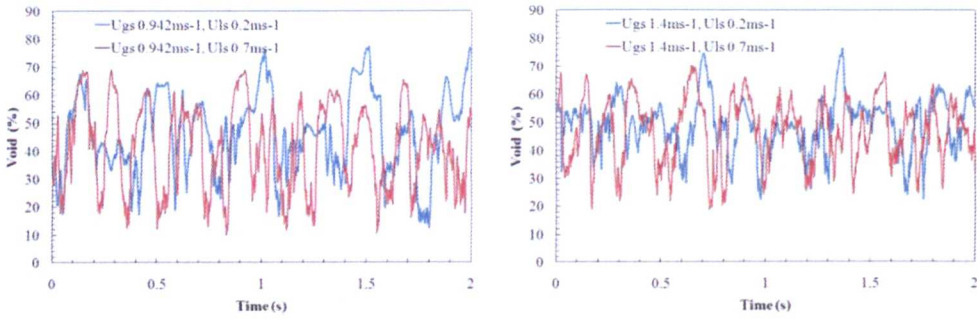


Figure 4.25- Time Series, capacitance WMS $U_{gs}=0.942, 1.4\text{m/s}$, $U_{ls}=0.2, 0.7\text{m/s}$

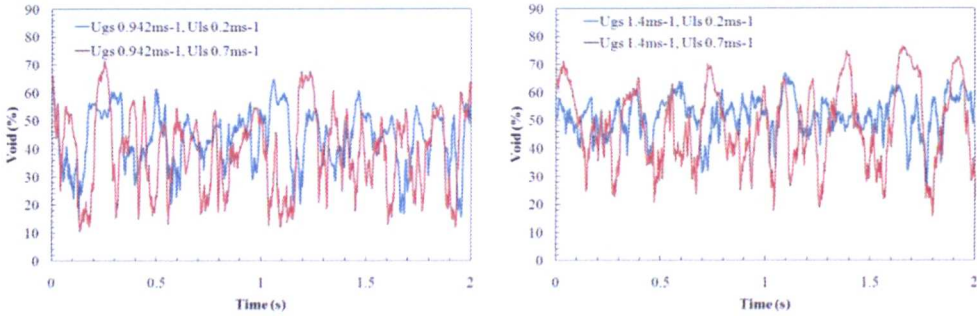


Figure 4.26- Time Series, conductance WMS $U_{gs}=0.942, 1.4\text{m/s}$, $U_{ls}=0.2, 0.7\text{m/s}$

4.7.4. PDF

From the time series plots it is possible to quantitatively identify the flow regime using the PDF, which gives a distinctive or characteristic footprint for each flow regime (Whalley et al, 1997). It also gives more meaning to the time series profile, which on its own can be difficult to interpret. The PDF for the CapWMS can be seen in Figure 4.27 and for the CondWMS in Figure 4.28.

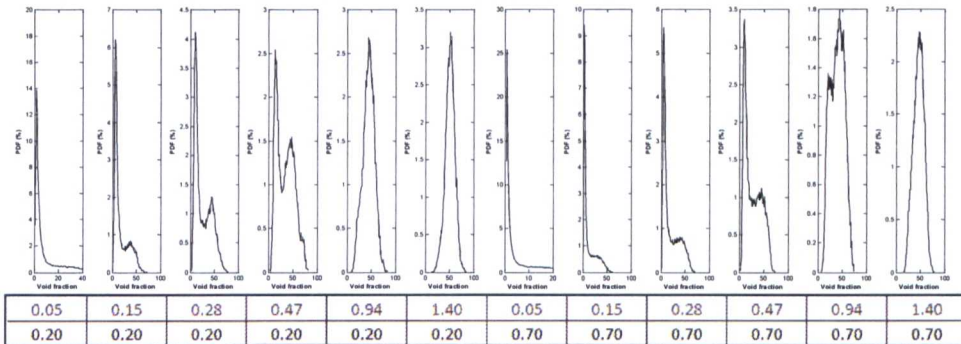


Figure 4.27- Capacitance WMS PDF plots for $U_{gs}=0.05-1.4\text{m/s}$, at $U_{ls}=0.2\text{m/s}$ and 0.7m/s

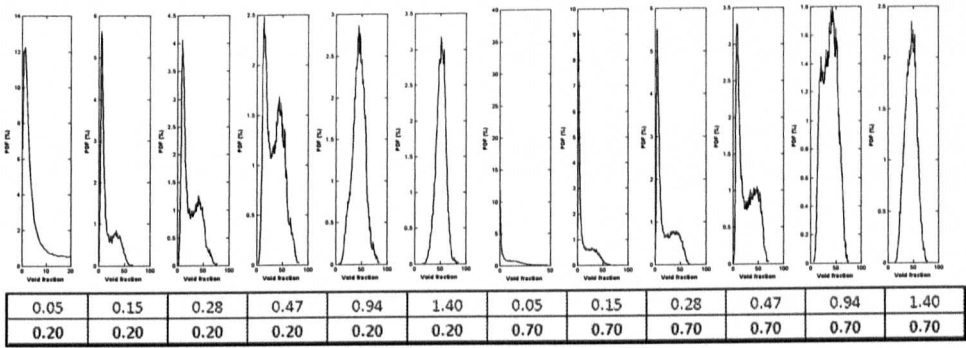


Figure 4.28- Conductance WMS PDF plots for $U_{gs}=0.05-1.4\text{m/s}$, at $U_{ls}=0.2\text{m/s}$ and 0.7m/s

There is a reasonable agreement if the PDFs are compared, with both sensors generating similar profiles for the same flow conditions. This is for the full range of gas and liquid superficial velocities covering bubble-slug-churn flow patterns.

4.7.5. Statistical Analysis

From the time series plots it is possible to analyse and compare the variation in terms of the Mean (1st Moment), Standard Deviation (2nd Moment), Skewness (3rd Moment) and Kurtosis (4th Moment) for the two sensors. Figure 4.29 shows these values for the capacitance WMS and Figure 4.30 for the conductivity WMS, for the same gas and liquid superficial velocities. There is a remarkable agreement between the two sensors.

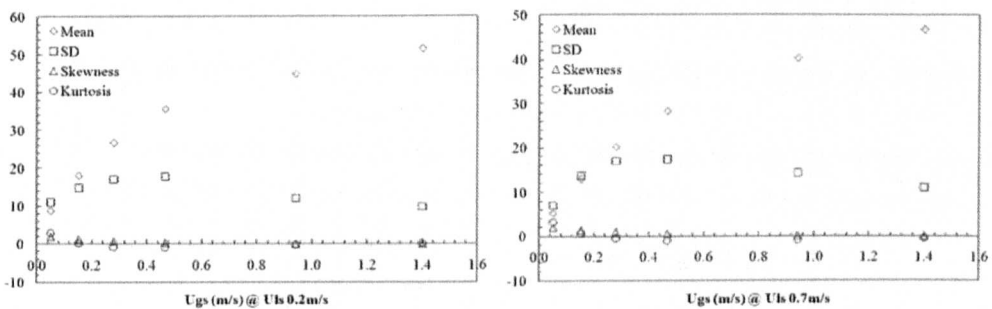


Figure 4.29- CapWMS plots for $U_{gs}=0.05-1.4\text{m/s}$, at $U_{ls}=0.2\text{m/s}$ (left) and 0.7m/s (right)

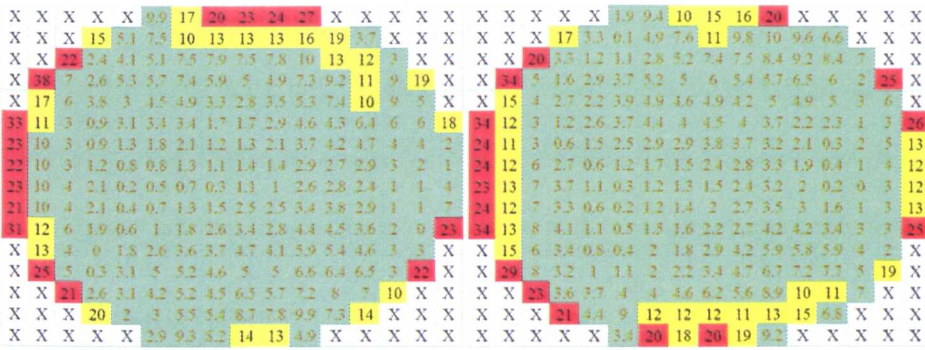


Figure 4.33- Local voids: (Left) $U_{gs} 0.942\text{m/s}$ $U_{ls} 0.2\text{m/s}$ (Right) $U_{gs} 1.401\text{m/s}$ $U_{ls} 0.2\text{m/s}$

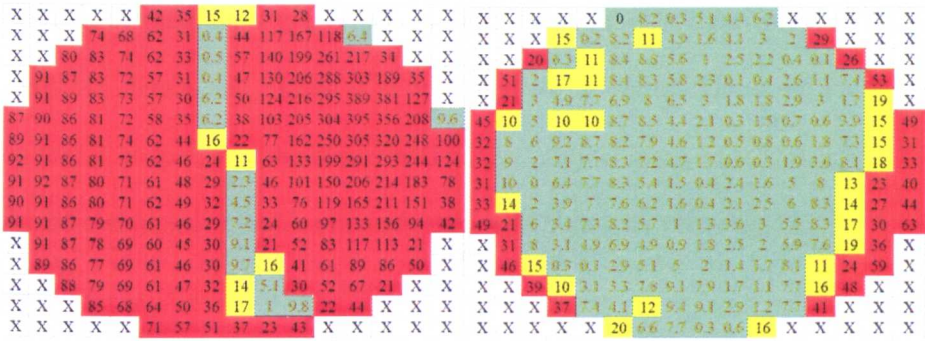


Figure 4.34- Local voids: (Left) $U_{gs} 0.051\text{m/s}$ $U_{ls} 0.7\text{m/s}$ (Right) $U_{gs} 0.153\text{m/s}$ $U_{ls} 0.7\text{m/s}$

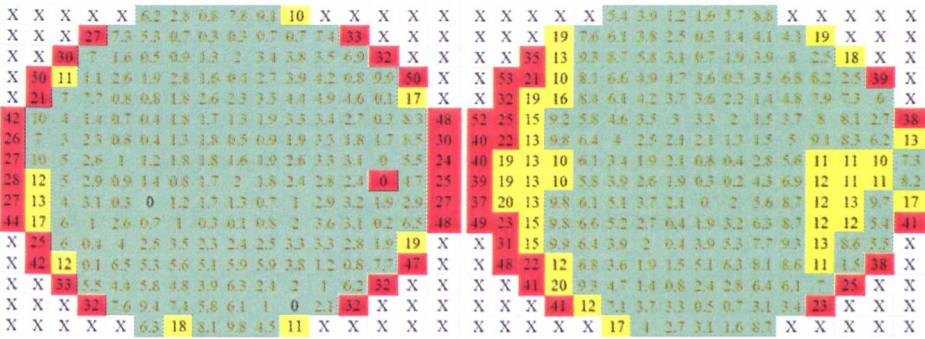


Figure 4.35- Local voids: (Left) $U_{gs} 0.280\text{m/s}$ $U_{ls} 0.7\text{m/s}$ (Right) $U_{gs} 0.467\text{m/s}$ $U_{ls} 0.7\text{m/s}$

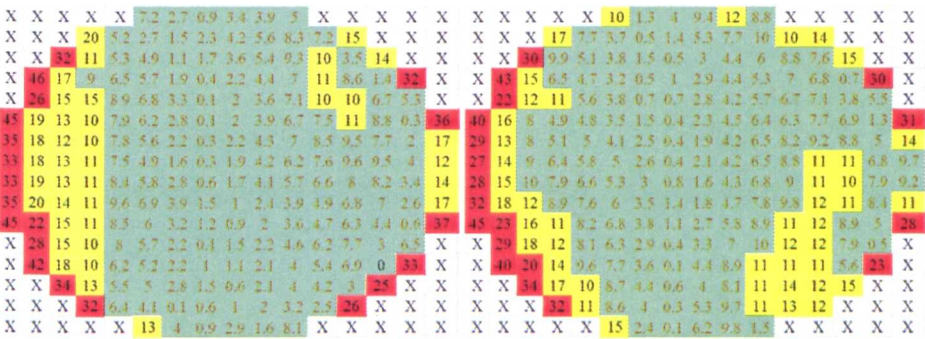


Figure 4.36- Local voids: (Left) $U_{gs} 0.942\text{m/s}$ $U_{ls} 0.7\text{m/s}$ (Right) $U_{gs} 1.401\text{m/s}$ $U_{ls} 0.7\text{m/s}$

In general there was good agreement between the two sensors, except on the periphery and also when $U_{ls}=0.7\text{m/s}$ and $U_{gs}=0.051\text{m/s}$, where there were larger differences. However, it is clear that most crossing points generated differences of less than 10% with varying gas and liquid superficial velocities, which is within acceptable limits.

4.7.7. Radial Profiles

The next exercise was to extract the radial profiles for both sensors for the same flow conditions, and again there is a very good agreement between the two. See Figure 4.37 for CapWMS results and Figure 4.38 for CondWMS results. The trend for the radial void is that it increases as the superficial gas velocity is increased. This is true for the two superficial liquid velocities investigated with both wire mesh sensors.

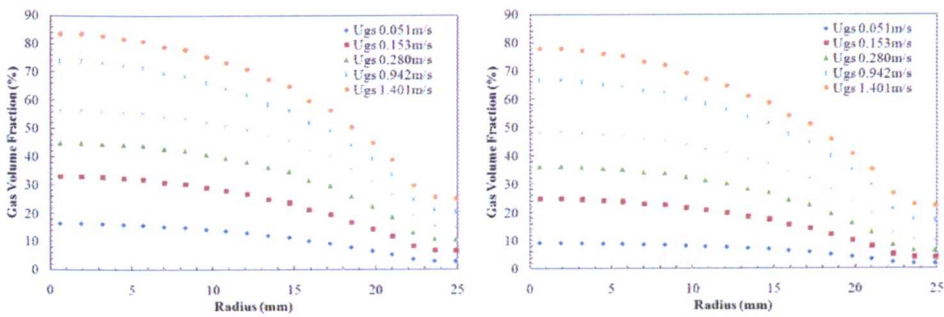


Figure 4.37-Radial voids for CapWMS. (Left) $U_{ls}=0.2\text{m/s}$, (right) $U_{ls}=0.7\text{m/s}$

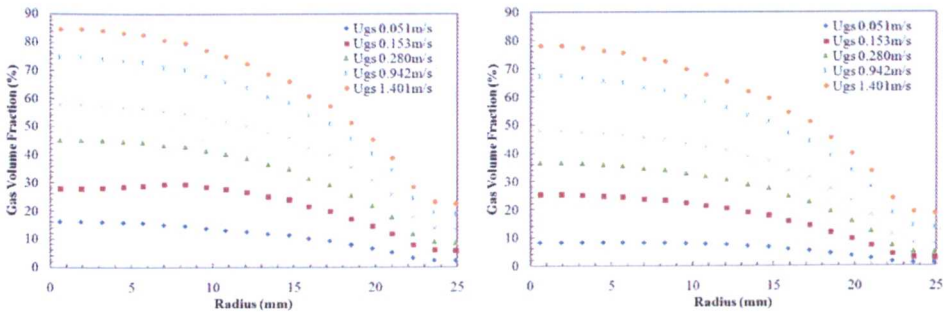


Figure 4.38- Radial voids for CondWMS. (Left) $U_{ls}=0.2\text{m/s}$, (right) $U_{ls}=0.7\text{m/s}$

The graph shows the radial profile for one half of pipe, and assumes symmetry, although in reality the other section of the pipe will not necessarily have the same values.

4.7.8. Bubble Size Distribution

A more advanced step is to compare the bubble size distribution (BSD) generated by the two sensors. Figure 4.39 shows the BSD for the CapWMS and Figure 4.40 for the CondWMS, again for the same gas and liquid superficial velocities.

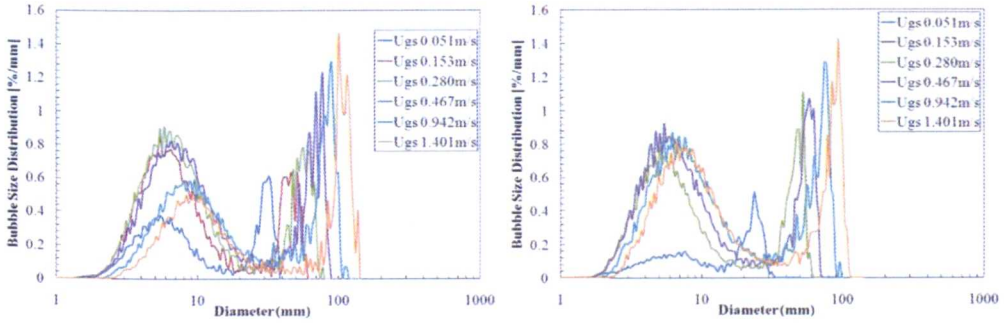


Figure 4.39- Bubble Size Distribution for CapWMS. (Left) $U_{ls}=0.2\text{m/s}$, (right) $U_{ls}=0.7\text{m/s}$

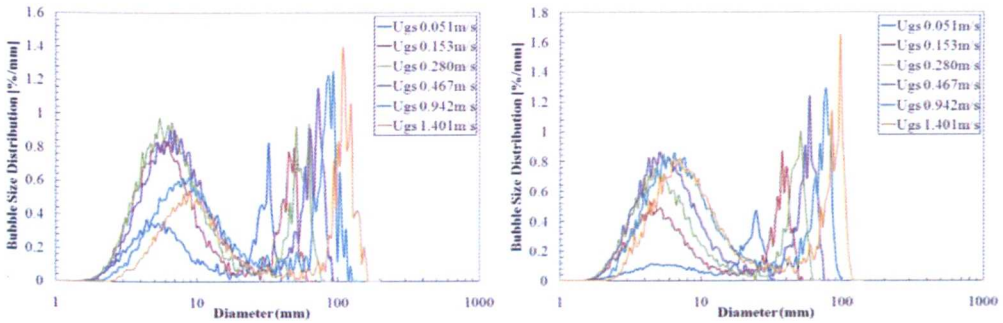


Figure 4.40- Bubble Size Distribution for CondWMS. (Left) $U_{ls}=0.2\text{m/s}$, (right) $U_{ls}=0.7\text{m/s}$

Both sensors show similar characteristics with respect to the variation in the size of bubbles. It is interesting to note how the bubble size changes as the superficial gas velocity is increased and as the flow pattern changes from bubbly to churn. It is worth noting that these graphs display the “equivalent” diameter calculated from the volume, and therefore may show diameters that exceed the diameter of pipe.

4.7.9. Further comparisons

The cross-sectionally and time averaged void fractions for all the runs collected from each sensor (6 U_{gs} per U_{ls} per wire, 8 wires=96 runs=96 voids) were plotted in Figure 4.41, and it is clear there is very good agreement between the two sensors.

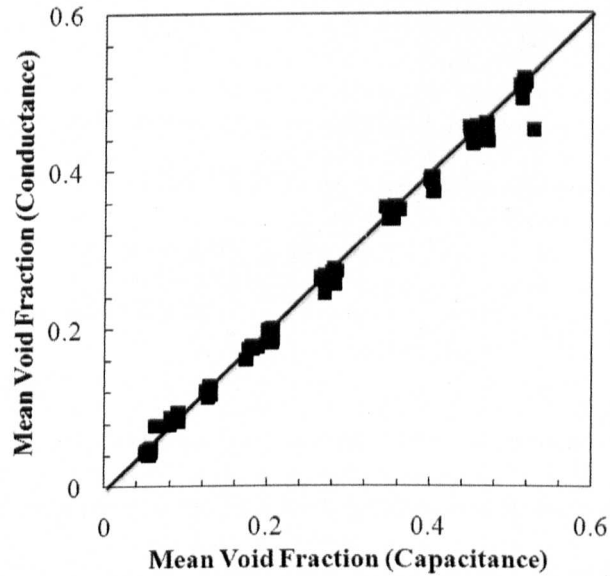


Figure 4.41-Comparison between CondWMS and CapWMS for all the runs

It is also possible to show the local voids in a 2D cross-sectional view and 3D surface plots to quantify the void fraction, and also track the void fraction and see how it changes in time for all 16 crossing points.

Measurements were taken on a 50 mm bubble column (details of apparatus in Chapter 3) with both the CapWMS and CondWMS, with water that had various levels of conductivity. This was in order to ascertain the conductivity limit for the CapWMS in the build standard that was used for this project. The electrical output in Figure 4.42 showed that the CapWMS coped with conductivity levels up to 1000 $\mu\text{S}/\text{cm}$; however, as the conductivity increased past this point, the electronics started to saturate. A more

conservative limit for the CapWMS is $100 \mu\text{S}/\text{cm}$. For higher conductivities than this, the CondWMS is recommended.

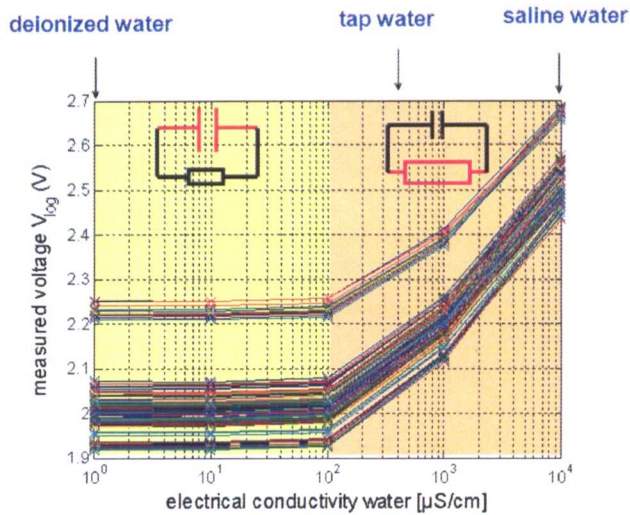


Figure 4.42-Electrical output from the CapWMS for conductivities of 1-10000 $\mu\text{S}/\text{cm}$

A further exercise was carried out in collecting data using both the CapWMS and CondWMS for different levels of conductivities for superficial gas velocities ranging from 0.008 to 0.067 m/s. Cross-sectional averaged void fraction values were extracted from both instruments, and then compared. A graph of the results is shown in Figure 4.43. Very good agreement is again demonstrated between the two instruments for varying levels of salinity and superficial gas velocities.

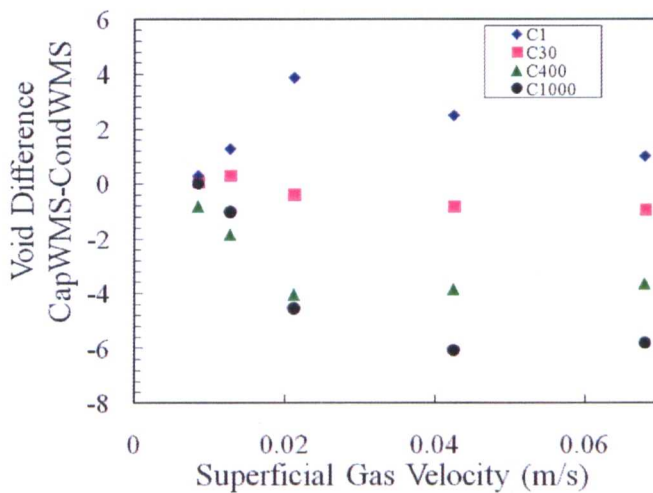


Figure 4.43-Difference in void fraction between CapWMS and CondWMS. Conductivity varied between 1-1000 $\mu\text{S}/\text{cm}$

4.8. Comparison between WMS and ECT

A number of experiments were conducted on an inclinable facility with a 67mm diameter pipe using the WMS and several other instruments, including ECT and Capacitance probes. The CondWMS was previously used for air-water experiments (Azzopardi et al, 2008a). The rig was subsequently modified and further studies were carried out at various inclinations of the pipe using CapWMS, ECT and capacitance probes with air-silicone oil as the two phase gas-liquid mixture. See Abdulkareem et al (2009, 2010, 2011) for further information on the facility and experimental details. In addition, recent experiments were carried out with the CapWMS and ECT to investigate 90 degree horizontal and vertical bends; see Abdulkadir et al (2010, 2011) for more information. Cross-sectionally averaged void fractions were extracted from these experiments for both the CapWMS and ECT for various gas and liquid superficial velocities with air-silicone oil, and were then plotted for comparison. Figure 4.44 shows ECT vs. WMS results with the pipe at 0° (Horizontal) and 90° (Vertical). Figure 4.45 shows ECT vs. WMS results with the pipe inclined at 10° and 60°.

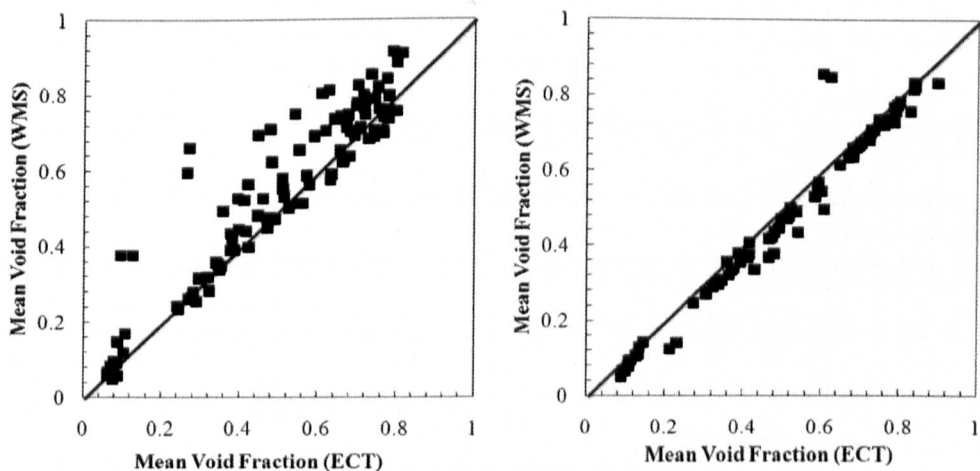


Figure 4.44-ECT vs. WMS. (Left) 0 Deg inclination and (right) 90 Deg inclination

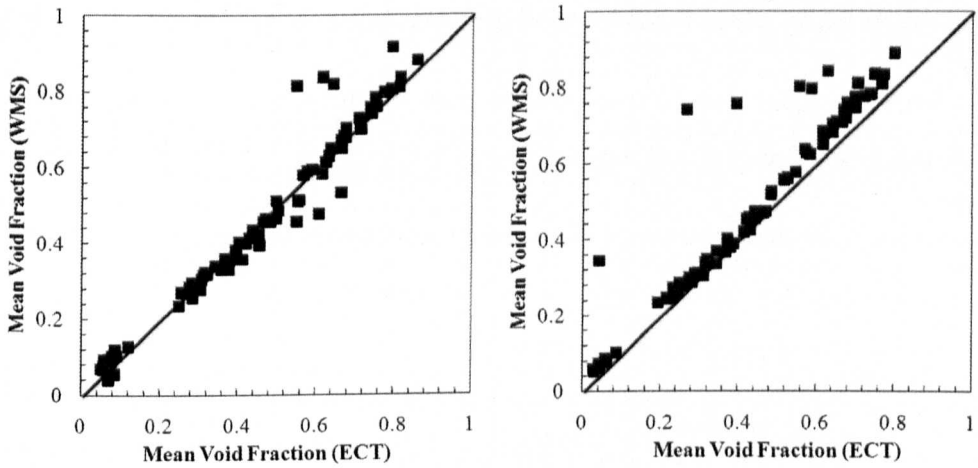


Figure 4.45-ECT vs. WMS. (Left) 10 Deg inclination and (right) 60 Deg inclination

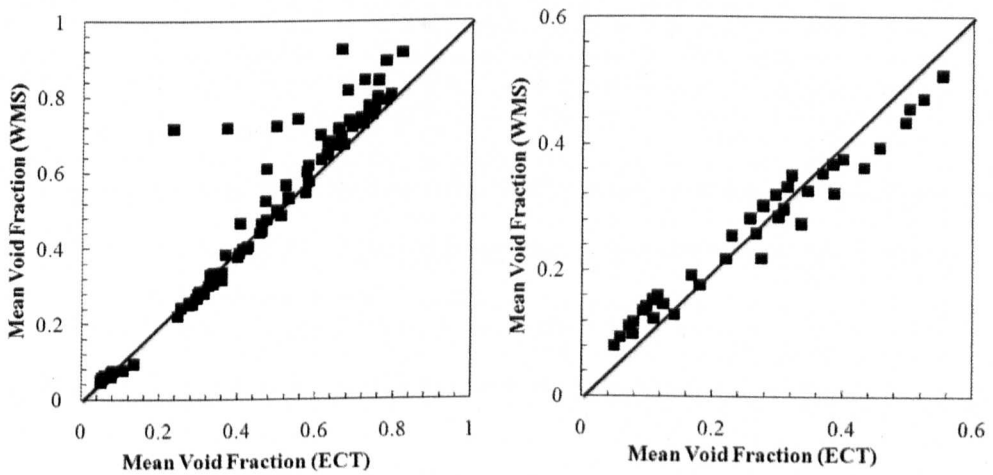


Figure 4.46-ECT vs. WMS. (Left) 80 Deg Inclination and (right) a data set at low gas superficial velocities with 90 Deg inclination

Figure 4.46 shows a plot for ECT vs. WMS with the pipe at 80° , and further data at low gas superficial velocities at 90° (vertical). It is clear from the above six plots, which contain a substantial number of runs, that there is very good agreement between the ECT and CapWMS on the 67mm diameter facility. This data was extracted for air-silicone oil as the two-phase mixture; however similar agreements can be expected between the two sensors for other non-conductive fluids.

4.9. Comparison between 50mm and 67mm pipe data

A final exercise was carried out to compare the time and space averaged voids generated on the 50mm pipe presented earlier in this chapter, with the time and space averaged voids generated on a 67mm diameter air-water vertical pipe (Azzopardi et al, 2008a).

Here, the comparison between the time and space averaged voids can be seen for both the CondWMS and CapWMS for a 50mm pipe, which is very good for liquid superficial velocities of 0.2m/s (Figure 4.47) and 0.7m/s (Figure 4.48). The gamma line voids were averaged across the whole cross-section. The gamma cross-sectional voids do not show a good agreement with the WMS as was previously demonstrated by comparing the chordal voids, and this could be again attributed to the disagreement between the two measuring techniques at the pipe wall. The results between the CapWMS and CondWMS are similar for the two pipe diameters for liquid superficial velocity of 0.2m/s; however, the lines diverge for 0.7m/s.

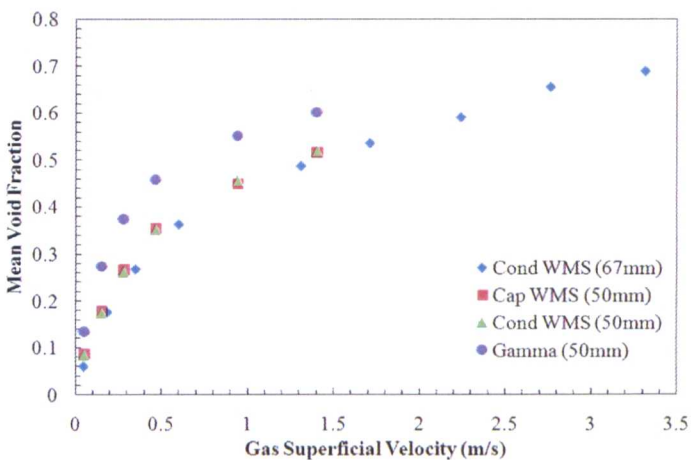


Figure 4.47-CondWMS (67mm) vs. Cap/CondWMS (50mm) vs. GD (50mm); $U_L=0.2$ m/s

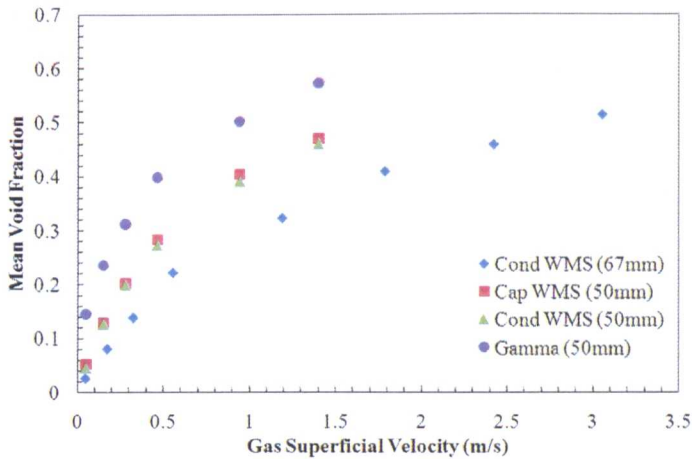


Figure 4.48- CondWMS (67mm) vs. Cap/CondWMS (50mm) vs. GD (50mm); $U_{ls}=0.7\text{m/s}$

4.10. High speed camera testing of the WMS

The wire mesh sensor is often described as an intrusive device; however, it was interesting to note the observations that were made during the filming of some high-speed images of a Taylor bubble passing through the sensor (artificially created by sudden injection of air) in a stagnant head of liquid inside a vertical pipe. These were taken through a transparent section of the pipe. The films showed that the Taylor bubble passed through the sensor before it momentarily split up, and then reformed a short distance further up the pipe. This was observed in air-silicone oil in a 67mm diameter column, and in air-water in a 127mm column (Figure 4.49) and (Figure 4.50) respectively. Two videos showing this are also provided on the DVD with this thesis and the videos provide better visualisation of the plug as it passes through the WMS. The WMS was also operated to capture an artificially created slug (plug) in the 127mm diameter bubble column with air-tap water. The processed WMS images captured the structure of the plug, and also showed bubbles in the liquid slug that follows the plug. Cross-sectional images, as well as a side view (centre), are shown in Figure 4.51. On the DVD, a video showing the variation of voids in 3D for the plug/slug is included.

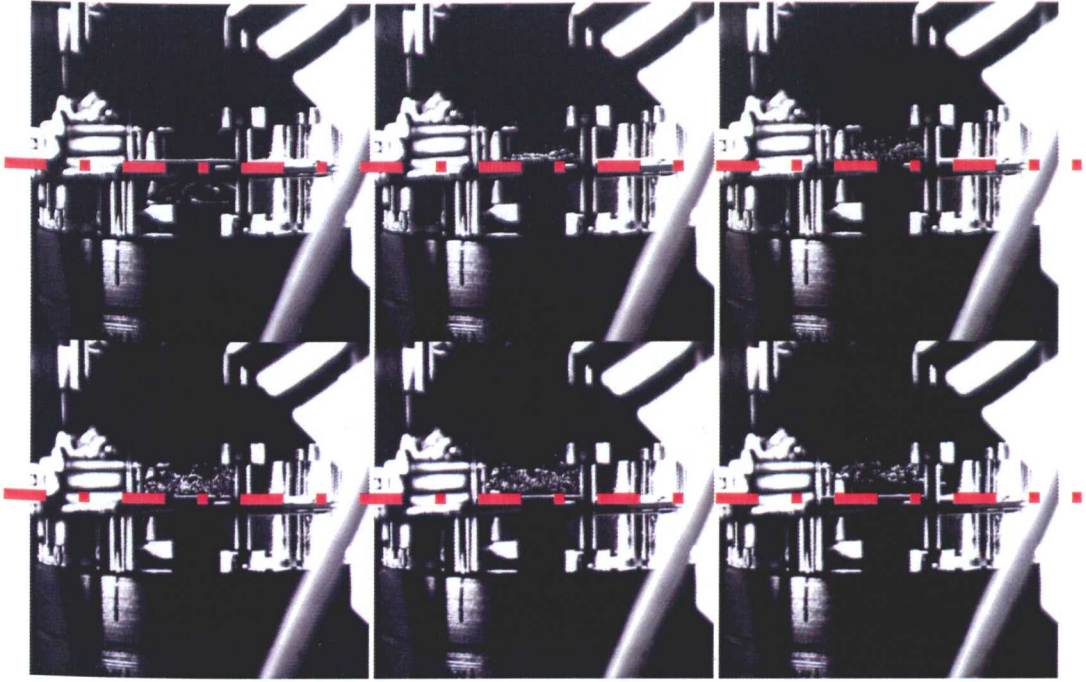


Figure 4.49- Six images showing the Taylor bubble progressively passing through a 24x24 sensor (dotted line) in silicone oil-air in a 67mm pipe.

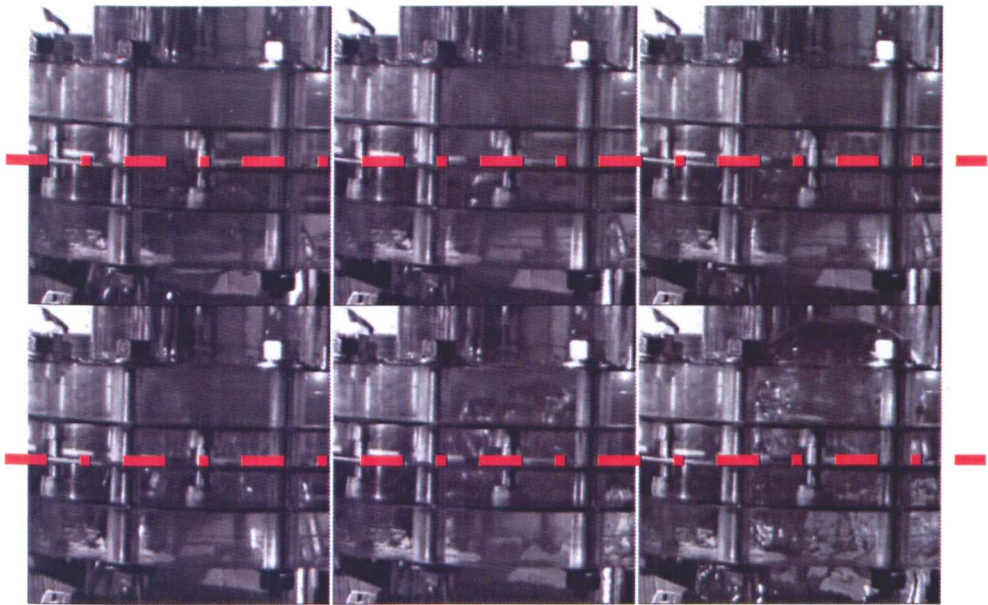


Figure 4.50- Six images showing the Taylor bubble progressively passing through a 32x32 sensor (dotted line) in air-distilled water in a 127mm diameter column.

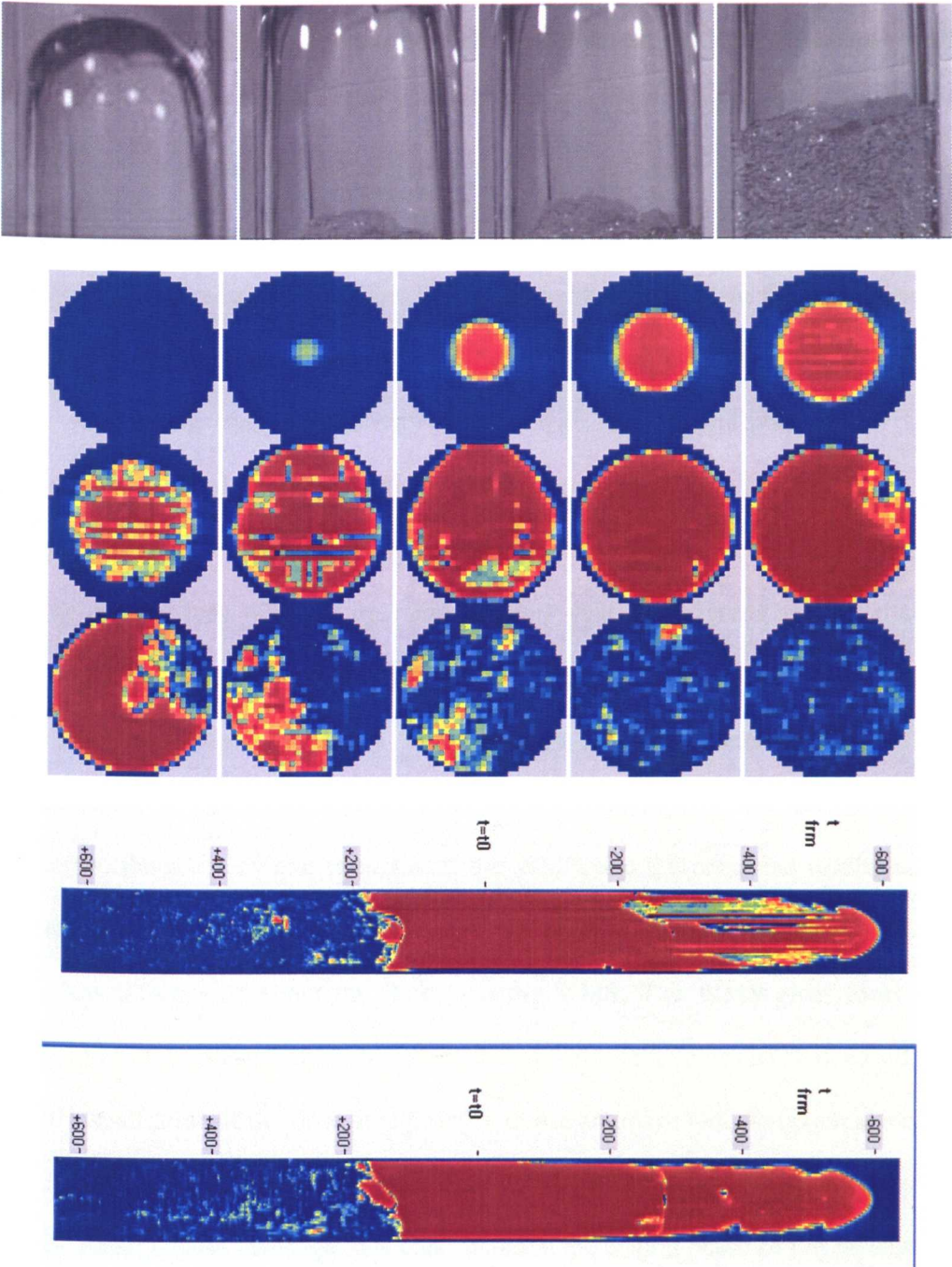


Figure 4.51-HS and WMS images of an artificially created plug. To save space, the last image is rotated 90 degrees.

4.11. Summary

It was shown that there is agreement in the void fraction measurements between the GD and both variants of the WMS to within +/-10% if the comparison is carried out in the central part of the pipe, which agrees with previous studies in this area. However, it was also shown there can be significant differences between these two measuring techniques at the edges of the pipe, due to inherent limitations in the instruments in measuring void fraction at the pipe wall. Further research could be conducted in this area. Comparing the conductivity WMS with the permittivity WMS gave exceptionally good results, which perhaps validates both sensors as they independently generated similar results, both qualitatively and quantitatively. This was despite the fact they were not operating at same time, or triggered at same time, or working in the same segment of cross-section of pipe. It was also shown that there was very good agreement between the WMS readings and ECT. Therefore, the WMS is validated and in agreement with two different instruments (ECT and GD). This work reinforced the accuracy and strengths of the WMS, and the presented results should contribute to the industrial needs of comparing the WMS with other instruments. GD gave less information about the flow than the WMS. The WMS gives local void fractions at each crossing point, from which cross-sectional voids can be deduced, and hence visualisation of the flow. It is possible to use an image reconstruction algorithm for the GD; however, the image resolution will be lower than that generated by the WMS. Finally, these investigations contributed in the testing phase of the capacitance WMS. The capacitance WMS is still a relatively new device, and it has not been subjected to the same rigorous studies as the conductance WMS. Following these tests, both the CapWMS and CondWMS were applied to two applications; which were bubble columns of different sizes and with different fluids, and also a large diameter pipe. These results will be presented in Chapters 5 and 6 respectively.

5. CHAPTER 5: BUBBLE COLUMNS

5.1. Introduction

Bubble column reactors belong to the general class of multiphase reactors without moving parts, which consists of three main categories; namely the trickle bed reactor (fixed or packed bed), the fluidised bed reactor and the bubble column reactor. The latter will be the focus of this Chapter. Deckwer (1991) presents a thorough background on the subject, and more recent publications include Zehner et al. (2000) [updated by Deen et al. (2010)], Jakobsen (2008) and Azzopardi et al. (2011).

Bubble columns are used extensively as multiphase contactors and reactors in the chemical, petrochemical, biochemical and metallurgical industries (Kantarci et al, 2005). Recent research carried out on bubble columns focussed on the following topics (Kantarci et al, 2005): gas hold-up studies, bubble characteristics, flow pattern investigations and computational fluid dynamics studies, local and average heat measurements, and mass transfer studies. Although a large number of studies exist in the literature, bubble columns are not particularly well understood due to the fact that many of the studies are often orientated on only one phase, i.e. liquid or gas hydrodynamics. Bubble column reactors have several advantages in terms of design and operation compared to other reactors. They have excellent heat and mass transfer characteristics, and they require very little maintenance and have low operating costs due to the lack of moving parts. They can be fairly compact, depending on the size of the column and measuring equipment.

Research interests in bubble columns have increased over the years (Zehner et al, 2000). This has led to many empirical correlations and theoretical studies being

published, thereby enabling mathematical modelling and simulations of bubble columns. Some of these correlations will be compared against experimental results in this work, and in addition, mathematical modelling of bubble columns will be attempted using Matlab and also compared to experimental results. The fundamentals of bubble columns will now be explained.

5.1.1. Bubble Column Design

There are several important parameters in the design of a bubble column, for example column height, diameter, and the distribution, type and size of holes. These need to be considered along with the gas and liquid densities, the liquid viscosity and the presence and concentration of chemicals (surfactants), for example salts and alcohols.

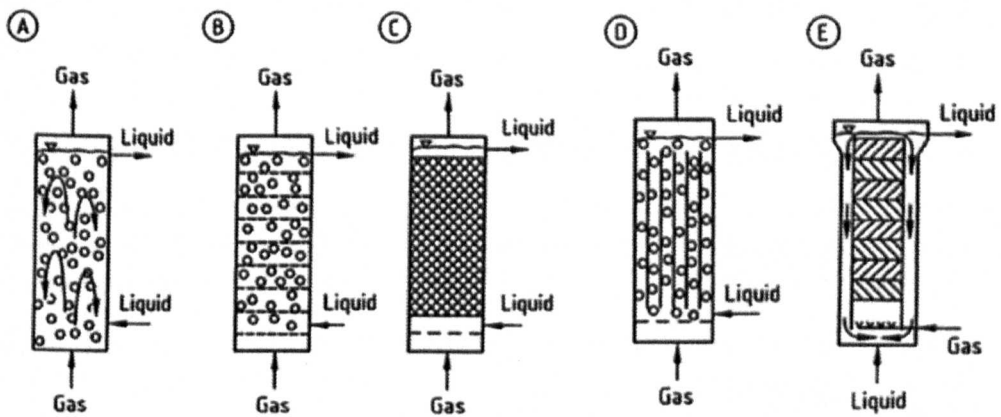


Figure 5.1-Bubble Column configurations - 5 different types

Possible designs are shown in Figure 5.1 (Zehner et al, 2000). A is a simple bubble column with gas fed in at the bottom, which is the configuration used in this research project. Other designs shown are B, which is a cascade bubble column with sieve trays, C, which is a packed bubble column, D, which is a multi-shaft bubble column, and finally E, which is a column with static mixers. The net liquid flow in the above

systems can be co-current, or counter-current to the gas flow direction. The systems can also be operated in batch mode with a stagnant pool of liquid, which is the technique that was used in this work. This is a major difference to two phase pipe flow, and Mudde et al. (2001) considered the hydrodynamic similarities between bubble column and bubbly pipe flow. There are three different mixing methods, the simplest being where the gas is sparged at the bottom as discussed above. It is also possible to have a downflow bubble column, with both gas and liquid supplied from the top. Finally, it is also possible to use a jet loop reactor.

5.1.2. Injection Methods

There are two types of spargers; static and dynamic, which are used to disperse the gas phase as bubbles into the liquid phase, and in this case, into a stagnant column of liquid. This work will mainly use static spargers, so called as they require no additional external energy for them to operate. There are four different types (Zehner et al, 2000) as shown in Figure 5.2. A is known as a dip tube and B shows a perforated plate (C-ring plate) with N holes. These holes need to be sufficiently separated to discourage coalescence of the bubbles. Perforated plates require a minimum gas flow rate to achieve a uniform distribution and prevent the liquid from flowing back into the sparger. A solution to this is to operate the gas flow first, before filling the bubble column up with water (as explained in Chapter 3). Finally, the fourth type of injector is a porous or sintered plate, which can generate very fine bubbles. However, this has the disadvantage of the pores being easily blocked.

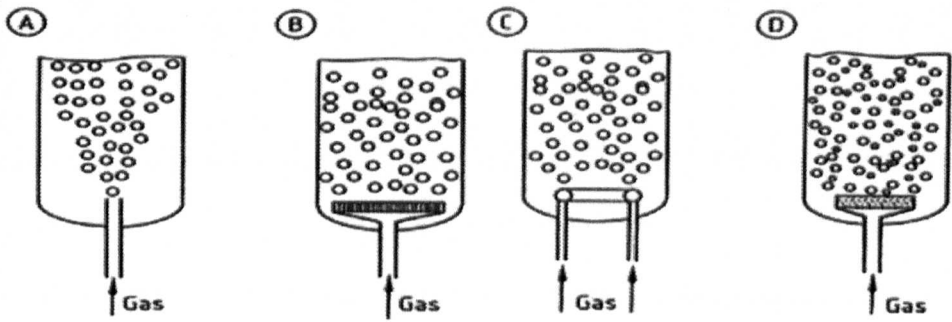


Figure 5.2-Static gas injectors; four different types.

Details of the design and size of the bubble column, and types of the spargers used, as well as operation of the bubble column, were given in Chapter 3.

5.1.3. Flow maps and patterns in bubble columns

Three basic flow patterns exist in bubble columns; homogeneous or bubble flow, churn-turbulent or heterogeneous flow and slug flow (Drahos et al, 1989). At low gas flow rates, the flow consists of small bubbles that are uniformly dispersed about the column, which is normally referred to as homogeneous flow. This differs from the use of this term in gas/liquid pipe flow, where equal gas and liquid velocities are implied and in general the liquid velocity is greater than zero. In bubble columns it implies the presence of well dispersed, small bubbles, where all the bubbles have the same diameter. At higher gas velocities, larger bubbles that are interspersed between the small ones appear. This is termed the heterogeneous flow pattern and all extra gas is believed to go into the large bubbles. In small diameter columns at high gas velocities, slug flow may also develop, with the large bubbles stabilised by the column wall. Some references refer to the presence of annular flow in bubble columns; however, this would require a closed system. From an industrial point of view, many bubble columns operate in the heterogeneous flow regime (Mudde et al 2009); therefore this regime is considered the most important.

A typical flow map for bubble columns can be seen in Figure 5.3, which is significantly different to the flow maps presented earlier in this report for pipe flow. For example, the Hewitt-Roberts map showed that dispersed bubble flow in two-phase flow only occurs at liquid velocities higher than 3 m/s, which is clearly not the case for bubble columns. There is a broad transition area due to various effects, for example due to the type of injector used. The map shows the dependence on diameter and gas velocity, but it is interesting to note that slug flow only prevails up to a diameter of 100 mm (Shah et al, 1982), which is similar to pipe flow. Is there a link, and is Churn-turbulent flow in bubble columns the same as churn flow in pipes? It is worth noting the prediction that the flow map makes for 67mm and 127mm diameter bubble columns. For a 67 mm diameter column, it is showing homogeneous/slug flow patterns. For a 127 mm diameter column, it is showing homogeneous flow at low velocities, before mainly operating in a transitional region.

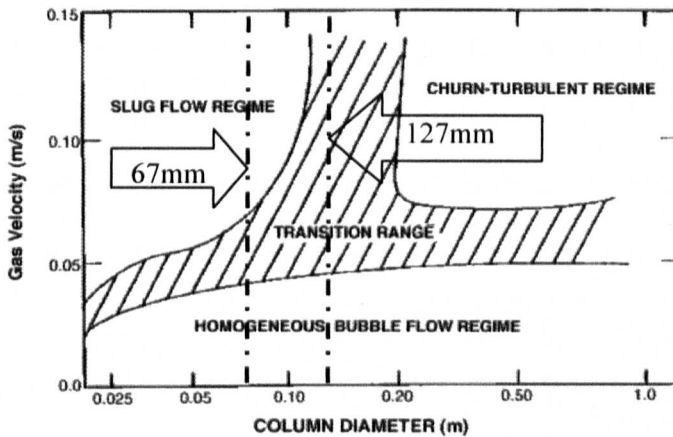


Figure 5.3-Flow map for bubble columns of various diameters. Several references use this map; Shah et al (1982), Zehner et al (2000), Kantarci et al (2005)

5.1.4. Void Fraction

A prime requirement for bubble column design is the void fraction (Azzopardi et al, 2011) and an early example of measuring void fraction was conducted by Hills (1976, 1993). The void fraction governs the phase distribution inside the column, and the gas

phase residence time. It also determines the gas-liquid interfacial area, which is crucial for mass transfer between the liquid and gas phases. It is dependent on the gas superficial velocity, and assumes a stagnant liquid in the column. It is defined in a similar way as for two-phase pipe flow i.e. the ratio of the volume of the gas phase V_g to the total volume of the dispersion ($V_g + V_l$). This essentially defines the volumetric void fraction as:

$$\varepsilon_g = \frac{V_g}{V_g + V_l} \quad (5.1)$$

The volume averaged void fraction or “level swell” can be calculated using:

$$\langle \varepsilon_g \rangle = \frac{H_{final} - H_{initial}}{H_{final}} \quad (5.2)$$

where H_{final} is the height of the liquid column after it has been injected with gas from the distributor and $H_{initial}$ is the stationary height of the liquid column before aeration, assuming the liquid volume inside the bubble column remains constant. The level swell is noted after steady state conditions are established in the experiments. In some publications, the level swell is also termed as bed expansion. The WMS measures the instantaneous local volumetric void fraction at every crossing point within the sensor, which in turn can be converted to cross-sectional and time averaged void fraction. This quantity can then be compared with the level swell measurements. This methodology was used before by Costigan et al (1997) and AlOufi et al (2010). There are numerous correlations published in the literature for the void fraction. Hikita et al. (1980) list several correlations and also propose their own. It is preferable to use physically-based or mechanistic models in a similar approach to pipe flow. For small bubbles, Wallis (1969) suggested the following equations for a zero liquid flow rate:

$$\varepsilon_g = 0.5 - \sqrt{0.25 - \frac{U_{gs}}{V_T}} \quad (5.3)$$

The drift flux model proposed by Zuber and Findlay (1965) can be applied:

$$\varepsilon_g = \frac{U_{gs}}{C_0(U_{gs} + U_{ls}) + V_T} \quad (5.4)$$

where V_T is known as the “drift velocity” or “slug velocity” in pipe flow. C_0 is the radial distribution parameter, which is given as: $\frac{\langle \varepsilon_g(r) U_g(r) \rangle}{\langle \varepsilon_g(r) \rangle \langle U_g(r) \rangle}$ with brackets

signifying the cross-sectional averaging. C_0 has been found to take values between 1 and 2.3. Hills (1976) suggested the following variation on the above equation:

$$\varepsilon_g = \frac{U_{gs}}{1.35(U_{gs} + U_{ls})^{0.93} + V_T} \quad (5.5)$$

The void fraction is also a function of the position in the bubble column, both axially and radially. Three types of radial void fraction profiles have been reported (Serizawa and Kataoka 1975, 1988), which are described as wall peak, intermediate peak and centre peak. Wall peaks show maxima close to the wall, which is actually an annular peak with a trough in the middle. This seems to be found only in columns/pipes with a diameter of ≤ 60 mm. For large diameter pipes, the norm is for the void fraction to be a maximum at the centre of the column, as determined by Hills (1974).

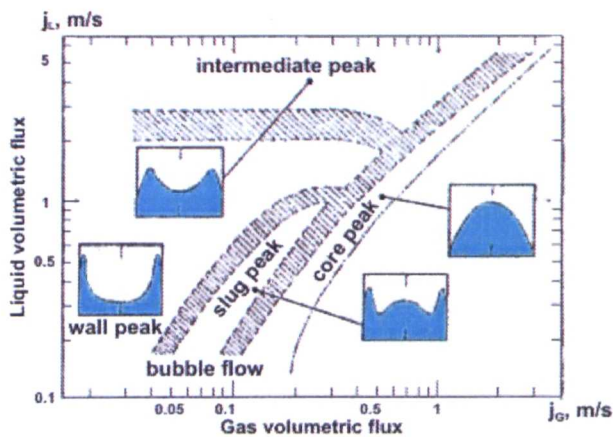


Figure 5.4-Radial void pattern map for air-water flow in vertical pipes, obtained by Serizawa and Kataoka (1988).

A radial void map can be seen in Figure 5.4, from which it can be inferred that wall peaks may occur at low superficial gas velocities and core peaks at higher values. The radial correlation for void fraction proposed by Wu et al. (2001) will be used later in this work. This correlation was also used by Abdulkadir et al. (2010c), and is expressed as:

$$\varepsilon_r = \tilde{\varepsilon}_g \left(\frac{n+2}{n} \right) \left(1 - c \left(\frac{r}{R} \right)^n \right) \quad (5.6)$$

$$n = 2.188 \times 10^3 \text{Re}_g^{-0.598} Fr_g^{0.146} Mo_l^{-0.004} \quad \text{and} \quad c = 4.32 \times 10^{-2} \text{Re}_g^{0.2492} \quad (5.7)$$

$$\text{Re}_g = \frac{DU_{gs}(\rho_l - \rho_g)}{\mu_l}, \quad Fr_g = \frac{U_{gs}^2}{gD}, \quad Mo_l = \frac{g\mu_l^4}{(\rho_l - \rho_g)\sigma_l^3} \quad (5.8)$$

where Re , Fr and Mo are Reynolds, Froude, and Morton numbers respectively.

5.1.5. Homogeneous/Heterogeneous Transition

A typical curve of void fraction against gas superficial velocity is shown in Figure 5.5. At low superficial gas velocities, the homogeneous regime (Line AB) may or may not form, depending on conditions, fluids and injectors. This is followed by a transition region (Line BCD) where the transition commences before the main peak at point C. At higher velocities, the heterogeneous flow regime (Line DE) sets in. The gradient of the line is smaller in the heterogeneous region than in the homogeneous region.

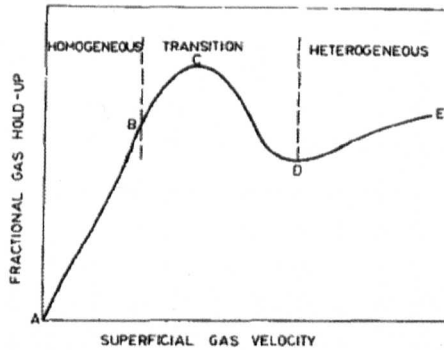


Figure 5.5- Representation of the void fraction profile and homogeneous/heterogeneous transition region (Zahradnik et al, 1997)

This transition region has been extensively studied, and further explanation can be found in Ruzicka et al. (2001). A number of equations have been proposed for the homogeneous/heterogeneous transition. Azzopardi et al. (2011) identified two correlations in particular. The first, by Wilkinson et al. (1992), gave the following equations for transition (tr) void and velocity:

$$\varepsilon_{gtr} = 0.5e^{-193\sigma^{0.11}\eta_l^{0.5}\rho_g^{-0.61}} \quad \text{and} \quad u_{tr} = 2.25 \left(\frac{\sigma\varepsilon_{gtr}}{\eta_l} \right) \left(\frac{\sigma^3 \rho_l}{g\eta_l^4} \right)^{-0.273} \left(\frac{\rho_l}{\rho_g} \right)^{0.03} \quad (5.9)$$

The second, by Reilly et al. (1994), who proposed the following:

$$\varepsilon_{gtr} = \frac{0.59.B^{1.5}\rho_g^{0.48}\sigma^{0.06}}{\rho_l^{0.5}} \quad \text{and} \quad u_{tr} = \frac{0.352\varepsilon_{gtr}(1-\varepsilon_{gtr})\sigma^{0.12}}{\rho_g^{0.04}} \quad (5.10)$$

where B is a fluid dependent parameter ($B \approx 4$ air-water).

Letzel et al. (1999) gave a corrected correlation for the void fraction in the heterogeneous region, derived by Krishna et al. (1996) and based on Reilly's correlation for transitional void fraction and velocity as follows:

$$\varepsilon_g = \varepsilon_B + (1 - \varepsilon_B)\varepsilon_{gtr} \quad \text{where} \quad \varepsilon_B = \frac{0.268(U_{gs} - u_{tr})^{0.58}}{D_t^{0.18}} \sqrt{\frac{\rho_g}{1.21}} \quad (5.11)$$

Letzel's correlation is capable of predicting the effect of system pressure on the void transition region for air-water systems, although it does not perform well for other liquids.

5.1.6. Bubble Size Distribution

Methods for analysis of the bubble size in bubble columns must distinguish between the bubble size at their creation at the injector, and the size distribution further away from the injector. Due to the break-up and coalescence of the rising bubbles, the two distributions can differ significantly. The bubble size can increase through

coalescence, which would take place further away from the distributor, and this will control the efficiency of the bubble column. The homogeneous flow regime is marked by a narrow and uniform bubble size distribution (BSD), and bubbles are distributed relatively uniformly over the cross section of the column, rising independently in the liquid phase i.e. where there is little or no bubble coalescence/break-up. At higher flow rates the void fraction increases, and hence so does the BSD; however, the distribution is not uniform (Zehner et al, 2000). With increasing gas velocity, bubbles start to combine into clusters, and plugs (slugs) may be formed. The larger bubbles in a heterogeneous flow move with higher velocities than the smaller bubbles in a homogeneous flow, and both local and gross liquid circulations may appear. Larger bubbles have a higher probability of being unstable, increasing their likelihood of breaking up. For low viscosity liquids, the maximum bubble diameter is as follows (Blaß, 1988):

$$\frac{We}{Fr} = \frac{d_{\max}^2 \cdot \Delta\rho g}{\sigma} \approx 9 \Rightarrow d_{\max} = \sqrt{\frac{9\sigma}{\Delta\rho g}} \approx \sqrt{\frac{9\sigma}{\rho_l g}} \quad (5.12)$$

However, this expression is far too simplistic. Akita and Yoshida (1974) used photographic methods to determine bubble size distributions for various systems, but Deckwer (1991) identified several weaknesses with their correlation. Akita and Yoshida (1973) also produced a correlation for the void fraction, although again this was suitable to comparable systems. By considering the drag, surface tension, buoyancy and momentum forces from first principles, it is possible to derive an equation for the bubble volume (Ramakrishnan et al, 1969). It is also possible to derive the following simplified correlation for the bubble size at the sparger level or the primary bubble size (Gaddis and Vogelpohl, 1986):

$$d = \left[\left(\frac{6d_o\sigma}{\rho_l g} \right)^{1.33} + \left(\frac{81\eta_l Q}{\pi\rho_l g} \right) + \left(\frac{135Q^2}{4\pi^2 g} \right)^{0.8} \right]^{0.25} \quad (5.13)$$

Equation 5.13 will be used below for bubble size estimation, the results of which will be compared with the bubble size generated by the WMS. However, it is worth emphasising that the WMS is not measuring the BSD at the creation point. The WMS is measuring the BSD across the full cross-section at some distance from the sparger. This can be considered as the equilibrium bubble size which is more relevant. The equilibrium bubble size is crucial in determining the interfacial area in the bubble column however it is influenced by the bubble coalescence and break-up. A general equation for the bubble size does not appear to exist due to the complications of bubble coalescence and break-up that occur in the middle of the column, particularly during heterogeneous flow, and this is why researchers are focussing on CFD for this the alternative to which is to measure the bubble size experimentally. The bubble rise velocity is estimated for the WMS by dividing the gas superficial velocity by the cross-sectional averaged void fraction. This value is then fed into the proprietary software and algorithm from HZDR to deduce the bubble size distribution. More details are given in the Appendices.

5.1.7. Bubble rise velocity and slip velocity

A number of different equations have been proposed for determining the bubble rise or terminal velocity. By comparing several correlations with experimental results (Azzopardi, 2011), it is possible to state two limits for the bubble rise velocity.

The Upper Limit (Mendelsohn (1967), Tomiyama et al. (1998)) is given by:

$$V_T = \sqrt{\left(\frac{2\sigma}{\rho_l d} + \left(\frac{\rho_l - \rho_g}{\rho_l}\right) \frac{gd}{2}\right)} \quad (5.14)$$

The Lower Limit is given by Tomiyama et al. (2002) as:

$$V_T = \frac{\sin^{-1} \sqrt{1-E^2} - E\sqrt{1-E^2}}{1-E^2} \sqrt{\left(\frac{8\sigma}{\rho_l d} E^{1.33} + \left(\frac{\rho_l - \rho_g}{\rho_l}\right) \frac{gd}{2} \frac{E^{0.67}}{1-E^2}\right)}$$

$$\text{where } E = \frac{1}{1 + 0.163 \left(\frac{gd^2(\rho_l - \rho_g)}{\sigma} \right)^{0.757}} \quad (5.15)$$

Harmathy (1960) proposed a simple equation, which is independent of the diameter:

$$V_T = 1.53 \left(\frac{g(\rho_l - \rho_g)\sigma}{\rho_l^2} \right)^{0.25} \quad (5.16)$$

According to Lapidus et al. (1957) the slip (relative) velocity U_s can be defined as:

$$U_s = \frac{U_{ls}}{(1 - \varepsilon_g)} \pm \frac{U_{gs}}{\varepsilon_g} = V_T f(\varepsilon_g) \quad (5.17)$$

This is positive for counter-current flow, and negative for co-current flow. Therefore, the slip velocity is a function of the bubble rise velocity and void fraction. For the homogeneous region it is possible to use the Richardson and Zaki function (1954), which considers the hindered rising of bubbles. The velocity of a bubble is lowered if it is surrounded by other bubbles, which is analogous to the hindered settling that occurs in particle sedimentation. Zaki and Richardson proposed the following correlation:

$$U_s = V_T (1 - \varepsilon_g)^{n-1} \quad (5.18)$$

So, if equation (5.17) and equation (5.18) are combined:

$$\frac{U_{ls}}{(1 - \varepsilon_g)} + \frac{U_{gs}}{\varepsilon_g} = V_T (1 - \varepsilon_g)^{n-1} \quad (5.19)$$

By assuming U_{ls} is zero in a stagnant level of liquid and rearranging equation (5.19), it is possible to calculate the void fraction using iteration, where n is dependent on the Reynolds no (Re). Therefore:

$$\varepsilon_g (1 - \varepsilon_g)^{n-1} - \frac{U_{gs}}{V_T} = 0 \quad (5.20)$$

5.1.8. Published experimental work

To improve the understanding of the important parameters in column behaviour, it is helpful to examine their effect on the relationships between void fraction, the fraction of the two-phase mixture that is gas and the flow rate of the gas as gas superficial velocity (Azzopardi et al, 2011).

From experiments on columns of 150mm, 225mm and 400mm diameters, Groen (2004) showed that there is little effect of the diameter on the overall void fraction/gas superficial velocity relationship. The effect of the column height was studied by Růžicka et al. (2003), who showed that the void fraction decreased as the height of the two-phase mixture increased. In contrast, in the heterogeneous pattern, little difference is seen between the data of Letzel et al. (1999) (bubble column with two hundred 0.5mm holes, 1.2m height) and that of Cheng et al. (1998) (6mm holes, 10m high column with measurements made at the 5 m level). Anderson and Quinn (1970) measured the void fraction in a bubble column with various types of water (Figure 5.6 [left]). Tap water has more impurities than deionised/distilled water, which suppress bubble coalescence and hence increase the void fraction.

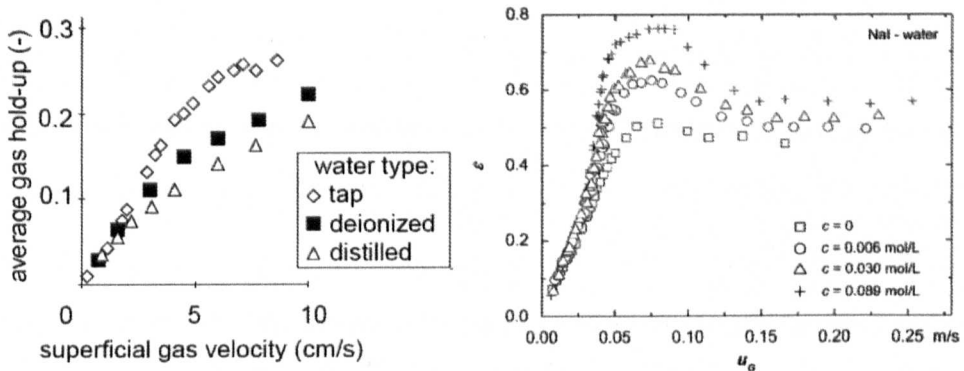


Figure 5.6-Experimental data of void fraction vs. U_{gs} for different types of water. Source(s): Left - Anderson Quinn (1970), right - Ribeiro et al. (2007)

A similar experiment was conducted by Ribeiro et al. (2007) who varied the concentration of salt in the water (Figure 5.6 [right]) and subsequently also reported an

increase in void fraction as the salt concentration is increased. Similar homogeneous injectors to the one used in this work have been investigated in the past, for example Drahos et al. (1992) and Zahradnik et al. (1997). More recent work on a similar sized bubble column and injector was reported by Hartevelde (2005) and Mudde et al. (2009). Figure 5.7 shows a comparison of void fractions obtained with the needle sparger by Hartevelde (2005) against data for a porous plate sparger (Groen, 2004) and perforated plate spargers with two pore sizes (Drahos et al, 1992). It is interesting to note that Drahos et al. (1992) found that injectors with 0.5 mm holes produced homogeneous flow, whereas injectors with 1.6 mm holes only produced a heterogeneous flow pattern.

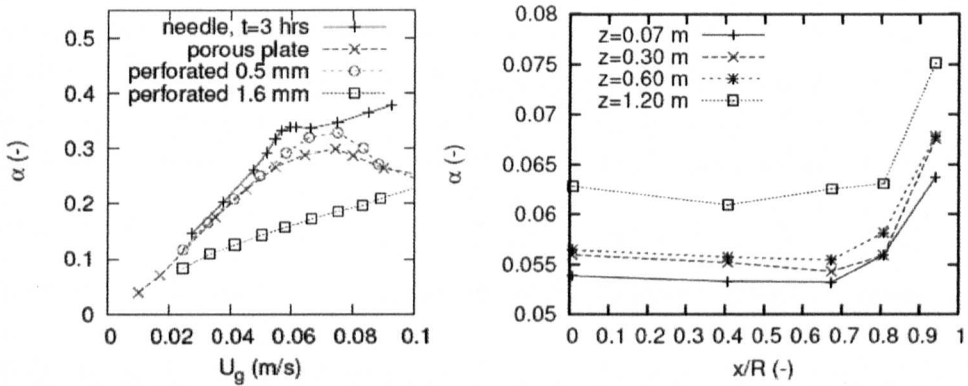


Figure 5.7-Left: Void for various injectors. Right: Radial void (Hartevelde 2005)

Figure 5.7 [right] also shows interesting wall peaks from readings taken at various heights inside the bubble column (Hartevelde, 2005) and (Mudde et al., 2009). In this case, these appear to occur at certain values of void fraction and gas superficial velocities. In the example shown here, wall peaks occurred at a void fraction of 6.1% and a U_{gs} of 0.015m/s. Other studies, for example Wang et al. (1987), found this wall peaking occurring at higher liquid flows. Hills (1974) conducted experiments using a distributor with 61 holes of 0.4 mm in diameter. His work showed the bubble frequency and radial profiles to be constant at low gas superficial velocities i.e. a homogeneous regime with a constant value in the centre of the column and peaks in

void fraction only near the pipe wall. A parabolic curve is formed at higher gas velocities i.e. a heterogeneous regime, as a consequence of the bubbles being concentrated and rising more in the centre of the pipe. There is a tendency for the radial void fraction to increase as the superficial gas velocity is increased.

5.2. Experimental Techniques applied to bubble columns

Comprehensive papers on the measuring techniques used in bubble columns have been published (Boyer et al, 2002) and (Mudde, 2010), and from these it is clear there are several instruments that may be used to study bubble columns, each with its own advantages and disadvantages. Al-Oufi et al. (2010) used point probes to investigate air-water in a column of 0.1 metres in diameter and height of 2.3 metres. Examples of tomographic investigations on bubble columns include Jin et al. (2007) who used an ERT system for air-water on a column of diameter 0.16 metres and height of 2.5 metres and Al Masry et al. (2010), who used an ECT system to investigate air-kerosene in a 150mm diameter bubble column of height 5 metres. Schmitz et al. (2000) used a resistance wire mesh sensor with air-water on a column of diameter 315mm and height of 2.1 metres, although the design of the sensor was different to the one used in this work. Zaruba et al. (2005) and Krepper et al. (2007) carried out air-water investigations on a rectangular bubble column using a dual layer wire mesh sensor system. The wire mesh sensor has been used to investigate trickle bed reactors (Llamas et al., 2008) and (Matusiak et al., 2010) and stirred vessels (Prasser, 2008). However, the WMS has not been extensively used to date on bubble columns (Mudde, 2010). Therefore, this Chapter will assess the suitability and limitations of this instrument for use on bubble columns, and will present some important results to aid in this evaluation. Bubble size can be determined from photography at low bubble concentrations, point probes (usually two probes in line to measure transit times and

contact times), multi-point probes and WMS tomography. For example, Lage et al. (1999) and Harteveld (2005) measured bubble size using photographic techniques. The mean void fraction can be measured using pressure drop techniques, and it can also be obtained from point probes (electrical or optical), γ or X-ray Computed Tomography, ERT/ECT or WMS Tomography (Azzopardi et al, 2011).

5.3. Experimental details for this work

The experimental facilities and procedures in this study were explained in Chapter 3. Preliminary experiments were carried out by measuring the level swell, which showed distinct trends but only gave one parameter, which was the void fraction. To get more detailed information, the WMS was applied to the bubble columns, although care had to be taken in applying the correct WMS electronics. Obviously for low conductivity liquids, the CapWMS is suitable, and for higher conductivity liquids, the CondWMS is more appropriate.

Therefore, an extensive amount of data for several bubble columns was collected with both the CondWMS and CapWMS for a variety of different fluids and injectors. The focus of analysis will be on the experiments conducted on a bubble column with a diameter of 127mm and height of 2 metres. This had a 32x32 WMS installed within it, at a height of 1 metre away from the static gas injection at the bottom. Emphasis was placed on ensuring the bubble column was always clean, to minimise any contamination that would affect the accuracy. The temperature and electrical conductivity were monitored throughout the experiments using a calibrated conductivity meter, model number WTW LF 340. The level swell was noted visually throughout these experiments and was taken concurrently with every WMS measurement. Any foaming was disregarded. Both variants of the WMS were

operated for between 30 and 60 seconds at a sampling frequency of 1000 cross-sections per second. The effect of changing the fluid, the injector and the diameter was directly observable. An exercise was also attempted to assess the impact of raising the sampling frequency from 1000Hz to 2500Hz on the results. A high speed camera was also used to record images for both types of injectors, and sample videos are provided in the DVD with this thesis. Results were regularly relayed back to the sensor designers at HZDR in Germany and as a result improvements were carried out on the CapWMS, both in terms of software and hardware. Since conducting these experiments, a mark II version of the CapWMS has been produced by HZDR. Five novel WMS data sets will be presented in this chapter and a summary of the whole experimental campaign can be seen in Figure 5.8. The gas superficial velocities for the 127mm bubble column were 0.004-0.047m/s for the spider and 0.02-0.145m/s for the homogeneous injector.

No	Fluid System	Column Diameter	Injector	WMS System	WMS Suitable?	U _{gs} (m/s)	Data Presented
1	Air-Water (Distilled)	127mm	Spider (2mm holes)	CapWMS	Yes	0.004-0.047	WMS+Lswell
2	Air-Water (Tap)	127mm	Spider (2mm holes)	CapWMS	No	0.004-0.047	Lswell Only
3	Air-Water (Distilled)	127mm	Homogeneous	CapWMS	No	0.02-0.145	Lswell Only
4	Air-Water (Deionised)	127mm	Homogeneous	CapWMS	No	0.02-0.145	Lswell Only
5	Air-Water (Tap)	127mm	Homogeneous	CapWMS	No	0.02-0.145	Lswell Only
6	Air-Silicone Oil	127mm	Homogeneous	CapWMS	Yes	0.02-0.145	WMS+Lswell
7	Air-Distilled (0.5% Butanol)	127mm	Homogeneous	CapWMS	No	0.02-0.06	Lswell Only
8	Air-Water (Deionised)	127mm	Homogeneous	CondWMS	No	0.02-0.145	Lswell Only
9	Air-Water (Tap)	127mm	Homogeneous	CondWMS	Yes	0.02-0.145	WMS+Lswell
10	Air-Silicone Oil	67mm	3mm holes	CapWMS	Yes	0.047-4.7	WMS only
11	Air-Water (Distilled)	50mm	Porous Media	CapWMS	Yes	0.008-0.068	No
12	Air-Silicone Oil	50mm	Porous Media	CapWMS	Yes	0.008-0.068	No
13	Air-Salinated Water	50mm	Porous Media	Cap/CondWMS	Yes	0.008-0.068	WMS only

Figure 5.8-Table summarising the experiments using the CapWMS and CondWMS with various bubble columns for different liquids and injectors.

The first set of results presented in this Chapter will be for the CapWMS with distilled water and the spider injector, which in essence generated heterogeneous flow. A new design of distributor with 121 holes of 0.5mm diameter, uniformly distributed to encourage homogeneous flow, was designed and produced by the Institute of Chemical Process Fundamentals (Czech Republic). The second set of results will be for the CapWMS with air-silicone oil on the 127mm diameter bubble column with the

homogeneous injector. It is interesting to note that there are many papers published on bubble columns with air-water, but there is a dearth of data for low surface tension liquids such as silicone oil. Data was also previously collected on a 67mm diameter rig, and further details can be found in Abdulkareem et al. (2009). This was carried out with air-silicone oil at various gas and superficial liquid velocities. This had a height of 6 metres and a sparger with 100 holes of 3mm in diameter. The 67mm diameter pipe therefore had a bigger aspect ratio than that for the 127mm diameter bubble column. One set of results was obtained with the liquid superficial velocity maintained at zero, but with gas superficial velocities of 0.047-4.7m/s. 28 runs in total were carried out, which will be the third data set presented in this chapter. Comparisons will be shown between the 67mm diameter column and 127mm diameter column with air-silicone oil; assuming the effects from the different injectors are negligible. The CondWMS was also applied to the 127mm bubble column with the homogeneous injector and various types of water. Therefore a fourth set of results for air-tap water will be presented for the CondWMS.

Two further trials were also carried out. The first was conducted on a 50mm bubble column with a 16x16 WMS, with both the CondWMS and CapWMS, and with water of varying levels of salinity (conductivity) with a porous injector. This will form the basis of the fifth data set presented towards the end of this chapter. The results will show how the salt concentration affected the void fraction as the superficial gas velocity was changed. This is in addition to the comparison between the CapWMS and CondWMS with this data set presented in the previous chapter. The second trial was conducted with the CapWMS with distilled water and 0.5% Butanol. Due to the large expansion in the liquid after aeration, this trial was limited and only the level swell was recorded and will be presented in this Chapter.

Therefore, an overall picture is conveyed regarding the level swell on the 127mm diameter bubble column, followed by the five data sets from the WMS in order of increasing level of complexity of the time series, PDF, dominant frequencies, cross-sectional averaged voids, radial voids, bubble size distribution and visual output. This last parameter incorporates 2D contour maps of the local voids and 2D/3D visualisation of the flow. The quantitative data will then be compared with some of the correlations presented earlier in this chapter. The experimental matrices for the five data sets can be found in the appendix. Due to the extensive quantity of data collected, a large amount of it has been located in the appendix.

5.4. Results

5.4.1. Level Swell

The void fraction can be calculated from the level swell measurements as explained earlier in this chapter. Figure 5.9 [left] shows the variation of the level swell with the superficial gas velocity using the spider injector for air-distilled water and air-tap water. It is interesting to note that the level swell for tap water was slightly higher, but that changing the liquid had a minimal effect on the void fraction. Figure 5.9 [right] shows the void fraction against superficial gas velocity for a variety of liquids with the homogeneous injector. Here, the difference is much more pronounced, and both homogeneous and heterogeneous flow can be observed.

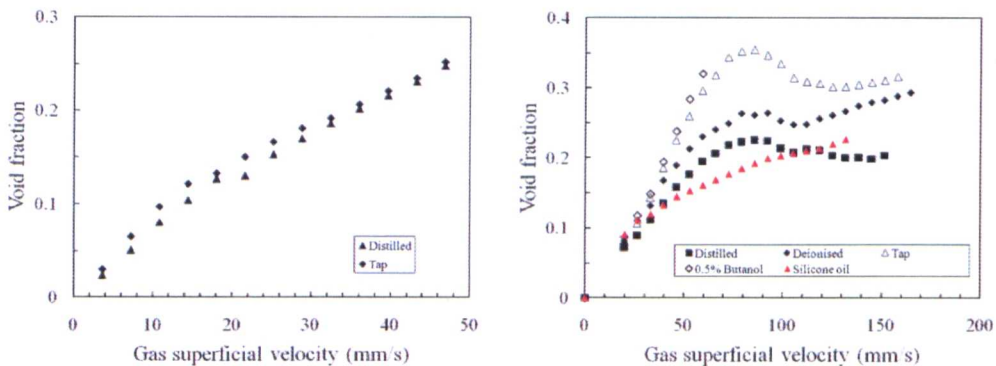


Figure 5.9-Level swell on the 127mm diameter column. (Left): Distilled/tap water with Spider injector. (Right): Various liquids with homogeneous injector.

5.4.2. Time Series and PDF

Figure 5.10 shows a selection of time series and PDF plots for the spider injector with distilled water, on the 127mm diameter bubble column. For the same column, Figures 5.11 and 5.12 show a selection of time series and PDF plots for tap water and silicone oil respectively, with the homogeneous injector. Figure 5.13 shows the time series and PDF data for a 67mm column with air-silicone oil. It is interesting to note how the PDF changes as the superficial gas velocity is increased. Initially, a single peak is observed before it develops a long tail similar to churn flow in a pipe.

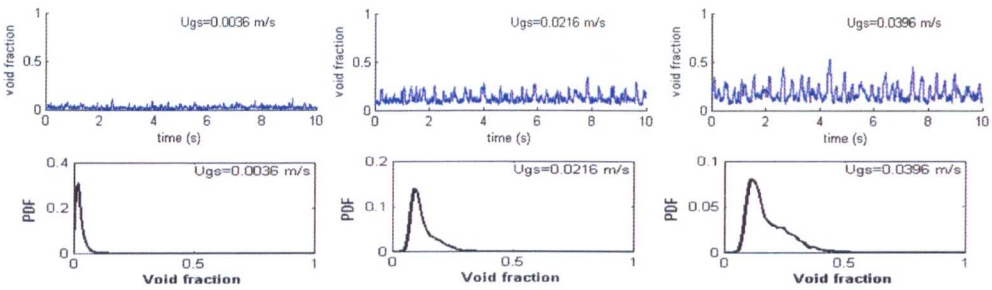


Figure 5.10-Low/Medium/High void fraction; air-distilled water with spider (127mm)

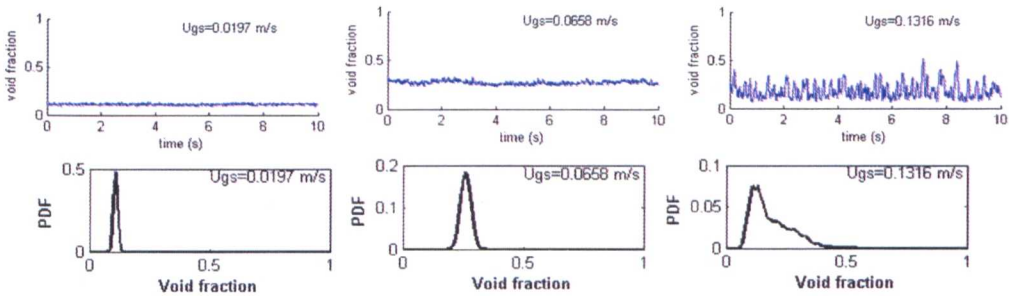


Figure 5.11- Low/Medium/High void fraction; air-tap water with hom. injector (127mm)

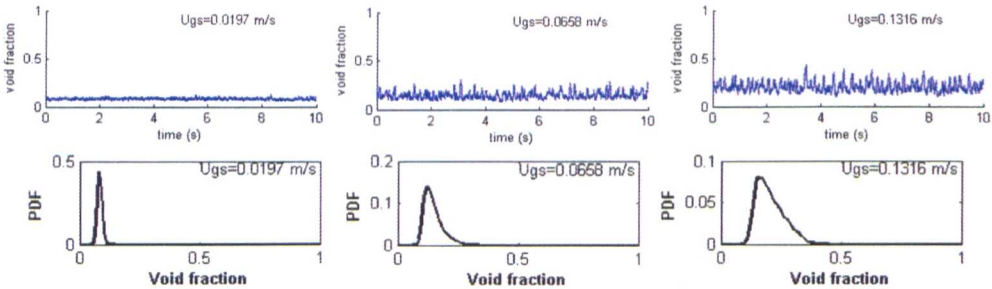


Figure 5.12-Low/Medium/High void fraction; air-silicone oil, hom. injector (127mm)

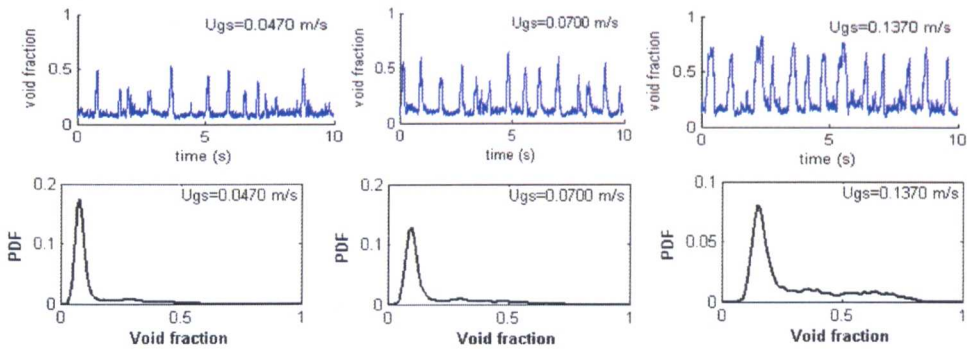


Figure 5.13 -Low/Medium/High void fraction; air-silicone oil, 3mm holes (67mm)

The absence of the second peak is particularly striking. For the 67mm bubble column, a second peak starts to develop around a value of gas superficial velocity of 0.137m/s. For higher superficial velocities, the second peak becomes more prominent, signifying slug flow (more profiles can be seen in the appendix). It seems that no slugs develop in the 127mm bubble column, and the flow patterns predicted by the flow map shown earlier in this chapter are confirmed here. In addition, churn-turbulent flow in bubble columns occurs at a lower void fraction than in two-phase pipe flow, however the PDF profile of a peak with a long tail is maintained. It is possible to extract the maximum/minimum from the time series for each run (Figure 5.14).

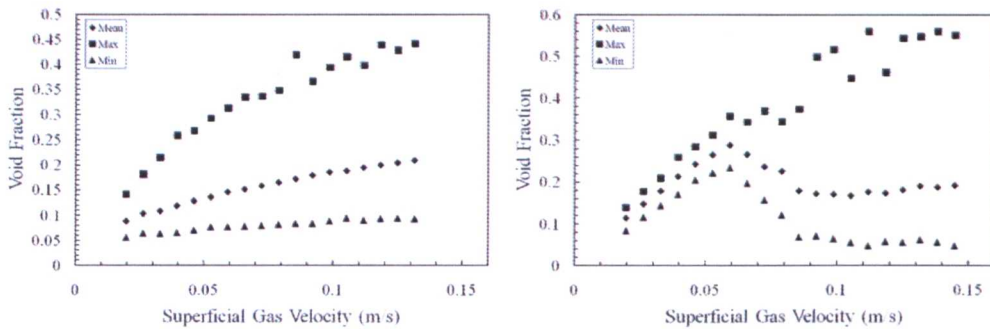


Figure 5.14-Maximum/Mean/Minimum void fraction for (left) Air-Silicone Oil and (right) Air-Tap water; both for homogeneous injector and a 127mm bubble column

Water has a higher surface tension than silicone oil and air-water flow generated higher mean void fractions than air-silicone oil.

5.4.3. Frequencies (PSD)

The dominant frequencies from the silicone oil time series data were extracted through spectral analysis using two different methodologies. The first data set was obtained using Matlab after defining a PSD function within the code. The second and third data sets were obtained using the visual basic program (VBA) developed by Kaji (2008), which was coded with and without a cosine window function. The windowing facility helps to smooth out the data particularly at higher frequencies. More details of this methodology can be found in Van Maanen (1999). The results can be seen in Figure 5.15, where each data point was obtained with 10,000 void data points. Matlab was much quicker in obtaining this data than VBA, as the data collected by the wire mesh sensor was in a binary format, which Matlab can readily solve. However, the PSD plots in Matlab were not as smooth as in VBA. Overall there is a reasonable agreement between the two approaches.

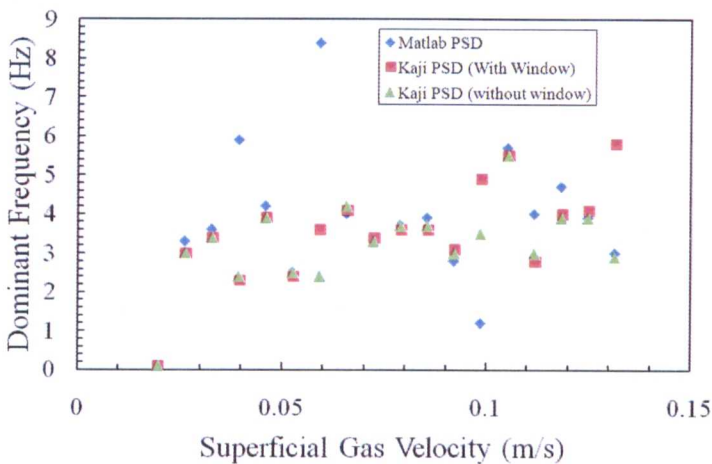


Figure 5.15-Frequencies for air-silicone oil (extracted from the time series). Data obtained from the 127mm diameter bubble column with homogeneous sparger.

5.4.4. Cross-sectional averaged void

The cross sectional and time averaged void fraction can be extracted from the time series presented above. This can then be compared with the level swell measurements.

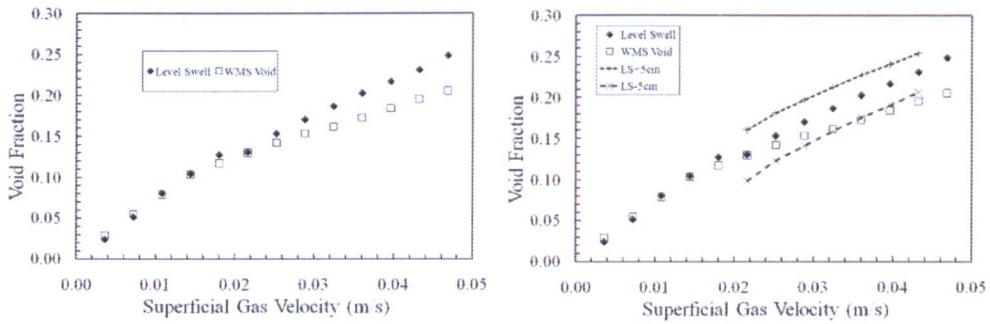


Figure 5.16-(Left) Air-Distilled Water level swell vs. CapWMS void fraction with the spider injector on 127mm column. (Right) +/-10% added to level swell values

Figure 5.16 shows the comparison between the level swell and CapWMS void fraction for air-distilled water. The spider injector is displaying heterogeneous flow. The level swell was difficult to measure in air-water due to significant fluctuations at higher gas velocities, and this therefore had to be estimated visually after several readings. This may explain the increasing difference between the WMS and level swell readings as the gas velocity is increased. The level swell fluctuation at the higher velocities was approximately 10 cm, or +/- 5cm, which equates to approximately 10% if the column is filled with liquid to a height of 1 metre. Therefore, the minimum and maximum values of void fraction can be estimated as shown in Figure 5.16 [right], with the dotted lines showing the error range for the level swell measurements, which covers most of the WMS values. Figure 5.17 [left] shows level swell vs. WMS void fraction for air-silicone oil using the homogeneous injector, measured with the CapWMS. A good agreement can be seen between the two sets of results.

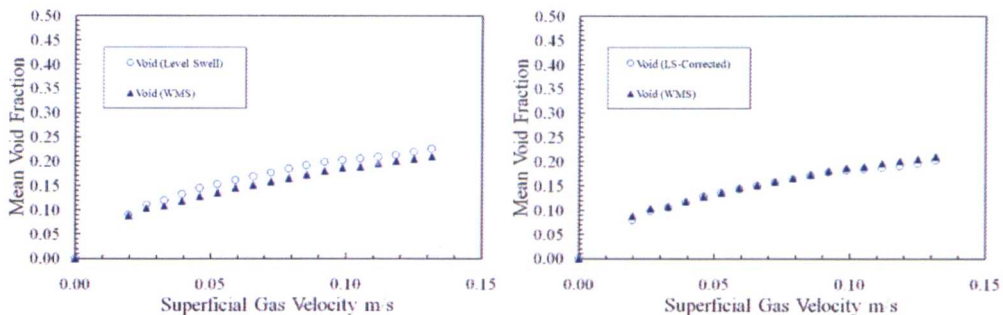


Figure 5.17-Hom. Injector on 127mm column: (Left) Air-silicone oil vs. CapWMS void. (Right) Air-silicone oil corrected level swell vs. CapWMS void.

It is possible to “correct” the level swell by calculating the swell where the WMS is located using differences in pressure. It can be seen in Figure 5.17 [right] that a slight improvement is obtained by performing this correction. It is interesting to note that despite utilising the homogeneous injector, the profile is flat with no point of inflection to signify transition from homogeneous to heterogeneous flow. Ruzicka et al. (2003) found that the viscosity had an adverse effect on whether homogeneous flow was developed or not with the void fraction in general decreasing with increasing viscosity, which could explain what is being observed here, as silicone oil has a viscosity that is five times higher than water. Finally, the level swell is compared with the cross-sectional void fraction for air-tap water using the CondWMS measurements of void fraction and the homogeneous injector. This is presented in Figure 5.18 [left].

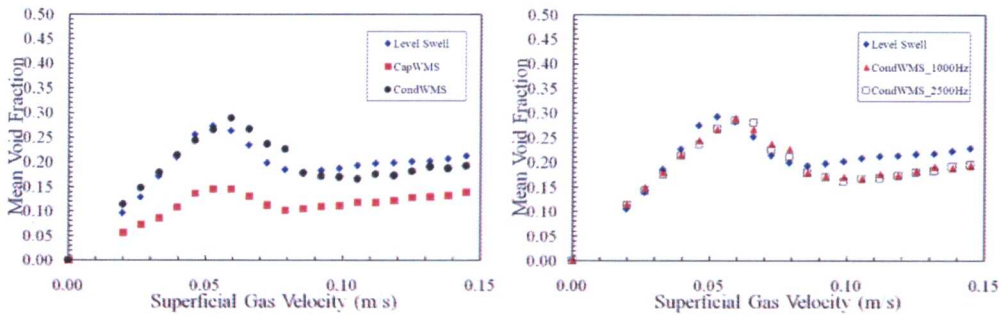


Figure 5.18- Homogeneous injector on 127mm diameter column:
 (Left) Air-tap water with CapWMS vs. CondWMS void fraction.
 (Right) Air-tap water level swell vs. CondWMS (1000/2500Hz).

It can be seen that the profile is initially homogeneous before changing to heterogeneous flow. This is clearly different from the results in Figure 5.17 for air-oil. In Figure 5.18 [left] it can be seen the CapWMS did not perform well with tap water in comparison with the CondWMS, although it registered a similar trend. Finally, an exercise was carried out to compare the void fraction against level swell for the WMS with two different temporal resolutions of 1000Hz and 2500 Hz (Figure 5.18 [right]). Increasing the acquisition rate of the sensor in this case did not have an impact on the results.

5.4.5. Radial profiles of void fraction

The time averaged radial profiles of void fraction can be extracted from the WMS data. These can be thought of as annuli; measuring the void fraction all around the pipe, starting in the centre and working outwards to the circumference. Figure 5.19 shows the radial profiles for air-distilled water measured using the CapWMS for superficial gas velocities from 0.0036 to 0.0432 m/s. There is a general trend of increasing radial void fraction with increasing superficial gas velocity. From this it can be inferred that this is a centre peak with heterogeneous flow.

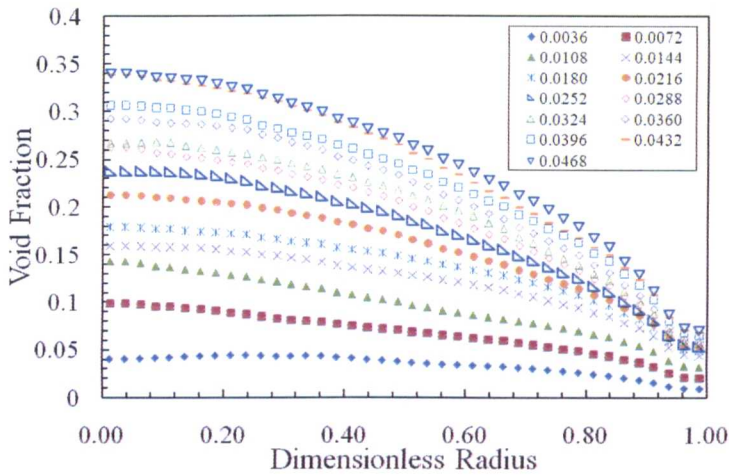


Figure 5.19-Radial Profiles for air-distilled water on 127mm diameter column, with spider injector and CapWMS.

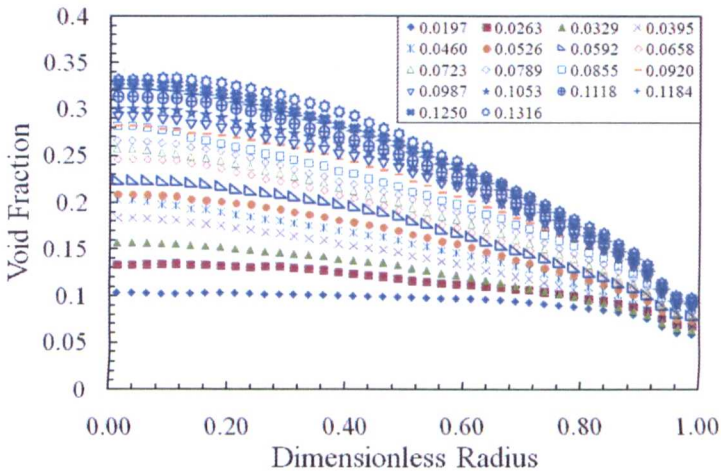


Figure 5.20- Radial Profiles air-silicone oil on 127mm diameter column, with homogeneous injector and the CapWMS.

The radial void fractions were also plotted for air-silicone oil in Figure 5.20, using the homogeneous injector, and for superficial velocities ranging from 0.012 to 0.132 m/s. The general trend is for increasing radial void fractions with increasing superficial gas velocities i.e. centre peak, as again the flow was mainly heterogeneous. Radial profiles were plotted for air-tap water using the homogeneous sparger (Figure 5.21) and superficial gas velocities of 0.012 to 0.145 m/s. In this case, the data is much more complex. Unlike the previous two cases, the profiles are not self similar, meaning they cannot just be scaled with maximum void fractions. At low gas velocities, the radial profiles are almost constant with small wall peaks, and it is only at higher velocities that the radial profiles start to take the characteristic parabolic shape. This could be explained by the flow pattern being homogeneous at lower gas flow rates and heterogeneous at the higher gas flow rates. The difference between Figure 5.19 and Figure 5.21 is clearly due to the change of injector.

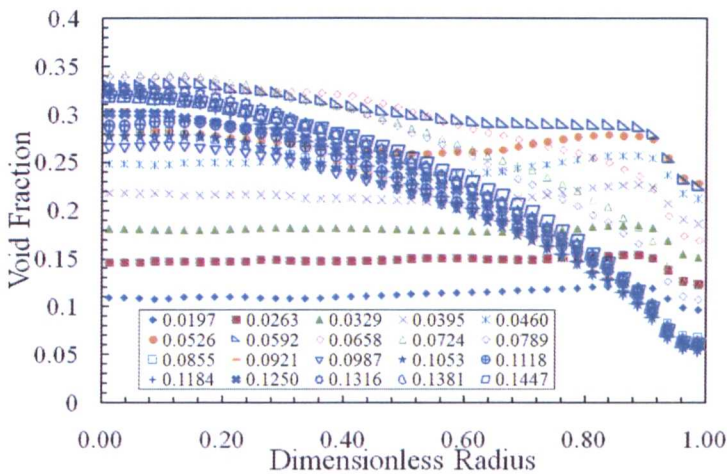


Figure 5.21- Radial Profiles for air-tap water on 127mm diameter column, with a homogeneous injector and the CondWMS.

5.4.6. Bubble size distribution

Using HZDR's proprietary software, it is possible to generate the bubble size distribution (BSD) from the WMS data, which can be plotted for varying gas velocities. A particular strength of the WMS over other sensors in this area is that it

measures the BSD across the whole cross-section as opposed to taking point measurements. The WMS software can generate both area and volume based BSD. The distribution of volumetric void fractions per bubble diameter classification, written as $\Delta\varepsilon_g / \Delta D_d$ and expressed as %/mm, will be used throughout this thesis. Integrating the area under the curve generates the time and cross-sectional averaged void fraction.

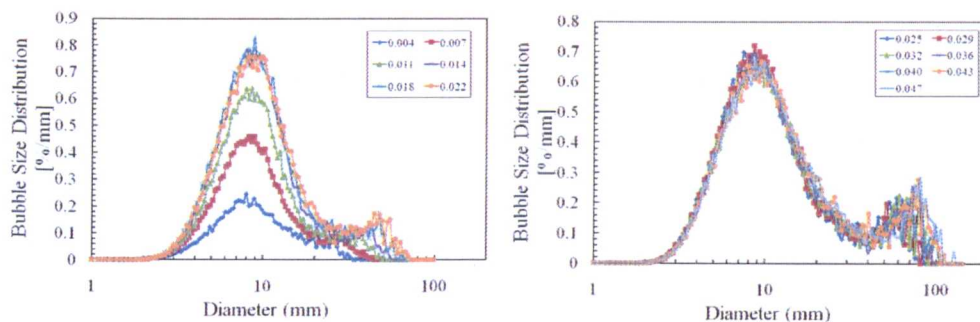


Figure 5.22 - BSD for air-distilled water on 127mm diameter column, with a spider injector and the CapWMS

Figure 5.22 shows the BSD for air-distilled water using the spider injector, for gas superficial velocities from 0.004 to 0.04m/s. Initially there is a single peak, which slowly decreases in height as the velocity is increased. The main peak then maintains its shape, and a second peak slowly develops at larger diameters.

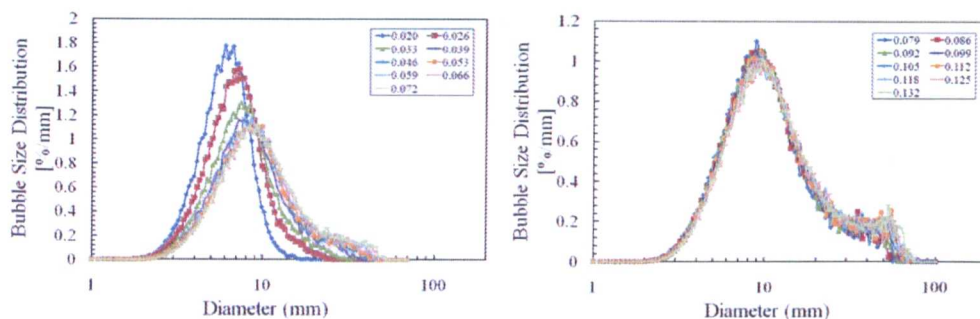


Figure 5.23- BSD for air-silicone oil on 127mm diameter column, with a homogeneous injector and the CapWMS

A similar observation is made from the air-silicone oil data in Figure 5.23, using the homogeneous injector for gas superficial velocities from 0.02 to 0.132 m/s. A more complicated result can be seen in Figure 5.24 for air-tap water for gas superficial velocities from 0.02 to 0.145 m/s, where the size and height of the distribution continues to change as the gas velocity is increased.

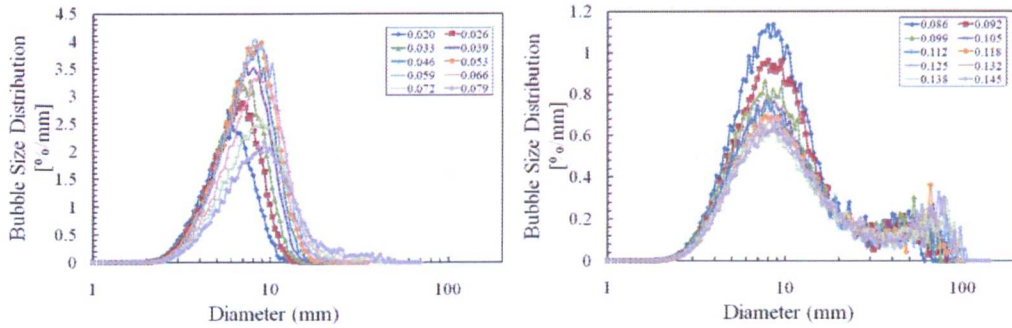


Figure 5.24- BSD for air-tap water on 127mm diameter column, with a homogeneous injector and the CondWMS.

Therefore, it can be concluded that at low superficial gas velocities mainly small bubbles are observed. However, their size increases as the gas velocity is increased, as does the formation of larger bubbles, which will contribute more to the overall void fraction. The overall void fraction is dependent on the area under the curve.

5.4.7. Visualisation: Local voids

For a 127mm diameter bubble column, a 32x32 matrix can be extracted from the data that gives a time averaged local void profile for each condition measured. 2D or 3D surface plots can then be generated. In this section, novel 2D contour profiles were plotted using Matlab. Figure 5.25 shows the plots for air-distilled water using the spider injector, and Figure 5.26 shows the profiles for air-tap water using the homogeneous injector. Figures 5.27 and 5.28 show the profiles for air-silicone oil from the 127mm and 67mm diameter columns respectively. It can be seen that the general trend is that the maximum local voids are in the centre of the pipe; however,

the area in which these are found changes with the velocity. It can also be seen that for the low velocities in air-water with the homogeneous injector, the maximum local voids are occurring near the circumference of the pipe and not in the centre, reinforcing the theory of the wall peaks that tend to occur in the homogeneous region of the flow.

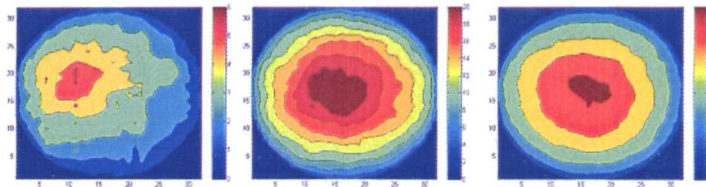


Figure 5.25-2D contour plots for air-distilled water with a spider injector (127mm). (Left) U_{gs} 0.0036 m/s, (middle) U_{gs} 0.0216 m/s, (right) U_{gs} 0.0396 m/s

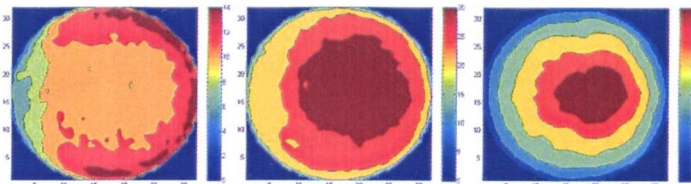


Figure 5.26 -2D contour plots for air-tap water with a hom. injector (127mm). (Left) U_{gs} 0.0197 m/s, (middle) U_{gs} 0.0658 m/s, (right) U_{gs} 0.1316 m/s

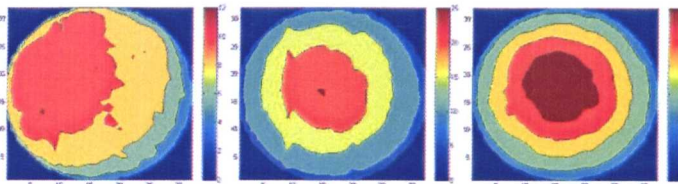


Figure 5.27- 2D contour plots for air-Silicone oil with a hom. injector (127mm). (Left) U_{gs} 0.0197 m/s, (middle) U_{gs} 0.0658 m/s, (right) U_{gs} 0.1316 m/s

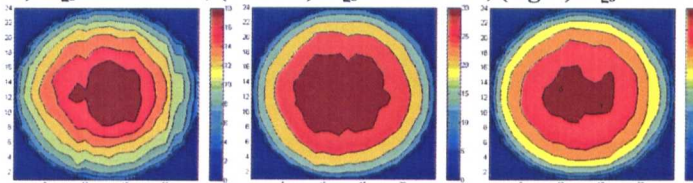


Figure 5.28-2D contour plots for air-Silicone oil with 3mm holes (67mm). (Left) U_{gs} 0.0197 m/s, (middle) U_{gs} 0.0658 m/s, (right) U_{gs} 0.1316 m/s

5.4.8. Visualisation: Cross-sectional voids

Visualisation of the flow can be processed from the wire mesh sensor results in both 2D and 3D. The WMS is able to show individual bubbles and complicated structures within the bubble column. It is possible to show two representations; the first is a virtual representation of the flow as if the column was transparent, and the second is the flow inside the column, which is generally chosen to be in the centre of the column. Both representations are shown in the four figures below. Figure 5.29 shows the visualisation for air-distilled water with the heterogeneous (spider) injector on the 127mm column. Figure 5.30 contains the visualisation of the flow for air-tap water using the homogeneous injector in the 127mm column. Figures 5.31 and 5.32 show the visualisation of the flow for air-silicone oil in the 127mm and 67mm columns respectively. Novel qualitative comparisons can be made between the spider injector and homogeneous injector, between the homogeneous injector with air-water and air-silicone oil, and finally between the 127mm and 67mm diameter columns with silicone oil.

High speed camera videos were recorded at a rate of 1000 frames per second for air-tap water using the heterogeneous injector, and for air-deionised water with the homogeneous distributor. Figure 5.33 shows the images captured for the latter with gas superficial velocities ranging from 0.02 m/s to 0.164 m/s. These images compare well qualitatively with those captured by the WMS for example in flow pattern identification although as expected at higher velocities the view from the transparent pipe is less clear, with the WMS identifying structures that are forming inside the column. These are not visible with the naked eye. Sample HS and WMS videos are provided on the DVD attached to this thesis. There is evidence from the HS videos that recirculation is taking place at the higher gas velocities.

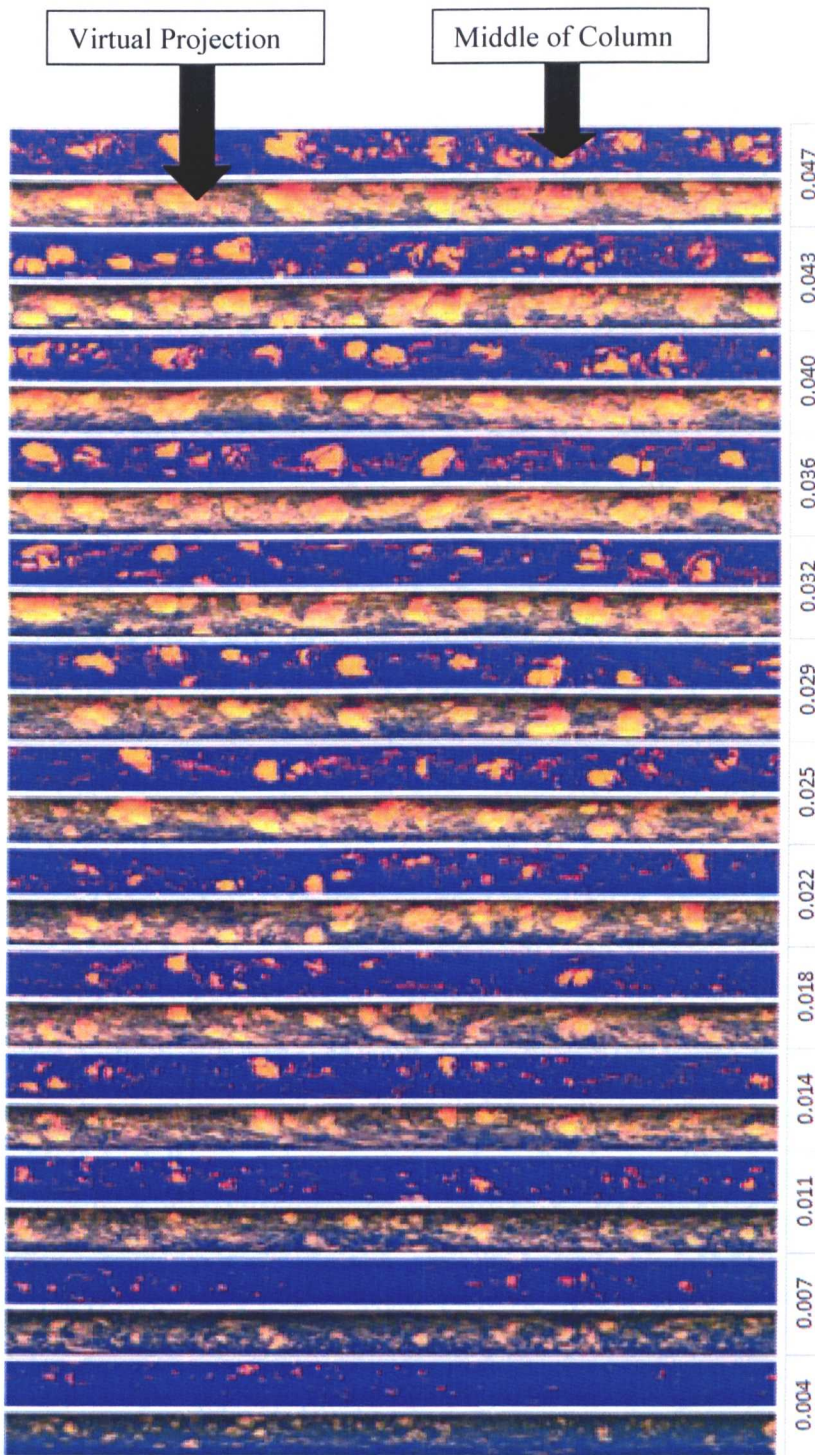


Figure 5.29-2D Air-distilled water visualisation with increasing gas superficial velocity in m/s, for the 127mm diameter column and spider injector.

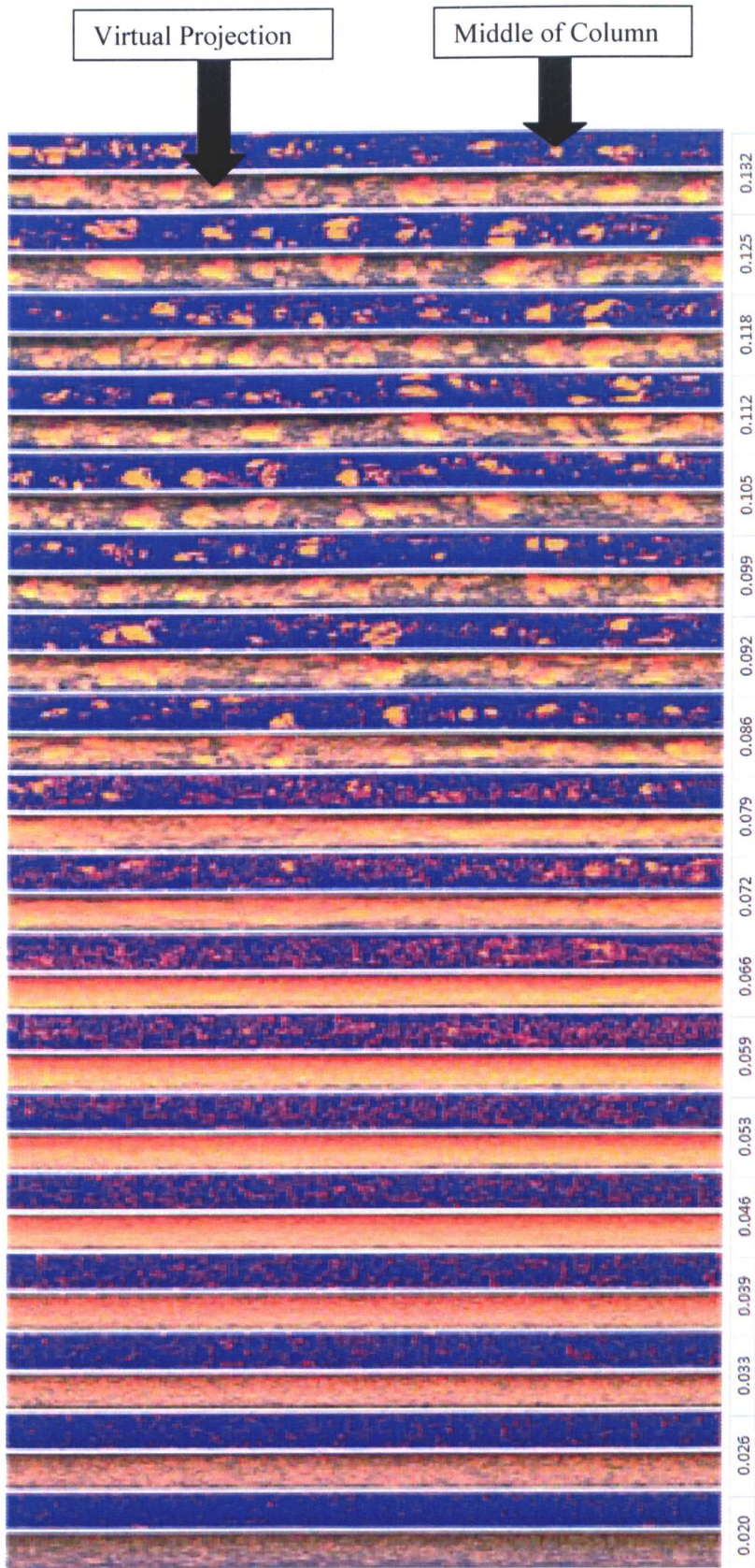


Figure 5.30-2D Air-tap water visualisation with increasing gas superficial velocity in m/s, for the 127mm diameter column and homogeneous injector

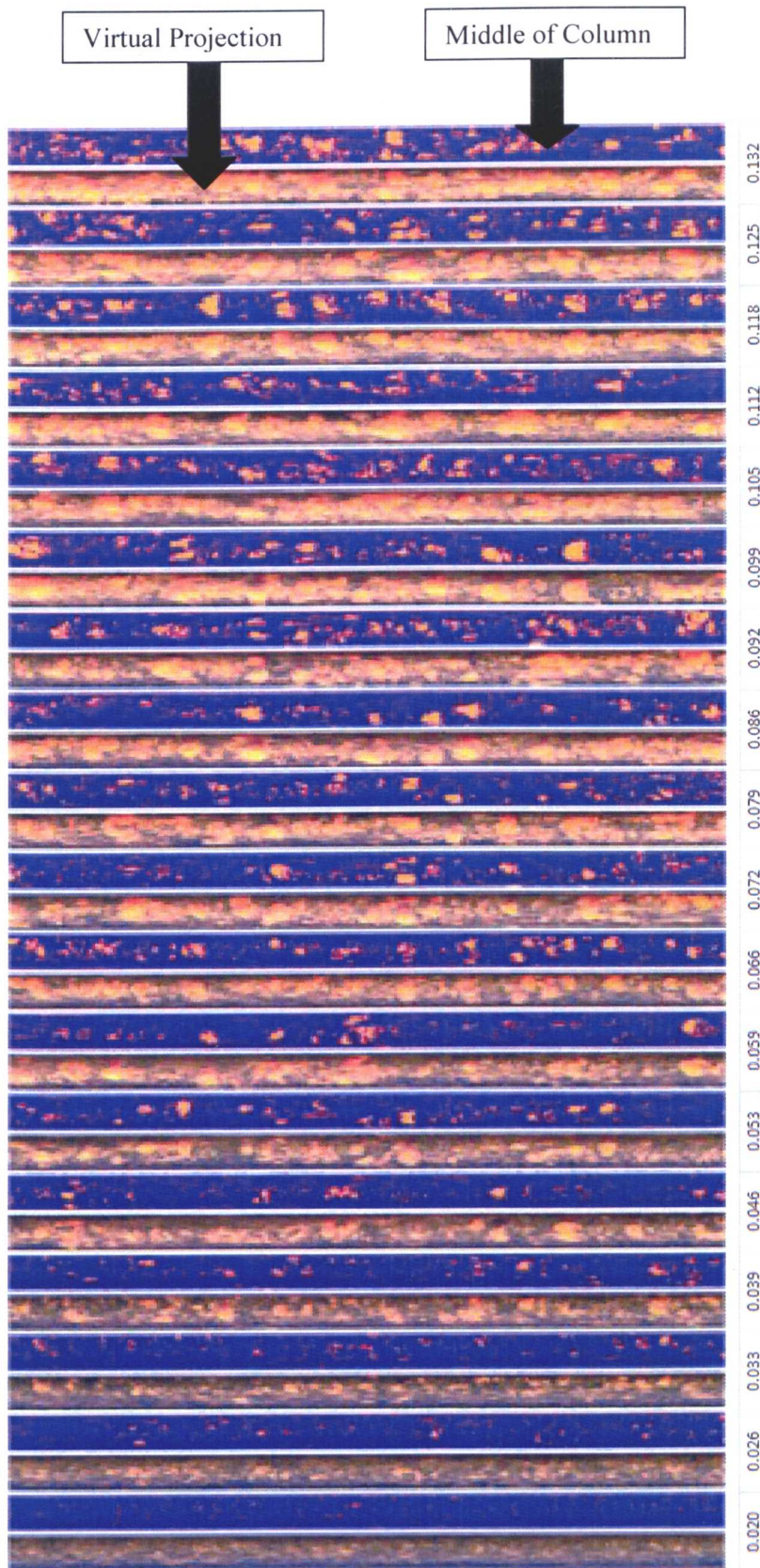


Figure 5.31-2D Air-silicone oil visualisation with increasing gas superficial velocity in m/s, for the 127mm diameter column and homogeneous injector

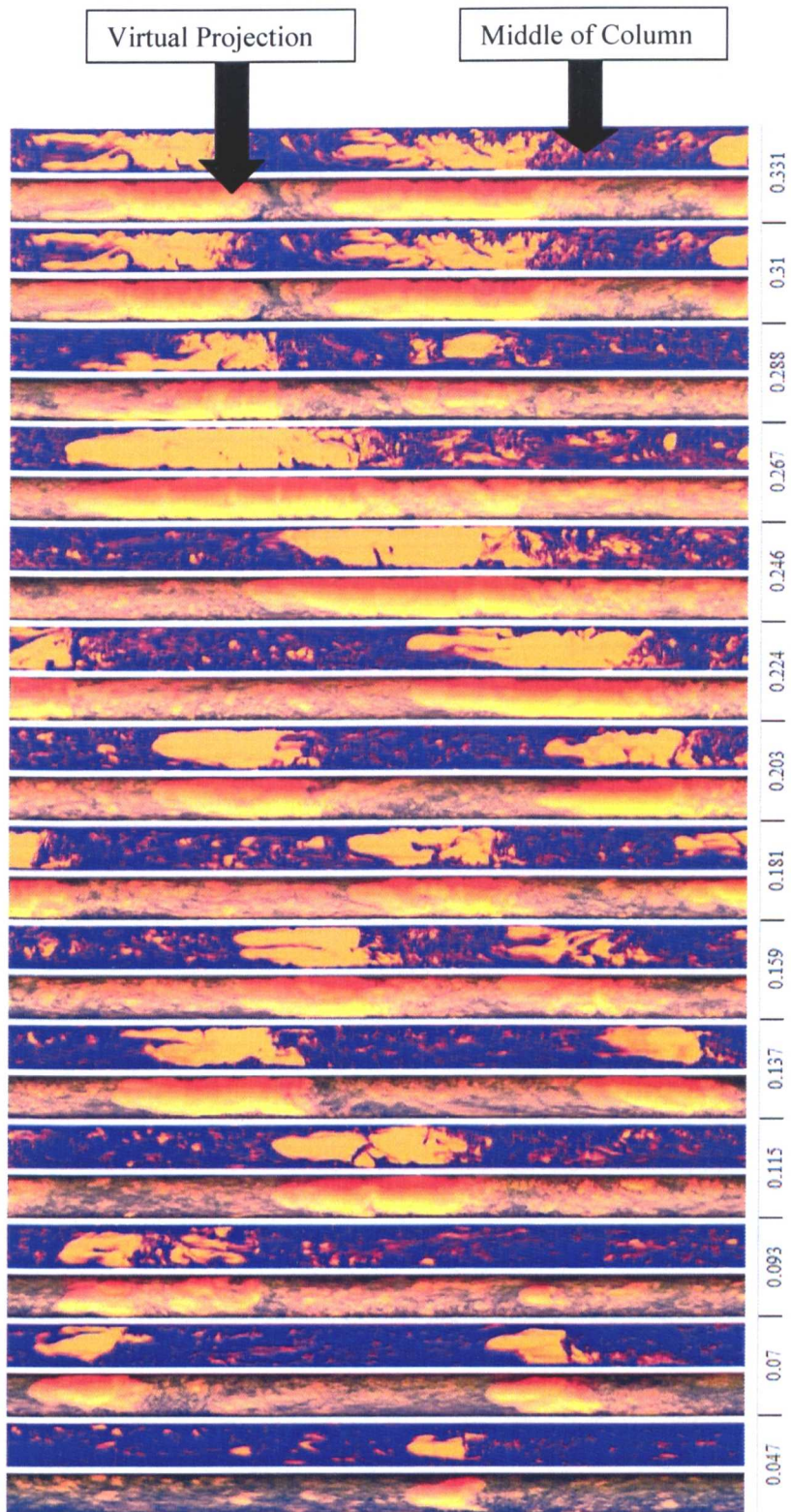


Figure 5.32-2D Air-silicone oil visualisation with increasing gas superficial velocity in m/s, for the 67mm diameter column and 3mm injector

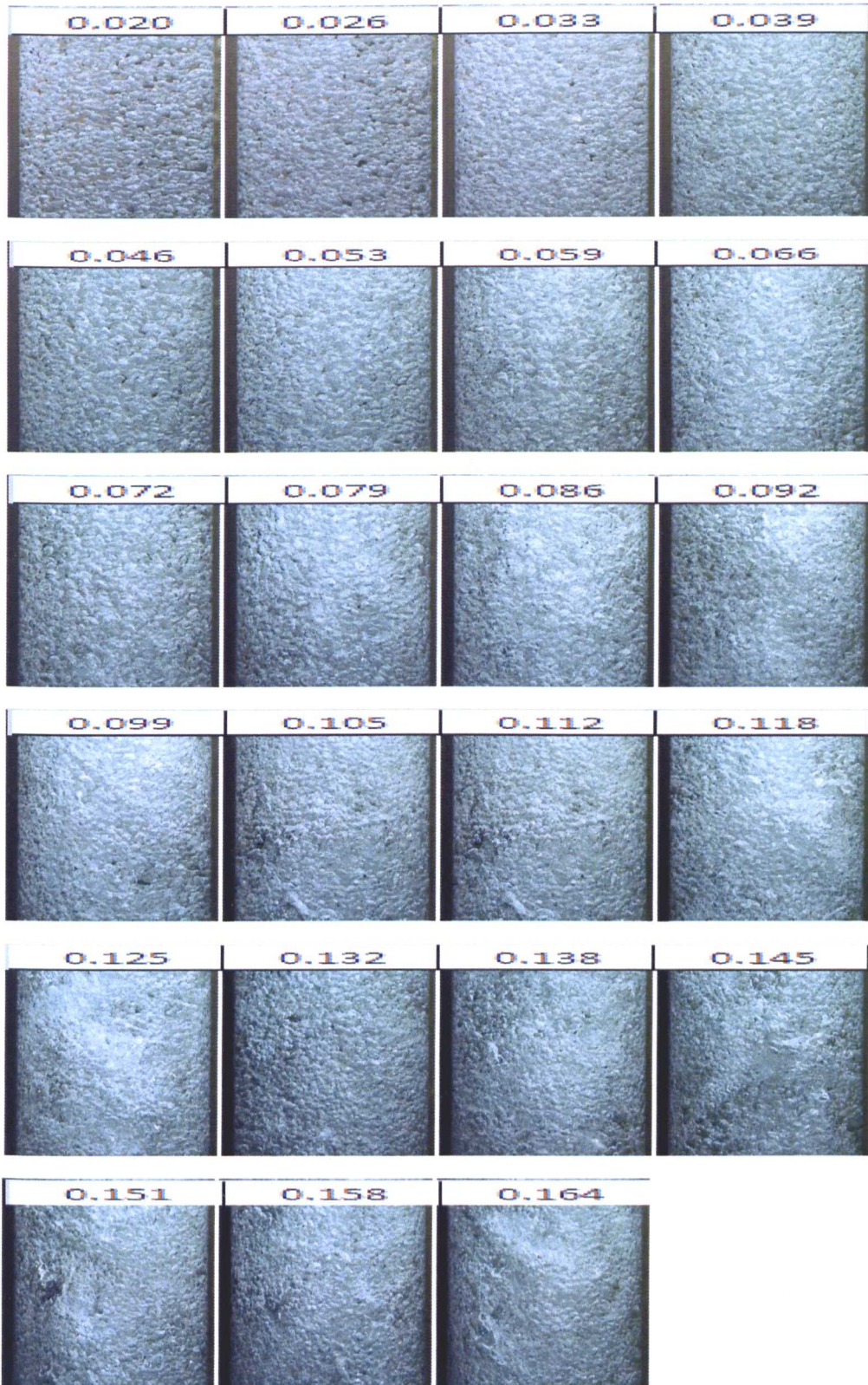


Figure 5.33-Images extracted from high speed videos for air-deionised water, in the 127 mm bubble column with a homogeneous injector. The gas superficial velocity is indicated above each image in m/s.

5.5. Comparison between 67mm and 127mm columns

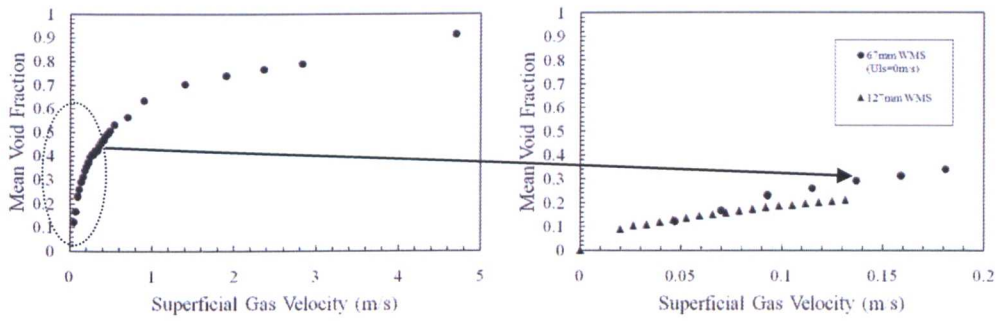


Figure 5.34-Mean Void Fraction. (Left) 67mm column, (right) 67mm vs. 127mm

Figure 5.34 shows the mean void fraction against gas superficial velocity for both 67mm and 127mm columns with air-silicone oil. It is clear that the trend of the mean void fraction for the larger diameter is lower than for the smaller diameter.

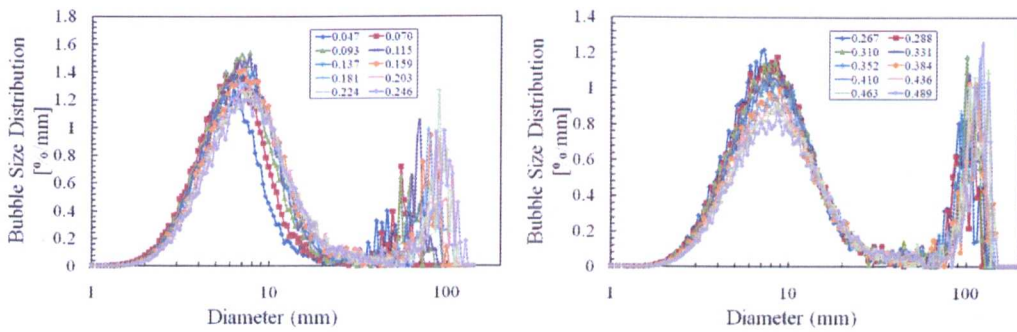


Figure 5.35-Bubble size distribution in the 67mm column at $U_{is}=0$ m/s

Figure 5.35 shows the bubble size distribution for the 67mm diameter pipe, which can be compared to the bubble sizes in Figure 5.23 for the larger diameter column. An exercise was carried out to extract values of the main peak (1st peak) from the bubble size distributions, which can be considered as the statistical mode (in this case bimodal), for both 67mm and 127mm columns with air-silicone oil. These were plotted against the gas superficial velocity, which can be seen in Figure 5.36. It is interesting to note that there is a trend of increasing bubble size with increasing superficial velocity, and that this trend is higher for the larger diameter column.

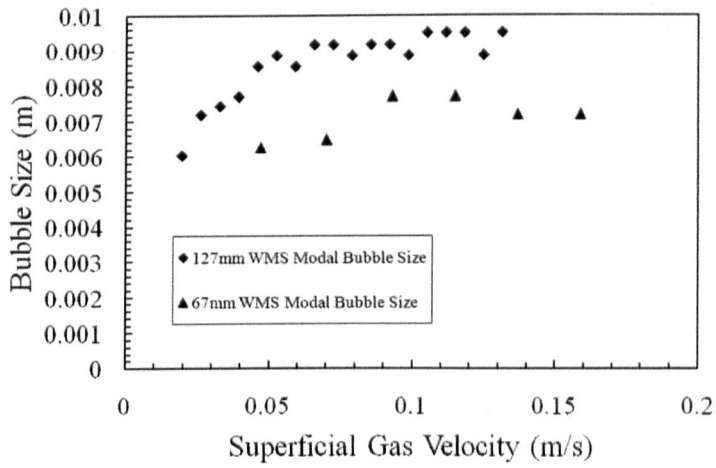


Figure 5.36-WMS bubble size (first mode) against superficial gas velocity; 67mm vs. 127mm.

The radial profiles were plotted for the 67mm pipe, which is shown in Figure 5.37.

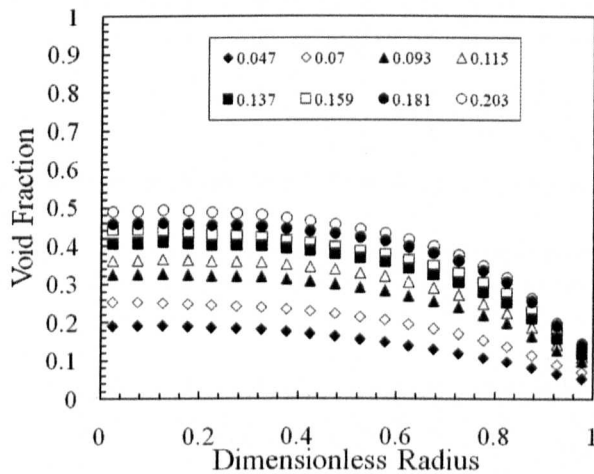


Figure 5.37-Radial profiles for the 67mm column with air-silicone oil; superficial gas velocities of 0.047 to 0.203 m/s

The general trend is clear: the radial void fractions are increasing with rising superficial gas velocity. This signifies a centre peak and heterogeneous flow. The radial profiles of the 67mm and 127mm columns were compared for the same gas velocities. These results can be seen in Figure 5.38, and the radial void fractions for the two diameters diverge as the superficial gas velocity is increased.

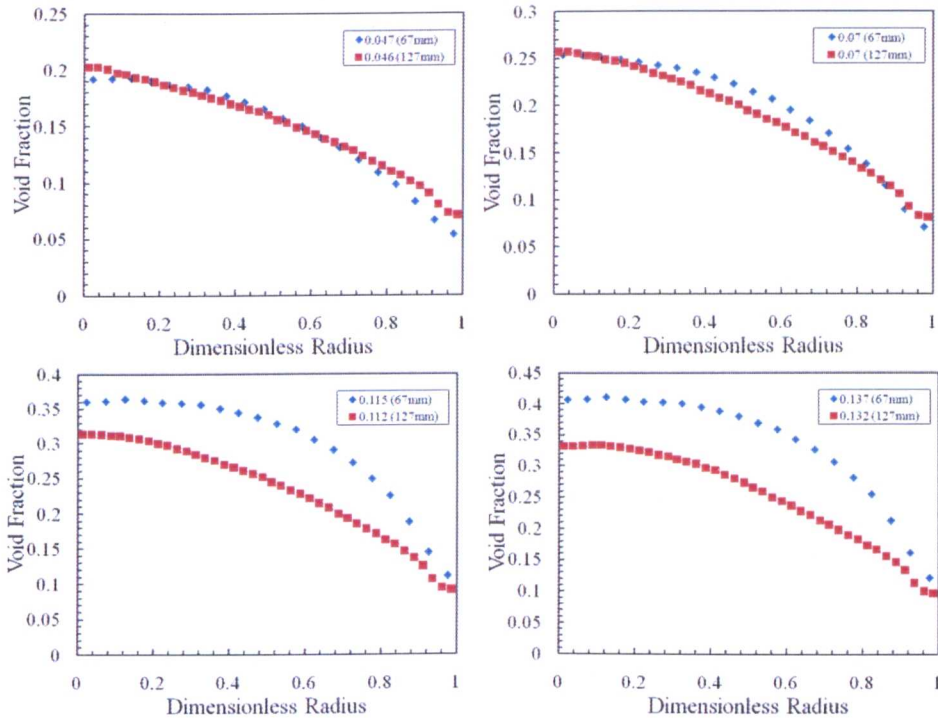


Figure 5.38-Radial profiles for the 67mm vs. 127mm columns for the corresponding gas velocities

Finally, the frequencies for the 67mm and 127mm pipes were plotted for similar gas velocities (Figure 5.39). The dominant frequencies for the 67mm column are lower than those for the 127mm column.

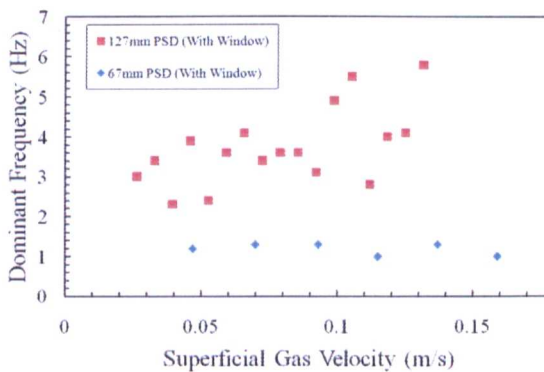


Figure 5.39-Dominant Frequencies for 67mm and 127mm columns with Air-Silicone Oil

5.6. WMS experiments with aqueous saline solutions

Data collected using the CondWMS on the 50mm bubble column with the porous injector was further analysed. Initially, the mean void fraction was plotted against the superficial gas velocity for four different levels of conductivity (Figure 5.40). The trend of increasing void fraction with rising conductivity is clear, which agrees qualitatively with trends obtained by Anderson and Quinn (1970).

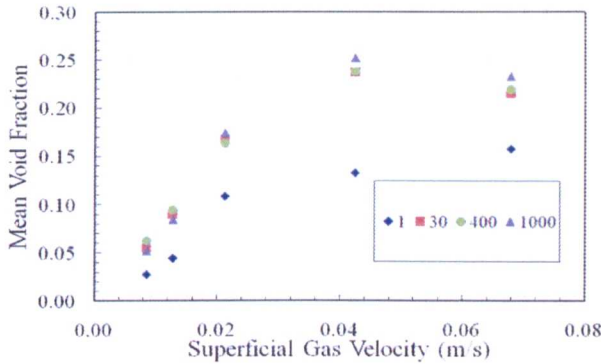


Figure 5.40-Mean void fraction vs. superficial gas velocity for the CondWMS. Conductivity varied between 1-1000 $\mu\text{S}/\text{cm}$

The radial profiles were also plotted in Figure 5.41 and Figure 5.42. The trend is generally the same; with a void profile that is flat at lower conductivities, turning into centre peaks at higher conductivities. Again, there is a tendency for the radial void fraction to increase with superficial gas velocity.

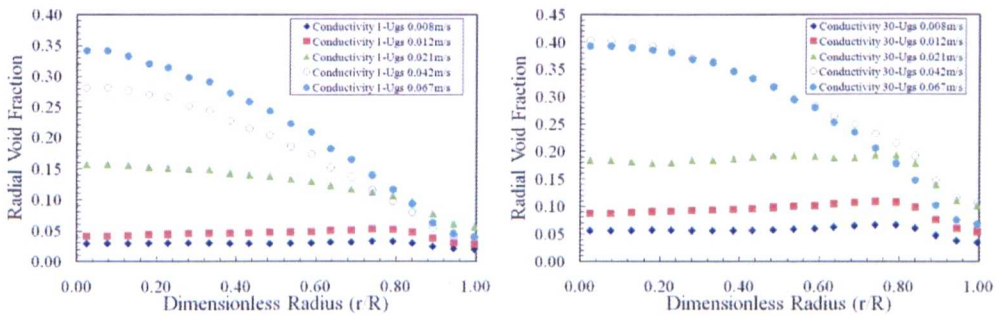


Figure 5.41-Radial void profiles. (Left) 1 $\mu\text{S}/\text{cm}$ and (right) 30 $\mu\text{S}/\text{cm}$

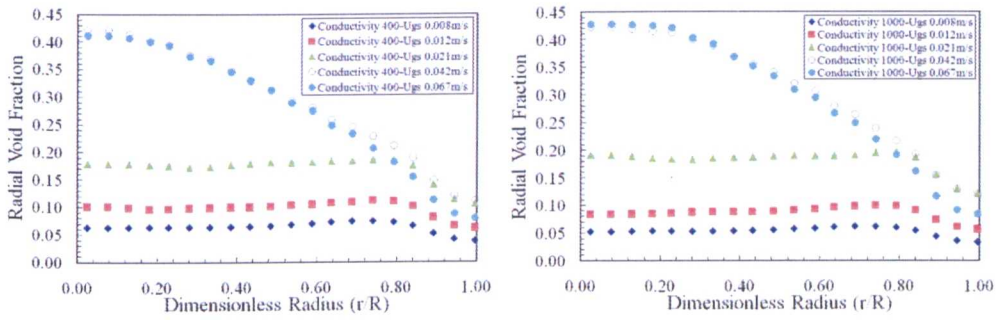


Figure 5.42- Radial void profiles. (Left) 400 $\mu\text{S/cm}$ and (right) 1000 $\mu\text{S/cm}$

5.7. Comparison of data with published correlations

Three exercises were carried out; first the level swell data was compared against physical models, then the cross-sectional void correlation was compared against the WMS data and finally the radial void correlation was compared against the WMS data.

5.7.1. Level Swell

A comparison was initially made between the level swell measurements and physical models for the 127mm column with the homogeneous distributor, as was also carried out by Azzopardi et al. (2011). Models such as those by Zaki-Richardson (1954) and Zuber and Findlay (1965) were chosen. This is shown in Figure 5.43. For the drift-flux equation (5.4), $C_o = 2$, $U_{ls} = 0$, and equation (5.16) was applied, where $V_T \approx 0.3$ m/s for air-water and $V_T \approx 0.2$ m/s for air-silicone oil. Clearly there is a trend of increasing mean void fraction as the impurities in the water increases. A similar effect is observed with the limited measurements taken with a surfactant (Butanol) which also acts as an impurity to suppress coalescence. Silicone oil has a lower surface tension and a higher viscosity than water and this may explain the fact it has lower void fractions and the reason why no homogeneous flow is formed.

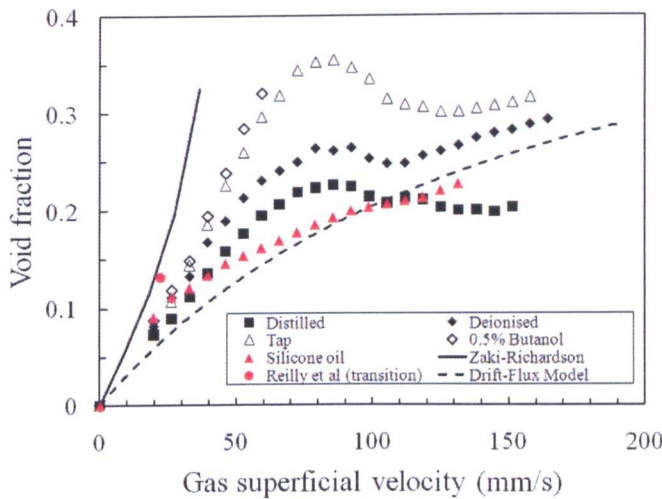


Figure 5.43- Level Swell data for the 127mm bubble column compared against published correlations. Zaki et al/Drift flux lines for air-water.

Zahradnik et al. (1979) also used values of $C_o = 2$ and $V_T \approx 0.3$ m/s for air-water systems. Values of $n=2.39$ ($Re>500$) for air-water and $n=4.45Re^{0.1}$ ($Re<500$) for air-silicone oil were determined. The Zaki-Richardson equation appears limited, as the maximum value for U_{gs}/V_T for air-water is 0.19, and for air-oil the equation stopped working for a value of U_{gs}/V_T higher than 0.165. Therefore, it can only be used for low superficial velocities. The transition velocity for the homogeneous injector with air-water was calculated using Reilly et al. as 0.02 m/s, and the transitional void fraction was calculated as 0.13. These values occur before the transitional peak as shown in Figure 5.43. The Wilkinson et al. equations also underestimate the transitional velocity and void fraction. Clearly for air-silicone oil, there is no transitional velocity as the profile is entirely heterogeneous. Another interesting observation can be made by inspecting Figure 5.43 and considering the bubble size data, in particular for air- tap water with the homogeneous injector (Figure 5.24). The occurrence of the second peak for the bubble size distribution seems to coincide with the transition point of the above curve at approximately 0.09 m/s.

5.7.2. WMS cross-sectionally averaged void fraction

WMS void fraction data collected on the 127mm diameter bubble column with the homogeneous distributor was compared with the drift flux using the Hills (1976) and Letzel et al. (1999) correlations. This comparison was done for both air-water (Figure 5.44) and air-silicone oil (Figure 5.45), specifically for the heterogeneous part of the WMS data.

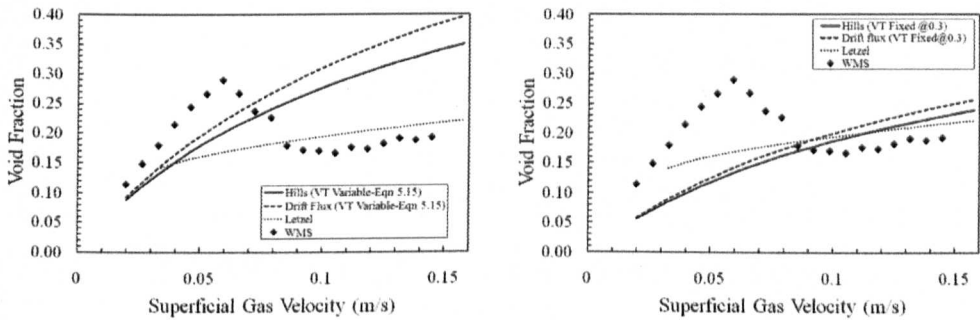


Figure 5.44-Void fraction correlations vs. WMS data for air-water

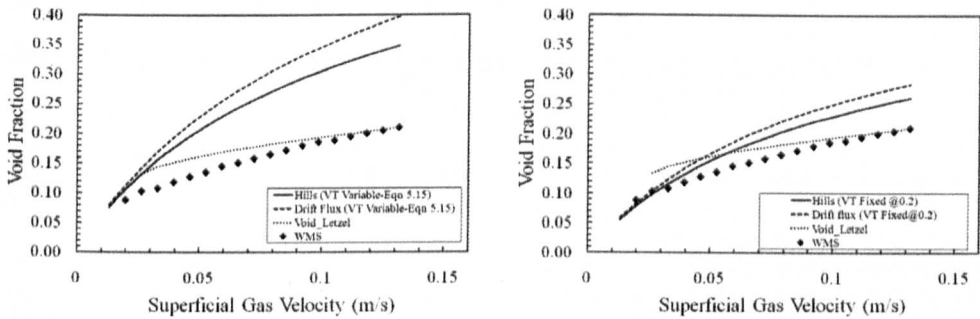


Figure 5.45 Void fraction correlations vs. WMS data for air-silicone oil

The Letzel correlation performed reasonably well in the heterogeneous part of the curve, whereas the Hills and Drift flux correlations tended to overestimate the void fractions if Tomiyama's correlation was used (equation 5.15) for the bubble velocity (V_T). If V_T was fixed at 0.3 m/s for air-water and 0.2 m/s for air-silicone oil, the agreement improved between the experimental data and the 2 correlations.

5.7.3. WMS radial profiles

Wire mesh data for air-silicone oil was compared with the radial void correlation (equations 5.6-5.8) by Wu et al. (2001) (Figures 5.46 to 5.48). The original equation clearly does not fit; however, if the correlation is modified such that n is divided by 4 and c is multiplied by 2.8, a better fit is obtained as demonstrated in the six graphs. It is interesting to note that Azzopardi et al. (2011) carried out similar adjustments to Wu's correlation to fit it to their own experimental data. For example, for Mudde-Saito radial profiles for a 149mm diameter column with air-water, n was divided by 4 and c multiplied by 2 to achieve a reasonable fit to the experimental data.

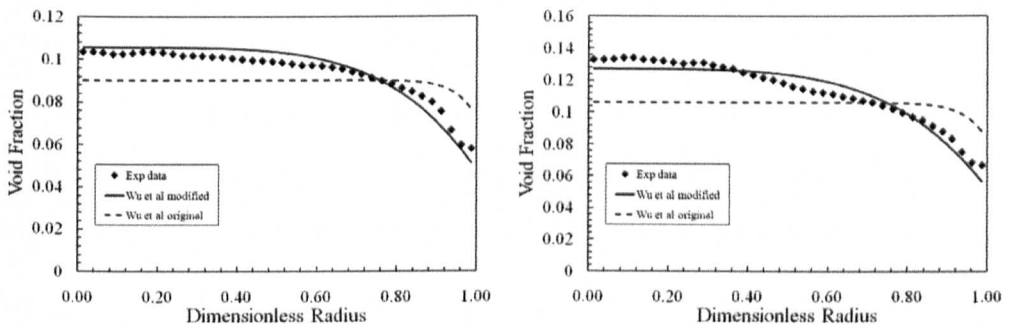


Figure 5.46-Radial profiles vs. Wu et al. modified/original.
(Left) $U_{gs}=0.020$ m/s, (right) $U_{gs}=0.026$ m/s

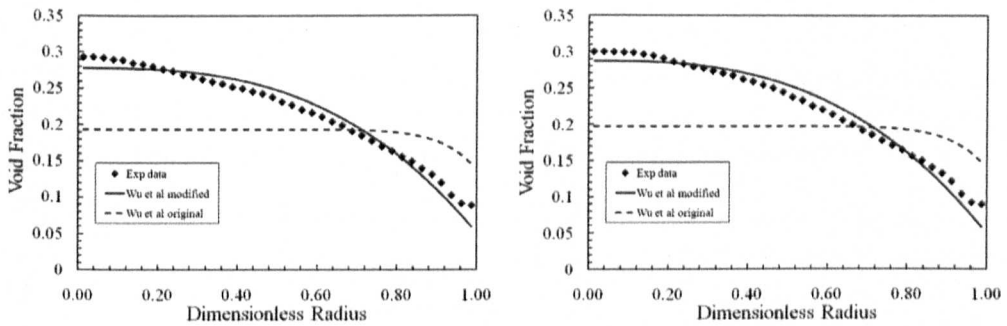


Figure 5.47- Radial profiles vs. Wu et al modified/original.
(Left) $U_{gs}=0.099$ m/s, (right) $U_{gs}=0.105$ m/s

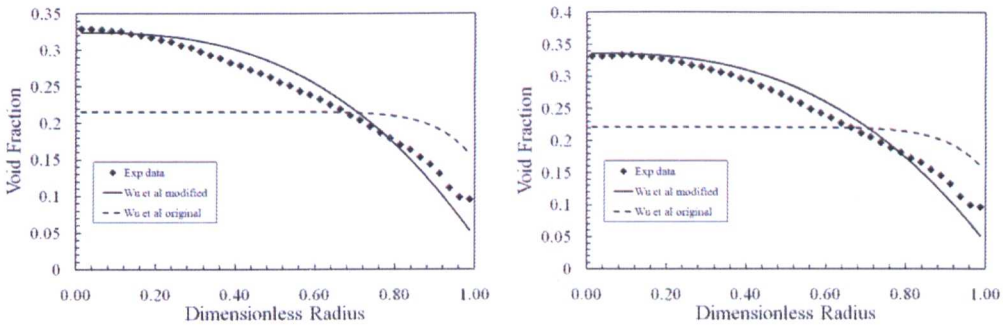


Figure 5.48- Radial profiles vs. Wu et al modified/original.
(Left) $U_{gs}=0.125$ m/s, (right) $U_{gs}=0.132$ m/s

5.7.4. Bubble size measured by WMS

An interesting result was found when the bubble size from the first peak (mode) was extracted from the wire mesh bubble size distribution for the homogeneous distributor for both air-water and air-silicone oil. These results were compared with the bubble size generated by Gaddis and Vogelpohl's correlation, the results of which are shown in Figure 5.49. The experimental data appears to track the values generated by Gaddis et al's correlation, and tends to converge at higher gas velocities. Lage et al (1999) verified that models such as the one by Gaddis and Vogelpohl for the bubble formation in orifices gave reasonable predictions of the mean bubble diameter inside the bubble column. It is also worth noting that the bubble sizes are predicted to be smaller in the air-silicone oil mixture, as the lower surface tension of the oil suppresses bubble coalescence and hence smaller bubbles are formed.

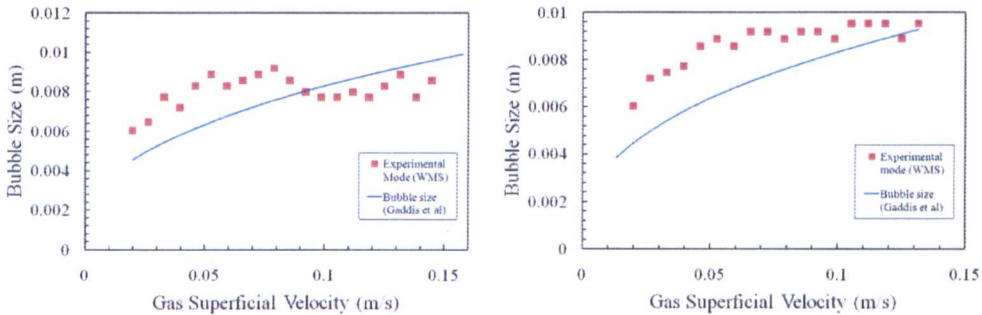


Figure 5.49-Bubble size vs. gas velocity. (Left) Air-water and (right) Air-oil

The bubble size equation (5.12) given earlier in this chapter predicts that the maximum diameter will be approximately 8 mm for the air-water system. However, it is clear from the plot above (Figure 5.49 [left]) that the bubble diameter exceeds this value. Hartevelde (2005) produced the bubble size distribution plot shown in Figure 5.50 [left]. It contains the elliptical diameters $2a$ and $2b$, which were taken over periods of 1 hour and 3 weeks respectively. The equivalent spherical diameter can be calculated, plotted for both time frames, and then compared with the bubble diameters calculated using the equation of Gaddis and Vogelpohl (Figure 5.50 [right]). The agreement that can be observed with this correlation is encouraging.

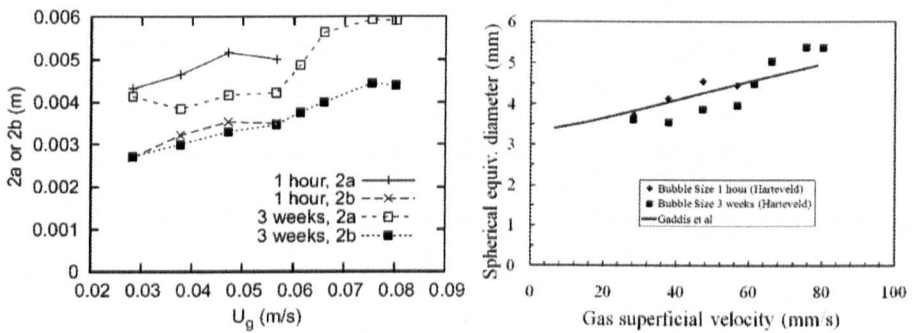


Figure 5.50-Data from Hartevelde (left); comparison of the bubble size by Hartevelde with the equation of Gaddis and Vogelpohl (right)

It is interesting to note the trend predicted by Gaddis and Vogelpohl is a straight line for data by Hartevelde, whereas it curves slightly for the 127mm bubble column results particularly at the low gas superficial velocities. This is a consequence of the number of holes in the distributor, as the injector of Hartevelde contained 559 holes (~5x more holes). There are three terms in the equation of Gaddis and Vogelpohl. With the injector of Hartevelde, the first term initially dominates before the third term takes over for higher velocities. However, with the homogeneous injector for both air-water and silicone-oil, the third term always dominates.

5.8. Bubble Column Modelling

Two-phase gas-liquid flow systems are complex, non-deterministic and difficult to predict. The usual empirical approach is to take a set of measurement data and fit a model around it. This chapter presents the comparison of empirical correlations with experimentally generated results, which shows that there was good agreement between them in several cases. However, these empirical models are restrictive, and normally should only be applied to systems that are comparable to the ones for which they were obtained. Other approaches are possible, which include the construction of a transfer function that relates the dynamic change of an input to an output i.e. a disturbance is applied to the input, and the response is then measured. This was carried out by Gluszek et al. (1983) who constructed a mathematical model based on linearised equations of continuity and motion relating the pressure variation above a distributor plate against the change in the gas flow rate. Dominant frequencies were also deduced for a bubble column of a diameter 0.14 metres and the model compared well with experimental results. A complementary approach to using empirical models is to construct a mathematical model that incorporates more physics about the system (often known as mechanistic modelling), and then assess what can be inferred about the system from the output of the model. Complex and coupled differential equations are required to analyse two-phase flow, which requires tools such as CFD to solve them in detail. The differential equations could be simplified into a first order or second order systems to make them more easily solved analytically.

To gain an improved understanding of the physics inside a bubble column, a simplified mathematical model representing a bubble column with a homogeneous distributor was developed in this research, based on simple geometry and with certain assumptions being made about bubble behaviour. Results were then compared with

some of the experimental data presented earlier in this chapter. A number of different scenarios were postulated and four different modelling methodologies are presented and outlined below. The code was developed for this study in Matlab in order to run the models, and simulations were carried out for both air-water and air-silicone oil. Some simplifications were essential to minimise the computational effort and complexity. The system was assumed to be operating at steady-state, although with the natural fluctuations that are shown in the time-series plots for the mean void fraction. The bubble size at creation was estimated using the work by Gaddis and Vogelpohl (1986), and the bubble rise velocity was estimated using the equations of Mendelsohn (1967) and Tomiyama et al. (1998), which were outlined earlier. The bubbles were assumed to be spherical, either with constant diameters or a given size distribution. The voidage was calculated from the sphere intersection with the sensor plane, as shown in Figure 5.51, which also shows an example of how the void fraction varies with time for one bubble. Bubble coalescence and break-up were disregarded, and the first two models assumed that bubbles were travelling upwards with the same velocity and in the same direction. In reality the bubbles tend to “drift” and recirculate; however, again this was neglected. For models 3 and 4, the diameter and velocity of the bubbles was allowed to vary.

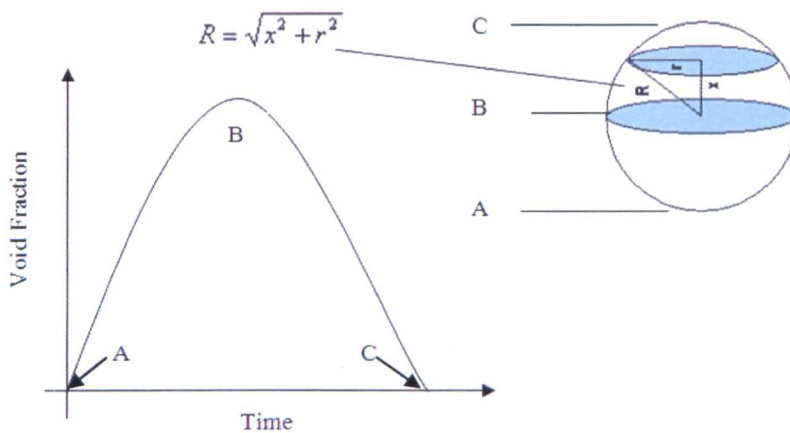


Figure 5.51-Voidage history for one bubble

5.8.1. First modelling methodology

The first model assumed there was simultaneous generation of the same-sized bubbles from the homogeneous distributor, which all crossed the wire mesh sensor at the same time. Figure 5.52 shows a schematic.

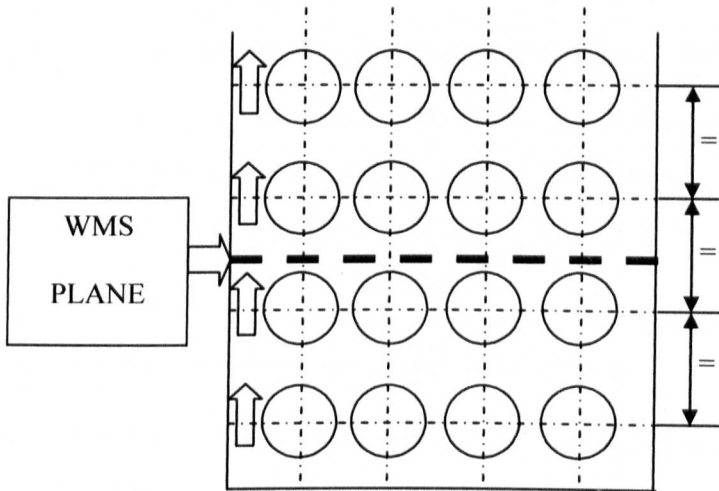


Figure 5.52- Model 1: Bubbles aligned

This model basically considers the bubble that crosses the sensor, which was shown in Figure 5.51. This was then multiplied by the number of holes in the distributor, which in this case is 121. The main physical parameters that were varied can be seen in Figure 5.53. The rows for the bubbles were equally spaced to match the required flow rate.

```

% Specify physical properties (l-liquid, g-gas)
sigma=0.073;      % surface tension N/m
rhog=1;          % Gas density kg/m^3
rho1=1000;       % Liquid density kg/m^3
mul=0.001;       % Liquid viscosity Pa.s
Qg=110;          % Gas flow rate l/min
DCol=0.127;      % Diameter of column m
Nholes=121;      % Number of holes in distributor
Dorifice=0.0005; % Diameter of each orifice in distributor m
g=9.81;          % Gravity m/s^2

```

Figure 5.53-Screenshot of the physical properties defined in the code for the model. Qg is varied appropriately.

The flow rate was varied from 15-110 l/min to match the experimental campaign. It was assumed that the bubbles were all crossing the sensor at the same time with no coalescence, which is an “idealised” situation and will deduce the maximum void fraction obtained. The results of the simulations using model 1 can be seen in Figure 5.54 for both air-water and air-silicone oil. The homogeneous part of the experimental curve for air-water matched well with the results from the simulation. However, there was a poor agreement in the heterogeneous part of the curve, which was also the case for air-silicone oil, because the flow was entirely heterogeneous.

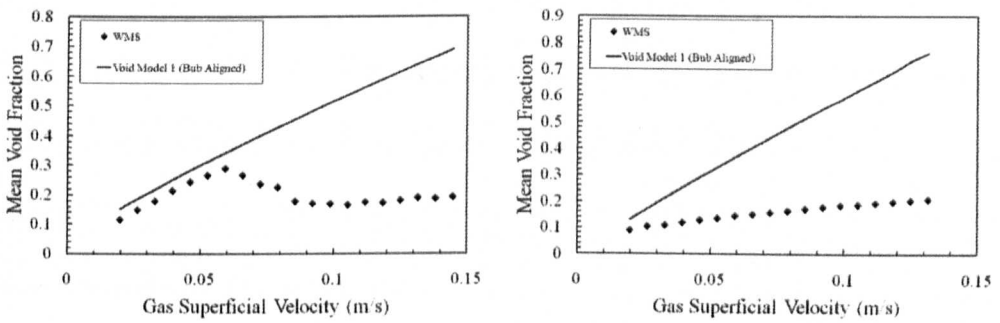


Figure 5.54- Model 1 vs. WMS data. Air-water (left), air-silicone oil (right)

5.8.2. Second modelling methodology

The second model assumed the array of bubbles to be of the same size, but instead of being all in line, in this case they were made to be staggered (Figure 5.55). Bubble spacing was again set-up in such a way to match the flow rate.

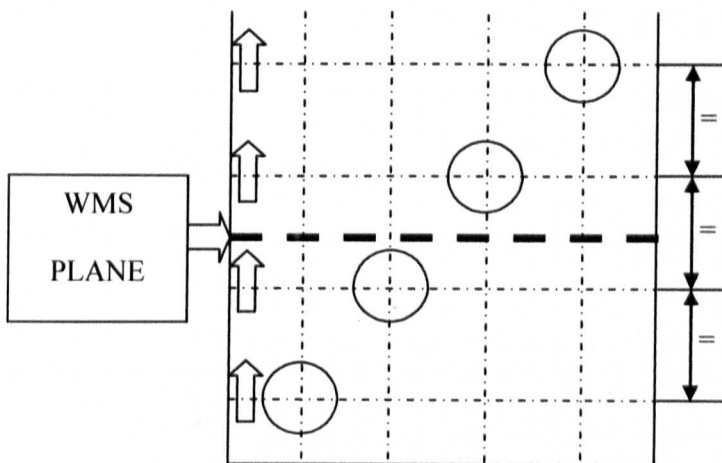


Figure 5.55-Model 2: Staggered bubbles

A typical plot of the void fraction for this model is shown in Figure 5.56. The ends of the time series were discounted and the mean voidage was calculated for 0.05 to 0.45s.

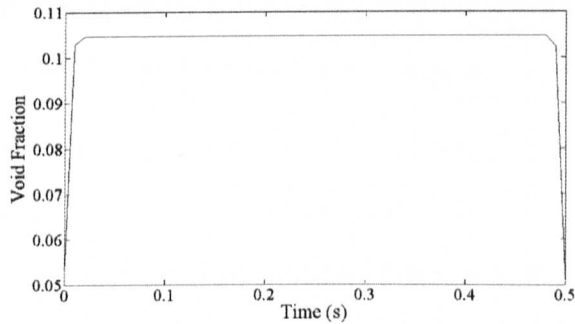


Figure 5.56-An example of void fraction variation with time for model 2

Figure 5.57 shows a comparison of the air-water simulations carried out for model 2 with the experimental results. It can be seen that again this model worked well for the homogeneous part of the curve, but that divergence is once more observed as the flow moved into the heterogeneous region.

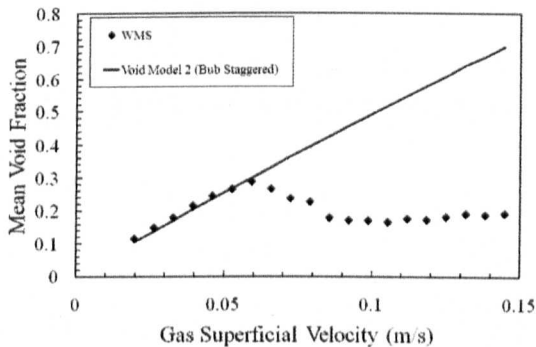


Figure 5.57-Model 2 vs. WMS data with air-water,

5.8.3. Third modelling methodology

The third model introduced an element of randomness to the diameter and velocity of the bubbles. This is based on the *Monte Carlo* method (Mackay, 1996), which is a stochastic method as opposed to a deterministic approach. It iteratively evaluates a deterministic model using sets of random numbers as inputs. This method is widely

used in many fields, such as engineering, energy, research and development, oil and gas, transportation, environment, risk in insurance, finance and project management. It is often used when the model is complex or nonlinear. Each bubble diameter and velocity was sampled from a normal distribution; where the mean was calculated from estimates of maximum and minimum using the aforementioned correlations for the bubble size and velocity, and the standard deviation was estimated to cover a 96% probability from the mean. A schematic is shown in Figure 5.58.

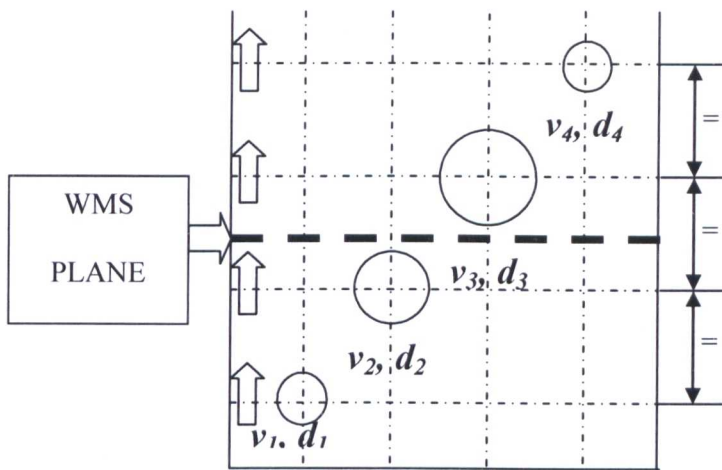


Figure 5.58-Model 3: Random bubbles with velocities (v) and diameters (d)

A typical plot of the void fraction from this model is shown in Figure 5.59. Here the void fraction is more representative of the experimental data, with a fluctuating trend.

The mean voidage was calculated as before.

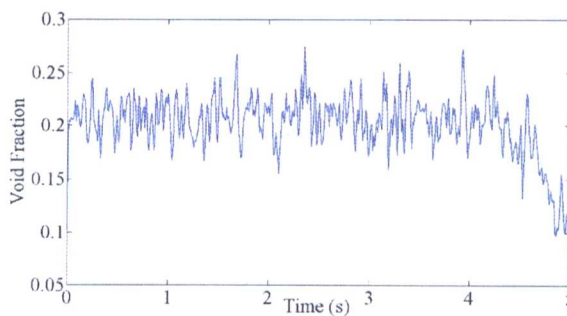


Figure 5.59-Typical void fraction profile for model 3.

Figure 5.60 shows a comparison of the experimental data with the average void fraction deduced from the simulations using model 3. Again, there is good agreement between the two for the homogeneous part of the curve only.

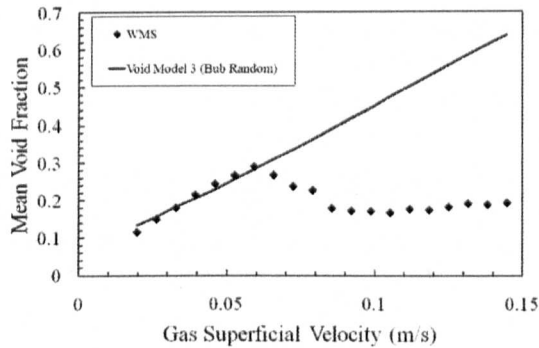


Figure 5.60-Model 3 vs. WMS data for air-water

5.8.4. Fourth modelling methodology

The fourth model was based on the third model; however, it was improved by applying the bubble size distribution obtained experimentally as opposed to using an assumed normal distribution. The WMS bubble size distribution is expressed in two ways; the first approach is based on the surface area of the bubble, and the second approach is based on the volume of the bubble. The experimentally generated distribution was imported into Matlab and converted to a cumulative probability curve, which was randomly sampled using linear interpolation. This is a semi-empirical approach. The void fraction was then calculated with this model and compared with the WMS data as shown in Figure 5.61. The model appears to track the experimentally generated voidage very well.

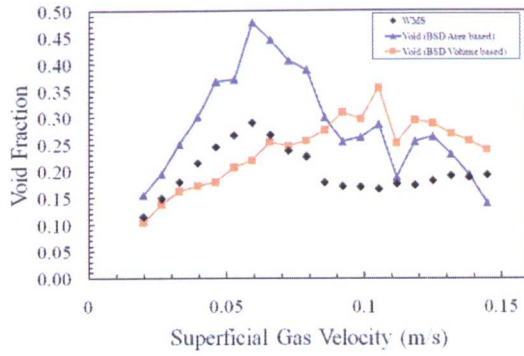


Figure 5.61-Model 4: Void fraction vs. WMS data using area-based and volume-based experimentally obtained bubble size distributions

Figure 5.62 shows that the bubble size sampling method adopted –Monte Carlo method- for this model gave realistic size distributions when compared with the experimentally generated distributions, which were either surface area or volume-based.

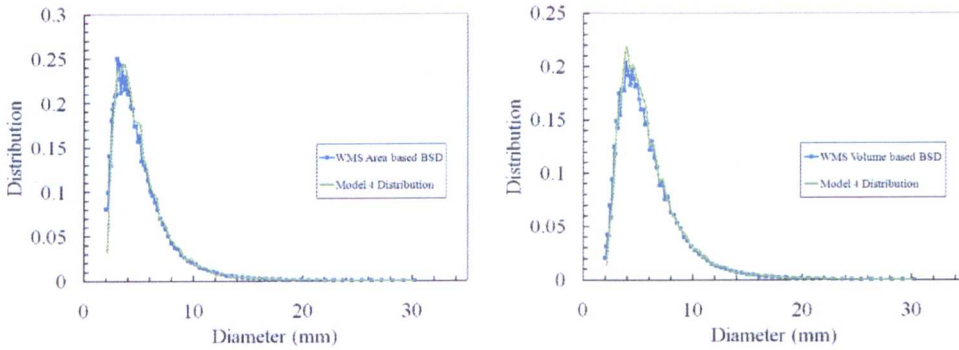


Figure 5.62- Distribution curves for the WMS vs. model 4 for one run with air-water. (Left): Area based BSD, (right): volume based BSD.

5.8.5. Bubble Shape

The above four models all considered the bubbles to be spherical, which in reality is not always the case. Other bubble shapes could be present in a column, for example ellipsoids (Figure 5.63). The following mathematical relationship can be derived (Azzopardi et al, 2011):

$$\frac{d_e}{2a} = E^{1/3} = \frac{d_e}{d_m} \Rightarrow E = \left(\frac{d_e}{d_m} \right)^3 \quad (5.21)$$

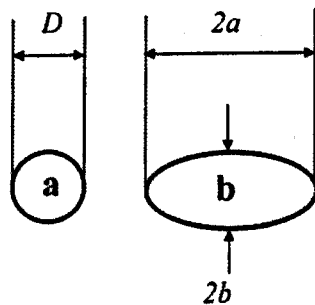


Figure 5.63- Bubble shapes: (a) spherical and (b) elliptical

where d_e is the spherical equivalent diameter, E is the aspect ratio and d_m is the measured diameter. These are all based on the geometry. Therefore:

$$d_e = d_m E^{1/3} \quad (5.22)$$

A number of relationships have been proposed for the aspect ratio E as a function of the equivalent diameter (Azzopardi et al, 2011). For example:

$$E = \frac{1}{1 + c_1 E_0^{c_2}} \quad (5.23)$$

Where values of $c_1 = 0.163$ and $c_2 = 0.757$ have been proposed. E_0 is the Eötvös number, which is the ratio of gravitational to surface tension forces, written as:

$$E_0 = \frac{g d_e^2 (\rho_l - \rho_g)}{\sigma} \quad (5.24)$$

Substituting equation (5.22) into equation (5.24):

$$E_0 = \frac{g (d_m E^{1/3})^2 (\rho_l - \rho_g)}{\sigma} \quad (5.25)$$

Substituting equation (5.25) into equation (5.23):

$$E = \frac{1}{1 + c_1 \left(\frac{g (d_m E^{1/3})^2 (\rho_l - \rho_g)}{\sigma} \right)^{c_2}} \quad (5.26)$$

$$E + Ec_1 \left(\frac{g(d_m E^{1/3})^2 (\rho_l - \rho_g)}{\sigma} \right)^{c_2} - 1 = 0 \quad (5.27)$$

Therefore solving for air-water, the following equation can be generated:

$$E + 0.163E \left(\frac{9.81(d_m E^{1/3})^2 (1000-1)}{0.073} \right)^{0.757} - 1 = 0 \quad (5.28)$$

For different values of d_m this equation can be solved by iteration e.g. if $d_m=10\text{mm}$, then:

$$E + 0.163E \left(\frac{9.81 \times 0.0001 * E^{2/3} (1000-1)}{0.073} \right)^{0.757} - 1 = 0 \quad (5.29)$$

A similar equation can be generated for air-silicone oil.

E	0.54	0.61	0.69	0.79	E	0.39	0.45	0.54	0.67
de (mm)	8.14	6.79	5.30	3.70	de (mm)	7.28	6.11	4.87	3.49
dm (mm)	10.00	8.00	6.00	4.00	dm (mm)	10.00	8.00	6.00	4.00
de/dm	0.81	0.85	0.88	0.92	de/dm	0.73	0.76	0.81	0.87

Figure 5.64-de/dm for air-water (left) and de/dm for air-silicone oil (right)

From Figure 5.64 it can be seen there is a 20% difference between the d_e and d_m values for air-water, with an even more significant difference in air-silicone oil of 30%. The difference tends to increase as the diameter of the bubbles is increased. It can be inferred that the bubble shape has an impact on the calculations.

5.8.6. Modelling conclusions and further modelling work

To conclude this section contained an introduction to modelling work on bubble columns. A number of different analytical models were considered and compared with experimental results. Agreement between the various models and experimental results was found to be very good at low gas superficial velocities which meant the assumptions used were reasonable. The agreement was mainly in the homogeneous part of curve. However the agreement was not as good for the heterogeneous part of

the curve. This was true for both air-water and air-silicone oil. Heterogeneous flow is significantly more complicated than homogeneous flow, and the effect of bubble coalescence and break-up, as well as the bubble shape need to be taken into consideration for heterogeneous flow. Model 4 showed the best agreement out of the four models, although this was not surprising since it made use of some of the experimental data as well as a physical model.

Therefore to build on the work presented in this section, Models 3 and 4 could be further developed by modifying the code to account for variables such as the bubble shape, which was demonstrated above to make an impact on the calculations. The bubble shape could be specified as elliptical instead of spherical. In addition, the bubble size distribution could be deduced using chords, as was demonstrated by Langston et al. (2001). This could be compared with the distributions generated experimentally, which were based on the area/volume of a sphere. Experiments with the same bubble column could be set up such that an external disturbance is imparted to the system to measure the change in output. In this way, the transfer function could then be deduced. Other factors, such as bubble coalescence and break up, could also be taken into account to improve the model performance, particularly for heterogeneous flows. However, this will increase the complexity of the model(s) significantly and CFD is probably a better tool for such analysis. However CFD will require more time to set up the model and subsequently to run the simulations which will be dependent on processor power. CFD has been used to study bubble columns in the past and therefore this work could be extended by creating model(s) in a CFD program similar to the bubble column used experimentally. The results from the CFD could then be directly compared with those obtained experimentally for both air-water and air-silicone oil.

5.9. Summary

Both the CapWMS and CondWMS were applied for the first time extensively on bubble columns and the results presented in this Chapter were for the experimental campaigns with a high level of confidence. Each variant of the WMS produced good agreement with the level swell. The agreement between the CapWMS and level swell for air-silicone oil, was particularly noticeable. This gives a reassurance that while the sensor is intrusive it does not have a significant effect on the flow. The WMS results also compared well with some of the published correlations.

It can be confirmed that the CapWMS is suitable for low conductivity liquids such as silicone oil, and the CondWMS is more appropriate for liquids with higher conductivities such as tap or salinated water. These limitations are more noticeable with no-flowing liquids, due to the additional factors that are discussed in the Appendix. Some modelling work was also attempted, and the semi-empirical approach of using some of the experimental data as part of the model proved the most effective strategy.

It is possible to conclude that the WMS is a suitable instrument for bubble column research and could be applied more extensively in a similar way to more established instruments in this area, such as ECT/ERT and point/optical probes. It is recommended that level swell measurements are always taken simultaneously whenever the WMS is used. This is a good way to compare and cross-check that the data being acquired by the instrument is acceptable and accurate.

6. CHAPTER 6: LARGE DIAMETER PIPES

6.1. Introduction

A comprehensive background on two-phase gas liquid flow in vertical pipes was given in Chapter 2, and Chapter 5 described the first application of the WMS to bubble columns. This Chapter contains details on a further application of the WMS to large diameter pipes, and a description of the five inch vertical facility was given in Chapter 3. The rig was originally designed with parameters supplied by industry that generated realistic values for deepwater risers in particular erosion limits. The work conducted here was for air-water on the 127mm (5 inch) riser.

This research extends the preliminary measurements taken by Ombere-Iyari (2006) on the same facility and using conductance probes. Their work was carried out with air-water, with gas and liquid superficial velocities of 1.1-15.3 m/s and 0.032- 0.3m/s respectively, at pressures of 1 and 2.2 bar(g). This author's work extended the range of those velocities, with the gas and liquid superficial velocities ranging from 3-17 m/s and 0.01-0.7 m/s respectively at 2 bar(g). A campaign of 700 runs was carried out using both the CondWMS and the conductance probes, which were explained in detail in Chapter 3. The measurements obtained with the WMS and presented in this chapter are quite unique. The CondWMS and Conductance probe data will be compared with the conductance probes being abbreviated by CP throughout this chapter. An experimental matrix is given in section 6.2, and entrance effects are ignored. Ombere-Iyari (2006) found that for this facility, the flow was fully developed at distances of approximately 64 diameters or 8 metres from the mixer at the bottom of the riser. As the WMS was placed at a height of 9.3 metres from the bottom of the pipe, the flow

was assumed to be sufficiently developed for all the measurements that were taken in this campaign.

6.2. Experimental Matrix

The matrix of values for the gas and liquid superficial velocities that were used in this research study is shown in Table 6.1. These values represent the limits of the equipment, meaning that it was not possible to go lower or higher than these values with the current experimental configuration. It is also important to note that as the liquid superficial velocity was increased, it proved increasingly difficult to set up the lower gas superficial velocities. This explains why some of the runs were missed out, as the compressors struggled to operate under those conditions. Repeats of the runs were carried out at the end of the experimental campaign to check for repeatability.

Compressor Rotational Speed (RPM)	Liquid flow rate (V/min)																																Exp #	Repetitions V/min / RPM
	3.25	6	10	15	20	25	30	40	45	55	65	70	80	95	110	125	140	160	180	200	225	250	280	315	350	385	425	465	542					
1500	075	100	001	125	026	150	175	200	225	051	250	275	300	325	350	374	398	421	444	467	490	513	536	559	581	603	625	647	669	690	3	6/1500		
1475	076	101	002	126	027	151	176	201	226	052	251	276	301	326	351	375	399	422	445	468	491	514	537	560	582	604	626	648	670	691	6	1450		
1450	077	102	003	127	028	152	177	202	227	053	252	277	302	327	352	376	400	423	446	469	492	515	538	561	583	605	627	649	671	692	10	1400		
1425	078	103	004	128	029	153	178	203	228	054	253	278	303	328	353	377	401	424	447	470	493	516	539	562	584	606	628	650	672	693	20	1350		
1400	079	104	005	129	030	154	179	204	229	055	254	279	304	329	354	378	402	425	448	471	494	517	540	563	585	607	629	651	673	694	40	1300		
1375	080	105	006	130	031	155	180	205	230	056	255	280	305	330	355	379	403	426	449	472	495	518	541	564	586	608	630	652	674	695	55	1250		
1350	081	106	007	131	032	156	181	206	231	057	256	281	306	331	356	380	404	427	450	473	496	519	542	565	587	609	631	653	675	696	70	1200		
1325	082	107	008	132	033	157	182	207	232	058	257	282	307	332	357	381	405	428	451	474	497	520	543	566	588	610	632	654	676	697	95	1150		
1300	083	108	009	133	034	158	183	208	233	059	258	283	308	333	358	382	406	429	452	475	498	521	544	567	589	611	633	655	677	698	125	1100		
1275	084	109	010	134	035	159	184	209	234	060	259	284	309	334	359	383	407	430	453	476	499	522	545	568	590	612	634	656	678	699	160	1050		
1250	085	110	011	135	036	160	185	210	235	061	260	285	310	335	360	384	408	431	454	477	500	523	546	569	591	613	635	657	679	700	200	1000		
1225	086	111	012	136	037	161	186	211	236	062	261	286	311	336	361	385	409	432	455	478	501	524	547	570	592	614	636	658	680					
1200	087	112	013	137	038	162	187	212	237	063	262	287	312	337	362	386	410	433	456	479	502	525	548	571	593	615	637	659	681					
1175	088	113	014	138	039	163	188	213	238	064	263	288	313	338	363	387	411	434	457	480	503	526	549	572	594	616	638	660	682					
1150	089	114	015	139	040	164	189	214	239	065	264	289	314	339	364	388	412	435	458	481	504	527	550	573	595	617	639	661	683					
1125	090	115	016	140	041	165	190	215	240	066	265	290	315	340	365	389	413	436	459	482	505	528	551	574	596	618	640	662	684					
1100	091	116	017	141	042	166	191	216	241	067	266	291	316	341	366	390	414	437	460	483	506	529	552	575	597	619	641	663	685					
1075	092	117	018	142	043	167	192	217	242	068	267	292	317	342	367	391	415	438	461	484	507	530	553	576	598	620	642	664	686					
1050	093	118	019	143	044	168	193	218	243	069	268	293	318	343	368	392	416	439	462	485	508	531	554	577	599	621	643	665	687					
1025	094	119	020	144	045	169	194	219	244	070	269	294	319	344	369	393	417	440	463	486	509	532	555	578	600	622	644	666	688					
1000	095	120	021	145	046	170	195	220	245	071	270	295	320	345	370	394	418	441	464	487	510	533	556	579	601	623	645	667	689					
975	096	121	022	146	047	171	196	221	246	072	271	296	321	346	371	395	419	442	465	488	511	534	557	580	602	624	646	668						
950	097	122	023	147	048	172	197	222	247	073	272	297	322	347	372	396	420	443	466	489	512	535	558											
925	098	123	024	148	049	173	198	223	248	074	273	298	323	348	373	397																		
900	099	124	025	149	050	174	199	224	249		274	299	324	349																				

Table 6.1-Experimental Matrix with run numbers. A crossed box indicates that a run was not conducted

6.3. Results

Quantitative results will now be presented in order of increasing complexity. From the matrix above it can be seen that 29 superficial liquid velocities were investigated. As the data set is extensive, only a selection will be shown in this chapter, with much of

the quantitative data being presented on the attached DVD. Towards the end of this chapter, the results from a CFD simulation are also given.

6.3.1. Time series

A selection of the time series plots obtained using the WMS and displaying the cross-sectionally averaged void fraction against time are shown in Figure 6.1. These are for the highest and lowest values of gas and liquid superficial velocities, and they show the data over a 10 second period. At low superficial liquid velocities the void fraction fluctuated within a narrow band at a value greater than 0.9. As the liquid velocity was increased, the fluctuations increased as did the range over which the fluctuations occurred. The time series for all the runs can be found on the enclosed DVD.

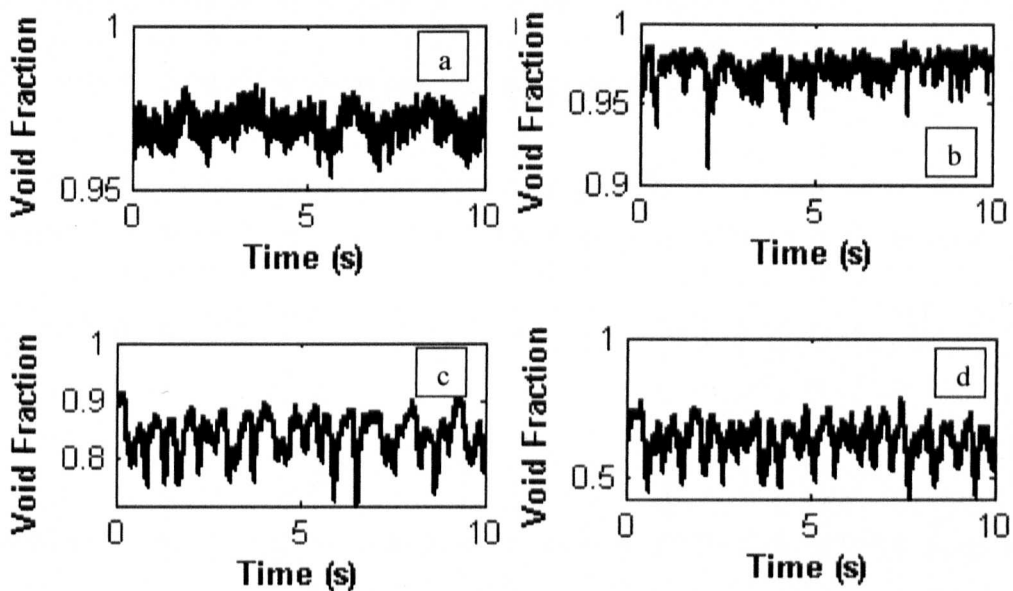


Figure 6.1 A selection of WMS time series data for the 127mm pipe.

a/b: gas superficial velocities=15.6 and 6.81 m/s, liquid superficial velocity=0.013 m/s
 c/d: gas superficial velocities=11.7 and 3 m/s, liquid superficial velocity=0.66 m/s

6.3.2. Time and space averaged void fraction

From the time series, the data for the WMS can be averaged over time. The mean void fractions are plotted in Figure 6.2, and the film thickness is related to the void fraction by equation 2.46. Using this equation, the mean film thickness was calculated for all

700 runs, and these were then plotted in Figure 6.3. The trend is clear, which is that as the superficial liquid velocity is increased; the mean void fraction tends to decrease, which in turn causes the film thickness to increase.

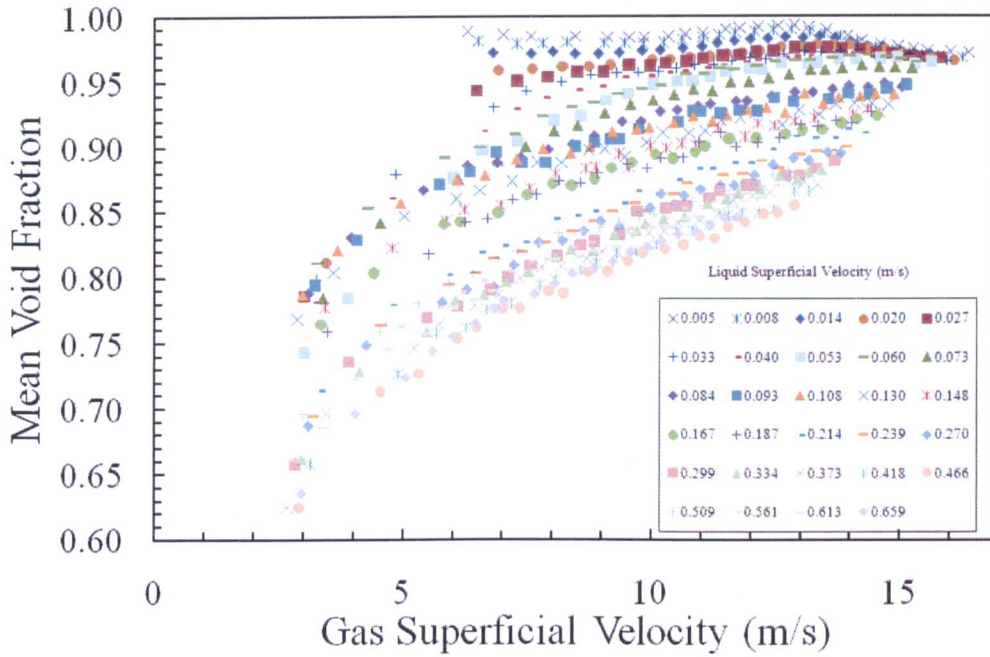


Figure 6.2- Effect of gas and liquid superficial velocities on the mean void fraction.

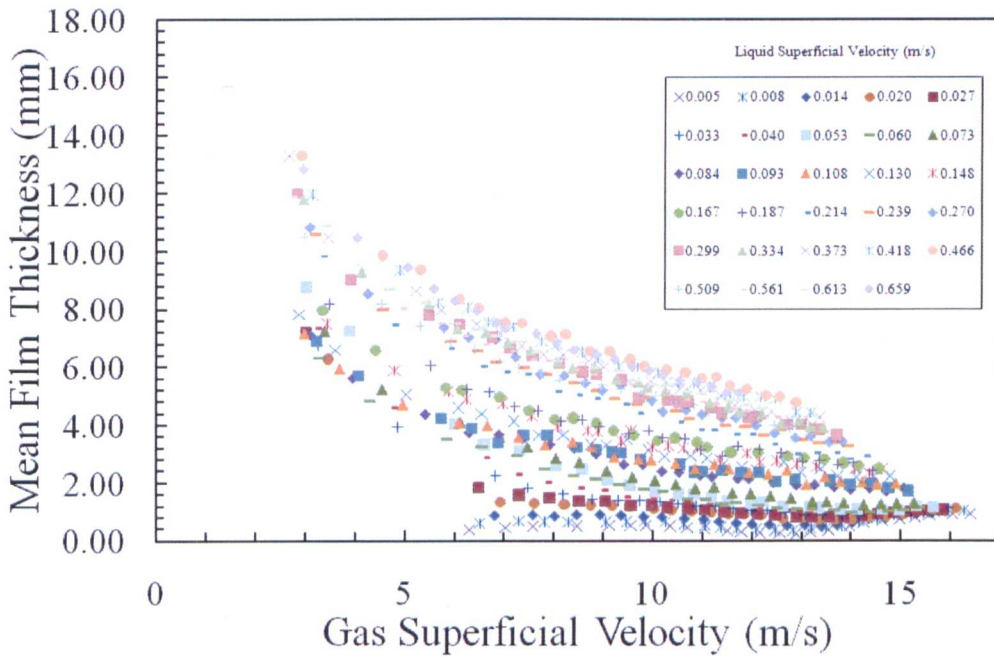


Figure 6.3- Effect of gas and liquid superficial velocities on the mean film thickness.

The experiments were conducted at 2 bar(g) i.e. 3 bar(abs), and therefore the density of air was approximately 3.6 kg/m^3 . The equivalent data for the WMS was obtained simultaneously using the conductance probes. Similar graphs to Figures 6.2 and 6.3 could therefore be produced for the conductance probes. The ratios of the mean void fractions between the two measuring techniques are plotted against the superficial gas velocity, as shown in Figure 6.4. This allows the comparison of the mean void fraction as measured by the two different instruments. The data from the two instruments could also be plotted as a scatter graph.

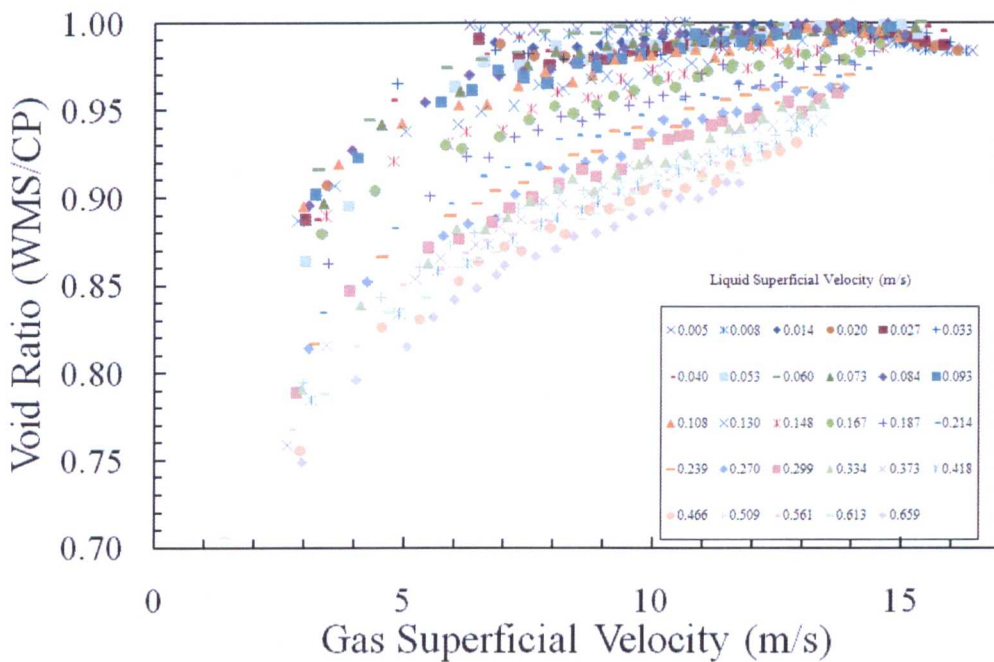


Figure 6.4-Effect of gas and liquid superficial velocities on the ratio of void fractions measured by the WMS to the void fractions measured by the conductance probes

There is a good agreement between the results from the two instruments at low film thicknesses (high void fractions), implying that the two instruments performed well in the annular flow regime. However, as the void fraction decreased and the flow transitioned into churn, the data from the two instruments started to diverge.

However, the above comparison only considered the mean values. A measure of the variation of values obtained in any run can be represented by the PDFs, which were extracted for all 700 runs for both the WMS and CP. A selection of these can be seen in Figure 6.5 for the time series shown above in Figure 6.2. The PDFs for all the other flow rates are provided on the DVD. Two main profiles can be seen in the PDF for the WMS data. The first is a single peak at a high void fraction, which has the characteristics of annular flow, and the second is a peak with a long tail, which signifies churn flow. Anomalies between these two shapes signify the churn-annular transition.

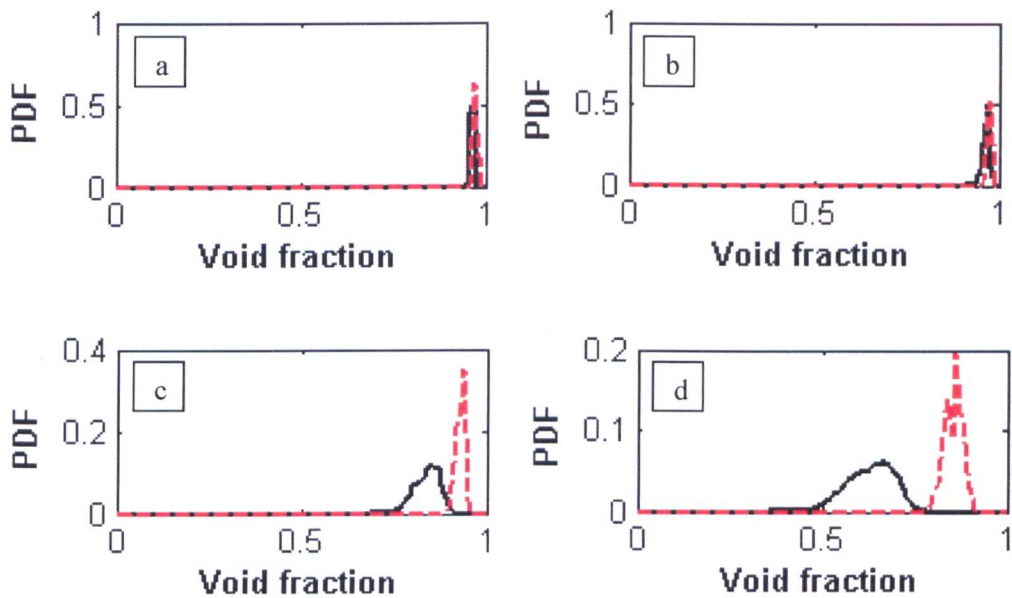


Figure 6.5-PDF profiles for the time series in Fig 6.1. Solid line: WMS; dotted line: CP
a/b: gas superficial velocities=15.6 and 6.81 m/s, liquid superficial velocity=0.013 m/s
c/d: gas superficial velocities=11.7 and 3 m/s, liquid superficial velocity=0.66 m/s

The WMS and CP did not always generate the same PDFs, both in terms of shape and value. For example, in Figure 6.5(a), the PDFs for both instruments are almost identical. However, as the gas superficial velocity is lowered, the output from the two instruments starts to diverge, as shown in Figure 6.5(b). This is observed for other gas and liquid velocities (again, see the enclosed DVD). The void fraction decreases as a

consequence of the gas velocity being decreased, and in addition as the liquid flow rates are increased, there is a significant shift to the left of the main peak of the PDF for the WMS. For the highest liquid velocity of 0.66m/s, the PDFs for the two instruments did not match for all 21 runs. This could be explained due to the different methods of calibration for the conductance probes. To date, three methodologies have been adopted. The first two methods were used by Ombere-Iyari (2006), where plastic spheres of various diameters were inserted into the pipe to simulate bubble flow, and subsequently a cylindrical plastic tube was placed inside the pipe to simulate annular flow. The third calibration method was devised by Van der Meulen (2010). This novel methodology placed a cylindrical tube of various thicknesses and beads in the film to simulate annular type flow of a gas core with a liquid film. The film may or may not contain bubbles, and this calibration took account of that possibility. This set of experiments was conducted entirely with this third type of calibration. At the lowest gas velocities and higher liquid velocities, the conventional annular type flow for which the CP was calibrated for did not take place inside the pipe. The PDF comparisons correlate well with the earlier data set that showed the comparison of the mean void fraction results from both instruments (Figure 6.4), where an agreement was observed at the higher void fractions, but as the void fraction reduced, the two instruments started to diverge. Ombere-Iyari (2006) also made similar observations regarding the PDFs for the CP results, as they did not agree with visual (high speed camera) observations. In those tests, the CP showed annular flow when the visuals displayed churn flow. A further statistical exercise could be carried out on the PDF plots for both the WMS and CP by measuring the difference in the main peaks from the PDF for both instruments. What can be concluded here is that the CP accurately measures annular flow, but struggles with the churn flow regime, meaning that it would be difficult to calibrate the CP for that flow pattern.

6.3.3. Radial void profiles

The radial profiles can also be extracted, four examples of which are shown in Figures 6.6 to 6.9. The other profiles can be found on DVD. It can be observed that the radial void fractions tend to get lower as the gas superficial velocity is decreased. It is also interesting to note that the profile is flat for the lower liquid velocities, but it transforms into a parabolic shape as the superficial liquid velocity is increased. This could also be related to the flow pattern, with the flat profiles tending to occur for annular type flow, whereas the parabolic shape is usually representing churn flow.

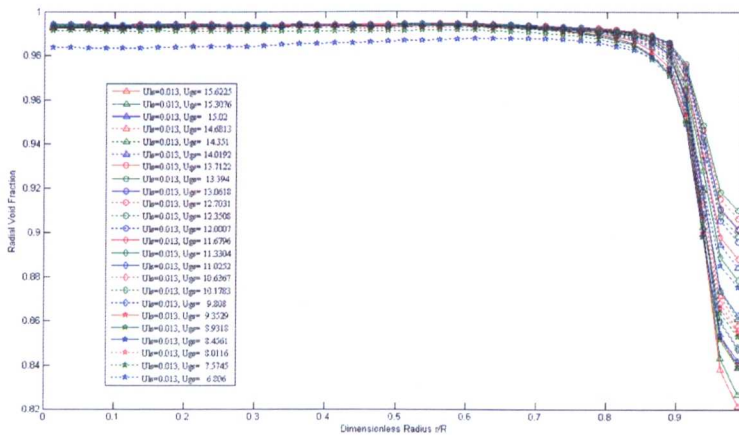


Figure 6.6-Radial Profiles for the 127mm pipe. Superficial liquid velocity 0.013 m/s

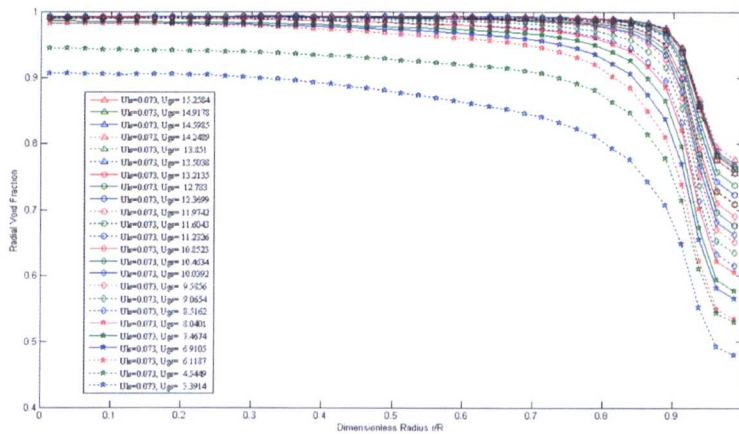


Figure 6.7- Radial Profiles for the 127mm pipe. Superficial liquid velocity 0.073 m/s

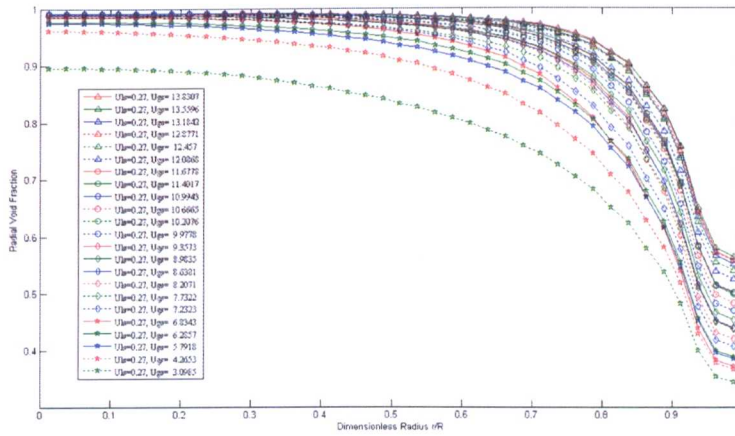


Figure 6.8- Radial Profiles for the 127mm pipe. Superficial liquid velocity 0.27 m/s

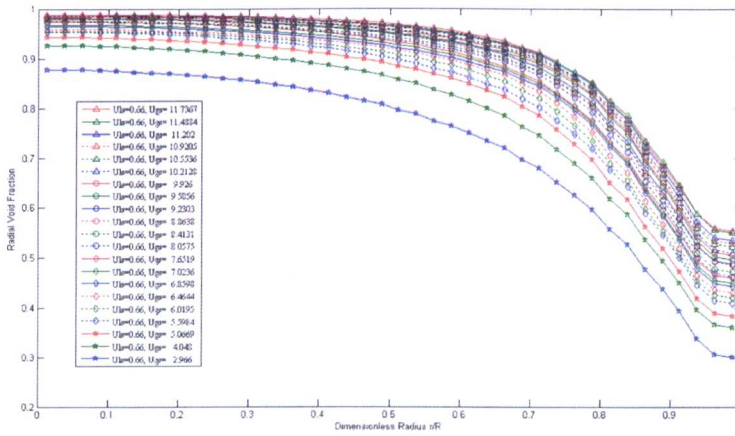


Figure 6.9- Radial Profiles for the 127mm pipe. Superficial liquid velocity 0.66 m/s

6.3.4. Bubble size distribution/bubble size resolved voids

Volume based bubble size distributions (BSD) were extracted for all the runs. Three examples are shown in Figures 6.10 to 6.12 and the remaining plots are on the DVD. The data for a superficial liquid velocity of 0.013 m/s has not been shown as the instrument did not detect any bubbles for this reading, because the flow was clearly annular.

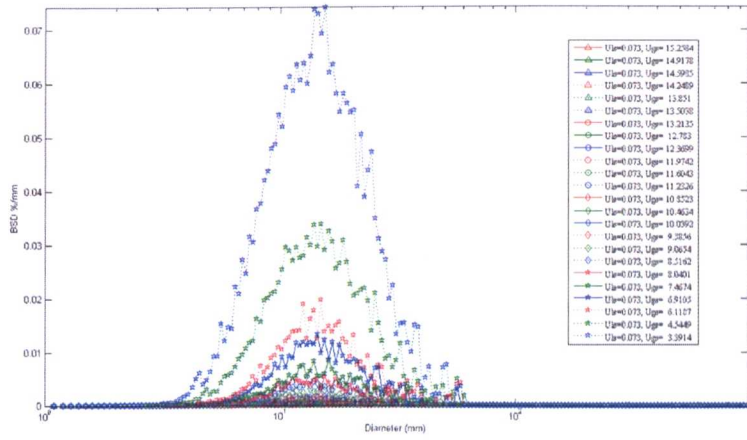


Figure 6.10- BSD for 127mm pipe. Liquid superficial velocity 0.073 m/s

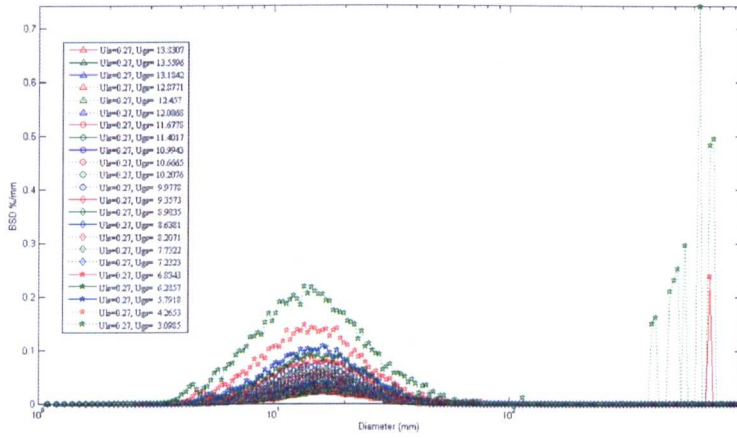


Figure 6.11- BSD for 127mm pipe. Liquid superficial velocity 0.27 m/s

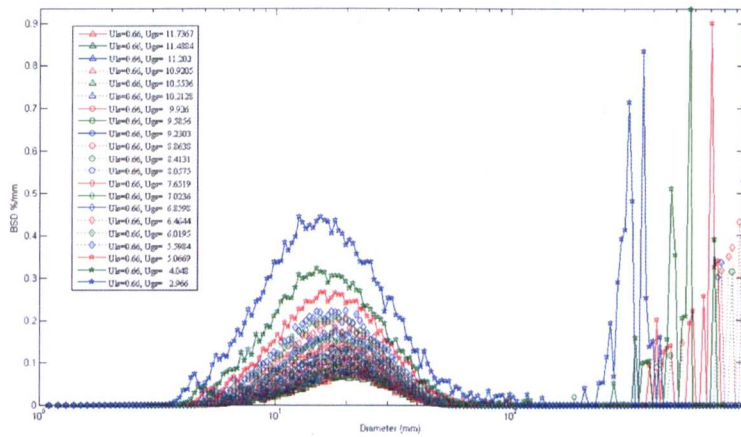


Figure 6.12- BSD for 127mm pipe. Liquid superficial velocity 0.66 m/s

A single peak is evident in Figure 6.10 for a liquid velocity of 0.073 m/s. A double peak appears to form as the liquid velocity is increased, which is demonstrated in Figures 6.11-6.12. The WMS appears limited in measuring the bubbles in the churn/annular region. This is because it is not able to detect very small bubbles that may be occurring, for example in the liquid film in annular flow. In addition to the above plots, the bubble size resolved as a time series can also be generated. This was processed for all the runs, and they are included on the DVD.

6.3.5. Visualisation (cross-sectional voids)

The strength of the WMS is its spatial resolution, hence its ability to visualise the flow. Images made up of the time sequences of the phase distribution across a pipe diameter have been created, which were processed for the central chord of the WMS i.e. in the middle of the pipe. Four liquid velocities are shown below in Figures 6.13-6.16.

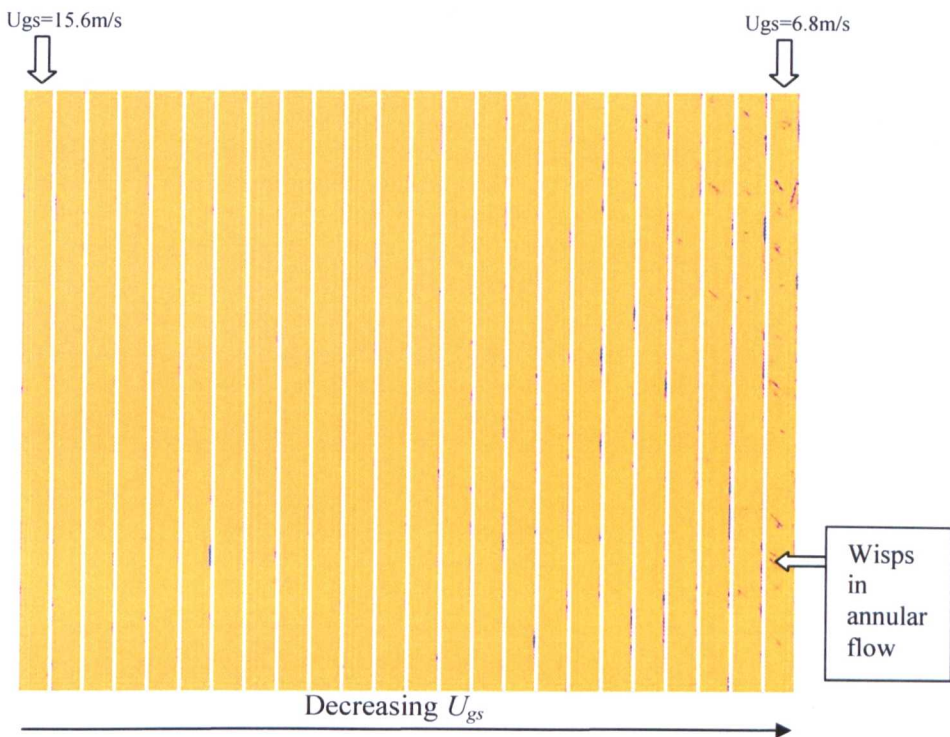


Figure 6.13-Flow Visualisation with the WMS in centre of pipe; $U_{ls} = 0.013 \text{ m/s}$; 24 runs

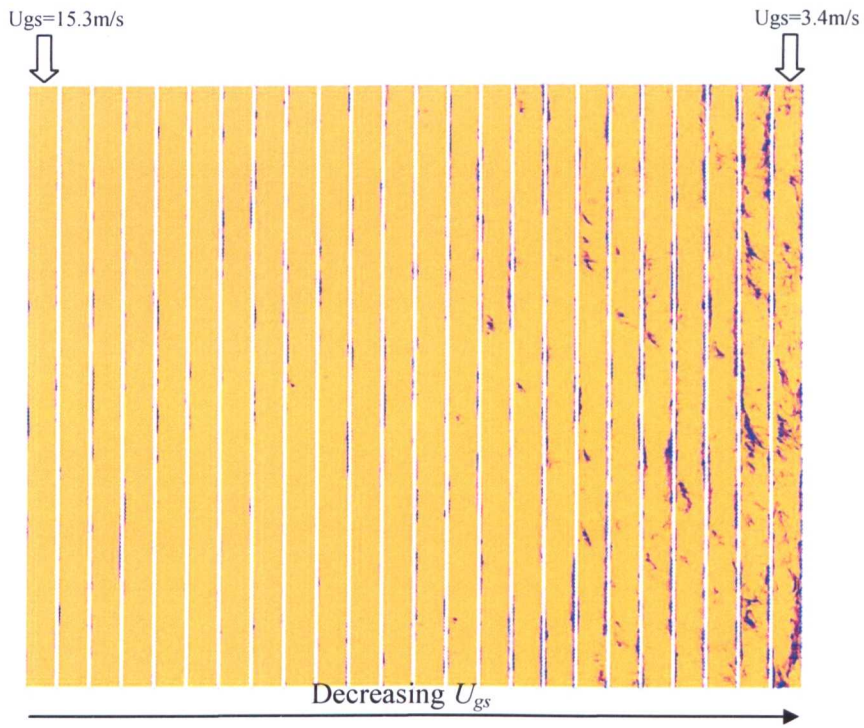


Figure 6.14- Flow Visualisation with the WMS in centre of pipe; $U_{ls} = 0.073 \text{ m/s}$; 24 runs

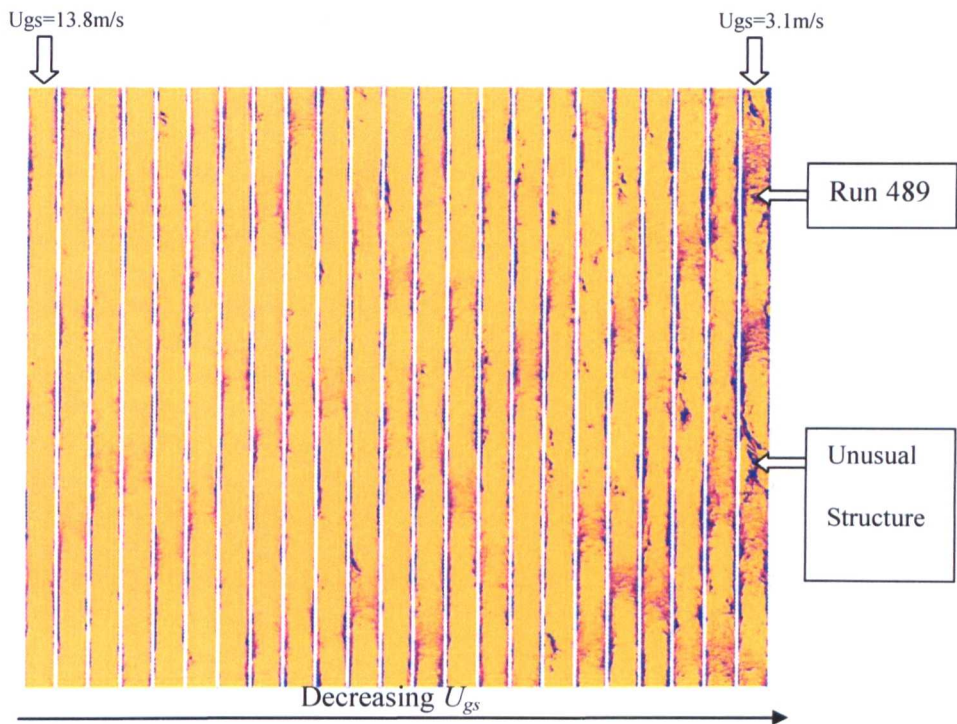


Figure 6.15- Flow Visualisation with the WMS in centre of pipe; $U_{ls} = 0.27 \text{ m/s}$; 23 runs

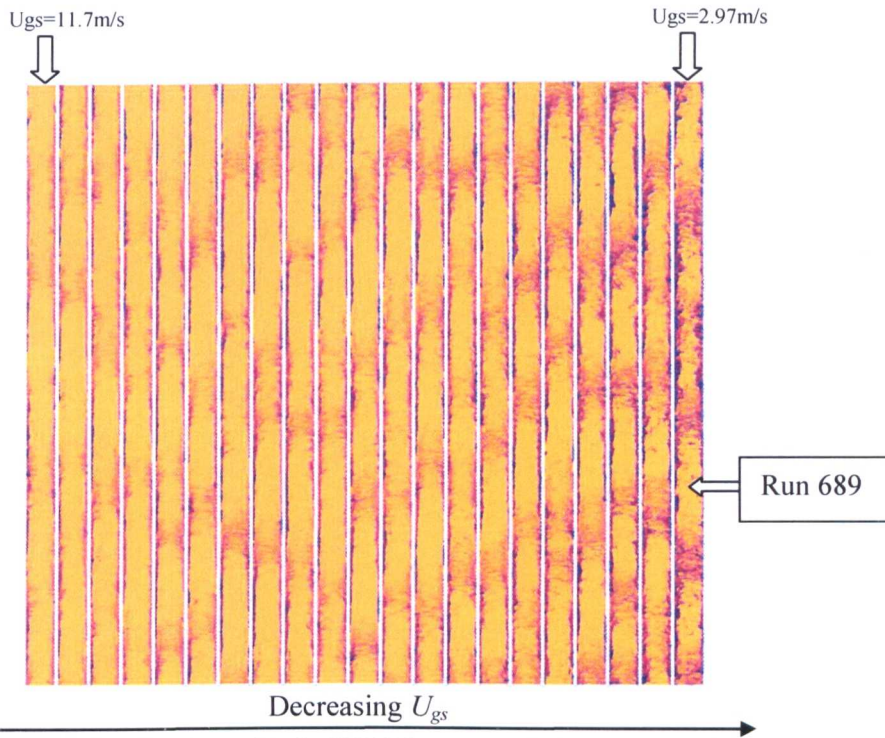


Figure 6.16- Flow Visualisation with the WMS in centre of pipe; $U_{ls} = 0.66$ m/s; 21 runs

The rest of the images are on the DVD. Although they are difficult to detect from these static images, when used in conjunction with the (.v files) movies that the WMS generates, three of the recognised flow patterns are evident from these visualisations; churn, annular and wispy-annular. It can be seen that the flow pattern moves from annular to churn flow as the superficial gas velocity is reduced, for example in Figure 6.14. Churn flow is depicted clearly from the WMS, as it is possible to zoom in on one run and inspect it in more detail. For example, run 689 was selected, which had the highest flow of liquid and lowest flow of gas in the experimental campaign. Figure 6.17 shows the axial visualisation of the flow.

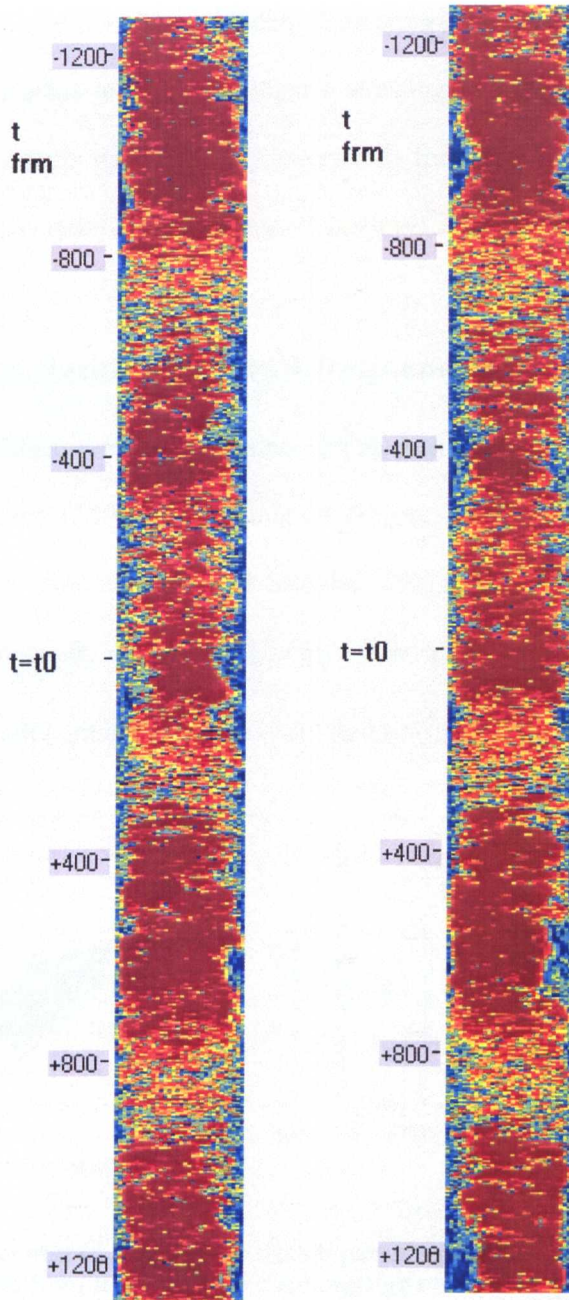


Figure 6.17- Run 689. (Left): vertical and (right): horizontal sectional view in the centre of the pipe

The complexity of churn flow is apparent. One limitation here is that the WMS will not show whether the mixture is moving up and down, as would usually be expected for churn flow. If the v.file (run 689 on DVD) is accessed using the display programme, it will show the whole mixture moving upwards. It seems that the

continuous gas core is not always evident. Sometimes the liquid bridges and virtually covers the entire cross-section. It is also interesting to note the periodicity of this bridging, which occurs approximately every 400 frames or 0.4 of a second. Churn flow was previously described as “chaotic”, however it has periodic structures.

6.4. Correlation of overall frequencies

The frequency of these periodic structures can be considered in terms of dimensionless quantities. Azzopardi (2004) showed that the frequency data for bubbly and slug flow may be correlated using a gas-based Strouhal (St) number, which is (fD/U_{gs}) , or a liquid-based St number, defined as (fD/U_{ls}) . The St number is plotted against the Lockhart–Martinelli parameter, which is defined as $([dp/dz]/[dp/dz]_g)^{0.5}$.

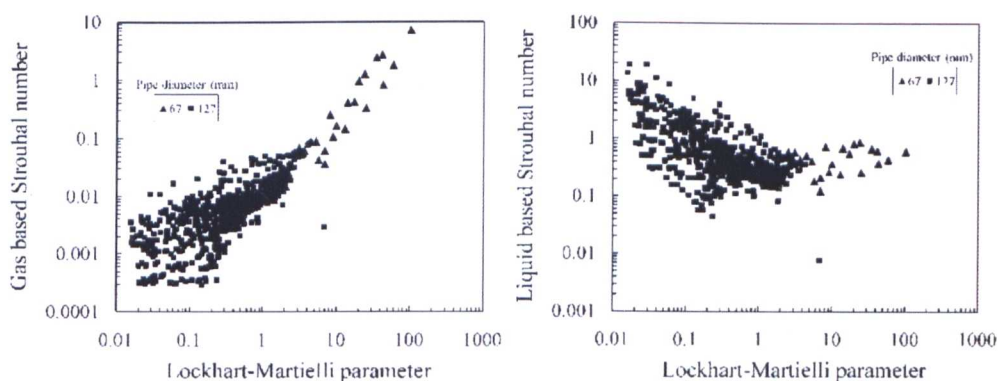


Figure 6.18-Effect of the Lockhart-Martinelli parameter on the gas and liquid based St Numbers. Data from this experimental campaign on 127mm pipe and previously obtained data on 67mm diameter pipe with air-water.

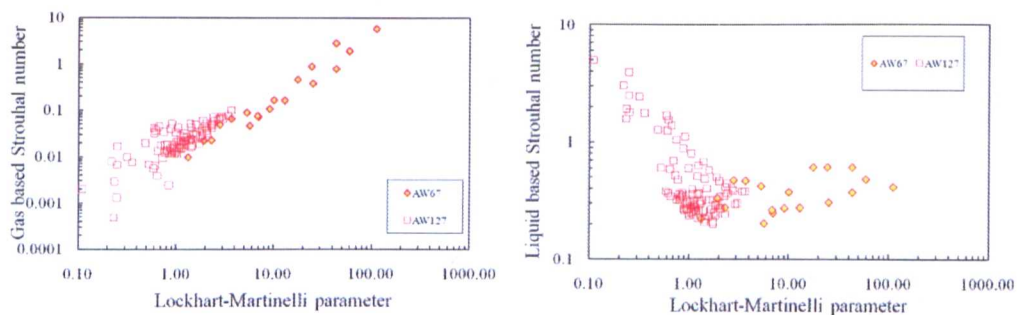


Figure 6.19- Effect of the Lockhart-Martinelli parameter on the gas and liquid based St Numbers (frequencies below 0.5Hz ignored)

The dominant frequencies for the WMS were extracted from the time series for each experimental run using code in Matlab. Figure 6.18 shows the gas and liquid-based Strouhal number plotted against the Lockhart-Martinelli parameter for the full data set of 700 runs measured with the WMS. Some scattering in the data is evident, although if frequencies of less than 0.5 Hz are neglected, less scattering is observed with approximately half of the 700 data points filtered out. Even more data points are filtered out if frequencies of less than 1 Hz are neglected (Figure 6.19). It could be argued that the very low frequency scatter is noise from the equipment as opposed to the actual frequencies of the void waves. However, from the above plots it is clear that for the 67mm pipe, the slope is +1 for the gas-based St number, and for the 127mm pipe, the slope is -1 for the liquid-based St number. The data set for the 67mm pipe shows that the flow was mainly operating in the bubble-slug-churn region, whereas the data set for the 127mm pipe demonstrated the flow was operating in the churn-annular region.

6.5. Test of engineering methods with WMS data

The data from the WMS can be compared against published empirical correlations, and can therefore be used to test the engineering methods commonly used in industry for void fraction and total pressure gradient calculations. Two comparisons will therefore be conducted; first for the pressure drop and second for the void fraction, where correlations will be compared with the WMS data. As outlined in Chapter 2, two of the most popular correlations are the Friedel and CISE methods, details of which are given in the Appendix A.

6.5.1. Test for pressure drop

The gravitational pressure drop can be calculated from the void fraction measured by the WMS. It can then be compared with the gravitational pressure drop (GPD) calculated by CISE's equation. The frictional pressure drop (FPD) can be determined using the correlation suggested by Friedel (1979). Another test of the data can also be carried out by calculating the overall pressure drop i.e. the GPD from the WMS added to the FPD as determined by Friedel. This can then be compared with the pressure drop obtained experimentally on the same rig by Zangana (2011). The dimensionless gas velocity can be calculated using Equation 2.21. Sample comparisons generated by following this procedure are shown in Figures 6.20 and 6.21, with the remaining plots presented on the enclosed DVD. The agreement between the results from the WMS and pressure drop (PD) transducer is very good, except for at the very low liquid velocities (Figure 6.20, left).

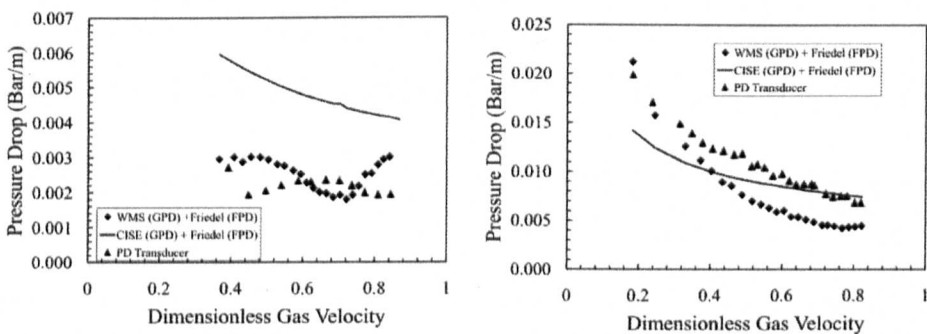


Figure 6.20-Comparison of pressure gradient obtained from Friedel/CISE equations and from Friedel/WMS void fraction against experimental values obtained by Zangana (2011). Liquid superficial velocities left: 0.013 m/s and right: 0.073 m/s

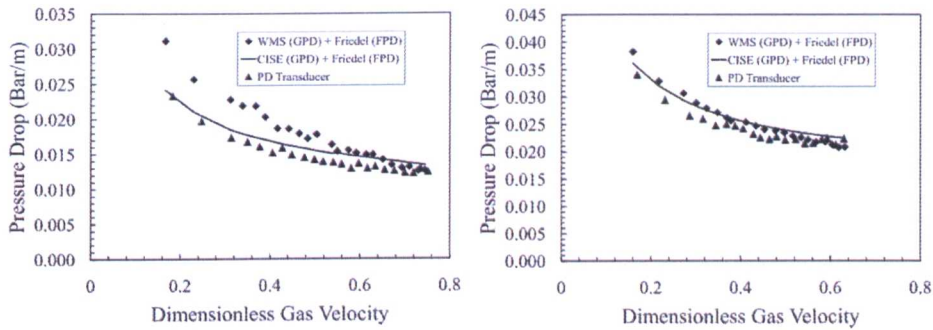


Figure 6.21- Comparison of pressure gradient obtained from Friedel/CISE equations and from Friedel/WMS void fraction against experimental values obtained by Zangana (2011). Liquid superficial velocities left: 0.27 m/s and right: 0.66 m/s

In addition, the agreement between the WMS and CISE equation results is again very good except for the very low liquid velocities (Figure 6.20, left). This is probably due to the CISE correlation being applied to a data range that is outside of the experimental data range for which it was constructed. A comparison of the full data set of the GPD for the WMS against the GPD calculated by CISE can be seen in Figure 6.22. Additionally, the total pressure drop generated by the results of the WMS plus the Friedel correlation was compared against the total pressure drop generated by the CISE equation plus the Friedel correlation, which is also shown in Figure 6.22. It can be seen that the agreement is very good in both cases.

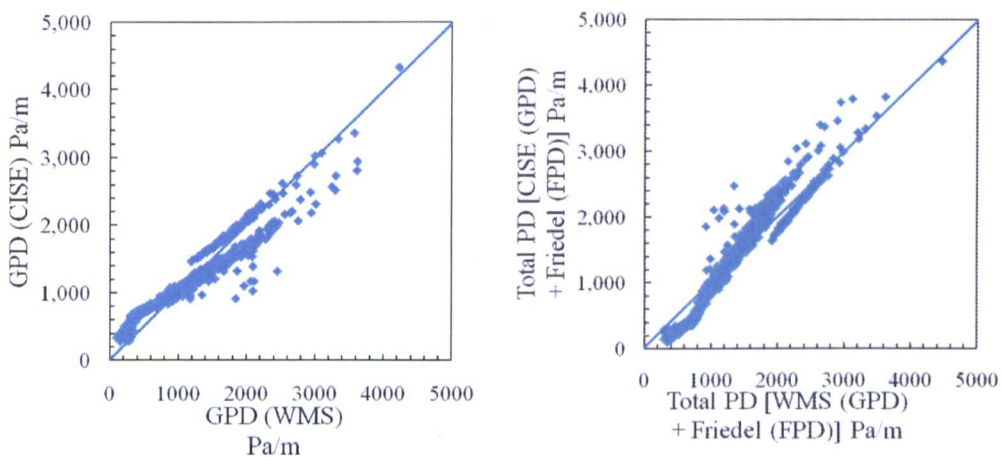


Figure 6.22-(Left): Gravitational pressure drop obtained using CISE against gravitational pressure drop obtained by the WMS. (Right): Overall pressure drop obtained using CISE/Friedel against overall pressure drop obtained by WMS/Friedel

6.5.2. Test for void Fraction

The void fraction determined by the WMS can also be compared against a number of published empirical correlations. Two of the most popular correlations are CISE and Chisholm. Figures 6.23 and 6.24 show a selection of plots to demonstrate how the void fractions for the WMS compare with those generated by CISE.

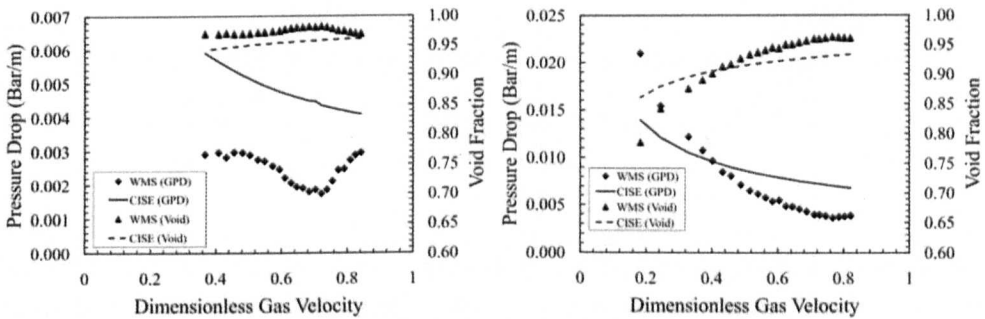


Figure 6.23- WMS void fraction compared against void fraction predicted by CISE. Superficial liquid velocities of (left): 0.013 m/s, (right): 0.073m/s

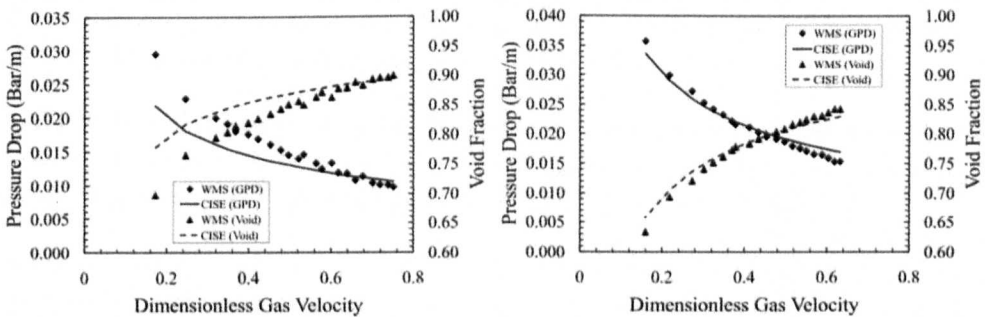


Figure 6.24- WMS void fraction compared against void fraction predicted by CISE. Superficial liquid velocities of (left): 0.27 m/s, (right): 0.66 m/s

On the same plots, the pressure drops that were presented in the previous section are also shown. The GPD is approximately equal to $g\rho_l(1-\epsilon_g)$ which explains why the void fraction curves are symmetrical to those of GPD about the horizontal. The agreement in general is very good, again except for the very low liquid velocities (Figure 6.23, left). The void fractions were calculated using the CISE and Chisholm correlations for the full data set, which were compared against the experimentally generated void fractions from the WMS. This is shown in Figure 6.25, where it can be seen that both

the CISE and Chisholm correlations perform well against the WMS data. An important finding is that although Chisholm's correlation is a much simpler expression, it produces similar results to the more complicated CISE expression.

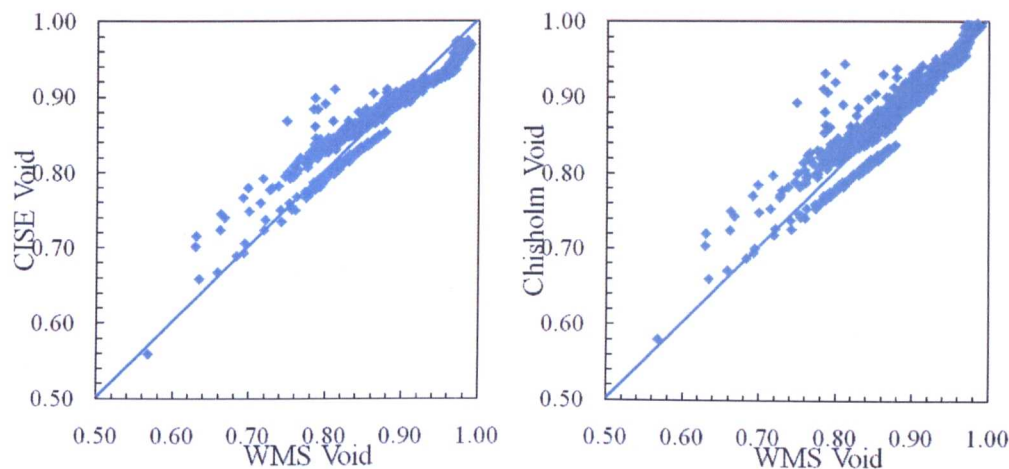


Figure 6.25- (Left): Void fraction predicted by CISE compared against WMS void fraction, (right): void fraction predicted by Chisholm compared against WMS void

Simulations were carried out using the industrial code WELLFLO and results were subsequently compared with those generated experimentally by the WMS. WELLFLO is a powerful software tool used mainly in the oil and gas industry to model wells and the flow within tubes. It allows the generation of flow maps, and the determination of the phase distribution and liquid content along the tube. It uses many different correlations, which may be mechanistic or empirical. A model representing the 127mm pipe was constructed in WELLFLO and the OLGAS mechanistic methodology was selected for the simulations. OLGAS is based on data obtained from the SINTEF two-phase flow laboratory, which operates under conditions similar to those experienced in the field. SINTEF's test loop was 800m long with a 203mm diameter pipe, with operating pressures of between 20 and 90 bar(g). Gas superficial velocities of up to 13 m/s and liquid superficial velocities of up to 4 m/s were obtained. Over 10,000 experiments were conducted on the test facility, and the OLGAS methodology outputs four flow regimes, which are stratified, annular, slug

and dispersed bubble flow. This model is recommended for void fraction predictions at all angles (i.e. horizontal and vertical). The results for four different simulations representing four different liquid superficial velocities can be seen in Figure 6.26.

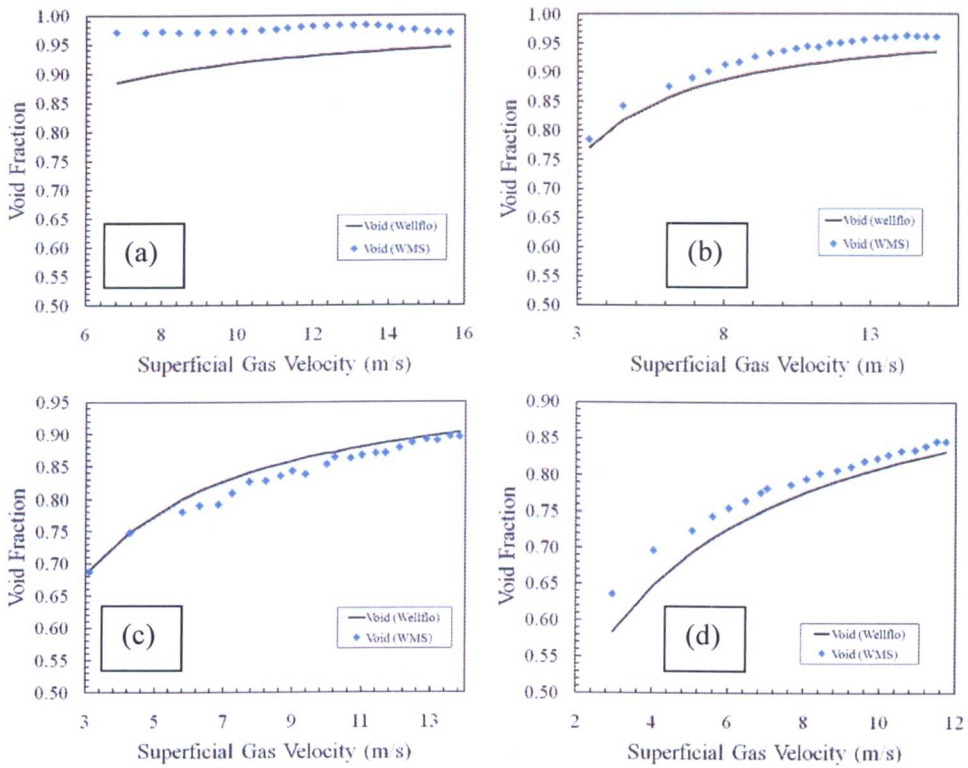


Figure 6.26-Comparison between computational (WELLFLO) generated void fraction and experimental (WMS) void fraction. Liquid superficial velocities of (a) 0.013 m/s, (b) 0.073 m/s, (c) 0.27 m/s and (d) 0.66 m/s

The agreement between the WMS and WELLFLO is clear. WELLFLO is also able to provide information on pressure drops, which is broken down into gravitational, frictional and accelerational components. Further analysis can be performed by comparing the WMS pressure drops presented earlier in this chapter with those generated by WELLFLO. It is worth noting that some of the major software packages used to simulate two-phase flow do not show churn flow on their flow maps, for example LEDAFLO, WELLFLO and OLGA. This reinforces the fact that churn flow is often entirely avoided as a flow pattern and it is poorly understood.

6.5.3. Test for flow pattern

Both Ombere-Iyari (2006) and Van der Meulen (2010) acquired high speed camera images from the 127mm pipe diameter facility. They identified that the pipe was operating mostly in the churn-annular region, and Ombere-Iyari (2006) presented the images from five runs using the high speed camera as shown in Table 6.2 below. The WMS in this campaign confirmed the flow patterns for four out of these five runs.

HS Video	Ugs	Uls	Pressure	HS Pattern	WMS Run	Ugs	Uls	Pressure	WMS Pattern
1	9.3	0.1	2.2 bar (g)	Churn	run315	9.2	0.11	2 bar (g)	Wispy-Churn
7	6.5	0.035	2.2 bar (g)	Churn	run172	6.8	0.033	2 bar (g)	Wispy-annular
8	5.6	0.3	2.2 bar (g)	Churn	run510	5.5	0.3	2 bar (g)	Churn
10	16.8	0.1	2.2 bar (g)	Annular	run300	14.9	0.11	2 bar (g)	Annular
11	17.6	0.031	2.2 bar (g)	Annular	run150	15.9	0.033	2 bar (g)	Annular

Table 6.2-Runs performed by Ombere-Iyari taken on the 127mm pipe using a HS Camera compared with WMS results taken on the same rig with similar flow conditions.

By inspecting the data generated in this experimental campaign using the WMS, it is clear that wisps were detected in both annular flow and in churn flow. As already mentioned in Chapter 2, wisps were reported by Hernandez-Perez et al (2010) to occur in a 67mm pipe in the churn flow regime, and prior to this, such wisps have not been reported to occur in large diameter pipes. For some of the runs, in annular flow, the frequency of wisps increases as the gas velocity is lowered, and sometimes the wispy annular flow transitions into a wispy churn regime. It is interesting on examination of video 1, that Ombere-Iyari (2006) labelled this as churn. However, for this run the WMS detected structures were also forming, as shown in Figure 6.27. Predictably, the wisps occurring within churn flow are fairly difficult to identify even using a high speed camera, as it records the flow as seen through the transparent section.

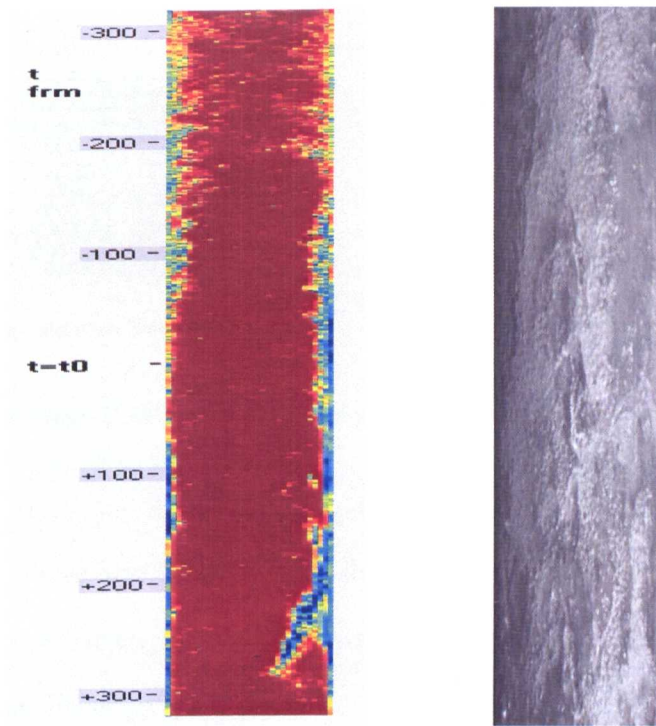


Figure 6.27-Wisps in churn flow. (Left): WMS axial view in the centre of the pipe. (Right): HS camera image taken by Ombere-Iyari (2006). Wisps were identified in the WMS sequence

A sequence of wispy annular flow in a 32mm diameter pipe was shown in Figure 2.1 in Chapter 2 (Rhodes, 1980). Though this is not totally clear, it has a similar appearance to Figure 6.27 (left), with structures occurring in the centre of the pipe.

6.6. Comparison between 67 and 127mm diameter pipes

As mentioned in Chapter 2, it is possible to represent data on different types of flow map. The usual approach is to plot the data on a superficial velocity map, although an improved approach is to use the momentum flux map as previously used by Hewitt-Roberts, shown in Figure 6.28. This represents the full data set for this experimental campaign expressed as gas or liquid velocities. This then allows the comparison of different diameter pipes.

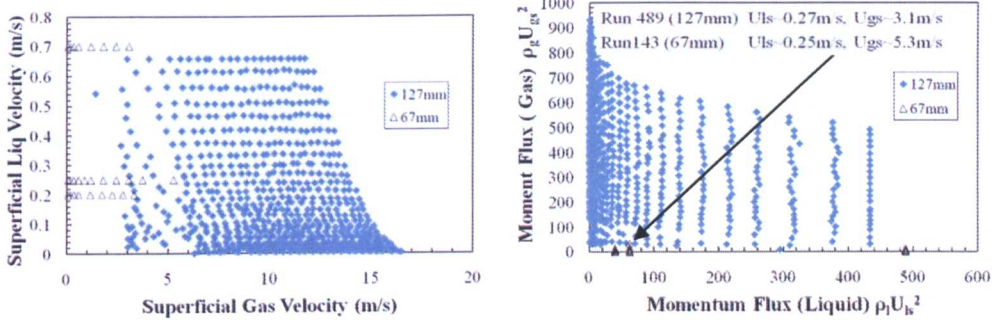


Figure 6.28-Flow maps. (Left): superficial velocity map and (right): momentum flux map

The flow maps above also show the runs that were carried out by Hernandez-Perez (2007) on a 67mm diameter pipe with air-water. Two runs that are close in value for the two different diameters were identified on the momentum flux map, which are run143 (67mm) for $U_{ls} \sim 0.27\text{m/s}$ and $U_{gs} \sim 3.1\text{m/s}$, and run489 (127mm) for $U_{ls} \sim 0.25\text{m/s}$ and $U_{gs} \sim 5.3\text{m/s}$.

Run143 was reported to be churn flow with wisps occurring in the flow pattern (Figure 6.29, left). It is clear from Figure 6.29 (right) that wisps also occurred in Run 489 in the 127mm diameter pipe. A detailed comparison will now be made between these two runs. First the time series, film thickness and the ratio of film thickness to diameter are plotted in Figure 6.30. From Figure 6.30, the mean void fraction and mean film thickness are extracted, which are summarised in Table 6.3. Evidence is observed that the film thickness depends on the pipe diameter, as the 127mm diameter is almost double that of the 67mm pipe, and the film thicknesses for the two diameters show a similar ratio. This agrees with equation (2.46) where the film thickness for the 127mm diameter pipe is predicted to be approximately double that of the 67mm diameter pipe.

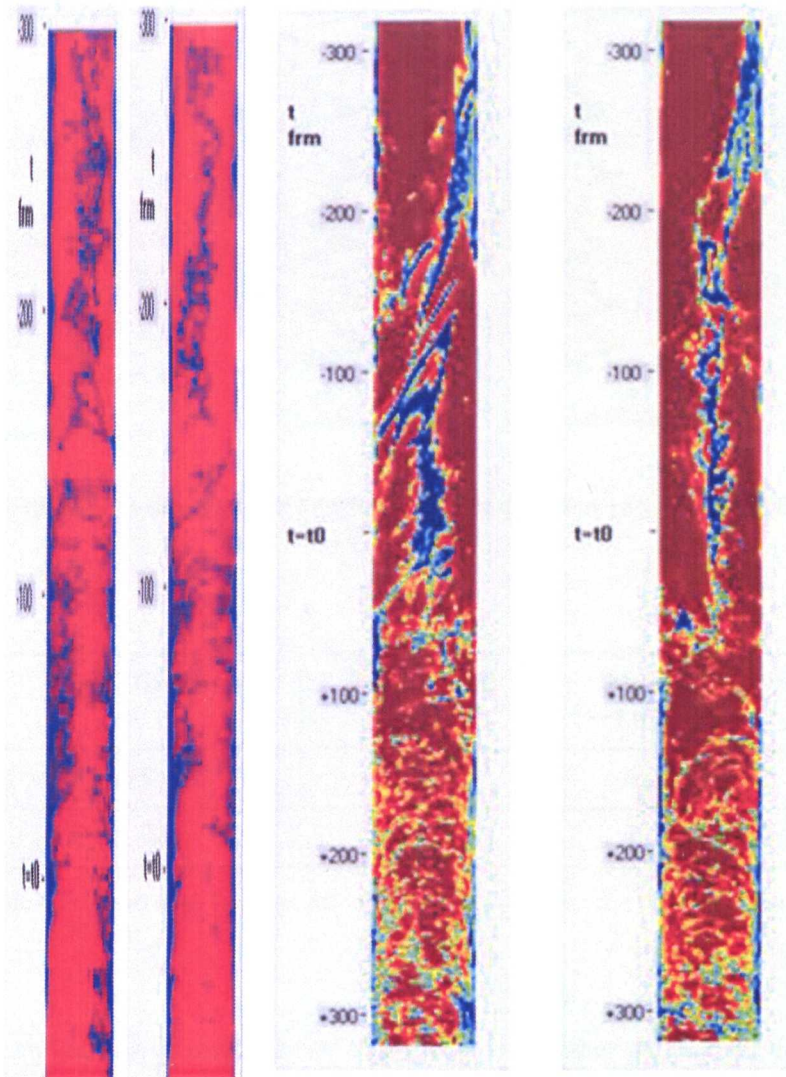


Figure 6.29-Two orthogonal diametric slices in the centre of the pipe. (Left): 67mm and (right): 127mm

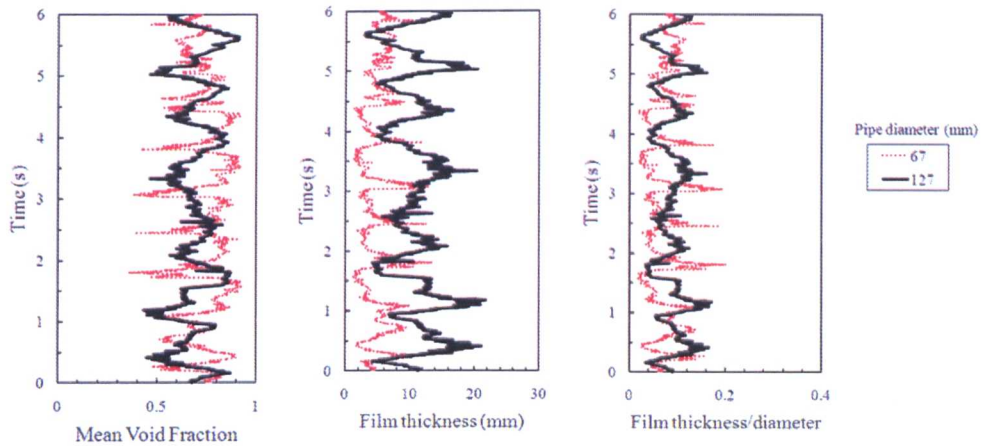


Figure 6.30-Time series, film thickness and film to diameter ratio plots for 67mm and 127mm pipes

Pipe Diameter	Mean Void Fraction	Mean Film Thickness
67mm (Run 143)	0.73	4.94mm
127mm (Run 489)	0.69	10.8mm

Table 6.3-Mean void fraction and mean film thickness for the two diameters

Further quantitative comparisons can be conducted on other parameters, for example between the PDF and PSD (Figure 6.31). The PDF is showing a peak with a long tail for both diameters, which implies churn flow. However, this is actually churn flow with wisps; therefore the PDF methodology is clearly not able to differentiate between churn flow with or without wisps. There is a similar observation for the PDF in the annular flow region, where again wispy-annular flow has a similar PDF footprint for annular flow alone, consisting of a single peak with a high void fraction. The PDF methodology therefore cannot be used to identify the presence of wisps in the experimental runs. The PSD shows a dominant frequency of approximately 1 Hz for both diameter pipes.

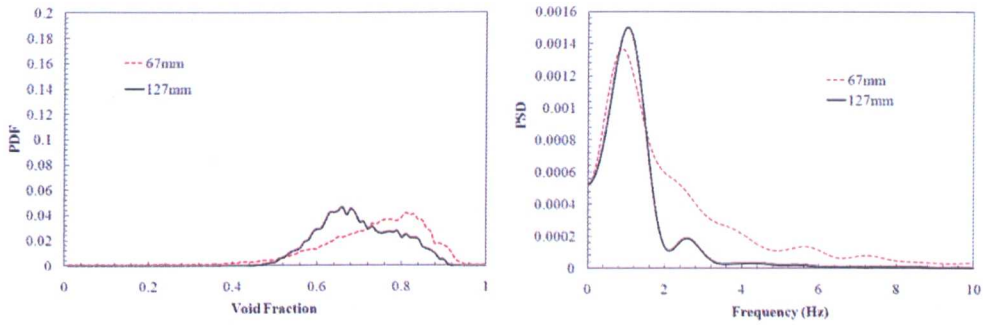


Figure 6.31-(Left): PDF and (right): PSD. Comparisons for 67mm and 127mm diameter pipes

Figure 6.32 shows the parabolic profile of the radial void fraction for both diameter pipes, along with the bubble size distribution that shows a double peak for both diameters.

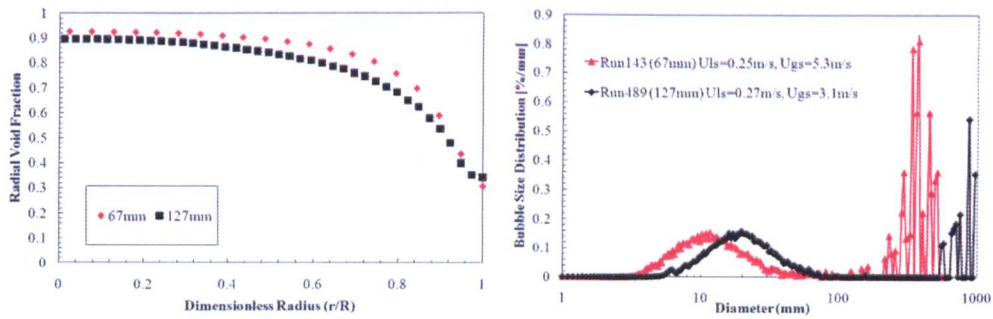


Figure 6.32-(Left): Radial profile and (right): BSD for 67mm and 127mm diameter pipes

Figure 6.33 breaks down the bubble sizes for both diameter pipes as a function of time, which can also be compared with the mean void fraction.

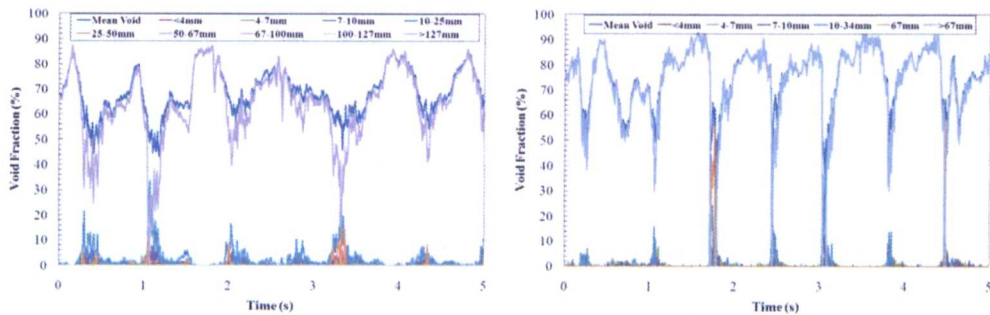


Figure 6.33- Time series of cross-sectionally averaged void fractions resolved by bubble size classes. (Left): 127mm and (right): 67mm

As the wire mesh sensor collects pipe cross-sections of local voids in a matrix form, it is possible to plot the void fraction at each crossing point as a function of time. Therefore, for a 32x32 sensor at a single condition, it is possible to generate 820 plots in total for all the crossing-point(s). This can be useful in quantifying how much liquid or gas there is in a particular part of the pipe. Therefore, for both the 67mm and 127mm pipe, the void fractions were extracted for the central part of the pipe. For the 67mm pipe, a 3x3 matrix, or 9 crossing points, and for the 127mm pipe, a 4x4 matrix, or 16 crossing points were generated. Figure 6.34 shows a typical plot for one of those crossing points for each diameter pipe, which is approximately in the middle of the pipe for each. It is interesting to note the amount of liquid the sensor is detecting in the centre of the pipe. These could be the wisps, which are tendrils of liquid covering certain parts of the cross-section of the pipe.

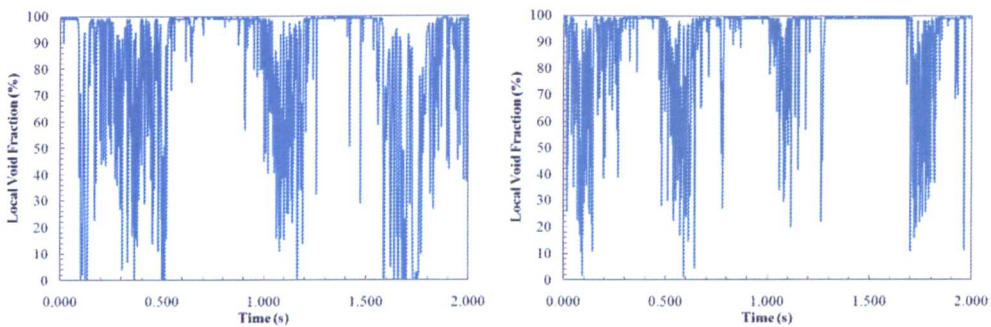


Figure 6.34- (Left): 127mm, point 16x16 and (right): 67mm, point 12x12

It is also possible to plot the mean local void fraction for both runs as a 2D contour map, where each crossing point is averaged for the full 30 seconds. The local void fractions for the full 700 runs on the 127mm pipe can be found on the DVD. Further visuals can be created from the WMS data, for example axial slices of the wisp can be generated, which are shown in Figure 6.35 (67mm pipe) and Figure 6.36 (127mm pipe). The axial slices clearly show the structures that are present in the centre of the pipe.

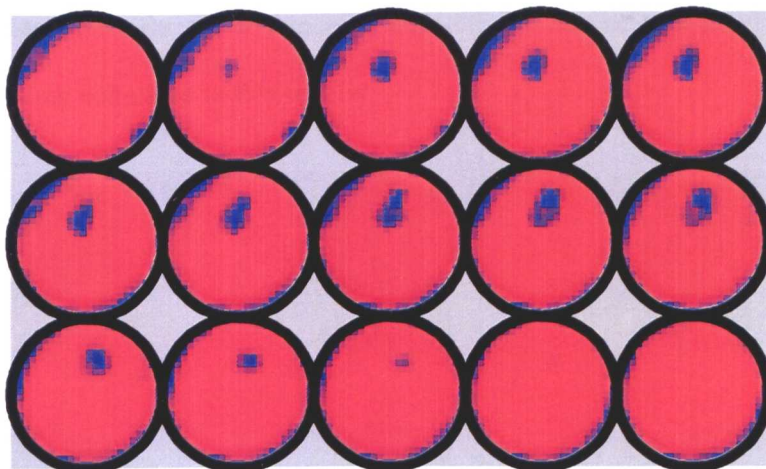


Figure 6.35-2D axial slices of void fraction data for run 143 on the 67mm pipe. Red represents the gas and blue is the liquid.

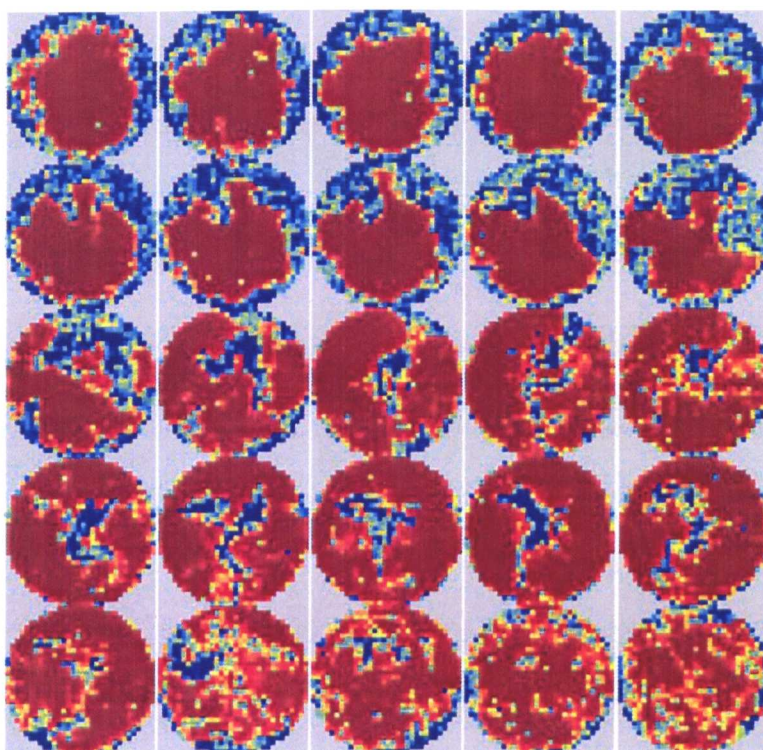


Figure 6.36-2D axial slices of void fraction data for run 489 on the 127mm pipe. Red represents the gas and blue is the liquid.

It is also possible to represent the 2D plots shown above quantitatively as 3D surface plots (Figure 6.37). This technique can be applied to both pipe diameters, and videos animating these plots can be generated. Two sample videos are on the DVD enclosed

with this thesis, one for the 67mm pipe and one for the 127mm pipe for the two conditions being compared in this section.

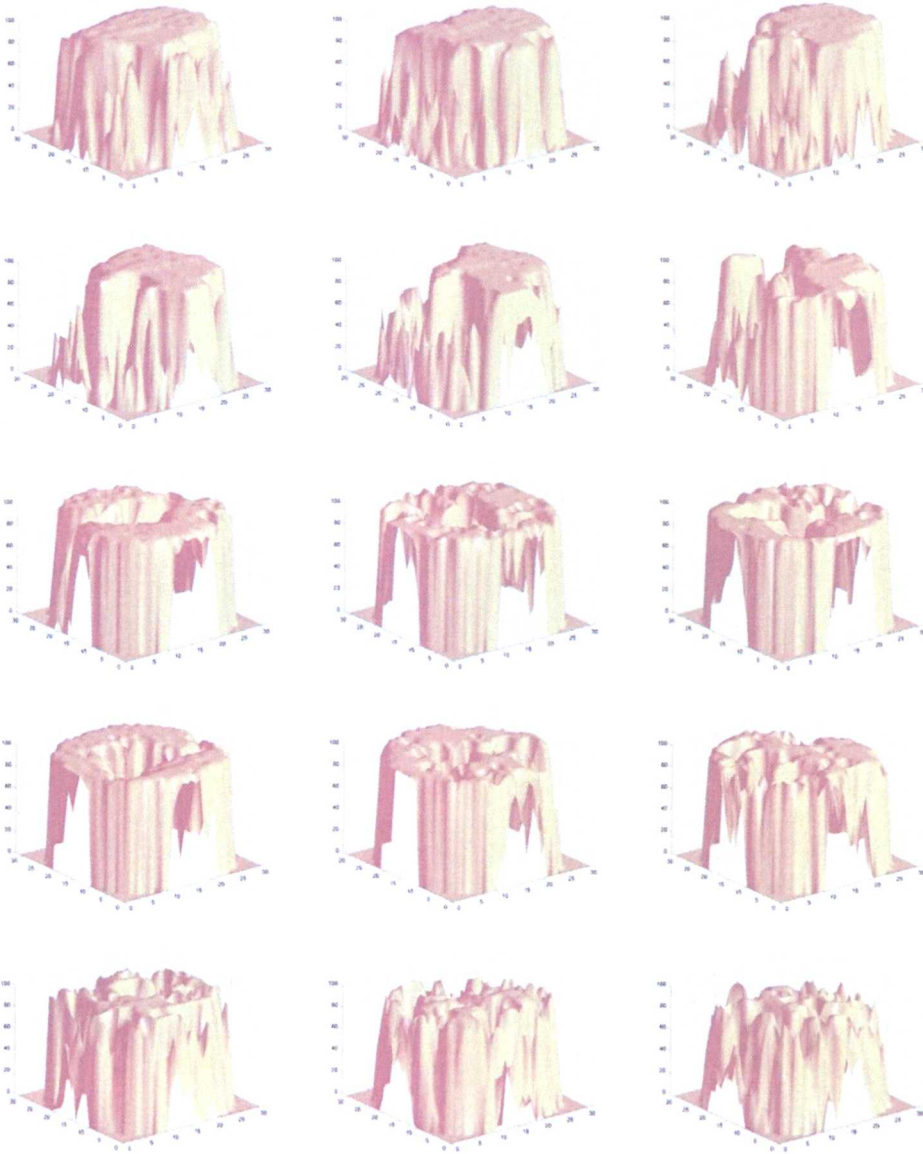


Figure 6.37-3D void maps for run 489 on the 127mm pipe.

It is also possible to use Matlab to display the wisps in 3D for both diameter pipes. These are shown in Figure 6.38, where it is clear that the size of these wisps is substantial.

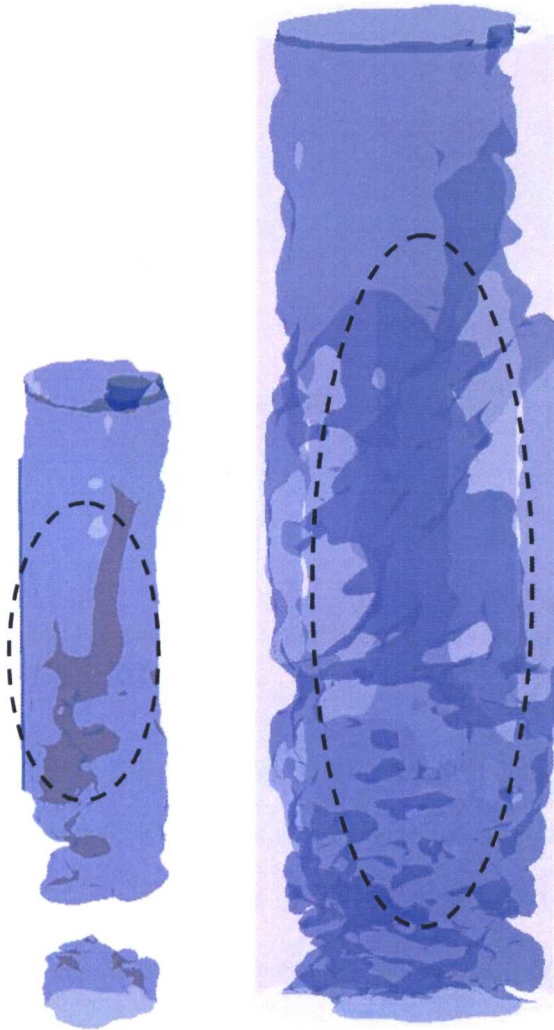


Figure 6.38-Wisps in 3D for (left): 67 mm pipe and (right): 127mm pipe

Experiments were conducted on the 67mm diameter pipe with air-silicone oil as previously discussed in this thesis. For conditions similar to those of air-water, wisps still occurred in the air-silicone oil mixture as shown in Figure 6.39, but they are not as large as those formed in air-water. This could be explained by the fact that silicone oil has a surface tension that is approximately four times lower than water, and therefore these structures are more likely to be broken up in the silicone oil. It can be concluded that for silicone oil the wisps are less likely to occur, their frequency is

likely to be lower than that for water and finally the length and size of the wisps will be smaller.

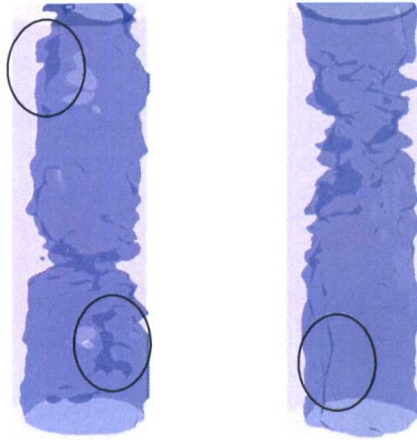


Figure 6.39- Comparison between air-water (left) and air-silicone oil (right) for the 67mm pipe. Liquid superficial velocity is 0.25 m/s and gas superficial velocity is 5.7 m/s

Hewitt and Roberts (1969) reported that wisps were occurring in annular flow, but they did not observe these structures in churn flow. If the range and conditions of data from Hewitt-Roberts is inspected, it can be seen that there was no data collected for the superficial liquid velocity range between 0.1 m/s and 0.7 m/s, where the majority of data was recorded in this experimental campaign. Therefore, not many researchers have studied the flow conditions that were carried out in this research study. In addition, previous studies did not have access to sensitive and high resolution instruments such as the WMS, which has enabled the discovery of these structures in churn flow. From the WMS images, it is clear that the wisp in the middle of the pipe is sometimes linked to the liquid film on the pipe wall (Figure 6.27, left) and (Figure 6.29, right). This clearly challenges the idea that these structures occur from the agglomeration or coalescence of drops entrained in the gas core as suggested by Hawkes (2000). The wisp appears to be a continuous liquid object of at least 10 mm in diameter, which is detached from waves on the wall film. It is hypothesised that the mechanism for the formation of wisps is the same as that suggested by Azzopardi

(1983), due to ligament/bag break-up (Figure 6.40). Ligaments tend to form at higher gas and liquid velocities, and structures can be seen in Figure 6.40 (b) that occur in the middle of the cross-section of the pipe. These structures are similar to those in the cross-sections shown in Figures 6.35 and 6.36.

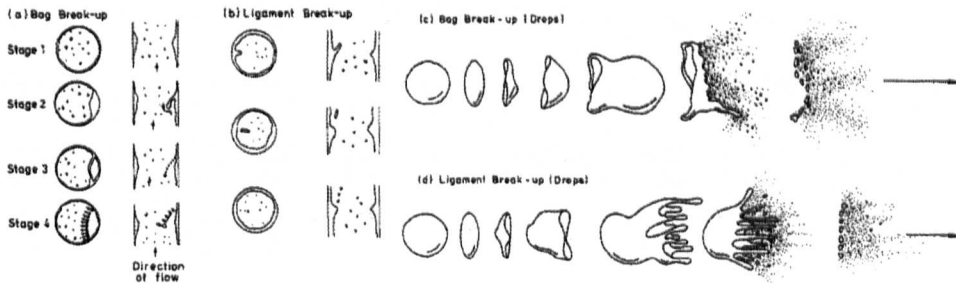


Figure 6.40- Mechanisms of atomisation and drop break up (Azzopardi, 1983)

This means that what is occurring is part of an incomplete atomisation process involving the gas shearing liquid off the film interface, which appears to take place at a critical gas velocity. The wisps form, then hit the liquid film and become reabsorbed. If the gas velocity is higher, complete atomisation occurs that creates a spray inside the pipe. This could be linked to the entrained fraction of drops in the gas core, which could also offer an explanation behind the occurrence of drops in annular flow. Some researchers label this as mist flow. The surface tension force tries to keep the wisp together, whilst the inertial force from the moving gas tries to break it apart. This is where a critical Weber (We) number could be linked to the formation of wisps, as it represents the ratio of those two forces. Azzopardi (1983) found that the boundary between the two mechanisms above occurred at a We_w of 25. Here the Weber number is defined as $We_w = \rho_g U_{gs}^2 h / \sigma$, where h is the wave height. If $h/\delta = 5$, it is possible to calculate the We_w for run 489 shown earlier, which contained wisps. δ was approximated to be 0.01 m, and therefore $We_w = 3.6 \times 3.1^2 \times 0.05 / 0.073 = 24$. This is almost the same value that Azzopardi (1983) reported. An important consideration is

whether these wisps occur naturally in the flow, or if they are caused by the intrusiveness of the WMS itself. The wisps have been observed in different flow patterns, such as churn and annular, and also in different diameter pipes, for example in 67mm as reported by Hernandez-Perez et al (2010). They have also been detected using different techniques, including (a) visually through a transparent pipe section, (b) with a WMS and (c) with x-ray photography. They have also been observed in different fluids. By studying the data from the large number of cross-sections that the WMS collects per second (Figure 6.35) and (Figure 6.36), it can be observed that the wisps do not remain in the WMS cross-section and that no two images are the same. Therefore, it can be concluded that these structures form independently of the WMS. The wisp does not appear to be a unique object or to take a predefined shape, and the wisps occur in different lengths and sizes anywhere along the cross-section of the pipe. They also occur in different conditions, in different fluids and for different diameters, both small and large.

6.7. Wisp frequencies in churn flow

Hernandez-Perez et al. (2010) reported that the wisps occurred at frequencies lower than those determined from the Power Spectral Density analysis of the WMS signals that pick up the void wave frequency. They also showed that the wisp frequency increased with an increasing gas superficial velocity, whereas the overall frequency decreased. This finding agrees with the earlier work carried out by Hawkes et al. (2000) who considered higher liquid velocities in what they identified as wispy-annular flow.

The overall and wisp frequencies have been extracted from the WMS data for the 127mm diameter pipe for two liquid velocities of ~ 0.2 and ~ 0.25 m/s. The wisps were

counted visually over 30 seconds, which was a slightly subjective methodology. An alternative approach to this could be to measure the lengths of individual wisps and present a distribution. Both small and large wisps were included and the wisp frequency was calculated. Overall frequencies for the 127mm pipe are plotted in Figure 6.41 along with those reported by Hernandez-Perez et al. (2010) for the 67mm pipe. The frequencies decrease with an increasing gas superficial velocity and given the higher velocities for the 127mm pipe, the frequencies tend to be lower than those for the 67mm pipe. The wisp frequencies for the 127mm diameter pipe were then plotted together with the overall frequencies for liquid superficial velocities of 0.2 and 0.25 m/s, as shown in Figure 6.42.

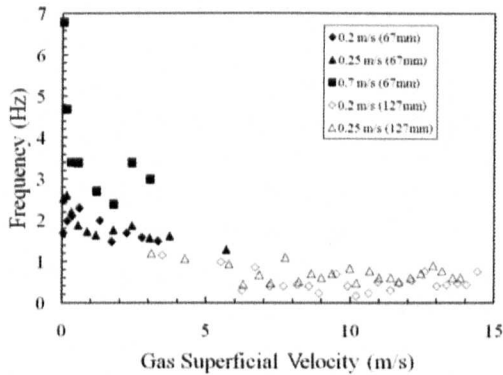


Figure 6.41- Effect of gas and liquid flow rates on overall frequency. Data for 67mm diameter pipe from Hernandez-Perez et al. and data for the 127mm pipe from the present work

Here, the frequency of the wisps tended to increase as the velocity was decreased; however, the wisp frequency was not always lower than the overall frequency, for example as reported by Hawkes (2000). For the 67mm pipe the flow patterns were slug and the lower end of the churn region, and for the 127mm pipe, the flow patterns encountered were the upper end of churn and the annular region, which could provide an explanation for the difference in wisp frequency versus overall frequency for the 127mm pipe.

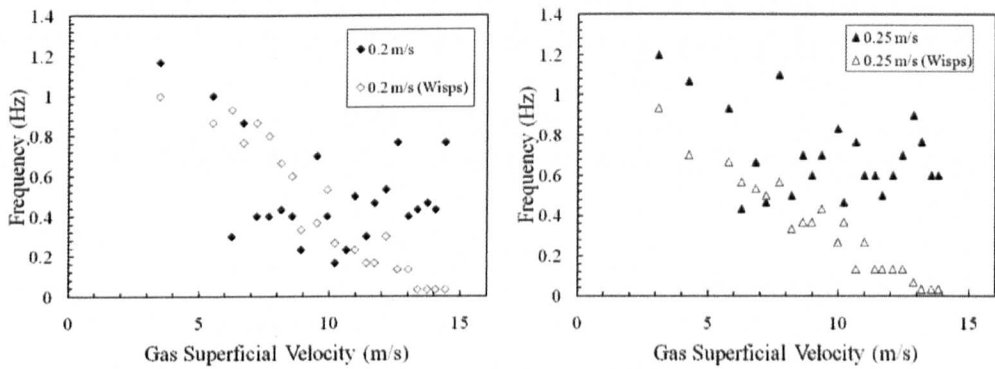


Figure 6.42-The effect of gas and liquid velocities on wisp and overall frequency for the 127mm diameter pipe. Liquid superficial velocities of (left): 0.2 m/s and (right): 0.25 m/s

The wisp frequencies for both the 67mm and 127mm pipes were plotted against the gas superficial velocity (Figure 6.43, left) and against the Weber number (Figure 6.43, right). Here the Weber number is defined as $We = \rho_g U_{gs}^2 D / \sigma$. The wisp frequency tends to increase for the 67mm diameter pipe as the gas velocity increases.

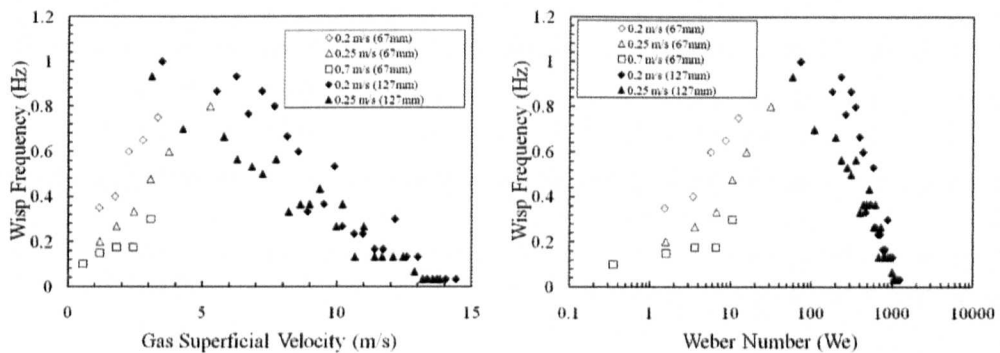


Figure 6.43-(Left): Effect of gas and liquid flow rate on wisp frequency. Data for 67mm diameter pipe from Hernandez-Perez et al. and data for the 127mm pipe from the present work. **(Right):** Effect of Weber number on wisp frequency. Data for 67mm diameter pipe from Hernandez-Perez et al. and data for the 127mm pipe from the present work

This is the opposite of what is occurring in the 127mm diameter pipe, where the wisp frequency tends to increase as the superficial gas velocity decreases. A similar trend was presented in Chapter 2 (Figure 2.22), for the huge wave frequency as measured by Sekoguchi and Mori (1997). Therefore, wisps may be what Sekoguchi and Mori were labelling as huge waves, which was also hypothesised by Azzopardi et al. (2004).

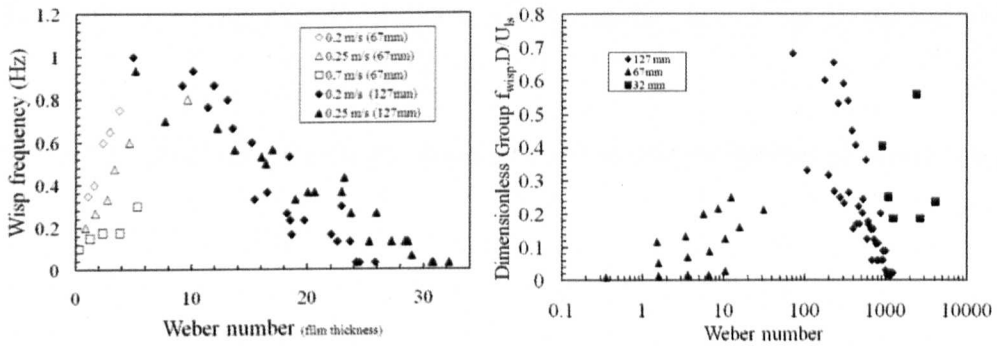


Figure 6.44-Wisp frequency plotted against a modified Weber number (left) and as a dimensionless group map (right).

Another way to show the data presented in Figure 6.43 can be seen in Figure 6.44 (left), where the wisp frequency is plotted against a modified Weber number that was multiplied by the film thickness δ such that $We(\text{film thickness}) = \rho_g U_{gs}^2 D / \sigma \times \delta / D = \rho_g U_{gs}^2 \delta / \sigma$. An attempt was made to plot the wisp frequencies obtained from three different diameters on a dimensionless map, which is shown in Figure 6.44 (right). This incorporates the data from this experimental campaign for the 127mm pipe, data from Hernandez-Perez et al. (2010) for a 67mm pipe and results from Hawkes et al (2000) for a 32mm pipe. Similar trends are again observed to those in Figure 6.44 (left). Recently collected data can be seen in Figure 6.45, which presents the liquid entrainment measured experimentally using Phase Doppler Anemometry (PDA) with laser equipment on the 127mm diameter pipe. This was compared against the published correlation outlined in Chapter 2 by Ahmad et al (2010), which was developed using data from a 32mm diameter pipe. The experimental data was collected at liquid velocities of 0.01-0.04 m/s and gas velocities of 10-50 m/s. There is good agreement between the experimental data collected on the 127mm diameter pipe and the correlation, which is encouraging, considering that the experimental data was collected on a pipe with a diameter that was four times larger. This shows the rate of entrained fraction tending to increase as the superficial gas velocity is increased. It decreases slightly if the liquid velocity is increased, and full atomisation appears to

occur with an unusual peak in entrainment occurring at a certain superficial gas velocity. With these higher velocities, the atomisation force becomes more powerful. This implies that the probability of forming wisps decreases, whereas the probability of drop formation increases.

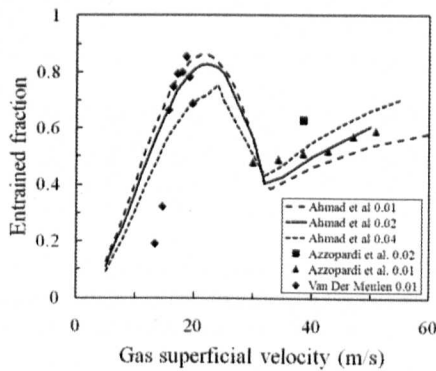


Figure 6.45-Entrainment fraction against gas superficial velocity 10-50 m/s

6.8. Flow pattern map(s) for the 127mm riser

An attempt was made to generate a flow map using the full data set. This was achieved by inspecting the movies (.v files), the PDF profiles and also the 2D cross-sectional images. Flow patterns were designated into four categories, which were annular, wispy-annular, churn and wispy-churn flows. The data was plotted on both the Hewitt-Roberts map, as well as the Weber number map that was derived from the Hewitt-Roberts flow map as explained in Chapter 2. However the x and y-axis were switched. The results of this can be seen in Figure 6.46. The dimensionless Weber flow map generates a similar profile to the one by Hewitt-Roberts, but clearly the boundaries need to be redefined. The data could be plotted on other flow maps as outlined in Chapter 2. For example, the data could be presented on a mechanistic type map (Shoham, 2006), which would have no slug/churn boundary, and therefore the data would lie between bubble/slug and annular. Schlegel et al (2009) showed only a straight line between churn-annular. Figure 2.12 in chapter 2 combined the flow maps

devised by several researchers, for example Duns and Ros, and Sekoguchi and Mori. The observations presented in this chapter reconcile the apparent differences between the flow pattern maps of Hewitt and Roberts and those of the other researchers.

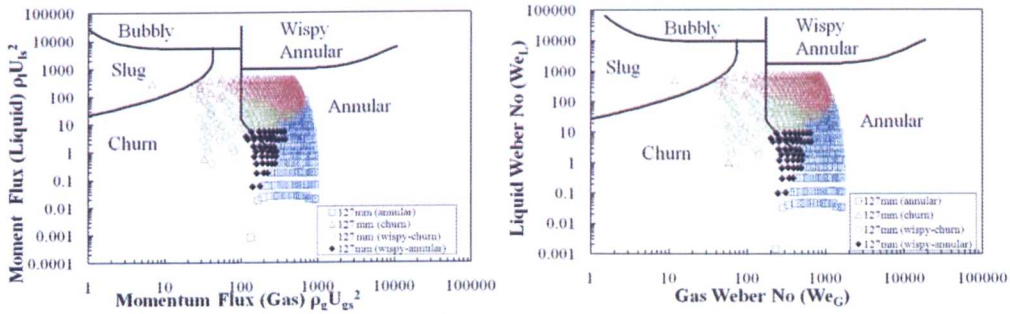


Figure 6.46-Flow map for the 127mm diameter pipe. (Left): The data set plotted on a Hewitt-Roberts map, (right): the data set plotted on a Weber map. The area of uncertainty is the wispy churn/annular region

For example, Duns and Ros presented a single pattern covering the churn and wispy annular regions that were designated as separate sections in the Hewitt and Roberts map. In the above map, the churn and wispy annular/churn regions are almost lumped together, and annular flow occupies a separate area of the map. However the boundary lines as originally drawn clearly do not accurately predict the transitions.

6.9. CFD Simulation

The 127mm diameter pipe was modelled in a CFD package provided by CD-Adaptco. A pipe of 10 metres was modelled with the meshing profile shown in Figure 6.47 using Star-CD. This is known as a “butterfly” mesh or grid. Though grid independence has not been tested for this particular exercise, the work here closely follows that of Hernandez-Perez et al (2011), who recommend this type of grid for two-phase pipe flow simulations as it generates good results when compared with experimental data. A measuring plane was placed in the model at a height of 9 metres, to correspond with the experimental set-up where the WMS was placed at a height of 9 metres from the injector. However, once a CFD simulation is finished it is possible to locate this measuring plane anywhere along the pipe. This is useful for creating

PDFs along the pipe, and inferences can then be made regarding how the flow develops along the pipe and whether the flow is developed or not. The Volume of Fluid (VOF) method was used, with certain assumptions made, such as a uniform velocity profile throughout the pipe. For the boundary conditions, the inlet was defined with a mixture velocity and at the outlet the pressure was assumed to be zero. The density of air was set at 3.6 kg/m^3 to represent a system pressure of 3 bar (abs). Run 489 was selected for the CFD simulation, and therefore the mixture velocity for that run was estimated to be 3.27 m/s. The simulation was run in Star-CCM+ on a desktop PC with 4 processors, and 3GB of RAM. It took approximately seven months to solve, which can be attributed to the large number of 885,000 cells used in the model. This was unavoidable considering the nature of the churn flow pattern, which is a complex and turbulent regime that requires a dense mesh. The simulation was deemed complete when the gas core reached the top of the pipe, which also passed the measuring plane. From the simulation, useful information can be extracted; for example, the area averaged void fraction showed a value of approximately 0.8. This is slightly higher than the experimentally measured void fraction for this run, which was approximately 0.7. The phase or void distribution along the pipe can be seen in Figure 6.48, and finally, the velocity profile along the pipe is shown in Figure 6.49. In Figures 6.48 and 6.49, the areas along the pipe have been magnified to allow a more detailed view of the flow. Liquid structures in the middle of the pipe can clearly be seen in Figure 6.48. This simulation has provided additional confirmation of the presence of wisps in churn flow.

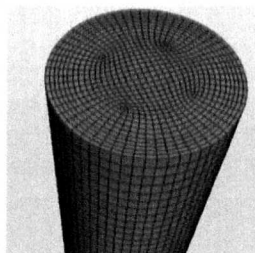


Figure 6.47-Mesh profile used for the CFD simulation

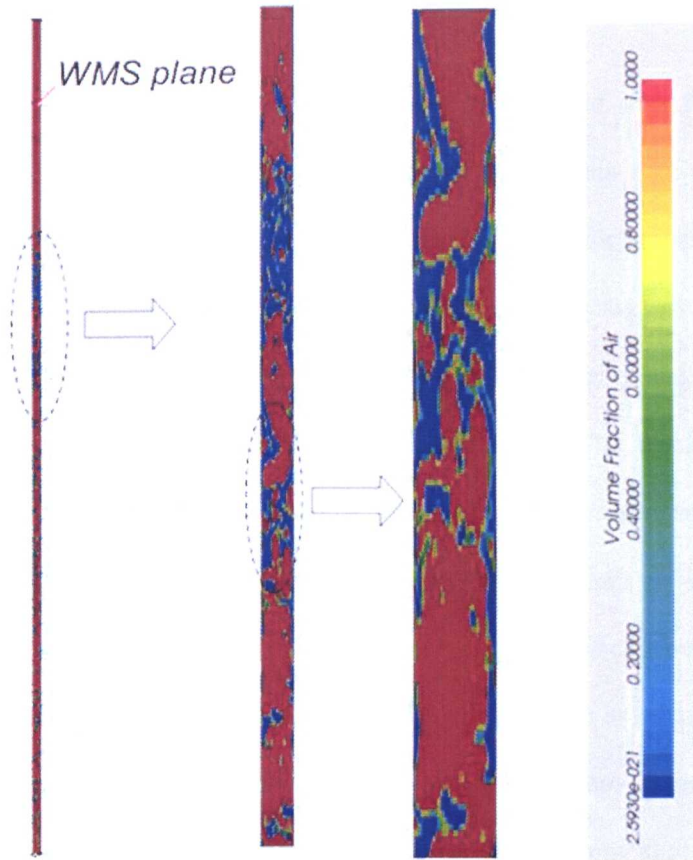


Figure 6.48 -CFD generated void fraction. Structures are clearly visible in the middle of the pipe, and the liquid film on the pipe wall is also visible.

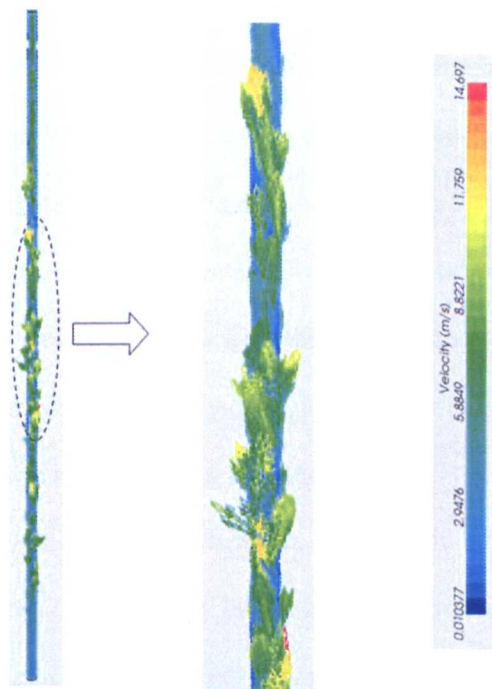


Figure 6.49-CFD generated velocity vectors

6.10. Summary

This chapter contained a large amount of novel data obtained with the WMS on a vertical large diameter pipe. The first level of analysis of this data considered the testing of empirical correlations, such as Friedel/CISE and mechanistic correlations, which was conducted using the WELLFLO software. The second level of data analysis looked deeper into the flow by considering and comparing runs from different diameters that showed surprisingly similar characteristics. The third level of data analysis was the CFD simulation of one of the runs that was considered numerically. An important conclusion is the existence of wisps in the churn flow area in large diameter pipes. This has not been reported previously, and it can be argued that it should be labelled as *wispy-churn* flow in the same convention as wispy-annular flow and allocated a specific area on the flow map with defined boundaries. It has been demonstrated that these unusual structures exist in both 67mm and 127mm pipes, which was confirmed with the CFD simulation carried out on the 127mm pipe.

While the WMS is an intrusive sensor, due to its high resolution it is able to identify these difficult to detect structures, which few other instruments can directly observe. For example, conductance probes are not able to measure structures such as wisps, which are not axi-symmetric or lie in the annulus, whereas the WMS can. These wisps could be considered relevant both scientifically and industrially, for example, the oil companies would be interested to know how these wisps could affect the pressure and hence the flow of oil inside the pipe. By changing the physical properties, for example the surface tension, the wisps appear to become smaller. To conclude, the WMS data was verified extensively against empirical and mechanistic correlations, against other instruments, and against CFD results. In general the agreement between the WMS readings and other methods was very good, and the only noticeable differences were for the lowest liquid velocities.

7. CHAPTER 7: CONCLUSIONS AND FURTHER WORK

7.1. Conclusions

During this research project a large number of experiments on two-phase gas-liquid flow using two variant wire mesh sensors have been carried out in order to satisfy the main scientific objectives set out in Chapter 1. The experimental campaign was carried out in two parts; the first being the testing phase, where the wire mesh sensor results were compared with gamma densitometry (GD) and ECT probes. The second part was the application phase, where the WMS was applied to (a) bubble columns and (b) large diameter vertical riser. It was shown that with this type of sensor, large amount of data can be generated. Averaging techniques were shown to be an effective methodology to deal with this data. The advantages of the sensor were demonstrated. The first advantage was clearly shown to be the visualisation capabilities of the sensor, due to its high resolution. The other strength of the sensor was the determination of the bubble size, both as a distribution and time resolved broken down into bubble classes. No other two-phase instrument available commercially is able to produce this kind of information across the full cross-section of a pipe.

Conclusions from the Testing Phase of the WMS

1. It was demonstrated that the WMS is accurate in measuring gas-liquid flow. Comparisons were carried out between the CapWMS and CondWMS against gamma densitometry as presented in Chapter 4. The agreement in results was shown to be within +/-10% between the WMS and GD data, which confirm previous comparisons. In addition, a large database of data from the WMS was compared with ECT measurements, and again the agreement was very good.

2. The capacitance WMS readings compared well with those obtained with the conductance WMS on the same experimental facilities using similar experimental conditions. This is an important finding, as the CapWMS is a newer instrument and to date has not been as extensively tested as the CondWMS. These instruments work in a similar way in principal; however, they are measuring different parameters. It is therefore encouraging that the instruments have indirectly validated each other by producing similar results.

Conclusions from the Application Phase of the WMS

1. The WMS was applied to bubble columns of various diameters with different fluids in an extensive experimental campaign for the first time. A large amount of novel and useful information about bubble columns has been extracted and presented in Chapter 5, including details on the bubble size distributions. The data from the WMS was compared with the level swell readings to check the accuracy, and in general the agreement was good. It can therefore be inferred that the WMS is suitable for investigations on bubble columns, which is an important conclusion as up to now research in bubble columns with this type of instrument has been limited. It is hoped that researchers will feel more encouraged in the future to use this type of sensor on bubble columns as a result of this work.

2. The WMS was applied to large diameter pipes in a substantial experimental campaign that collected 700 runs of data, and these were presented and discussed in Chapter 6. Novel structures (wisps) were discovered experimentally using the WMS, which were found to occur in churn flow. These wisps were also captured in CFD simulations, providing further evidence of their existence. These structures are similar to those seen by Hernandez-Perez et al (2010) in smaller diameter pipes.

3. Data from the WMS was compared with that from conductance probes. Interesting differences were seen between the results from the two instruments, and it was shown that the WMS was far superior to the conductance probes in operating in different flow patterns.

4. Data from the WMS was compared with published correlations, and in general there was a remarkable agreement between the WMS and correlations such as CISE. This was true for both void fraction results and the overall pressure drop. As a further check, experimental pressure drop data was also compared with the WMS results, and again very good agreement was observed except for very low liquid velocities.

5. As a direct result of these investigations, the manufacturers of the WMS were able to fine tune the capacitance wire sensor and produce a second version, which has been improved in many areas (both in software and hardware) due to this research. The latest version is easier to operate and calibrate with fewer error messages generated.

7.2. Future Work

A substantial amount of experimental work could be carried out in the future using the WMS on bubble columns and large diameter pipes. The WMS could be combined with other instruments, which has been demonstrated to be a powerful methodology in conducting multiphase flow experiments. Suggestions in this chapter will involve simple modifications to existing facilities. Much of the equipment and instrumentation required to do this has already been acquired by the University of Nottingham. Therefore the experiments could be conducted effectively onsite within a reasonable time frame and cost.

Experimental work on bubble columns

1. It is possible to combine the CondWMS/ERT or CapWMS/ECT together to collect more information about the two-phase characteristics that occur inside a bubble column. This methodology was used previously by Abdulkareem et al. (2009) on a 67 mm pipe. Similar techniques could be applied to expand the work presented in Chapter 5, in order to investigate larger diameter columns for example by using a 127mm ECT sensor and combining it with a 32x32 CapWMS on a 127mm diameter column, and taking measurements with air-silicone oil as the two-phase mixture.

2. In previous studies it was demonstrated that the WMS worked quite well in other type of reactors, such as stirred vessels. It is recommended that further research is carried out in this area in order to build on the work completed on bubble columns. In addition investigations could be carried out with the WMS with various surfactants such as alcohol as was done by Al-Oufi et al (2010) using conductance probes.

Experimental work on large diameter pipe flow

1. The limitations of both gamma densitometry and the WMS in measuring void fractions at the pipe wall were clearly shown. This requires further investigations using other instrumentation, such as the Film Measurement Sensor (FMS). The University of Nottingham recently took delivery of a FMS from HZDR, which could be installed on the 127mm closed loop facility in order to conduct several useful experiments. The FMS is a powerful instrument capable of sampling 5000 cross-sections per second, with a resolution of approximately 6mm ($\pi \times 127\text{mm}/64$ circumferentially placed probes).

2. A new design of injector could be installed on the 127mm facility to investigate bubbly flow using the WMS, which would allow the investigation of the low gas superficial velocities of 0-3m/s that were not covered in this project. A design of injector could be developed so that the same injector is used on both the 127mm bubble column and the 127mm vertical facility, which will allow a direct comparison between large diameter pipes and bubble columns. Another possibility is to use injectors that have a similar design to those employed at HZDR. HZDR has a large database of results from experiments conducted at TOPFLOW on 50mm and 200mm diameter pipes with both air-water and steam-water, which also covered bubbly flow and transitions from bubbly flow which again was not covered in this study. The injectors used by HZDR are different in design to the ones applied in this study. The 127mm facility at Nottingham lies approximately in the middle of the 50mm and 200mm range, and therefore a three way comparison could be conducted. No doubt important conclusions could then be drawn; for example if there is any evidence of up-scaling as the diameter is varied from a small to a large diameter. It is important that the same conditions that were applied in Germany are replicated at Nottingham if such experiments are conducted there; i.e. the temperatures, pressures and the positions of the WMS along the pipes all need to be the same. It is possible to install two WMS sensors and cross-correlate signals between them to extract more information about the flow, as was previously investigated in Germany. This author's research study was entirely carried out using one WMS.

3. Other two-phase mixtures could be investigated with this facility, for example SF₆-water, air-Oil or SF₆-Oil. The oil used could be silicone oil or high flash point kerosene; both of which are non conductive, have the same permittivity of around 2.7 and will operate with the CapWMS. From the oil and gas industry perspective,

experiments on fluids that have a low surface tension are preferred as these are encountered in the field, hence the choice of silicone oil, which is also an inert non-combustible fluid. SF₆ is five times heavier than air (at atmospheric pressure) and as it is a heavier gas, it is expected that interesting results will be generated. Another possibility is to modify the 127mm rig to allow it to operate at higher pressures, for example between 10 and 20 bar. With the higher pressure the air will be denser, which could be an alternative approach to using SF₆ as it has safety, cost and environmental implications that must be considered. Another modification to the rig could be to incline the pipe at up to 10 degrees from the vertical, and the rig was designed to allow this to be possible. Comparisons could then be carried out against the 67mm rig, which is also an inclinable facility. Investigations could be carried out with air-water and air-silicone oil for the two diameters at different inclinations (up to 10 degrees from the vertical). This could give further evidence of scaling-up in the data.

4. It is possible to install an ECT system on the 127mm facility. The sensor obviously needs to be installed before the WMS along the pipe. The fluid mixture could be air-silicone oil and SF₆-silicone oil and a large experimental campaign is then possible to compare ECT performance against the CapWMS on a large diameter pipe, in a similar way to the campaign proposed above for bubble columns of the same diameter with these two instruments. The ECT will only work with non-conductive fluids such as silicone oil; however, it has the advantage of having two sensors and therefore the researcher can cross-correlate signals. It is important to use the same conditions applied in this research study, for example from the matrix in Chapter 6, using the same pressures and temperatures. Then a comparison of air-water vs. air-silicone oil for the 127mm diameter pipe will be possible.

Other future work

Further developments could be carried out on the WMS itself. Already trials have been conducted at HZDR in order to produce a temperature measuring WMS, and in addition, consideration should be given to combining the CondWMS and CapWMS into one electronics box. A diagnostic tool for the WMS could also be developed, which would prove helpful in performing checks of continuity on the wires of the sensor that sit inside the pipe. Trials could be carried out with the WMS on three-phase gas-liquid-liquid flow, at facilities similar to those at Cranfield University. Preliminary tests with the WMS have already been conducted in the past on three phase flow, which showed promising results. Expanding the WMS for three-phase flow will be of significant interest to several industries; in particular to the oil and gas industry that regularly encounter it in the form of gas-water-oil. It is therefore recommended that an experimental campaign is initiated in this research area.

From a modelling perspective an attempt to develop a 3D-flow pattern map would be valuable as most of the maps in the literature appear to be in 2D. This could be diameter dependent (z-axis) with the x-y axis using the dimensionless Weber numbers or alternatively the momentum flux as explained in Chapter 2. A 3D flow pattern map could be generated for both bubble columns and risers with two-phase flow. A more concerted effort could be made on modelling wisps and indeed churn flow. Further simulations of these could also be carried out in CFD. The potential for further modelling work for bubble columns was discussed in Chapter 5. Finally the data collected during this research study is substantial, and therefore further analysis, processing and interpretation is possible. For example it is possible to derive the bubble size from the WMS data decomposed radially as opposed to presenting the bubble size as a distribution across the full cross-section as was done in this thesis.

PUBLICATIONS

Author's Publications-Journal Papers

Hernandez Perez, V., Abdulkareem, L. A., Azzopardi, B. J., Sharaf, S., Thiele, S., Da Silva, M. (2011), Application and assessment of different techniques to investigate the behaviour of gas-liquid flow. *Experimental Thermal & Fluid Science*. Submitted.

Sharaf, S., Da Silva, M., Hampel, U., Zippe, C., Beyer, M., Azzopardi, B.J. (2011), Comparison between wire mesh sensor and gamma densitometry void measurements in two-phase flows. *Measurement Science & Technology*. Accepted for publication.

Abdulkadir, M., Zhao, D., Sharaf, S., Abdulkareem, L.A., Lowndes, I.S., Azzopardi, B.J. (2011), Interrogating the effect of 90° bends on air-silicone oil flows using advanced instrumentation. *Chemical Engineering Science*. Volume 66, Issue 11, Pages 2453-2467.

Abdulkadir, M., Hernandez-Perez, V., Sharaf, S., Lowndes, I.S., Azzopardi, B.J. (2010a), Experimental investigation of phase distributions of two-phase air-silicone oil flow in a vertical pipe. *World Academy of Science, Engineering and Technology*, 61.

Author's Publications-Conference papers

Abdulkareem, L.A., Hernandez-Perez, V., Sharaf, S., Azzopardi, B.J. (2011), Characteristics of air-oil slug flow in inclined pipe using tomographic techniques. ASME / JSME 8th Thermal Engineering Joint conference, March 13-17, 2011, Honolulu, Hawaii, USA.

Abdulahi, A., Abdulkareem, L.A., Sharaf, S., Abdulkadir, M., Hernandez-Perez, V., Azzopardi, B.J. (2011), Investigating the effect of pipe inclination on two-phase gas-liquid flows using advanced instrumentation. ASME / JSME 8th Thermal Engineering Joint conference. March 13-17, 2011, Honolulu, Hawaii, USA.

Abdulkareem, L.A., Sharaf, S., Azzopardi, B.J., Hunt, A. (2010), Effect of inclination on slug flow characteristics. ASME International Mechanical Engineering Congress & Exposition. IMECE2010. Vancouver, Canada.

Sharaf, S., Da Silva, M., Hampel, U., Zippe, C., Azzopardi, B.J., Beyer, M. (2010), Comparison between wire mesh sensor technology and gamma densitometry. 6th World Congress on Industrial Process Tomography. China. *Conference Attended*.

Sharaf, S., Azzopardi, B.J. (2010), Experimental investigations of gas-liquid flow using wire mesh sensor technology. ETPFGM'10. 48th European Two-Phase Flow Group Meeting. 28th-30th June 2010, Brunel University, London, UK. *Conference Attended by author*.

Azzopardi, B.J., Lange, S.A., Sreevasan, D., Sharaf, S., Licence, P. (2010b), Gas/liquid flow in bubble columns – air/ionic liquids. 8th Japan-UK Seminar on Multiphase Flows - Otaru 2010.

Azzopardi, B.J., Abdulkareem, L.A., Sharaf, S., Abdulkadir, M., Ijioma, A. (2010c), Using tomography to interrogate gas liquid flow. Keynote lecture. XXVIII Congresso UIT sulla Trasmissione del Calore Brescia, 21-23 Giugno.

Abdulkadir, M., Zhao, D., Abdulkareem, L.A., **Sharaf, S.**, Lowndes, I.S., Azzopardi, B.J. (2010b), Interrogating the effect of bends on two-phase gas-liquid flow using advanced instrumentation. ICMF 2010, Florida, US.

Abdulkadir, M., Hernandez-Perez, V., **Sharaf, S.**, Lowndes I. S., and Azzopardi B. J. (2010c), Phase distributions of an air-silicone oil mixture in a vertical riser. HEFAT 2010. 7th Int. conference on heat transfer, fluid mechanics and thermodynamics.

Azzopardi, B.J., **Sharaf, S.**, Zhao, D., Hernandez Perez, V. (2009), Gas-liquid flows in bubble columns and loop reactors. ETPFGM '09 and EFCEmultiphase Conference. Slovenia.

Abdulkareem, L.A., Hernandez-Perez, V., Azzopardi, B.J., **Sharaf, S.**, Thiele, S., Da Silva, M. (2009). Comparison of different tools to study gas-liquid flow. ExHFT-7 Conference. Poland. *Conference Attended by author.*

NB-Some of the above references were quoted in the main text of the thesis, however to avoid duplication they were not listed again in the bibliography section.

BIBLIOGRAPHY

- Ahmad, M., Peng, D., Hale, C., Walker, S., and Hewitt, G. (2010), Droplet entrainment in churn flow. 7th International Conference on Multiphase Flow. USA.
- Akagawa, K., Terushige F., Takagi, S., Takeda, M., and Tsuji K. (1984), Performance of Hero's turbine using two-phase mixture as working fluid (Experimental results in air-water two-phase system). *Bulletin Of JSME*, Vol 27, No. 234.
- Akita, K. and Yoshida, F. (1974), Bubble size, interfacial area, liquid-phase mass transfer coefficient in bubble columns, *Ind. Eng. Chem. Proc. Des. Dev.*, 13, 84-91.
- Akita, K. and Yoshida, F. (1973), Gas holdup and volumetric mass transfer coefficient in bubble columns, *Ind. Eng. Chem. Proc. Des. Dev.*, 12, 76-80.
- Ali, S.F. (2009), Two phase flow in large diameter vertical riser. PhD thesis. Cranfield University.
- Al-Masry, W.A., Ali, E.M., Alshebeili, S.A., Mousa, F.M. (2010), Non-invasive imaging of shallow bubble columns using electrical capacitance tomography, *Journal of Saudi Chemical Society*, Volume 14, Issue 3, Pages 269-280.
- Al-Oufi, F.M., Cumming, I.W. and Rielly, C.D. (2010), Destabilisation of a homogeneous bubbly flow in an annular gap bubble column, *The Canadian Journal Of Chemical Engineering*, 88(4), 482-490.
- Anderson, J., Quinn, J. (1970), Bubble columns: flow transitions in the presence of trace contaminants. *Chemical Engineering Science*. Vol 25, P373-380.
- Azzopardi, B. J., Mudde, R. F., Lo, S., Morvan, H., Yan, Y. and Zhao, D. (2011) Bubble Columns, in *Hydrodynamics of Gas-Liquid Reactors: Normal Operation and Upset Conditions*, John Wiley & Sons, Ltd, UK.
- Azzopardi, B.J. (2010), Multiphase systems lecture notes. University of Nottingham.
- Azzopardi, B.J., Abdulkareem, L., Zhao, D., Thiele, S., Da Silva, M., Beyer, M. (2010), Comparison between Electrical Capacitance Tomography and Wire Mesh Sensor output for air/silicone oil flow in a vertical pipe. *Ind. Eng. Chem. Res.*, 49.
- Azzopardi, B.J. (2009), Lecture: Is churn flow like chaos? Structures within a confused flow situation. Eng. Mechanics Symposium 2009, University of Nottingham.
- Azzopardi, B.J., Hernandez Perez, V., Kaji, R., Da Silva, M. J., Beyer, M., Hampel, U. (2008a), Wire mesh sensor studies in a vertical pipe. Fifth International Conference on Transport Phenomena in Multiphase Systems, HEAT 2008, Poland.
- Azzopardi, B.J., Jackson, K., Robinson, J.P., Kaji, R., Byars, M., Hunt, A. (2008b), Fluctuations in dense phase pneumatic conveying of pulverised coal measured using Electrical Capacitance Tomography. *Chemical Engineering Science*, Volume 63.

Azzopardi, B.J. (2008). Flow patterns: does gas/solids flow pattern correspond to churn flow in gas/liquid flow. *Industrial & Eng. Chem. Research*, 47, P7934-7939.

Azzopardi, B.J. (2006), Gas-liquid flows. Begell House, New York.

Azzopardi, B.J., and Wren, E. (2004), What is entrainment in vertical two-phase churn flow? *International Journal of Multiphase Flow*, vol. 30, P89-103.

Azzopardi, B.J. (2004), Bubbles, drops and waves: differences or underlying commonality. 42nd European Two-Phase Flow Group Meeting, Genoa, 23-25 June.

Azzopardi, B.J., Hills, J. (2003), "Flow Patterns, transitions, models for specific flow patterns", "One dimensional models for pressure drop, empirical equations for void fraction and frictional pressure drop". *Modelling & Experimentation in Two-Phase Flow*. Bertola, V (Ed). Springer, Wien, New York.

Azzopardi, B. J., and Gibbons, D. B. (1983), Annular two phase flow in a large diameter tube. *The Chemical Engineer* No 298, 19-21.

Azzopardi, B.J. (1983), Mechanisms of entrainment in annular two-phase flow. UKAEA Report AERE-R 11068.

Barbosa, J. R., Hewitt, G.F., König, G., and Richardson, S.M. (2002), Liquid entrainment, droplet concentration and pressure gradient at the onset of annular flow in a vertical pipe. *International Journal of Multiphase Flow* vol. 28, P 943-961.

Barbosa, J., Richardson, S., and Hewitt, G.F. (2001a), Churn flow: myth, magic and mystery. 39th European Two-Phase Flow Group Meeting, Aveiro, Portugal.

Barbosa, J. R., Govan, A.H., Hewitt, G.F. (2001b), Visualisation and modelling studies of churn flow in a vertical pipe. *Int. J. of Multiphase Flow*. Vol 27, 2105-2127.

Barnea, D. (1986), Transition from annular flow and from dispersed bubble flow - unified models for the whole range of pipe inclinations, *International Journal of Multiphase Flow*, Vol. 12, No. 5, P733-744.

Barua, S., Sharma, Y., Brosius, M. (1992), Two-phase flow model aids flare network design. *Oil and Gas Journal*. P90-94.

Beggs, H., and Brill, J. (1973), A study of two phase flow in inclined pipes. *Journal of Petroleum Technology*, vol 25, P607-617.

Bennett, A. W., Hewitt, G. F., Kearsey, H. A., Keeys, R. K., Lacey, P. M. (1965), Flow visualisation studies of boiling at high pressure. *UKAEA Report AERE-R4874*.

Bertola, V. (2003), *Modelling & experimentation in two-phase flow*. Springer, NYork.

Beyer, M., Lucas, D., Kussin, J. (2010), Quality check of wire-mesh sensor measurements in a vertical air/water flow. *Flow measurement and instrumentation, Volume 21, Issue 4, Pages 511-520*.

- Bieberle A., Schubert M., Da Silva, M.J., Hampel, U. (2011), Measurement of liquid distributions in particle packing using wire mesh sensor versus transmission tomographic imaging, *Ind. Eng. Chem. Res.*, 49 (19), P9445–945.
- Biesheuvel, A. and Gorissen, W. C. M. (1990), Void fraction disturbances in a uniform bubbly fluid, *Int. J. Multiphase Flow*, 16, 211-231.
- Blaß, E. (1988), *Chem.-Ing.-Tech.* 60, No. 12, P935 – 947. (In German).
- Boyer, C., Duquenne, A.-M., Wild, G. (2002), Measuring techniques in gas-liquid and gas-liquid-solid reactors, *Chemical Engineering Science*, Volume 57, Issue 16.
- Brauner, N., and Barnea, D. (1986), Slug/churn transition in upward gas-liquid flow. *Chemical Engineering Science* vol. 40, P159-163.
- Cheng, H., Hills, J.H. and Azzopardi, B.J. (1998), A study of the bubble-to-slug transition in vertical gas-liquid flow in columns of different diameters. *Int. J. Multiphase Flow*, 24, 431-452, (1998).
- Chexal, B., and Lellouche, G., (1986), A full range drift flux correlation for vertical flows, EPRI Report NP-3989-SR , Rev. 1.
- Chisholm, D. (1983), Two-phase flow in pipelines and heat exchangers. G. Godwin in association with the Institution of Chemical Engineers.
- Chisholm, D. (1973), Pressure gradients due to friction during the flow of evaporating two-phase mixtures in smooth tubes and channels. *Int. J. Heat Mass Transfer*, Vol 16, P347-358.
- Chisholm, D. (1972), An equation for velocity ratio in two-phase flow. *NEL 535*.
- Collier, J.G. and Thome, J.R. (1994), Convective boiling and condensation, 3rd edition, Oxford University Press, Oxford.
- Corradini, M. (1998), Multiphase flow gas-liquid; Chapter 17. *The Handbook of Fluid Dynamics* by R.C. Johnson (Ed). CRC Press.
- Costigan, G., Whalley, P.B. (1997), Slug flow regime identification from dynamic void fraction measurements in vertical air-water flows. *Int. J. Multi. Flow*, 23, No 2.
- Crowe, C. (ed) (2006), *Multiphase Flow Handbook*. Taylor & Francis.
- Crowe, C. (1998), *Multiphase Flows with Droplets & Particles*, CRC Press.
- Da Riva, E. and Del Col, D. (2009), Numerical simulation of churn flow in a vertical pipe. *Chemical Engineering Science*, 64, P3753-3765.
- Da Silva, M. J., Thiele, S., Abdulkareem, L., Azzopardi, B. J., Hampel, U. (2010), High-resolution gas oil two-phase flow visualization with a capacitance wire-mesh sensor. *Flow Meas. Instrum.*, V 21, p. 191-197.

- Da Silva, M. J. (2008), Impedance Sensors for Fast Multiphase Flow Measurement and Imaging. PhD Thesis. Technische Universität Dresden.
- Da Silva, M. J., Schleicher, E., Hampel, U. (2007a), Capacitance wire-mesh sensor for fast measurement of phase fraction distributions. *Measurement Science and Technology*, Vol 18, 2245-2251.
- Da Silva, M., Schleicher E., Hampel, U. (2007b), Capacitance wire-mesh tomograph for multiphase flow applications. 5th world congress on industrial process tomography, Norway. P624-629.
- Da Silva, M., Schleicher E., Hampel, U. (2007c), Novel wire mesh sensor for the investigation of non-conducting fluids. 6th International conference on multiphase flow, ICMF 2007. S7_Thu_B_51.
- Da Silva, M. J. (2007), Capacitance Wire-mesh sensor, available at <http://www.fzd.de/db/Cms?pNid=1693>
- Da Silva, M.J., Schleicher, E., Hampel, U., Prasser, H.-M. (2006), Patent: Grid sensor for the two-dimensional measurement of different components in the cross section of a multiphase flow, WO 2007 121708, DE 10 2006 019178.
- Damsohn, M., Prasser, H.-M. (2009), High-speed liquid film sensor for two-phase flows with high spatial resolution based on electrical conductance. *Flow Measurement and Instrumentation* 20, P1-14.
- Deckwer, W.D. (1991), Bubble column reactors. Wiley, New York.
- Delhaye, J. M., Giot, M., and Riethmuller, M. L. (1979), Two-phase flows in nuclear reactors. Hemisphere Pub. Corp/McGraw-Hill.
- Drahos, J., Zahradník, J., Fialová, M., and Bradka, F. (1992). Identification and modelling of liquid flow structures in bubble column reactors. *Chem. Eng. Sci.*, 47, P3313-3320.
- Drahos, J. and Cermák, J. (1989), Diagnostics of gas—liquid flow patterns in chemical engineering systems. *Chemical Engineering and Processing*, Volume 26, Issue 2, Pages 147-164.
- Duangprasert, T., Sirivat, A., Siemanond, K., Wilkes, J. (2008), Vertical two-phase flow regimes and pressure gradients under the influence of SDS surfactant. *Experimental Thermal and Fluid Science*, 32, P808–817.
- Dukler, A. E. and Taitel, W. (1986), Flow Pattern transitions in gas-liquid systems: Measurement and Modelling, Chapter 1 of *Multiphase Science and Technology*, Vol. 2 (Ed. G. F. Hewitt, J. M. Delhaye and N. Zuber), Hemisphere Publishing Pubs.
- Duns, H., Ros, N. (1963), Vertical Flow of gas and liquid mixtures in wells. 6th world petroleum congress.

- Fischer, F. and Hampel, U. (2010), Study of gas liquid two phase flow in pipes with ultra fast electron beam x-ray CT. 6th World Congress on Industrial Process Tomography, China.
- Fischer, F., Hoppe, D., Schleicher, E., Mattausch, G., Flaske, H., Bartel, R. and Hampel, U. (2008), An ultra fast electron beam x-ray tomography scanner, *Measurement Science and Technology* 19: 094002.
- Friedel, L. (1979), Improved friction pressure drop correlations for horizontal and vertical two-phase pipe flow. European two-phase flow group meeting, Italy.
- Gaddis, E.S. and A. Vogelpohl, A. (1986), Bubble formation in quiescent liquids under constant flow conditions, *Chem. Eng. Sci.*, 41, 97-105.
- Geraci, G. (2005), Gas-liquid flows in inclined pipes and Venturi. PhD Thesis, University of Nottingham.
- Ghajar, A. (2005), Non-Boiling heat transfer in gas-liquid flow in pipes-a tutorial. *J. of the Braz. Soc. Of Mech. Sci. & Eng.* P46-73.
- Gluszek, J. and Marcinkowski, R. (1983), Pressure oscillations in bubble columns. *The Chemical Engineering Journal*, 26, 181-187.
- Govan, A. H., Hewitt, G. F., Richter, H. J., and Scott, A. (1991), Flooding and churn flow in vertical pipes. *International Journal of Multiphase Flow* vol. 17, P27-44.
- Groen, J.S. (2004), Scales and structures in bubbly flows, Ph.D. Thesis, Technical University of Delft.
- Hampel, U. (2008), Advanced two-phase flow measurement techniques at Research Centre Dresden-Rossendorf, sensors, systems, and applications. Seminar presented at the University of Nottingham.
- Harmathy, T.Z., (1960), Velocity of large drops and bubbles in media of infinite or restricted extent, *A.I.Ch.E.J.*, 6, 281-288.
- Harms, A., Laratta, F. A. R. (1973), The dynamic-bias in radiation interrogation of two-phase flow, *Int. J. Heat Mass Transfer*, 16, 1459-1465.
- Harteveld, W. (2005), Bubble columns: structures or stability? Ph.D. thesis, Delft University of Technology.
- Hasan, N.M. and B.J. Azzopardi, B.J. (2007), Imaging stratifying liquid-liquid flow by capacitance tomography, *Flow Measurement and Instrumentation* 18, P241-246.
- Hawkes, N.J., Lawrence, C.J., Hewitt, G.F. (2001), Prediction of the transition from annular to wispy-annular flow using linear stability analysis of the gas-droplet core. *Chem. Eng. Sci.* 56, 1925-1932.
- Hawkes, N.J., Lawrence, C.J., Hewitt, G.F. (2000), Studies of wispy-annular flow using transient pressure gradient and optical measurements. *Int. J. Multiphase Flow*, 26, 1562-1592.

- Hawkes, N.J. and Hewitt, G.F. (1995), Experimental studies of wispy annular flow. International Symposium on Two-Phase Flow Modelling and Experimentation, 9-11 October 1995, Rome.
- Hernandez-Perez, V., Abdulkadir, M. and Azzopardi, B.J. (2011), Grid generation issues in the CFD modelling of two-phase flow in a Pipe. *The Journal of Computational Multiphase Flows*. Volume 3, Number 1.
- Hernandez Perez, V., Azzopardi, B.J., Kaji, R., Da Silva, M.J., Beyer, M., Hampel, U. (2010), Wisp-like structures in vertical gas-liquid pipe flow revealed by wire mesh sensor studies. *International Journal of Multiphase Flow*, 36, P908-915.
- Hernandez-Perez, V. (2007), Gas-liquid two-phase flow in inclined pipes. PhD thesis, University of Nottingham.
- Hewitt, G.F. (2005), http://www.thermopedia.com/toc/chapt_g/GAS-LIQUID_FLOW.html, Begell house.
- Hewitt, G.F. (Ed) (1998), Heat Exchanger Design Handbook, Begell house.
- Hewitt, G.F. (1997), Wisps in the pipe: Annular flow at high mass fluxes. Experimental Heat Transfer, Fluid Mechanics and Thermodynamics 1997 (Ed. M. Giot, F. Mayinger and G.P. Celata), Vol. 1, P 1-14, Edizioni ETS, Pisa.
- Hewitt, G.F. (1996), In search of two-phase flow, *Journal Of Heat Transfer-Transactions Of The ASME*, Vol:118, P518-527.
- Hewitt, G.F., and Jayanti, S. (1993), To churn or not to churn. *International Journal of Multiphase Flow* vol. 19, P527-529.
- Hewitt, G.F., Martin, C.J., and Wilkes, N.S. (1985), Experiment and modelling studies of annular flow in the region between flow reversal and the pressure drop minimum. *Physico-Chemical Hydrodynamics* vol. 6, P69-86.
- Hewitt, G.F. (1978), Measurement of two-phase flow. Parameters (New York).
- Hewitt, G.F. and Hall-Taylor, N.S. (1970), Annular two-phase flow, Oxford.
- Hewitt, G.F., Roberts, D.N. (1969), Studies of two-phase patterns by simultaneous X-ray and flash photography. *UKAEA Report AERE M2159*.
- Hikita, H., Asai, Tanigawa, S.K., Segawa, K. and Kitao, M. (1980), Gas Hold-up in Bubble Columns. *The Chemical Engineering Journal*, 20, 59 - 67.
- Hills, J. H., Jones, W. E., Ibrahim, A. (1997), The behaviour of a pilot-scale horizontal themosyphon reboiler. *Trans IChemE*, Vol 75, Part A.
- Hills, J. H. (1993), The behaviour of a bubble column at high throughputs II. Radial voidage profiles. *The Chemical Engineering Journal*, Volume 53, P115-123.
- Hills, J. H. (1976), The operation of bubble column at high throughputs I: Gas hold measurements. *The Chemical Engineering Journal*, Volume 12, P89-99.

- Hills, J.H. (1974), Radial non-uniformity of velocity and voidage in a bubble column at high throughput, *Trans.I.Chem. Engs.*, 52, 1-9.
- Hinze, J.O. (1955), Fundamentals of the hydrodynamic mechanism of splitting of dispersion processes. *American Institute Chemical Engineers Journal* vol 1, P289-295.
- Holt, A.J., Azzopardi, B.J., and Biddulph, M.W. (1999), Calculation of two-phase pressure drop for vertical upflow in narrow passages by means of a flow pattern specific model. *Chemical Engineering Research and Design* vol. 77, P7-15
- Hubbard, M. B., and Dukler, A. E. (1966), The characterisation of flow regimes for horizontal two-phase flow, *Proc. of 1966 Heat Trans. Fluid. Mech. Inst.*, P101-121.
- Ito, D., Prasser, H.-M., Kikura, H., Aritomi, M. (2011), Uncertainty and intrusiveness of three-layer wire-mesh sensor. *Flow Meas. and Inst.*, 22 (4), 249-256.
- Jakobsen, H. (2008), *Chemical Reactor Modeling*. Springer.
- Jayanti, S., Hewitt, G.F., Low D.E.F. and Hervieu, E. (1993), Observation of flooding in the Taylor bubble of co-current upwards slug flow. *Int. J. Multiphase Flow*, 19, 431-434.
- Jayanti, S, and Hewitt, G.F. (1992), Prediction of the slug-to-churn transition in vertical two-phase flow. *International Journal of Multiphase Flow* vol 18, P847-860.
- Jiang, Y., Rezkallah, K. (1993), An experimental study of the suitability of using a gamma densitometer for void fraction measurements in gas-liquid flow in a small diameter tube. *Measurement Science & Technology*. Vol 4, P496-505.
- Jin, H., Yang, S., Wang, M., Williams, R.A. (2007), Measurement of gas holdup profiles in a gas liquid co-current bubble column using electrical resistance tomography, *Flow Measurement and Instrumentation*, Volume 18, Issues 5-6, Process Tomography and Flow Visualization, October-December 2007, Pages 191-196.
- Johansen, G.A. & Jackson P. (2004), *Radioisotope Gauges for Industrial Process Measurements*. Wiley.
- Johnson, I. (1987), US Patent Number 4,644,263. Method and apparatus for measuring water in crude oil.
- Jones, O., Zuber, N. (1975), The interrelation between void fraction fluctuations and flow patterns in two-phase flow. *Int. J. Multiphase flow*. Vol 2, P273-306.
- Kaji, R., Hills, J.H., Azzopardi, B.J. (2009), Extracting information from time series data in vertical upflow. *Multiphase Sci. Tech.* 21, 1-12.
- Kaji, R. (2008), Characteristics of two-phase flow structures and transitions in vertical upflow. PhD Thesis, University of Nottingham.
- Kantarci, N., Borakb, F., Ulgena K. (2005), Bubble column reactors. *Process Biochemistry* 40, 2263-2283

- King, N (Ed) (1990), Multiphase flow in large pipelines. Bernan Press.
- Kleinstreuer, C. (2003), Two-phase flow: theory & applications. Taylor & Francis.
- Krepper, E. et al. (2007), Experimental and numerical studies of void fraction distribution in rectangular bubble columns. *Nuclear Eng. and Design* 237, P399–408.
- Krepper, E., Lucas, D., Prasser, H.M. (2005), On the modelling of bubbly flow in vertical pipes. *Nuclear Engineering and Design*, 235, P597–611.
- Kumar, S., Moslemian D., Dudukovic' M. (1995), A gamma-ray tomographic scanner for imaging voidage distribution in two-phase flow systems. *Flow Meas. Instrum.* 1995; 6(1):61–73.
- Kumara, W., Halvorsen, B., Melaaen, M. (2010), Single-beam gamma densitometry measurements of oil–water flow in horizontal and slightly inclined pipes. *Int. Journal of Multiphase Flow*, 36, 467–480.
- Lage, P.L.C., Espo'sito, R.O. (1999), Experimental determination of bubble size distributions in bubble columns: prediction of mean bubble diameter and gas hold up. *Powder Technology*, 101, 142–150.
- Langston, P.A., Burbidge, A.S., Jones, T.F. and Simmons, M.J. (2001), Particle and droplet size analysis from chord measurements using Bayes' theorem. *Powder Technology*, 116(1), 33-42
- Lapidus, L. and Elgin, J. C., (1957), Mechanics of vertical-moving fluidized systems. *A.I.Ch.E. Journal*, 3, 63-68.
- Letzel, H.M., Schouten, J.C., Krishna, R. and van den Bleek, C.M. (1999), Gas holdup and mass transfer in bubble column reactors operated at elevated pressure, *Chem. Eng. Sci.*, 54, 2237-2246.
- Levy, S. (1999), Two-phase flow in complex systems, Wiley-IEEE.
- Llamas, J.D. et al (2008), Wire mesh tomography applied to trickle beds: A new way to study liquid maldistribution. *Chemical Engineering and Processing* 47 (2008) 1765–1770.
- Lo, S, (2008), STAR-CD training course. University of Nottingham.
- Lockhart, R. W., Martinelli, R. C. (1949), Proposed correlation data for isothermal two-phase two-component flow in pipes, *Chem. Eng. Progr.* Vol 45, P39-45.
- Lucas, D., Beyera, M., Szalinski, L., and Schütza, P. (2010), A new database on the evolution of air–water flows along a large vertical pipe. *International Journal of Thermal Sciences*, Volume 49, Issue 4, P664-674.
- Mackay, D.J.C. (1996), An introduction to Monte Carlo methods, in Proceedings of the 1996 Erice Summer School, <http://www.cs.toronto.edu/mackay/abstracts/erice.html>.

- Manera, A., Ozarc, B., Paranjapec, S., Ishii, M., Prasser, H-M. (2009), Comparison between wire-mesh sensors and conductive needle-probes for measurements of two-phase flow parameters. *Nuclear Engineering and Design*. 239, P1718–1724.
- Manera, A., Prasser, H.-M., van der Hagen, T., Mudde, R., de Kruijf, W. (2007), A comparison of void-fraction measurements during flashing-induced instabilities obtained with a wire-mesh sensor and a gamma transmission set-up. 6th International conference on multiphase flow, ICMF2007.
- Manera, A., Prasser, H.-M., Lucas, D., van der Hagen, T.H.J.J. (2006), Three-dimensional flow pattern visualization and bubble size distributions in stationary and transient upward flashing flow. *Int. Journal of Multiphase Flow*, 32, P996–1016.
- Mao, Z.S. and Dukler, A.E. (1993), The myth of churn flow? *International Journal of Multiphase Flow* vol. 19, P 377-383.
- Matusiak, B., Da Silva, M., Hampel, U., Romanowski, A. (2010), Measurement of Dynamic Liquid Distributions in a Fixed Bed Using ECT and Capacitance Wire-Mesh Sensor. *Ind. Eng. Chem. Res.*, 49, 2070–2077.
- McQuillan, K.W. and Whalley, P.B. (1985a), Flow patterns in vertical two-phase flow. *International Journal of Multiphase Flow* vol. 11, P 161-176.
- McQuillan, K.W., and Whalley, P.B. (1985b), A comparison between flooding correlations and experimental flooding data for gas-liquid flow in vertical circular tubes. *Chemical Engineering Science* vol. 40, P 1425-1440.
- McQuillan, K.W., Whalley, P.B., and Hewitt, G.F. (1985), Flooding in vertical two-phase flow. *International Journal of Multiphase Flow* vol. 11, P 741-760.
- Mendelson, H.D. (1967), The prediction of bubble terminal velocity from wave theory, *A.I.Ch.E.J.*, 13, 250-253.
- Mishima, K., Ishii, I. (1984), Flow regime transition criteria for two-phase flow in vertical tubes. *Int. J. Heat Mass Transfer*, 27, 723–734.
- Mudde, R. F. (2010), Advanced measurement techniques for GLS reactors. *The Canadian Journal of Chemical Engineering*, 88: 638–647.
- Mudde, R.F., Hartevelde, W.K. and van den Akker, H.E.A. (2009), Uniform Flow in Bubble Columns. *Ind. Eng. Chem. Res.*, 48, 148–158.
- Mudde, R., Saito, T. (2001), Hydrodynamical similarities between bubble column and bubbly pipe flow. *Journal of Fluid Mechanics*. Vol 437, P203-228.
- Nicklin, D.J., and Davidson, J.F. (1962), The onset of instability in two-phase slug flow. Institution of Mechanical Engineers Symposium on Two-Phase Flow, London.
- Ohnuki, A., Akimoto, H. (2000), Experimental study on transition of flow pattern and phase distribution in upward air–water two-phase flow along a large vertical pipe. *International Journal of Multiphase Flow*. Volume 26, Issue 3, P367-386.

- Omebere-Iyari, N., Azzopardi, B.J., Lucas, D., Beyer, M., H-M Prasser, H. (2008), The characteristics of gas-liquid flow in large risers at high pressures. *International Journal of Multiphase flow*. Vol 34, P461-476.
- Omebere-Iyari, N. and Azzopardi, B.J. (2007), A study of flow patterns for gas/liquid flow in small diameter tubes. *Chemical Eng Research and Design*, 85(A2), 180-192.
- Omebere-Iyari, N. (2006), The effect of pipe diameter and pressure in vertical two-phase flow. PhD Thesis, University of Nottingham.
- Owen, D. (1986), An equilibrium and theoretical analysis of equilibrium annular flows. PhD Thesis. University of Birmingham.
- Petrick, M., Swanson, B. (1958), Radiation attenuation method of measuring density of a two-phase fluid. *Rev. Sci. Instr.*, 29, 1079.
- Pickering P. F., Hewitt, G.F., Watson, M.J., Hale, C.P. (2001), The Prediction of flows in production risers - Truth & Myth, IIR Conference, Aberdeen, June 2001.
- Pietruske, H. and Prasser, H. M. (2007), Wire-mesh sensors for high-resolving two-phase flow studies at high pressures and temperatures. *Flow Meas. Instrum.* 18 87-94.
- Piper, T.C. (1974), Dynamic gamma attenuation density measurements. *Aerojet Nuclear Company. Report Number ANCR-1160*.
- Porteous (1969), Prediction of the upper limit of the slug flow regime, *Brit. Chem. Eng.*, 14, No. 9, 117-119.
- Prasser, H.-M. (2008). Novel experimental measuring techniques required to provide data for CFD Validation. *Nuclear Engineering and Design*, 238, 744-770.
- Prasser, H.-M., Beyer, M., Carl, H., Manera, A., Pietruske, H., Schütz, P. (2007a), Experiments on upwards gas-liquid flow in vertical pipes. Report FZD-482. Available online at: <http://www.fzd.de/publications/010475/10475.pdf>.
- Prasser, H.-M. et al (2007c), Evolution of the structure of a gas-liquid two-phase flow in a large vertical pipe. *Nuclear Engineering and Design*, 237, P1848-1861.
- Prasser, H.-M., Misawa M., Tiseanu I. (2005a), Comparison between wire-mesh sensor and ultra-fast x-ray tomography for an air-water flow in a vertical pipe. *Flow Measurement and Instrumentation*, 16, P73-83.
- Prasser, H.-M., Beyer, M., Böttger, A., Carl, H., Lucas, D., Schaffrath, A., Schütz, P., Weiß, F.-P., Zschau, J. (2005b), Influence of the pipe diameter on the structure of the gas-liquid interface in a vertical two-phase pipe flow. *Nuclear Technology*, Vol 152.
- Prasser, H.-M., Beyer, M., Böttger, A., Carl, H., Lucas, D., Schaffrath, A., Schütz, P., Weiss, F.-P., Zschau, J. (2004), TOPFLOW tests on the structure of the gas-liquid interface in a large vertical pipe. Annual Meeting on Nuclear Technology, Germany.

- Prasser, H.-M.; Zschau, J.; Peters, D.; Pietzsch, G.; Taubert, W.; Trepte, M. (2002a), Fast wire-mesh sensors for gas-liquid flows - visualisation with up to 10 000 frames per second. International Congress on Advanced Nuclear Power Plants (ICAPP), June 9-13, 2002 - Hollywood Florida, USA, Proc. CD-ROM, paper #1055.
- Prasser, H.-M., Krepper, E., Lucas, D. (2002b), Evolution of the two-phase flow in a vertical tube, decomposition of gas fraction profiles according to bubble size classes using wire-mesh sensors. *Int. J. Therm. Sci.* 41, P17-28.
- Prasser, H.-M., Scholz, D., Zippe, C. (2001), Bubble size measurement using wire-mesh sensors. *Flow Measurement and Instrumentation*, 12, P299-312.
- Prasser, H.-M. (2000), High speed measurement of the void fraction distribution in ducts by wire mesh sensors. International meeting on reactor noise 11; (Athens).
- Prasser, H.-M., Böttger, A., Zschau, J. (1998), A new electrode-mesh tomograph for gas-liquid flows. *Flow measurement and instrumentation*. Vol 9, P111-119.
- Premoli, A., Francesco, D., and Prina, A. (1970), An empirical correlation for evaluating two-phase mixture density under adiabatic conditions. European Two-Phase Flow Group Meeting.
- Ramakrishnan, S., Kumar, S.R., Kuloor, N.R. (1969), Studies in bubble formation-I bubble formation under constant flow conditions, *Chemical Engineering Science*, Volume 24, Issue 4, Pages 731-747.
- Reilly, I.G., Scott, D.S., De Bruin, J.W. and MacIntyre, D. (1994), The role of gas phase momentum in determining gas hold up and hydrodynamic flow regimes in bubble column operations, *Can. J. Chem. Eng.*, 72, 3-12.
- Reinecke, N., Petritscha, G., Boddema, M., Mewes, D. (1998), Tomographic imaging of the phase distribution in two-phase slug flow. *Int. J. Multiphase flow*, Vol 24, No 4, P617-634.
- Reinecke, N., Boddem, M., Petritsch, G., Mewes, D. (1996), Tomographisches Messen der relativen Phasenanteile in zweiphasigen Strömungen fluider Phasen, *Chemie Ingenieur Technik* 68, 11, 1404-1412.
- Rhodes, E. (1980), Gas-Liquid Flow. Video by UKAEA, Harwell, UK.
- Ribeiro, C.P. and Mewes, D. (2007), The influence of electrolytes on gas hold-up and regime transition in bubble columns, *Chem. Eng. Sci.*, 62, 4501-4509.
- Richardson, J.F. and Zaki, W.N. (1954), Sedimentation and Fluidization: Part I, *Trans. I. Chem. Engrs.*, 32, 35-53.
- Richter, S., Aritomi, M., Prasser, H.-M., Hampel, R. (2002), Approach towards spatial phase reconstruction in transient bubbly flow using a wire-mesh sensor, *International Journal of Heat and Mass Transfer*, 45, P1063-75.
- Rouhani, S., and Soheli, M. (1983), Two-phase flow pattern: A review of research result. *Progr. Nuclear Energy*, 11, 217-259.

- Růžicka, M., Drahoš, J., Mena, P.C. and J.A. Teixeira, J.A. (2003), Effect of viscosity on homogeneous–heterogeneous flow regime transition in bubble columns, *Chem. Eng. J.*, 96, 15-22.
- Růžicka, M., Zahradnik, J., Drahoš J. and Thomas, N.H. (2001), Homogeneous–heterogeneous regime transition in bubble columns, *Chem. Eng. Sci.*, 56, 4609–4626.
- Saleh, J. (Ed) (2002), *Fluid flow handbook*. McGraw-Hill.
- Schlegel, J., Hibiki, T., Ishii, M. (2010), Development of a comprehensive set of drift-flux constitutive models for pipes of various hydraulic diameters. *Progress in Nuclear Energy*, 52, P666-677.
- Schlegel, J. P., Sawant, S., Paranjape, S., Ozar, B., Hibiki, T., Ishii, M. (2009), Void fraction and flow regime in adiabatic upward two-phase flow in large diameter vertical pipes. *Nuclear Engineering And Design*. Vol 239, Issue 12, Pages 2864-2874.
- Schmitz, D., Mewes, D. (2000), Tomographic imaging of transient multiphase flow in bubble columns. *Chemical Engineering Journal* 77, 99–104.
- Schrock, V.E. (1969), Radiation attenuation techniques in two-phase flow measurements. 11th National ASME/AICHE Heat transfer Conference, P24.
- Sekoguchi, K., and Mori, K. (1997), New development of experimental study on interfacial structure in gas-liquid two-phase flow. *Experimental Heat Transfer, Fluid Mechanics and Thermodynamics*.
- Serizawa, A., and Kataoka, I. (1988), Transient phenomena in Multi-phase flow. *Afghan, N.H. Hemisphere, New York*, P179-224.
- Serizawa A., Kataoka I., Michiyoshi I. (1975), Turbulence structure of air-water bubbly flow-II: Local properties. *Int J Multiphase Flow*, 2, P235-246.
- Shah, Y.T., Kelkar, B.G., Godbole, S.P. and Deckwer, W.D. (1982), Design parameters estimations for bubble column reactors, *A.I.Ch.E. J.*, 28, 353-379.
- Shoham, O. (2006), Mechanistic modelling of gas-liquid two-phase flow in pipes. *Society of Petroleum Engineers, USA*.
- Shollenberger, K., Torczynski, J.R., Adkins, D.R., O'Hern, T.J., and Jackson, N. B. (1997), Gamma-densitometry tomography of gas holdup spatial distribution in industrial-scale bubble columns. *Chemical Engineering Science*. Vol 52, No 13.
- Song, C.H., No, H.C., and Chung, M.K (1995), Investigation of bubble flow developments and its transition based on the instability of void fraction waves. *International Journal of Multiphase Flow* vol. 21, P 381-404.
- Stahl, P., Rohr, P.R.V. (2004), On the accuracy of void fraction measurements by single-beam gamma-densitometry for gas–liquid two-phase flows in pipes. *Experimental Thermal and Fluid Science*. Vol 28, P533–544.

- Sun, B., Yan, D., and Zhang, Z. (1999), The instability of void fraction waves in vertical gas-liquid two-phase flow. *Communications in Nonlinear Science and Numerical Simulation*, Volume 4, Issue 3, Pages 181-186.
- Szalinski, L., Abdulkareem, L.A., Da Silva, M.J., Thiele, S., Beyer, M., Lucas, D., Hernandez-Perez, V., Hampel, U., Azzopardi, B.J. (2010), Comparative study of gas-oil and gas-water two-phase flow in a vertical pipe. *Chem. Engineering Science*, 65.
- Taitel, Y., Barnea, D., and Dukler, A.E. (1980), Modelling flow pattern transitions for steady upward gas-liquid flow in vertical tubes. *American Institute of Chemical Engineers Journal* vol. 6, P345-354.
- Taitel, Y., and Duckler, A. (1976), Model for predicting flow regime transitions in horizontal and near horizontal gas-liquid flow. *AIChE J*, 22, P45-55.
- Takacs, G. (2005). *Gas Lift Manual*. Penwell books.
- The Engineer (2009), Article: Meeting the energy mix challenge. Published on the 19th November 2009.
- Thiele, S., Da Silva, M., Hampel, U., Abdulkareem, L., Azzopardi, B.J. (2008), High-resolution oil-gas two-phase flow measurement with a new capacitance wire-mesh tomography. 5th International Symposium on Process Tomography, Poland.
- Thome, J. (2004), *Engineering Data Handbook III*. Wolverine Tube Inc.
- Tomiyaama, A., Celata, G.P., Hokosawa, S. and Yoshida, S. (2002), Terminal velocity of single bubbles in surface tension force, *Int. J. Multiphase Flow*, 28, 1497-1519.
- Tomiyaama, A., I. Kataoka, I., Zun, I., Sakaguchi, T. (1998), Drag coefficients of single bubbles under normal and micro-gravity conditions. *JSME Int. J. Ser. B.*, 41, 2.
- Tomiyaama, A. (1998), Struggle with computational bubble dynamics. Third International Conference on Multiphase Flow, ICMF'98, Lyon, June 8-12.
- Trick, M.D. (2003), Comparison of correlations for predicting wellbore pressure losses in gas-condensate and gas-water wells, Canadian International Petroleum Conference 2003, Calgary, Alberta. Canada, June 10-12.
- Van der Meulen, G.P., Zangana, M., Zhao, D. and Azzopardi, B.J. (2010), Film measurements in two-phase gas-liquid flow by conductance techniques in vertical large diameter pipes. 7th International Conference on Multiphase Flow. USA.
- Van der Meulen, G.P., Zangana, M., Zhao, D. and Azzopardi, B.J. (2009), Phase distribution measurements by conductance probes and pressure drop in gas-liquid flows, ExHFT-7, Krakow, Poland.
- Van Maanen, H.R.E. (1999), Retrieval of turbulence and turbulence properties from randomly sampled laser-anemometry data with noise, Ph.D. Thesis, Technische Universiteit Delft, Netherlands.
- Wallis, G.B. (1969), *One dimensional two-phase flow*, McGraw-Hill.

- Wallis, G.B. (1962), The onset of entrainment in annular gas-liquid flow. General Electric Report No. 62 GL127.
- Wang S.K., Lee S.J., Jones Jr O.C., Lahey Jr R.T. (1987), 3-D turbulence structure and phase distribution measurements in bubbly two-phase flows. *Int J Multiphase flow* 13(3):327-343.
- Wangjiraniran, W., Motegi, Y., Richter, S., Kikura, H., Aritomi, M., Yamamoto, K. (2003), Intrusive effect of wire mesh tomography on gas-liquid flow measurement. *J. Nucl. Sci. Technol.*, 40, 11, pp. 932-940.
- Warsito, W. and Fan, L.S. (2001), Measurement of real-time flow structures in gas-liquid and gas-liquid-solid flow systems using electrical capacitance tomography (ECT), *Chem. Eng. Sci.*, Vol. 56, pp 6455-6462.
- Watson, M.J. and Hewitt, G.F. (1999), Pressure effects on the slug to churn transition. *International Journal of Multiphase Flow* vol. 25, P1225-1241.
- Whalley, P. B. (1987), Boiling, condensation, and gas-liquid flow, Oxford.
- Whalley, P. B. (1980), See Hewitt, G. F. (1983). Multiphase flow and pressure drop. Heat Exchanger Design Handbook, Hemisphere, Washington, DC, Vol. 2, 2.3.2-11.
- Wilkinson, P.M., Spek, A.P. and van Dierendonck, L.L. (1992), Design parameters estimation for scale-up of high-pressure bubble columns, *A.I.Ch.E.J.*, 38, 544-554.
- Wu, Y., Ong, B.C. and Al-Dahhan, M.H. (2001), Predictions of radial gas holdup profiles in bubble column reactors, *Chem. Eng. Sci.*, 56, 1207-1210.
- York, T. A. (2001), Status of electrical tomography in industrial applications. *Journal of Electronic Imaging*, 10, P608-19.
- Zahradnik, J., Fialova, M., Ruzicka, M., Drahos, J., Kastanek, F., Thomas, N.H. (1997), Duality of the gas-liquid flow regimes in bubble column reactors. *Chemical Engineering Science*, Volume 52, Issues 21-22, Pages 3811-3826.
- Zahradnik J. and F. Kastanek F. (1979), Gas holdup in uniformly aerated bubble column reactors. *Chem. Eng. Commun.*, 3, P413-429.
- Zangana, M. (2011), Film behaviour of vertical gas-liquid flow in a large diameter pipe. PhD. Thesis. University of Nottingham.
- Zaruba, A., Krepper, E., Prasser, H.-M., Reddy Vanga, B.N. (2005), Experimental study on bubble motion in a rectangular bubble column using high-speed video observations. *Flow Measurement and Instrumentation* 16, 277-287.
- Zehner, P. and Kraume, M. (2000), Bubble Columns. Ullmann's Encyclopedia.
- Zuber, N., and Findlay, J.A. (1965), Average volumetric concentration in two-phase flow systems. *Journal of Heat Transfer* vol. 87, P 453-468.

NOMENCLATURE

Main symbols

A	Area	(m ²)
A_1	Friedel parameter	(-)
A_2	Friedel parameter	(-)
C_0	Radial distribution parameter	(-)
c	Constant	(-)
D	Pipe diameter	(m)
d	Diameter	(m)
E	Entrainment rate	(kg/m ² s)
E_1	CISE parameter	(-)
E_2	CISE parameter	(-)
f	Friction factor	(-)
f	Frequency	(Hz)
Fr	Froude number	(-)
g	Acceleration due to gravity	(m/s ²)
h	wave height	(m)
H	Height of liquid in a column	(m)
j	CISE parameter	(-)
Ku	Kutataledze number	(-)
L	Length	(m)
\dot{m}	Mass flux	(kg/m ² s)
Mo	Morton Number	(-)
n	Wu et al parameter	(-)
P	Pressure	(kg/ms ²)
Q	Volumetric flow rate	(m ³ /s)
r, R	Pipe radius	(m)
Re	Reynolds number	(-)
St_g	Strouhal number based on gas superficial velocity	(-)
St_l	Strouhal number based on liquid superficial velocity	(-)
S	Perimeter	(m)
t	Time	(s)
T	Temperature	(°C)
U	Velocity	(m/s)
U_R	Slip ratio	(-)
u	Velocity	(m/s)
u^*	Dimensionless velocity	(-)
V	Volumetric void fraction	(-)
V_T	Terminal velocity of bubbles	(m/s)
We	Weber Number	(-)
x_g	Quality	(-)
X	Lockhart Martinelli parameter	(-)
V	Velocity	(m/s)
v_{gd}	Drift velocity	(m/s)
z	Axial distance	(m)

Greek symbols

β	Inclination from horizontal	(deg)
δ	Mean film thickness	(m)
ε	Gas or void fraction	(-)
ε_g	Gas or void fraction	(-)
ε'	Gas or void fraction (accelerational)	(-)
ϕ	Two phase multiplier	(-)
η	Dynamic viscosity	(kg/ms)
μ	Dynamic viscosity	(kg/ms)
ν	Kinematic viscosity	(m ² /s)
ρ	Density	(kg/m ³)
σ	Surface tension	(N/m)
τ	Shear stress	(N/m ²)

Subscripts

l	liquid
lo	all flow as liquid
ls	liquid superficial
m	mixture
g	gas
gs	gas superficial
H	homogeneous
max	maximum
min	minimum
MP	multiphase
r	radial
s	slip
TP	two phase
Tr	transition
w	wave

Abbreviations

BSD	Bubble Size Distribution
Cap	Capacitance
CFD	Computational Fluid Dynamics
Cond	Conductance
CP	Conductance Probes
ECT	Electrical Capacitance Tomography
ERT	Electrical Resistance Tomography
FPD	Frictional Pressure Drop
GD	Gamma densitometer
GPD	Gravitational Pressure Drop
HTFS	Heat Transfer & Fluid Flow Service
HZDR	Helmholtz-Zentrum Dresden-Rossendorf (Research Institute in Germany, formerly FZD)
PDF	Probability Density Function
PSD	Power Spectral Density
TPD	Total Pressure Drop
WMS	Wire Mesh Sensor
VOF	Volume of Fluid

APPENDIX A

Some definitions used in Chapter 2 are expanded more mathematically in this section.

Homogeneous Flow

$$\left(\frac{dp}{dz}\right)_{friction} = \frac{-P}{S} \quad (A1)$$

$$\left(\frac{dp}{dz}\right)_{acceleration} = m \frac{d}{dz} \left(\frac{1}{\rho_H} \right) \quad (A2)$$

where ρ_H is the homogeneous density.

$$\rho_H = \rho_g \varepsilon_{gH} + \rho_l (1 - \varepsilon_{gH}) \quad (A3)$$

$$\rho_H = \frac{\rho_g \rho_l}{x_g \rho_l + (1 - x_g) \rho_g} \quad \text{and} \quad x_g = \frac{U_{gs} \rho_g}{m} \quad (A4)$$

x_g is known as the quality, or dryness fraction or vapour mass fraction.

$1 - x_g$ is known as the wetness fraction or liquid mass fraction.

$$\left(\frac{dp}{dz}\right)_{grav} = \rho_H g \sin \beta \quad (A5)$$

$$\therefore -\frac{dp}{dz} = \frac{-P}{S} + m \frac{d}{dz} \left(\frac{1}{\rho_H} \right) + \rho_H g \sin \beta \quad (A6)$$

Heterogeneous Flow

For each of the above constituents of the pressure drop, it can be shown that

(Azzopardi, 2006):

$$-\left(\frac{dp}{dz}\right)_{acceleration} = \frac{d}{dz} \left[m \left(\frac{x_g^2}{\varepsilon_g \rho_g} + \frac{(1 - x_g)^2}{(1 - \varepsilon_g) \rho_l} \right) \right] \quad (A7)$$

$$\Rightarrow -\Delta p_{acceleration} = \left[m \left(\frac{x_g^2}{\varepsilon_g \rho_g} + \frac{(1 - x_g)^2}{(1 - \varepsilon_g) \rho_l} \right) \right]_{z_1}^{z_2} \quad (A8)$$

The void fraction in the accelerational might not be the same as the one in the gravitational term therefore the need to include ε'_g . An alternative method for calculating accelerational pressure drop in two-phase compressible gas-liquid flow has also been developed by Barua et al (1992).

$$\left(\frac{dp}{dz}\right)_{\text{grav}} = [\varepsilon_g \rho_g + (1 - \varepsilon_g) \rho_l] g \sin \beta \quad (\text{A9})$$

$$\Rightarrow -\Delta p_{\text{gravitational}} = \int_{z_1}^{z_2} [\varepsilon_g \rho_g + (1 - \varepsilon_g) \rho_l] g \sin \beta dz \quad (\text{A10})$$

$$\left(\frac{dp}{dz}\right)_{\text{frict}} = \frac{\bar{\tau} P}{S} = \frac{4 f_{TP} \dot{m}_{TP}^2}{d 2 \rho_{TP}} \quad (\text{A11})$$

Based on definition of single phase, changing subscripts to *TP*

$$\frac{4 f_{SP} \dot{m}_{SP}^2}{d 2 \rho_{SP}} \phi^2 = \frac{4 f_{lo} \dot{m}}{d 2 \rho_l} \phi_{lo}^2 \quad (\text{A12})$$

$$\Rightarrow -\Delta p_{\text{frictional}} = \int_{z_1}^{z_2} \frac{4 f_{lo} \dot{m}}{d 2 \rho_l} \phi_{lo}^2 dz = \frac{4 f_{lo} \dot{m}}{d 2 \rho_l} \int_{z_1}^{z_2} \phi_{lo}^2 dz \quad (\text{A13})$$

Therefore an expression for the overall pressure drop can be written as:

$$-\frac{dp}{dz} = \frac{\bar{\tau} P}{S} + [\varepsilon_g \rho_g + (1 - \varepsilon_g) \rho_l] g \sin \beta + \frac{d}{dz} \left[\dot{m}^2 \left(\frac{x_g^2}{\varepsilon_g \rho_g} + \frac{(1 - x_g)^2}{(1 - \varepsilon_g) \rho_l} \right) \right] \quad (\text{A14})$$

$$-\Delta p = \int_{z_1}^{z_2} \frac{4 f_{lo} \dot{m}}{d 2 \rho_l} \phi_{lo}^2 dz + \int_{z_1}^{z_2} [\varepsilon_g \rho_g + (1 - \varepsilon_g) \rho_l] g \sin \beta dz + \left[\dot{m}^2 \left(\frac{x_g^2}{\varepsilon'_g \rho_g} + \frac{(1 - x_g)^2}{(1 - \varepsilon'_g) \rho_l} \right) \right]_{z_1}^{z_2} \quad (\text{A15})$$

A significantly more complicated expression than the homogeneous model with the addition of the void fraction in the accelerational and frictional terms. Once ε_g is

worked out, then the gravity term in the pressure drop equation can be deduced. Together with the frictional pressure drop, the overall pressure drop can therefore be calculated for vertical flow. In vertical or slightly inclined pipes, accelerational pressure drop can be neglected (Takacs, 2005). This is only where there is no major phase change. It is small even if condensation or evaporation is occurring (Azzopardi, 2003). Therefore:

$$-\Delta p = \int_{z_1}^{z_2} \frac{4 f_{lo}}{d} \frac{\dot{m}^2}{2 \rho_l} \phi_{lo}^2 dz + \int_{z_1}^{z_2} [\varepsilon_g \rho_g + (1 - \varepsilon_g) \rho_l] g \sin \beta dz \quad (\text{A16})$$

In horizontal flow $\beta=0^\circ$ and hence the gravitational term is zero. In vertical flow angle β is taken to be 90° . Hence $\sin(90)=1$. Therefore for vertical:

$$-\Delta p = \int_{z_1}^{z_2} \frac{4 f_{lo}}{d} \frac{\dot{m}^2}{2 \rho_l} \phi_{lo}^2 dz + \int_{z_1}^{z_2} [\varepsilon_g \rho_g + (1 - \varepsilon_g) \rho_l] g dz \quad (\text{A17})$$

In vertical flow, if the frictional term is disregarded the pressure drop reduces to:

$$-\Delta p = \int_{z_1}^{z_2} [\varepsilon_g \rho_g + (1 - \varepsilon_g) \rho_l] g dz \quad (\text{A18})$$

Other Pressure Drop Equations

Beggs and Brill (1973) published an alternative equation for the pressure drop based on the homogeneous model, that includes an accelerational component:

$$\frac{dp}{dz} = \frac{g \sin \beta [\rho_g \varepsilon_g + \rho_l (1 - \varepsilon_g)] + \frac{f_{TP} \dot{m} (U_{gs} + U_{ls})}{2 D_i}}{1 - [\rho_g \varepsilon_g + \rho_l (1 - \varepsilon_g)] \frac{(U_{gs} + U_{ls}) U_{gs}}{p}} \quad (\text{A19})$$

It is also possible to derive an alternative equation for the pressure drop using the conservation of energy giving the following expression (Whalley, 1987):

$$-\frac{dp}{dz} = \rho_H \frac{dF}{dz} + \rho_H g \sin \beta + \frac{\rho_H \dot{m}^2}{2} \frac{d}{dz} \left[\left(\frac{x_g^3}{\epsilon_g^2 \rho_g^2} + \frac{(1-x_g)^3}{\epsilon_g^2 \rho_l^2} \right) \right] \quad (\text{A20})$$

Most correlations for frictional pressure drop, and void fraction are based on the momentum approach not the energy approach, and hence this will be the approach used in this work.

CISE Correlation

$$U_R = 1 + E_1 \left(\frac{j}{1 + E_2 j} \right)^{0.5} \quad \text{for} \quad \frac{j}{1 + E_2 j} > E_2 \quad (\text{A21})$$

$$U_R = 1 \quad \text{for homogeneous flow} \quad (\text{A22})$$

$$\text{where } j = \frac{\epsilon_{gH}}{1 - \epsilon_{gH}} \quad (\text{A23})$$

$$E_1 = 1.578 \text{Re}^{-0.19} \left(\frac{\rho_l}{\rho_g} \right)^{0.22} \quad (\text{A24})$$

$$E_2 = 0.0273 \text{We} \text{Re}^{-0.51} \left(\frac{\rho_l}{\rho_g} \right)^{-0.08} \quad (\text{A25})$$

Re and Weber numbers used here are defined as

$$\text{Re} = \frac{(\dot{m}_g + \dot{m}_l) D_t}{\eta_l} \quad \text{We} = \frac{(\dot{m}_g + \dot{m}_l)^2 D_t}{\sigma \rho_l} \quad (\text{A26, A27})$$

Friedel Correlation

Friedel (1979) proposed the following correlation:

$$\phi_{lo}^2 = A_1 + A_2 \quad (\text{A28})$$

$$\text{where } A_1 = (1 - x_g)^2 + x_g^2 \frac{\rho_l f_{go}}{\rho_g f_{lo}} \quad (\text{A29})$$

$$\text{and } A_2 = \frac{3.24 x_g^{0.78} (1-x_g)^{0.224} \left(\frac{\rho_l}{\rho_g}\right)^{0.91} \left(\frac{\eta_g}{\eta_l}\right)^{0.19} \left(1-\frac{\eta_g}{\eta_l}\right)^{0.7}}{Fr^{0.045} We^{0.035}} \quad (\text{A30})$$

for horizontal and vertically upward flow. In these equations, f_{lo} and f_{go} are the single phase friction factors if all the flow were liquid or gas respectively and

$$We = \frac{m_{TP}^2 D_i}{\rho_{TPH} \sigma} \quad \text{where } \rho_{TPH} \text{ is the homogeneous two-phase density}$$

$$\rho_{TPH} = \left(\frac{x_g}{\rho_g} + \frac{(1-x_g)}{\rho_l} \right)^{-1} \quad (\text{A31})$$

Drift Flux Model

The flow in this model is described in terms of a distribution parameter and an averaged local velocity difference between the phases. Bubbles will rise in liquids. How fast those bubbles are rising in the liquid is the drift flux velocity.

$$\varepsilon_g = \frac{U_{gs}}{C_0 (U_{gs} + U_{ls}) + v_{gd}} \quad (\text{A32})$$

$$\text{Drift velocity } v_{gd} = K \left(\frac{\sigma g (\rho_l - \rho_g)}{\rho_l^2} \right)^{0.25} \quad (\text{A33})$$

Commonly used value for C_0 is 1.2, and for K values of 1.4 or 1.53 are suggested. It is interesting to note that this equation is predicting a lower ε_g as U_{ls} is increased.

APPENDIX B

Background Information on the Wire Mesh Sensor

How the two variant wire mesh sensors process the data can be found in several references. For the conductivity version, Prasser et al (1998, 2000, 2005) and for the capacitance version Da Silva et al (2007, 2010). This summary is adapted from Szalinski et al, 2010. Let's consider one crossing point as shown in Figure B1.

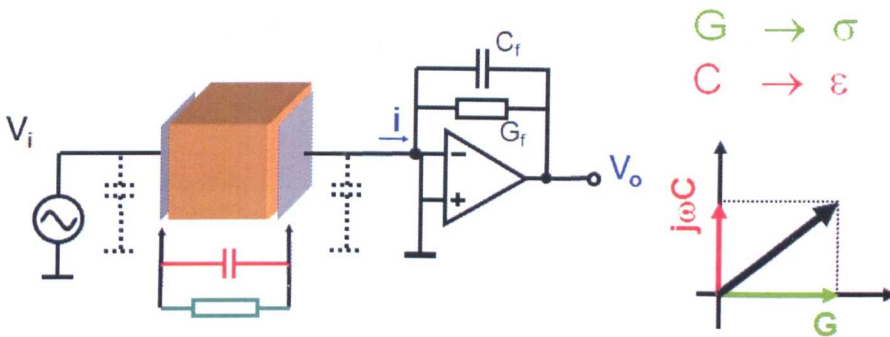


Figure B1-One crossing point processing of wire mesh sensor

The impedance Z is the ratio of the voltage to the current in complex notation.

Admittance Y is the inverse of impedance Z .

$$Y = \frac{1}{Z} = \frac{V_i}{i} \quad (\text{B1})$$

The following mathematical relationships can be derived for Y where G is the conductance in the real part and C is capacitance in imaginary part.

$$Y = G + j\omega C \text{ and } \epsilon_{\text{complex}} = \epsilon_r - j \frac{\sigma}{\omega \epsilon_0} \Rightarrow Y = \epsilon_r j\omega \epsilon_0 K_g \quad (\text{B2})$$

The conductivity WMS measures the real part “ G ” or the conductance and then converts it to conductivity. The capacitance WMS measures the imaginary part “ $j\omega C$ ” and converts this into permittivity. The capacitance C_x is proportional to the relative permittivity value of the fluid between the electrodes ϵ_r . Therefore:

$$C_x = \epsilon_r \epsilon_0 K_g \quad (\text{B3})$$

ϵ_0 is the permittivity in a vacuum and k_g is a geometrical constant. The equivalent equation for conductance G_x where σ is the electrical conductivity:

$$G_x = \sigma K_g \quad (\text{B4})$$

For conductivity measurements the transmitter electrodes are excited by a bipolar DC voltage while for permittivity measurements AC voltage is applied. In both cases the receiver currents are converted to voltages by a trans-impedance amplified circuit. This is followed by a DC voltage detector in the conductivity-measuring electronics and by a log demodulation circuit in the permittivity-measuring electronics. For conductivity measurements the output voltages V_k of receiver circuits correspond to the conductivity value κ at the crossing points according to

$$V_k = K \cdot \kappa \quad (\text{B5})$$

K is a proportionality factor which depends on electronic circuit constants. In this way, conducting and non-conducting phases (e.g., air and water) can be discriminated by evaluating the output voltage V_k . The permittivity-measuring electronics generates a voltage V_{\log} which is proportional to logarithm of the rms-value of the transmitted AC current which is itself proportional to the relative permittivity ϵ_r of the fluid present at a crossing point (Da Silva et al., 2007). The relative permittivity is related to the output voltage

$$V_{\log} = a \ln(\epsilon_r) + b \Rightarrow \epsilon_r = \exp\left(\frac{V_{\log} - b}{a}\right) \quad (\text{B6})$$

where a and b are constants determined by geometry and circuit parameters.

The wire-mesh sensor produces sequences of cross-sectional images which are further processed as a three-dimensional data matrix of electrical voltage values denoted by $V_{(i,j,k)}$. They correspond to either conductivity or permittivity values in the crossing points, as described above. Further, i and j are the spatial indices of the image pixels (corresponding to the wire numbers) and k is the temporal index of each image. Equations (B5) and (B6) hold for every crossing point in the wire grid. The constants in these equations are different for all crossing points.

A calibration procedure is required to extract flow parameters from the raw data. Calibration is performed by acquiring data from measurements in conditions of “pipe completely filled with liquid” and “pipe completely filled with gas”. Data is saved into calibration matrices as described below. In the case of conductivity-based electronics, due to the linear relationship between measured voltage and liquid conductivity, only one reference point is required and the gas void fraction matrix can be obtained by

$$\varepsilon_{i,j,k} = 1 - \frac{V_{K,mix}(i,j,k)}{V_{K,water}(i,j)} \quad (B7)$$

where $V_{k,mix}$ represents the measured voltage of the two-phase mixture and $V_{k,water}$ is reference measurement with water. Eq. (B7) assumes a linear relationship between gas phase fraction and conductivity values, as extensively used in earlier investigations (Prasser et al. 1998).

There are various models that relate the permittivity to the void fraction ε_g . The simplest model is known as the parallel model and considers a linear relationship between the mixture permittivity ε_m and gas or void fraction ε_g . There are other

models e.g. series and Maxwell models and the differences can be seen in Figure B2 (Hampel, 2009). The default is Parallel model (linear). Also possible to do log model.

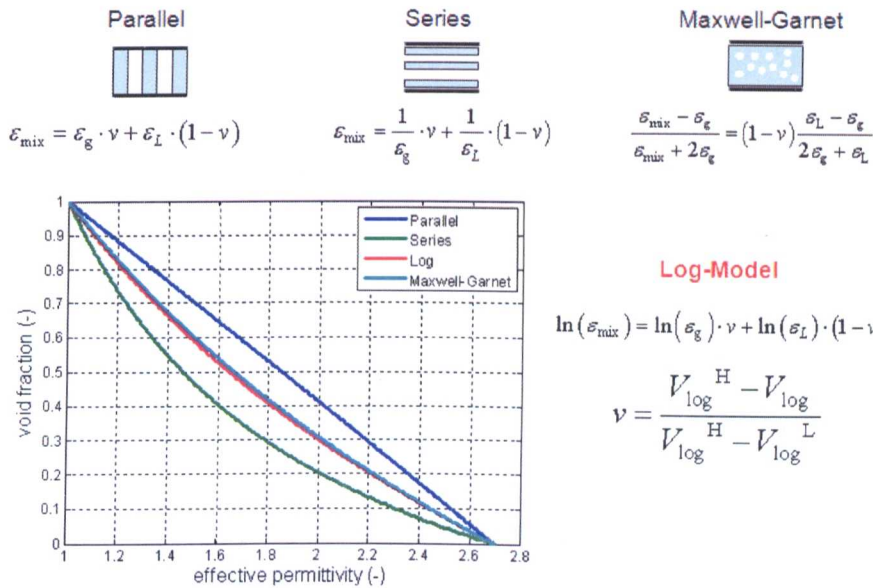


Figure B2-Capacitive models used for the CapWMS

The parallel model can be written as

$$\epsilon_g(i, j, k) = \frac{\epsilon_r^H - \epsilon_m(i, j, k)}{\epsilon_r^H - \epsilon_r^L} \quad (\text{B8})$$

However, due to the logarithmic dependence of the measured voltage V_{\log} , with relative permittivity values, calculating gas void fraction is not as simple as for conductivity-based electronics. Thus, measured mixture permittivity is calculated by

$$\epsilon_m(i, j, k) = \exp\left(\frac{V_{\log, m}(i, j, k) - V_{\log, L}(i, j)}{V_{\log, H}(i, j) - V_{\log, L}(i, j)} \ln(\epsilon_r^H)\right) \quad (\text{B9})$$

where the subscripts ‘mix’ denotes the voltage measured of the two-phase mixture, ‘H’ for the condition of pipe filled with liquid, and ‘L’ for empty pipe. In this way, the

measured mixture permittivity along with the known relative permittivity of water and air are used in Eq. (12) to obtain the gas void fraction matrix in the case of air/water experiments. A description of the calibration routine for permittivity-based electronics is given by Da Silva et al. 2010. From gas void fraction matrix $\varepsilon_{i,j,k}$, axial and radial gas fraction profiles as well as integral gas fraction values can be determined by integration of the measured data over appropriate partial volumes. Further post-processing of the matrix $\varepsilon_{i,j,k}$ can be performed to identify single bubbles or determine characteristic bubble or interfacial area parameters.

For the graphical presentation of the wire-mesh sensor data two different visualisation techniques are used: axial slice images and virtual side projections. The first method extracts the phase fraction distribution along a central chord of the cross-section. The resulting two-dimensional image shows the phase distribution along the diameter (x-axis) for successive temporal steps (y-axis). Virtual side projections are obtained from application of a simplified ray-tracing algorithm as described by Prasser et al. (2005). In this visualisation technique an illumination of the three-dimensional phase fraction distribution by parallel white light is simulated and the light intensity emitted into the direction of a virtual observer is calculated. This method gives an instructive pseudo-3D view which is close to flow observations with a video camera through a transparent test section. In both cases the vertical axis represents a virtual length which is scaled according to the averaged gas velocity. This scaling allows the display of gas structures in the flow and thus visualisations of different gas velocities can be directly compared. The data processing software generates several "special" files that can be imported into Excel for data manipulation and analysis.

A summary of the important electronic file is as follows:

.epst file: This is ASCII file. It is the space averaged time series of the cross-sectional void. In mathematical terms:

$$\bar{\varepsilon}_k = \varepsilon(t) = \sum_i \sum_j a_{i,j} \varepsilon_{i,j,k} \quad (\text{B10})$$

An example of how the weighting coefficient works is shown in Figure B4.

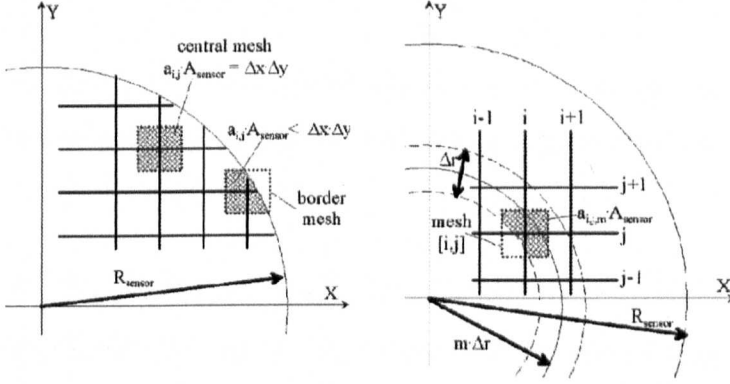


Figure B3-coefficient $a_{i,j}$ for averaging the void fraction, and $a_{i,j,m}$ for radial gas fraction profiles.

.epsxy file: This is an ASCII file. It is time averaged local void fraction. See Figure B3. In mathematical terms:

$$\bar{\varepsilon}_{i,j} = \frac{1}{k_{\max}} \sum_{k=1}^{k_{\max}} \varepsilon_{i,j,k} \quad (\text{B11})$$

$$\bar{\varepsilon} = \frac{1}{k_{\max}} \sum_{k=1}^{k_{\max}} \bar{\varepsilon}_k = \frac{1}{k_{\max}} \sum_{k=1}^{k_{\max}} \varepsilon_{i,j,k} \quad (\text{B12})$$

$$\bar{\varepsilon} = \frac{1}{k_{\max}} \sum_{i=1}^{i_{\max}} \sum_{j=1}^{j_{\max}} \sum_{k=1}^{k_{\max}} a_{i,j} \varepsilon_{i,j,k} = \sum_{i=1}^{i_{\max}} \sum_{j=1}^{j_{\max}} a_{i,j} \cdot \bar{\varepsilon}_{i,j} = \frac{1}{k_{\max}} \sum_{k=1}^{k_{\max}} \varepsilon_k \quad (\text{B13})$$

.epsrad 40: This is an ASCII file. It is the radial void fraction. In mathematical terms:

$$\bar{\varepsilon}_m = \frac{1}{k_{\max}} \sum_{i=1}^{i_{\max}} \sum_{j=1}^{j_{\max}} \sum_{k=1}^{k_{\max}} a_{i,j,m} \varepsilon_{i,j,k} = \sum_{i=1}^{i_{\max}} \sum_{j=1}^{j_{\max}} a_{i,j} \cdot m \cdot \bar{\varepsilon}_{i,j} \quad (\text{B14})$$

How the weighting coefficient works is explained in Figure B4, with a worked example.

Bubble Size generated by the WMS (extracted from HZDR documentation)**First Stage-Bubble Identification**

The bubble identification and the determination of important characteristics for the bubbles can be done using special evaluation algorithms. Thereby, a bubble is defined as a region of connected gas-containing elements in void fraction data $\varepsilon_{i,j,k}$ which is completely surrounded by elements containing the liquid phase. To each element which belongs to one bubble, the same identification number is assigned. Different bubbles receive different identification numbers. These numbers are stored in the elements $b_{i,j,k}$ of a second array that is saved in a binary file of the type *.b. This array has the same dimension as the void fraction array. After the bubble recognition algorithm is completed, each element $b_{i,j,k}$ carries the number of the bubble to which the given element with the indexes i,j,k belongs.

Local instantaneous gas fractions can have values between 100 % (gas) and 0 % (liquid), if the corresponding measurement volume formed by two crossing wires contains both gas and liquid at the same time. Furthermore, signal noise may also lead to such intermediate values. Consequently, a sharp distinction between elements filled with gas and elements filled with water is not possible. To recognise the unique bubbles even under these difficult conditions HZDR use a so called recursive extended decremental fill algorithm. It is based on the idea that the local gas fraction can only decrease or remain equal if the identification is started at the point of the highest gas fraction found inside a bubble. Before the identification starts all elements of $b_{i,j,k}$ are set to zero (which means not assigned to any bubble) and a bubble counter n is set to unity (i.e. bubble number one). Then, beginning with a void fraction of 100%, the filling procedure starts with a search for an element (measurement volume) that is not yet occupied by a bubble, which is the case, if $b_{i,j,k} = 0$, if its indices are within the

boundaries of the data array. If this check ends with a positive result (it means a seed of a bubble was found), the corresponding element in the bubble identification array is set to the current bubble number, i.e. $b_{i,j,k} = n$. Now, all six neighbouring elements are tested by calling the procedure itself with single indices (i, j, k) modified by ± 1 .

After the bubble recognition for the first bubble is finished, which happens if the test condition is not fulfilled for none of the recursive calls of the fill procedure, the program control returns from this routine. The bubble counter n is increased by one and the search for the next starting point begins. The previously used start element is no more available, since the element is now labelled by a non-zero bubble identifier. That means the entire bubble identification loop can just be repeated until the gas fraction in the last free maximum element falls below a chosen threshold. This threshold – we call it initiation threshold - defines the minimum size of bubbles which can be detected with the wire-mesh sensor. It should be greater than the noise level in the signal. In our experience a good initiation threshold is 10 – 12 %.

To avoid unrealistic fragmentations in case of presence of signal noise it is necessary to allow for a certain increase of the local gas fraction in a fill step. On the other hand, saddles in the gas fraction distribution are found at places where two bubbles are so close to each other that both of them contribute to the local instantaneous gas fraction at the saddle point. A reasonable criterion has to be formulated that allows distinguishing between those saddle points that are caused by noise and those that are the result of a close approach of two bubbles. This criterion cannot be solely based on local gradients of the gas fraction, since a local small positive gradient does not tell anything about the trend at greater distance.

In the adopted solution, a real saddle is defined as a point of contact between two neighbouring bubbles that possesses a local gas fraction that is significantly lower than the smaller of both maximum gas fractions of the pair of involved bubbles. The maximum gas fractions may be found at a certain distance from the saddle point. For this reason, the maxima are stored for each bubble number individually. Since the fill process remains decremental, the gas fraction in the location where the fill is initialised represents the maximum for the given bubble. This criterion is used to unite a pair of unrealistic bubble fragments with the identifiers n_1 and n_2 in case that the gas fraction $\varepsilon_{i,j,k}$ at the point of contact is not significantly lower than the smaller of both maximum gas fractions. A threshold ε_{tr} is defined that quantifies the condition for the unification:

$$\varepsilon_{tr} > \min(\varepsilon_{\max,n_1}, \varepsilon_{\max,n_2}) - \varepsilon_{i,j,k} \rightarrow \text{unite}$$

The repair process by unifying unrealistic fragments was implemented directly into the bubble recognition algorithm. If the fill process for a bubble with the current number n_1 arrives at an element that has before already identified to belong to a different bubble n_2 , the aforementioned condition is checked. If the condition fires the fill process is terminated in this direction. In the opposite case, the currently identified bubble acquires the identifier of the bubble that was found before and the bubble identifier n_1 can be distributed for the next bubble. Using the results of various tests with synthetic bubbles it was found that the optimal differential threshold ε_{tr} for the repair mechanism of the extended decremental fill process is near the peak-to-peak amplitude of the noise of the wire-mesh sensor. This value was defined at HZDR at ~15%. After successful completion of the bubble detection the results (bubble identification matrix) are saved in the binary file *.b. Using this new data together with the information about the void fraction, now important parameters can be determined for each bubble. They are stored in text files of the type *.a. It has to be

noted that in the code the index i refers to the serial number of the frames, while j and k , in this case, serve as indices in the measurement plane. This assignment of the indices is also used in the equations given in this section. The volume of a bubble with the number n is obtained by integrating the local void fraction of all elements owning the given bubble number:

$$V_{b,n} = \Delta x \Delta y \Delta t b w_b \sum_{i,j,k} \varepsilon_{i,j,k} \forall [i,j,k]: b_{i,j,k} = n \quad (\text{B15})$$

The sum of void fractions is multiplied by the measurement volume, which is the product of the distance of the electrodes in x and y directions and the sampling period, as well as the bubble velocity.

$$\Delta t = \frac{1}{f_{\text{sample}}} \quad (\text{B16})$$

Due to the fact that the individual velocity of bubbles is unknown, the gas phase velocity obtained by cross-correlation is taken as an approximation at the location of the centre of mass of the given bubble:

$$w_b = w_G(r_n) \quad \text{where} \quad r_n = \sqrt{(x_{CM,n} - x_0)^2 + (x_{CM,n} - y_0)^2} \quad (\text{B17})$$

The coordinates of the centre of mass can be obtained by averaging the measurement coordinates of all elements belonging to the selected bubble using the local void fraction values as a weight function:

$$x_{CM,n} = \frac{\sum_{i,j,k} j \Delta x \varepsilon_{i,j,k}}{\sum_{i,j,k} \varepsilon_{i,j,k}} \quad (\text{B18})$$

$$y_{CM,n} = \frac{\sum_{i,j,k} k \Delta y \varepsilon_{i,j,k}}{\sum_{i,j,k} \varepsilon_{i,j,k}} \quad (\text{B19})$$

$$z_{CM,n} = \frac{\sum_{i,j,k} i\Delta z \varepsilon_{i,j,k}}{\sum_{i,j,k} \varepsilon_{i,j,k}} \quad (\text{B20})$$

$$\Delta z = w_b \Delta t \quad \forall [i,j,k] : b_{i,j,k} = n \quad (\text{B21})$$

After that, the equivalent diameter of the bubble can be determined, which is defined as the diameter of a sphere that has the volume according to:

$$D_{b,n} = \sqrt[3]{\frac{6V_{b,n}}{\pi}} \quad (\text{B22})$$

$$\text{Volume of Sphere } V = \frac{4}{3} \pi r^3 \quad (\text{B23})$$

For the evaluation of asymmetries of the bubble, moments for each bubble are calculated. Likewise, the void fraction served as weight function:

$$rm_{x,n} = \sqrt{\frac{5 \sum_{i,j,k} (j\Delta x - x_{CM,n})^2}{\sum_{i,j,k} \varepsilon_{i,j,k}}} \quad (\text{B24})$$

$$rm_{y,n} = \sqrt{\frac{5 \sum_{i,j,k} (k\Delta y - y_{CM,n})^2}{\sum_{i,j,k} \varepsilon_{i,j,k}}} \quad (\text{B25})$$

$$rm_{z,n} = \sqrt{\frac{5 \sum_{i,j,k} (i\Delta z - z_{CM,n})^2}{\sum_{i,j,k} \varepsilon_{i,j,k}}} \quad (\text{B26})$$

From the moments for the coordinates x and y in the measurement plane of the wire-mesh sensor, the radial moment results:

$$rm_{r,n} = \sqrt{rm_{x,n}^2 + rm_{y,n}^2} \quad (\text{B27})$$

Further information on the distortion of the bubble can be obtained by calculating the maximum equivalent diameter in the x-y plane. For this matter, the area being

occupied by the bubble in the x-y plane is added. The sum of the local instantaneous void fractions of the measurement volumes belonging to the bubble is multiplied by the area of the measurement volume in the x-y plane. This procedure is done for each single sampling time characterised by index i:

$$A_{xy,n,i} = \Delta x \Delta y \sum_{j,k} \varepsilon_{i,j,k} \quad \forall [i,j,k]: b_{i,j,k} = n \quad (\text{B28})$$

Maximum area is found and converted into the diameter of an area equivalent circle:

$$D_{xy,n} = \sqrt{\frac{4A_{xy,n,\max}}{\pi}} \quad \text{with} \quad A_{xy,n,\max} = \max(A_{xy,n,i}) \quad (\text{B29})$$

In addition to these bubble characteristics, the minimum and maximum coordinates of the bubbles are determined. For the calculation of these values, it is necessary to define a threshold value of the gas fraction which represents the bubble interface. Experiences at HZDR show that for bubble sizes > 20 mm a threshold 50 % is a good approximation. If bubble diameters are smaller this value is reduced to approx. 20 %. The maximum of gas fraction in the bubble (starting at 100 % for large bubbles) also reduces with decreasing bubble diameter. This reduction is observed for bubbles with a diameter less than approx. 20 mm. This effect results from the limited spatial resolution of the wire-mesh sensor which is e.g. 3 x 3 mm. Small bubbles cannot completely fill the associated measurement volumes. For this reason maximum gas fractions lower than 100 % are observed. Taking these boundary conditions into consideration, as a compromise, the gas fraction threshold representing the bubble interface is taken as half of the maximum gas content of the bubble.

Another important parameter for the characterisation of gas bubbles is the volume fraction of the bubble related to the total volume of the flow:

$$\varepsilon_{b,n} = \frac{V_{b,n}}{V_{all}} \quad (\text{B30})$$

$$V_{all} = t_{meas} \cdot f_{meas} \cdot \Delta x \Delta y \Delta t \cdot \bar{w}_G \sum_j \sum_k a_{j,k} \cdot \bar{w}_G = \frac{J_G}{\varepsilon} \quad (B31)$$

Apart from the already mentioned parameters, the maximum gas fraction and the number of measurement volumes per bubble are determined. All values are stored in an ASCII file (*.a) as table for each identified bubble. The required geometrical data in the bubble property table (*.a file) is converted into real 3D information, e.g. the volume equivalent diameter of the bubble is converted from 32mm*ms into mm. If a *.inf file exists, which contains information about the configuration of the wire-mesh sensors and the electronic device, the routine gets the measurement time from this file. If the *.inf file does not exist a constant value is used which can be changed in the constant value block of the source code. Furthermore, it is necessary to set the inner diameter of the sensor and the number of ring-shaped domains as constant values.

Second Stage-Bubble Size Distribution

After evaluation of the data, three-dimensional information for gas fraction distribution and for bubble identification is available. Additionally, a list with characteristics of each bubble is generated for each measurement. The combination of this data makes it possible to obtain bubble size distributions. To do this, histograms are calculated in which the void fraction per bubble class is summed. This is done related to the volume equivalent diameter as well as related to the area equivalent diameter of the gas bubbles. This information is available in a representation with a linear bubble class width of 0.25 mm and also for a logarithmically increasing width of the bubble classes. The smallest bubble size class for the logarithmic representation has a lower boundary of 0.1 mm. The bubble size distributions are stored in ASCII files with the extensions *.his_lin and *.his_log, respectively. The linear distributions are preferably used for the numerical investigations and the logarithmic information

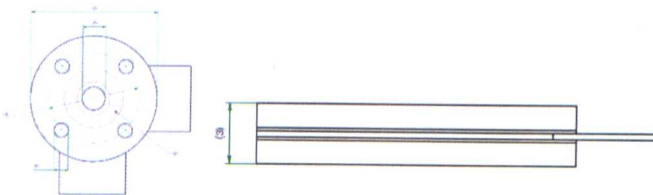
for visualisation. In both types of bubble size distributions, the void fraction that is related to the bubble class width is represented by $(\Delta\varepsilon/\Delta D_b)$, which gives:

$$\varepsilon_{all} = \sum_0^{D_{b,max}} \frac{\Delta\varepsilon}{\Delta D_b} \Delta D_b \quad (B32)$$

In addition these distributions related to the total gas content $(\Delta\varepsilon/\Delta D_b/\varepsilon_{all})$ are listed in both files. Furthermore, the files contain the bubble number distributions with which the absolute number of bubbles per bubble class is referred to the bubble class width and the total measurement time. Further details can be found in Prasser et al (2000-2002), Richter et al (2002), and Manera et al (2006).

Sample WMS Specification

inner diameter (1):	<u>Ø127 ±0.2mm</u>
outer diameter (2):	<u>Ø 254mm</u>
standard / norm	<u>ISO 1302/ISO2768/ISO13715</u>
flange material (steel, acrylic, POM)	<u>Acrylic</u>
installation height (3):	<u>39mm</u>
pitch circle of holes (4):	<u>Ø 210mm</u>
number of holes:	<u>8</u>
diameter of holes (5):	<u>Ø 17mm</u>
inner diameter of mating surface (6):	<u>Ø 130 ±0.1mm</u>
outer diameter of mating surface (6):	<u>Ø 165 ±0.1</u>
wire separation:	<u>2mm</u>
operation pressure (max.):	<u>Atmospheric Pressure i.e. 1 bar (abs)</u>
operation temperature (max.):	<u>30°C</u>
flow velocity (max.):	<u>10 m/s</u>
electrical conductivity (min./ max.)	<u>0-550 micro Siemens/Cm</u>



APPENDIX C

Densitometric calculations

Void fraction determination: A suitable monoenergetic source of radiation is collimated to a thin photon beam. This beam penetrates a pipe along a chord of length d . Behind the pipe a detector records the radiation intensity I . For an empty pipe the measured intensity is denoted as I_E . In case of two-phase flow the beam passes the liquid phase on a length $d_L=(1-\varepsilon)d$, where ε is the gas fraction along the chord, and experiences attenuation. With μ_L being the linear attenuation coefficient of the liquid phase this gives the intensity

$$I = I_E e^{-\mu_L d_L} = I_E e^{-(1-\varepsilon)\mu_L d} . \quad (C1)$$

If μ_L and d are known, the gas fraction can be determined directly. Otherwise one may perform a reference measurement for a full pipe ($d_L=d$, $\varepsilon=0$) and gets the reference intensity

$$I_F = I_E e^{-\mu_L d} . \quad (C2)$$

Combining equations (1) and (2) gives

$$\varepsilon = \frac{\log(I/I_E)}{\log(I_F/I_E)} \quad (C3)$$

Note that this derivation only holds if the photon beam is very thin such that the chordal void fraction is constant across the beam cross-section for a broader beam

(Petrick & Swanson, 1958; Stahl et al, 2004). This derivation also holds for homogeneous and non-homogeneous flows.

Measurement uncertainty: For gamma densitometry, if properly applied, the main source of error is photon statistics (Schrock, 1969). Let N be the number of photons measured in a given time interval. The probability distribution for the sampled count rate values in such an interval is given by the Poisson distribution, with expectation value $\langle N \rangle$ and standard deviation $\sigma = \sqrt{\langle N \rangle}$. The signal-to-noise ratio is given by

$$SNR = \langle N \rangle / \sigma = \sqrt{\langle N \rangle}. \quad (C4)$$

The lowest count rate will occur when the pipe is full of liquid. Let us now require that the noise power (σ) should be in the same range as a count rate change due a certain change in gas fraction. If there was a length Δd changing from liquid to gas the corresponding change in count rate expectation value would be

$$\begin{aligned} \Delta N &= \langle N_E \rangle e^{-\mu_L d} - \langle N_E \rangle e^{-\mu_L (d - \Delta d)} \\ &= \langle N_F \rangle (1 - e^{\mu_L \Delta d}) \end{aligned} \quad (C5)$$

and consequently it can be stated that $\langle N_F \rangle$ is large enough such that

$$\sigma = \sqrt{\langle N_F \rangle} \leq \Delta N = \langle N_F \rangle (1 - e^{\mu_L \Delta d}) \quad (C6)$$

Rearranging (C6) gives

$$\langle N_F \rangle \geq (1 - e^{-\mu_L \Delta d})^{-2}. \quad (C7)$$

With $\mu_L = 0.00846 \text{ mm}^{-1}$ for water and photon energy 662 keV and $\Delta d = 0.5 \text{ mm}$ (the noise power in the count rate is in the same range as the count rate change cause by 1% gas fraction variation or in other words a bubble of 0.5mm diameter) this gives $\langle N_F \rangle \geq 5.57 \cdot 10^4$. For $\Delta d = 1 \text{ mm}$ it is $\langle N_F \rangle \geq 1.34 \cdot 10^4$. Referring to Chapter 4, this gives an uncertainty smaller than 2% for the measurements in this work.

Bias error: A dynamic bias error occurs if the void fraction changes while the gamma densitometer takes a single count rate sample over a certain time interval (Harms et al, 1973). A simulation was performed to estimate this effect for the given geometry and radiation. A virtual flow was considered consisting of elementary cells of size $50 \text{ mm} \times 50 \text{ mm}$. In each cell there is a centred bubble of random diameter smaller than the elementary cell edge length. A virtual gamma ray scans the flow every 1 mm. The count rate is assumed sufficiently high such that statistical uncertainty can be neglected. The simulation determines the given gas fraction (length of beam in bubble / 50 mm) and the integral count rates for the virtual scans. With no loss of generality it is assumed that $N_0 = 0$, and therefore $N_E = 1$ and $N_F = e^{-\mu_L 50 \text{ mm}}$. For K samples with instantaneous beam lengths in gas d_i this gives a total count rate of

$$N = \frac{1}{K} \sum_{i=1}^K e^{-\mu_L (50 \text{ mm} - d_i)}. \quad (C8)$$

Note that the bias error comes from averaging of counts over K different chord lengths in gas. Figure C1 shows the simulation results for the given scenario. The maximum error is about 2% gas fraction overestimation.

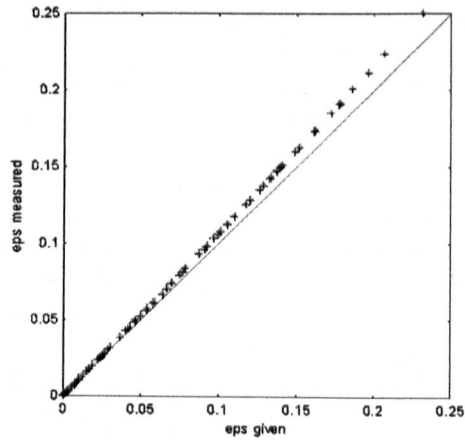


Figure C1-Measured vs calculated gamma void fraction with dynamic bias error.

Appendix D

D1 Experimental Matrix

Four experimental matrices are shown in Table D1 to Table D4.

Run No	cond ($\mu\text{S/cm}$)	Temp $^{\circ}\text{C}$	Flow rate l/min	Ugs (m/s)	H(Initial)mm	H(Final)mm	L. Swell
water	1.0	22.2	0	0.000	119.50	119.50	0.000
run001	1.0	22.2	10	0.004	120.30	123.20	0.024
run002	2.0	22.2	20	0.007	121.20	127.70	0.051
run003	2.0	22.2	30	0.011	121.60	132.20	0.080
run004	2.0	22.2	40	0.014	122.00	136.20	0.104
run005	3.0	22.2	50	0.018	122.40	140.20	0.127
run006	3.0	22.3	60	0.022	122.80	141.20	0.130
run007	3.0	22.2	70	0.025	123.00	145.20	0.153
run008	3.0	22.2	80	0.029	123.00	148.20	0.170
run009	3.0	22.1	90	0.032	123.00	151.20	0.187
run010	4.0	22.4	100	0.036	123.00	154.20	0.202
run011	4.0	22.3	110	0.040	123.20	157.20	0.216
run012	4.0	22.3	120	0.043	123.20	160.20	0.231
run013	4.0	22.3	130	0.047	123.40	164.20	0.248

Table D1- CapWMS matrix for air-distilled water; Spider Injector; 127mm bubble column

Run No	cond ($\mu\text{S/cm}$)	Temp $^{\circ}\text{C}$	Flow rate l/min	Ugs (m/s)	H(Initial) mm	H(Final) mm	L. Swell
water	510.0	19.2	0	0.000	1091	1091	0.000
run001	509.0	19.1	15	0.020	1091	1208	0.097
run002	510.0	19.1	20	0.026	1091	1253	0.129
run003	517.0	19.1	25	0.033	1091	1318	0.172
run004	517.0	19.1	30	0.039	1091	1383	0.211
run005	519.0	19.1	35	0.046	1091	1468	0.257
run006	511.0	19.1	40	0.053	1091	1503	0.274
run007	513.0	19.1	45	0.059	1091	1483	0.264
run008	513.0	19.1	50	0.066	1092	1428	0.235
run009	518.0	19.0	55	0.072	1095.5	1368	0.199
run010	518.0	19.0	60	0.079	1098	1348	0.185
run011	514.0	19.0	65	0.086	1098	1338	0.179
run012	514.0	19.0	70	0.092	1100.5	1348	0.184
run013	513.0	19.0	75	0.099	1103	1358	0.188
run014	511.0	19.0	80	0.105	1103	1368	0.194
run015	511.0	19.0	85	0.112	1105.5	1378	0.198
run016	515.0	18.9	90	0.118	1108	1383	0.199
run017	513.0	18.9	95	0.125	1108	1388	0.202
run018	507.0	18.9	100	0.132	1110.5	1393	0.203
run019	514.0	18.9	105	0.138	1108	1398	0.207
run020	519.0	18.9	110	0.145	1108	1408	0.213

Table D2- CondWMS matrix for air-tap water; Hom Injector; 127mm bubble column

Run No	cond ($\mu\text{S/cm}$)	Temp $^{\circ}\text{C}$	Flow rate l/min	Ugs (m/s)	H(Initial) mm	H(Final) mm	L Swell
water	0.0	19.2	0	0.000	905	905	0.000
run001	0.0	19.1	15	0.020	904.5	995	0.091
run002	0.0	19.1	20	0.026	904	1018	0.112
run003	0.0	19.1	25	0.033	904	1028	0.121
run004	0.0	19.1	30	0.039	904	1043	0.133
run005	0.0	19.1	35	0.046	904	1058	0.146
run006	0.0	19.1	40	0.053	904	1068	0.154
run007	0.0	19.1	45	0.059	904	1078	0.161
run008	0.0	19.1	50	0.066	904	1088	0.169
run009	0.0	19.0	55	0.072	903.5	1098	0.177
run010	0.0	19.0	60	0.079	903	1108	0.185
run011	0.0	19.0	65	0.086	903	1118	0.192
run012	0.0	19.0	70	0.092	903	1128	0.199
run013	0.0	19.0	75	0.099	903	1133	0.203
run014	0.0	19.0	80	0.105	903	1138	0.207
run015	0.0	19.0	85	0.112	903	1143	0.210
run016	0.0	18.9	90	0.118	903	1148	0.213
run017	0.0	18.9	95	0.125	903	1158	0.220
run018	0.0	18.9	100	0.132	903	1168	0.227

Table D3- CondWMS matrix for air-silicone oil; Hom Injector; 127mm bubble column

Run No	cond ($\mu\text{S/cm}$)	Temp $^{\circ}\text{C}$	Flow rate l/min	Ugs (m/s)
run001	0.0	14.3	10	0.047
run002	0.0	13.4	15	0.07
run003	0.0	12.8	19.78	0.093
run004	0.0	12.6	24.4	0.115
run005	0.0	12.4	29.1	0.137
run006	0.0	12.2	33.8	0.159
run007	0.0	12.2	38.5	0.181
run008	0.0	12	43.19	0.203
run009	0.0	11.8	47.66	0.224
run010	0.0	11.6	52.34	0.246
run011	0.0	11.5	56.8	0.267
run012	0.0	11.5	61.27	0.288
run013	0.0	11.4	61.9	0.31
run014	0.0	11.4	70.4	0.331
run015	0.0	11.3	74.89	0.352
run016	0.0	11.2	81.7	0.384
run017	0.0	11.1	87.23	0.41
run018	0.0	11.1	92.76	0.436
run019	0.0	11	98.5	0.463
run020	0.0	11.7	104	0.489
run021	0.0	12.2	115.31	0.542
run022	0.0	16	150	0.7
run023	0.0	15.7	200	0.9
run024	0.0	15.5	300	1.4
run025	0.0	15.4	400	1.9
run026	0.0	15.6	500	2.36
run027	0.0	15.9	600	2.83
run028	0.0	15.7	1000	4.7

Table D4-CapWMS matrix for air-silicone oil, 67mm vertical column, 3mm hole injector

D2 Time Series

The corresponding time series plots are presented in Figure D1 to Figure D5.

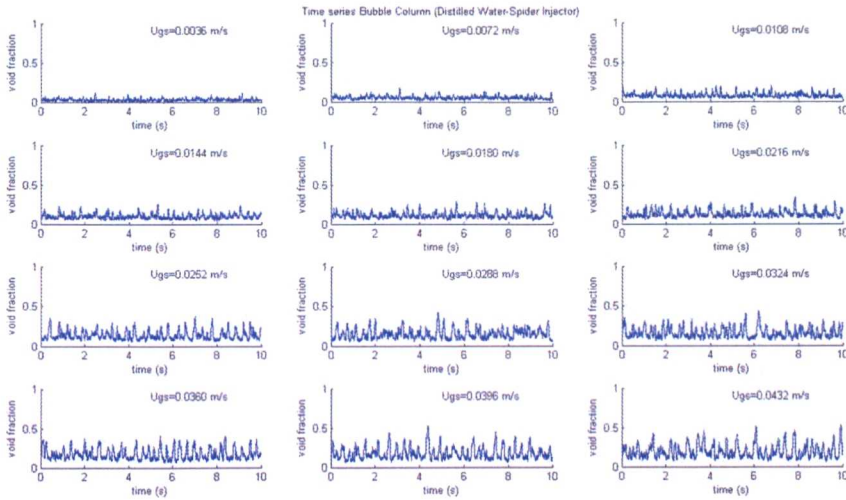


**Figure D1– Time series: air-distilled water; Spider Injector; 127mm bubble column;
CapWMS**

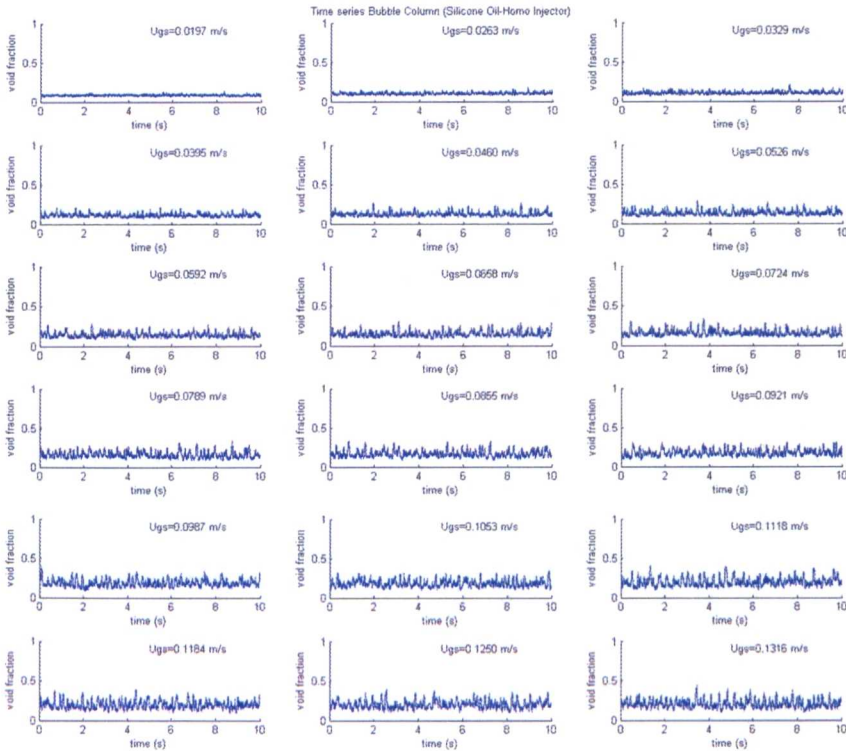


Figure D2- Time series: air-tap water; Hom. Injector; 127mm column; CondWMS

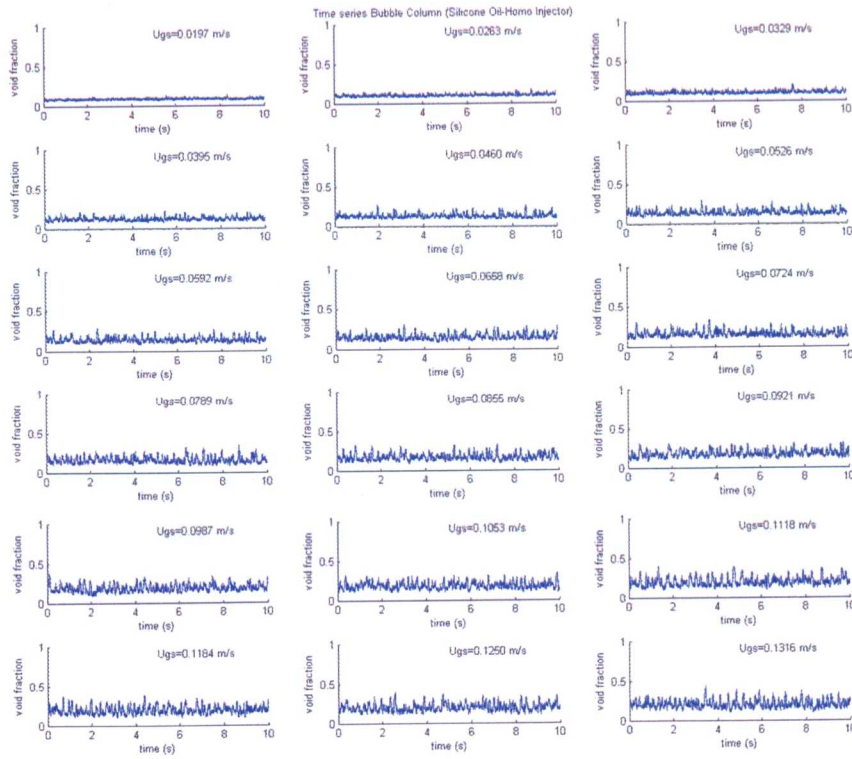


Figure D3- Time series: air-silicone oil; Hom. Injector; 127mm column; CapWMS

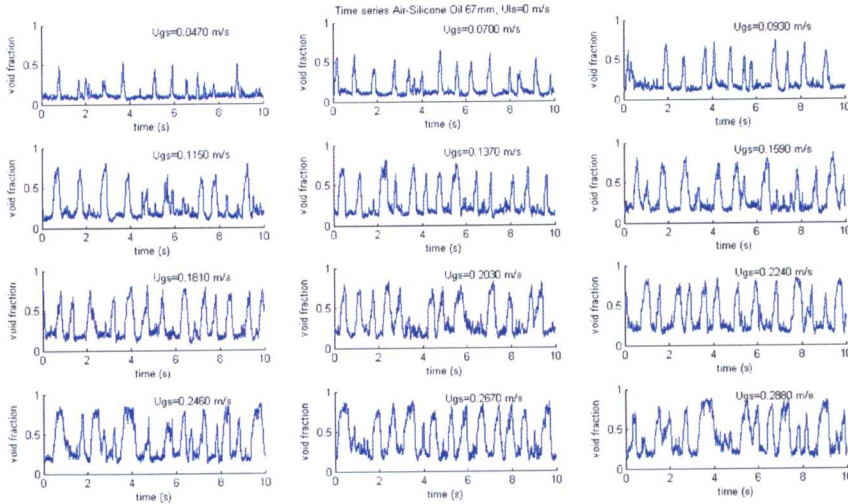


Figure D4- Time series: air-silicone oil; Hom. Injector; 67mm column; CapWMS (I)

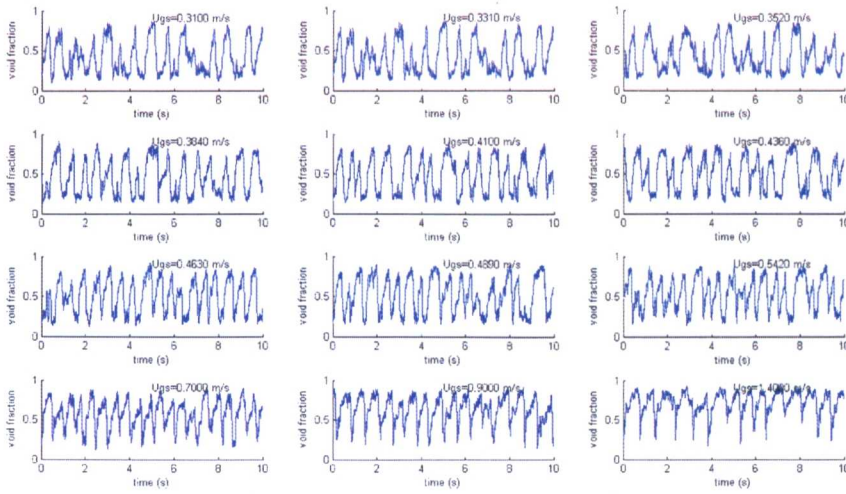


Figure D5- Time series: air-silicone oil; Hom. Injector; 67mm column; CapWMS (II)

D3 Probability Density Function

The probability density function (PDF) can be extracted from the time series using Matlab by using the **hist** or **histc** command. However, on comparison with the MS Excel frequency command, which can also generate PDF profiles, it was noted that **histc** gave more comparable results, and therefore will be used for this analysis. Figure D6 shows the PDF for increasing superficial gas velocity for air-distilled water using the spider injector. Figure D7 shows air-tap water with the homogeneous injector. Figure D8 and Figure D9 show the PDF plots for air-silicone oil for 127mm and 67mm columns respectively.

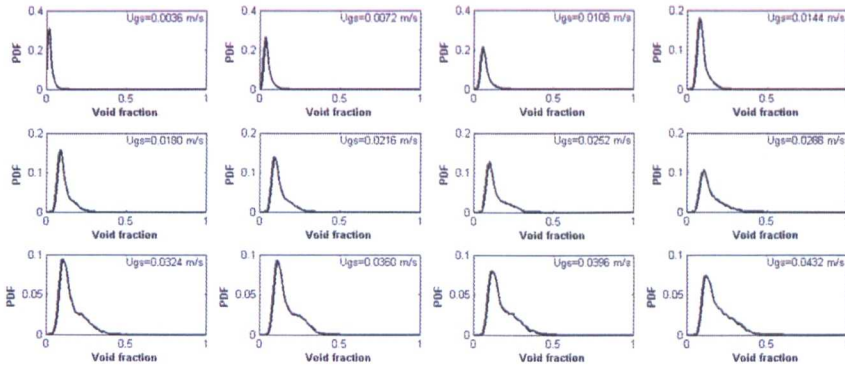


Figure D6 - PDF: air-distilled water; Spider Injector; 127mm bubble column; CapWMS

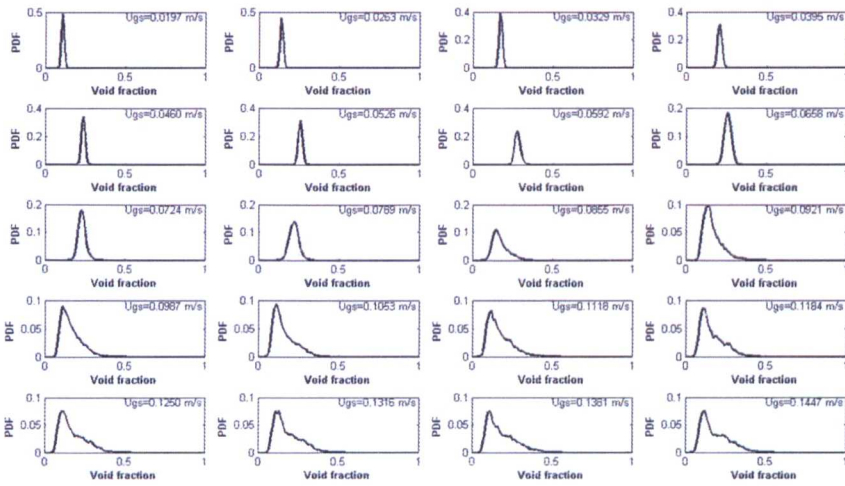


Figure D7- PDF: air-tap water; Hom. Injector; 127mm column; CondWMS

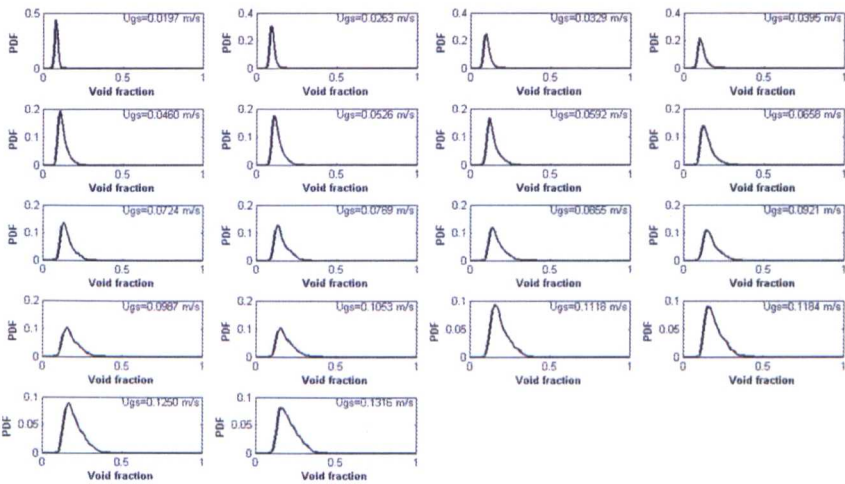


Figure D8- PDF: air-silicone oil; Hom. Injector; 127mm column; CapWMS

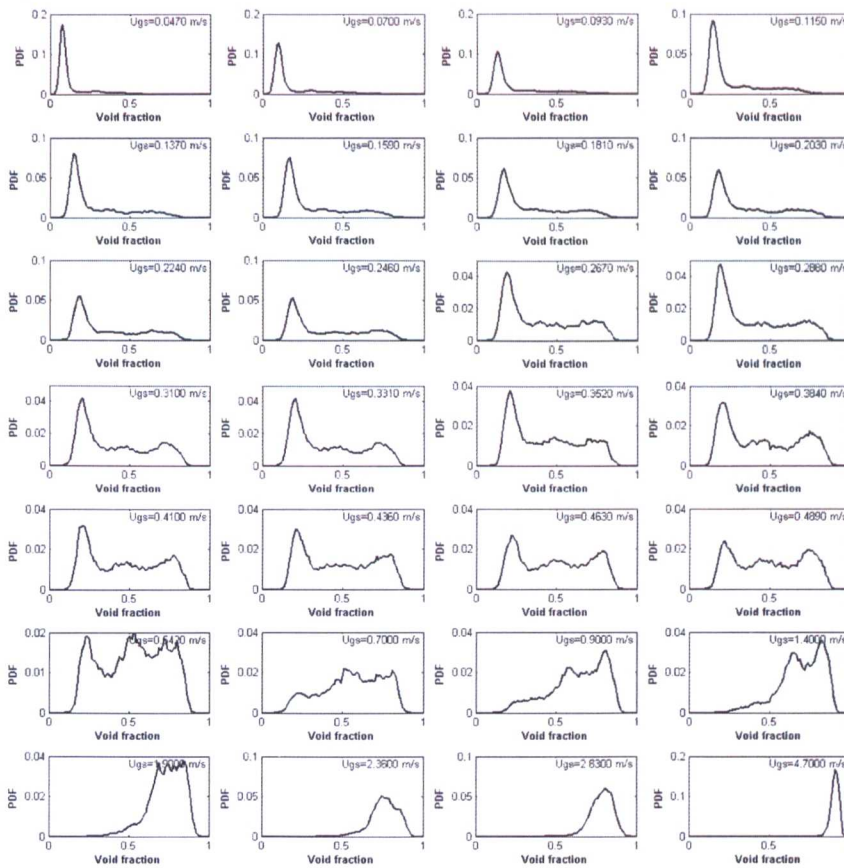


Figure D9- PDF: air-silicone oil, hom. injector, 67mm column, CapWMS

D4 Local Void Profiles

Time averaged local fractions can be extracted and are presented Figures D10-D13.

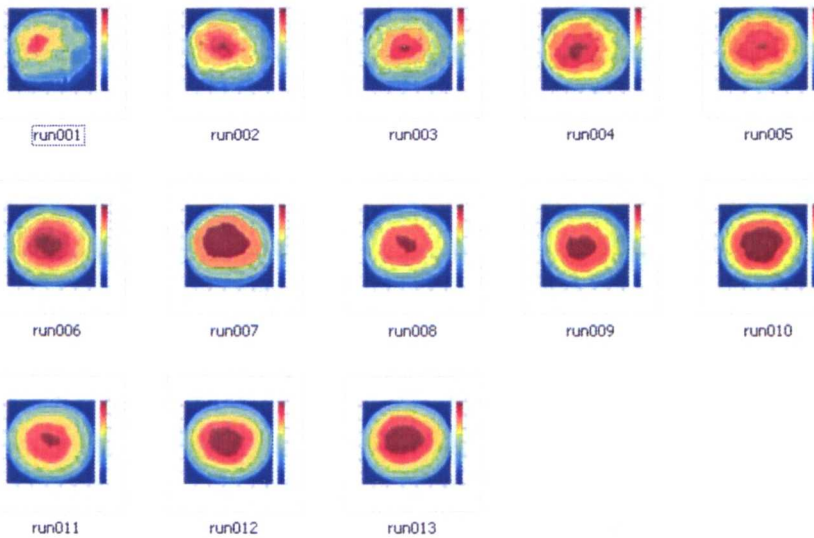


Figure D10– Local voids: air-distilled water; Spider Inj; 127mm column; CapWMS

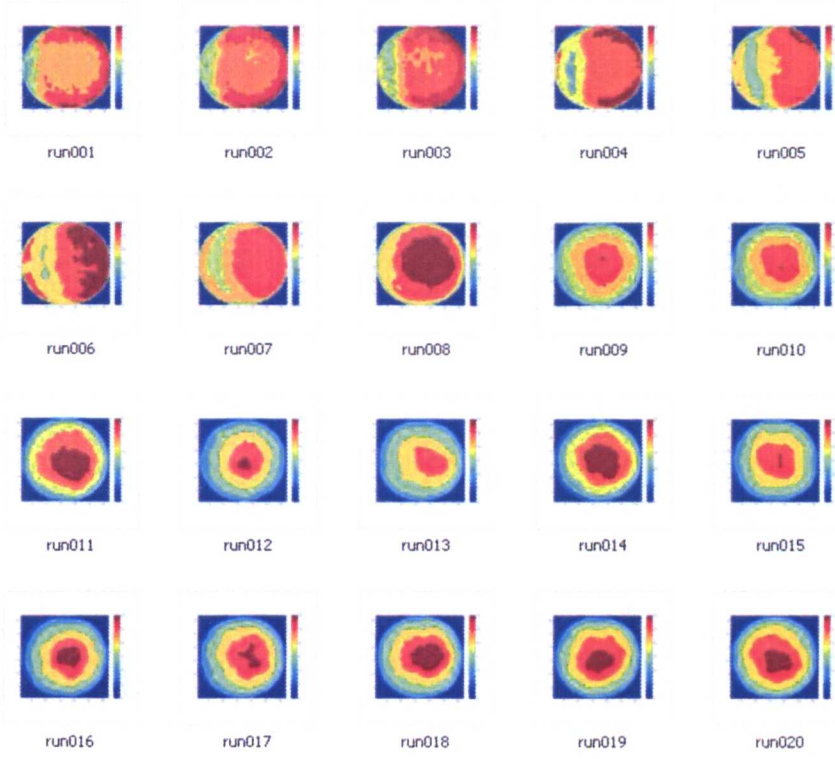


Figure D11- Local voids: air-tap water; Hom. Injector; 127mm column; CondWMS

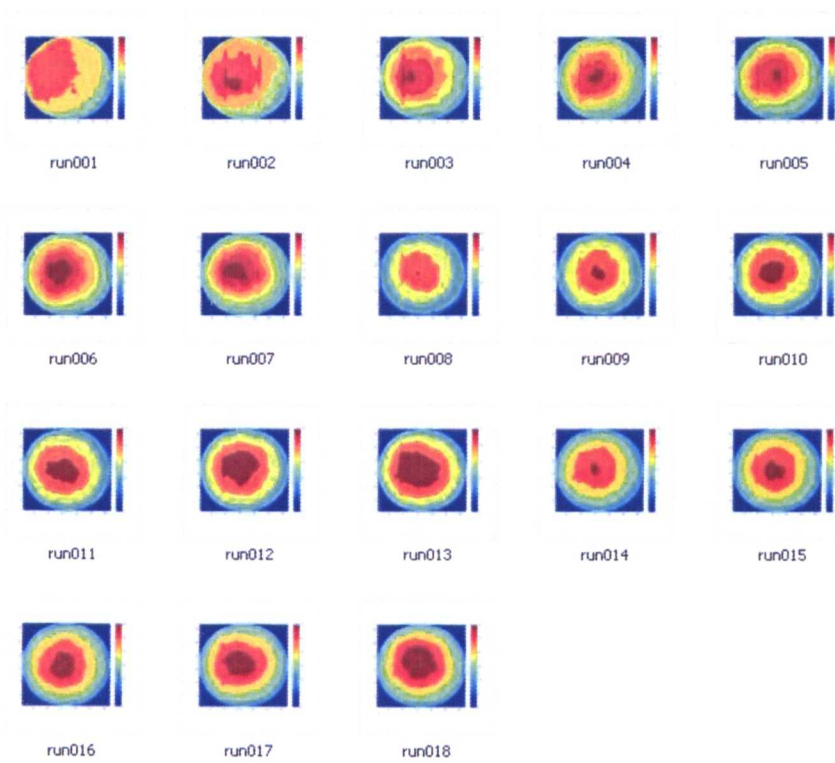


Figure D12- Local voids: air-silicone oil; Hom. Injector; 127mm column; CapWMS

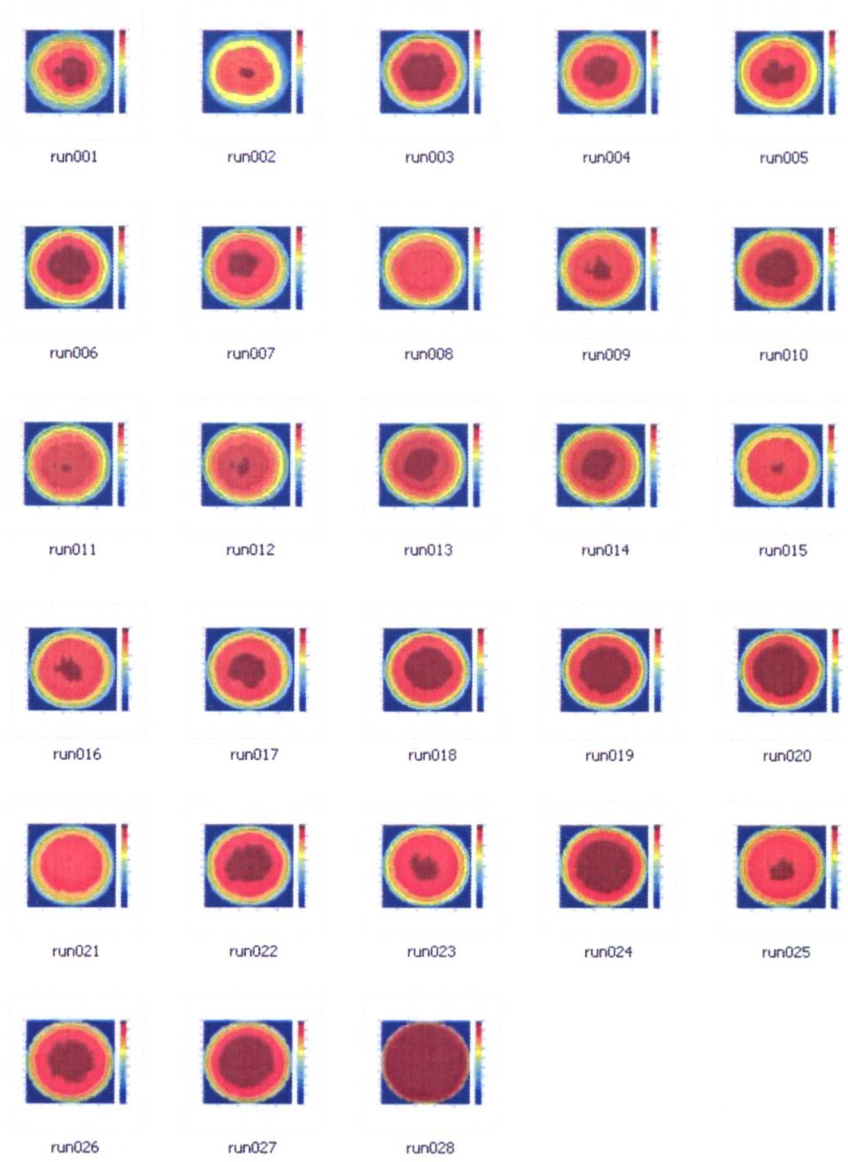


Figure D13 - Local voids: air-silicone oil; Hom. Injector; 67mm column; CapWMS

D5 Limitations of the WMS

Bubble column limitations

The limitation of the wire mesh sensor in stagnant liquids resembling conditions similar to those created by bubble columns were previously investigated by Prasser et al (2001), Richter et al (2002), Wangjiraniran et al. (2003) and more recently by Ito et al (2011). Due to surface tension, the bubbles may stick to the wires as previously mentioned, which is particularly noticeable during the calibration process. In addition, the moving bubbles can be decelerated by the wires. Prasser et al (2001) suggested a minimum limit for the liquid superficial velocity of 0.1m/s, whereas Richter et al. (2002) gave a minimum water mass flux of 100 kg/m²s for the bubble inertial forces to overcome the surface tension forces. However, how rigid are these limits and what about the gas superficial velocities? Visually, the swarm of bubbles at higher gas velocities are able to force their way through the sensor in a stagnant head of liquid, therefore the intrusiveness of the sensor is perhaps more of a problem at low gas velocities.

Bubble size measurements using the wire-mesh sensors showed that even in stagnant liquid, the WMS measures the undisturbed flow. This is independent of the bubbles being broken up by the wires, which may or may not occur, as has been demonstrated with slug flow. The sensor is able to reconstruct the flow structures and measure the void fraction fairly accurately when compared with the level swell. As mentioned in Chapter 3, the sensor is only able to measure bubbles of a certain size, and therefore it is not able to detect the very small (micro) bubbles that are often observed in bubble columns. This is important, as it means the sensor will underestimate the measured void fraction. Conversely, the sensor is not able to measure small drops, and the minimum drop size is estimated to be the drop that can fill the gap between the send

and receive wires to complete the circuit. It is worth mentioning that the sensor is not able to detect solids, porous media, or even surfactants that can be present in bubble columns. Other limitations include cross-talk, and the fact that the DC signal leads to water electrolysis, although this last effect disappears in organic fluids such as oil. As already mentioned, one WMS inside the pipe is not able to detect velocities. It also assumes the flow is in one direction; however, as was demonstrated in this work, some recirculation or flow reversal takes place in bubble columns, which clearly the WMS isn't able to detect.

Viscous fluids

Highly viscous fluids are being used in novel experiments in collaboration between volcanologists and chemical engineers at the University of Nottingham. "Idealised" models of volcanoes are being simulated using large diameter bubble columns, meaning that phenomena such as 'outgassing' that occur in volcanoes can then be studied using glucose syrup, with viscosities up to 200,000 times that of water. This viscosity is comparable to the viscosity of the lava/magma. This level of viscosity presents considerable challenges to the instruments currently being used to study multiphase flows. Clearly the intrusive nature of the WMS means that it struggles to deal with this level of viscosity, with bubbles failing to clear the wires. Pressure builds up and eventually the bubbles manage to pass through the sensor however causing the liquid to overflow from the column. Investigations were conducted to ascertain the viscosity limit for a 16x16 WMS in a 50 mm bubble column (using a liquid that can also be used with ECT). Silicone oil of viscosity 30000 Cs was initially trialled, which was found to be too viscous. Further trials of silicone oil with a viscosity of 5000 Cp was again found to be too viscous. Glucose syrup was diluted with some distilled water to reduce the viscosity to around 1000 Cp, and a viscosity meter was used to

check the viscosities. The WMS operated successfully with 1000 Cp glucose syrup; however, due to the fact that it was slightly conductive, the ECT electronics saturated. A further test was made using golden syrup diluted with distilled water to reduce the viscosity; however, ECT electronics again saturated. The ECT and WMS both worked successfully with silicone oil with a viscosity of 1000 Cp, and therefore this appears to be the upper limit of viscosity for a WMS with a wire spacing of around 3-4 mm. A model volcano with silicone oil that had a viscosity of 1000 Cp with both ECT and the WMS was exhibited for the Royal Society's 350th anniversary. The author demonstrated during that exhibition how the wire mesh sensor is being applied to measure the void fraction in model volcanoes. A more systematic study could be conducted to relate the viscosity to the wire mesh spacing; for example, a higher viscosity liquid than 1000 Cp could be trialled on a 50 mm bubble column, but with fewer wires on the WMS e.g. 8x8. This would however mean a lower resolution.

This type of investigation would be advisable if the sensor is to be used with viscous fluids in the future, and little research has been carried out in this area to date. This has direct industrial applications, for example some oil that is extracted from reservoirs is extremely viscous, and the oil companies try to reduce the viscosity by using steam to make the oil easier to extract. However, this can be a costly method of oil recovery. A further study could also be carried out to investigate volcanoes directly using multiphase instruments. However, they need to be developed to withstand the high temperatures and pressures inside volcanoes. The wire mesh sensor is capable of withstanding high pressures and temperatures up to around 300°C; however, there will be the problem of expansion of the wires at higher temperatures. Further research could be conducted in this area.